National Measurement Laboratory

1979 Technical Highlights

72

National Measurement Laboratory

1979
Technical Highlights

Foreword

This report of technical highlights of the National Measurement Laboratory is the first in a series of annual reviews. It covers selected scientific accomplishments of the Laboratory for the calendar year 1979. A general Laboratory Overview as well as more specific Center and Program Overviews set the framework for the individual technical reports. These reports represent the wide range of Laboratory activities, the breadth of which should be apparent from the overviews themselves. Future editions of this report will present different, but nevertheless representative, selections of technical highlights reporting research activities of the preceding year.

Contents

National Measurement Laboratory Overview

John D. Hoffman
Director

Donald R. Johnson
*Deputy Director
for Resources &
Operations*

Cary C. Gravatt, Jr.
*Deputy Director
for Programs*

Arthur O. McCoubrey
*Associate Director for
Measurement Services*

David T. Goldman
*Associate Director for
Long Range Planning*

Ian R. Bartky *
Edmund A.
  Dimarzio
Lois J. Frolen
David T. Goldman
Charles M. Guttman
Ruth A. Haines
Robert E. Huie, III
Michael J. Kurylo,
  III
Rosemary S.
  Maddock
George P. Lamaze
John Mandel
Arthur O.
  McCoubrey
Hans J. Oser
Robert C. Paule
Gaylon S. Ross, Sr.
Joe D. Simmons
Gilbert M. Ugiansky
Robert W. Zwanzig

* *Staff as of December
31, 1979*

*John D. Hoffman is studying, by means
of a polarizing optical microscope, a
polymer sample which has been crystal-
lized under controlled temperature
conditions while co-workers, Gaylon S.
Ross and Lois J. Frolen look on. This
work is part of an ongoing project
directed toward an understanding of the
nature of crystals and the crystallization
process in industrially important polymers.*

NBS was created by Congress in 1901 to meet the needs of a growing Nation for a unified measurement system. For more than 70 years the Bureau has contributed to advances in science and technology, the growth of industry, and efficiency in the marketplace. In so doing, the Bureau has built a scientific facility and staff that stand with the world's best.

The basic enabling legislation of 1901, as amended, establishes these main purposes and functions of the Bureau:

- The custody, maintenance, and development of the national standards of measurement, and the provision of means and methods for making measurements consistent with those standards, including the comparison of standards.

- The determination of physical constants and properties of materials, of great importance to scientific or manufacturing interests "and not to be obtained of sufficient accuracy elsewhere."

- The development of methods for testing materials, mechanisms, and structures, and the testing of materials, supplies, and equipment.

- Cooperation with other Government agencies and with private organizations in the establishment of standard practices incorporated in codes and specifications.

- Advisory service to Government agencies on scientific and technical problems.

- Invention and development of devices to serve special needs of the Government.

Thus, NBS has both unique and special functions in relation to the Nation's science and technology, and very broad responsibilities as well. As part of the U.S. Department of Commerce, the Bureau carries out its mission in a variety of ways.

The cornerstone of the NBS mission is to serve, for the United States, as the authoritative source of accurate, compatible, and useful physical measurements and, further, to ensure their international compatibility. As the world's leading technological Nation, the United States has a vital interest in ensuring that the world system of measurement is not only internationally compatible but is also sufficiently sophisticated to meet U.S. needs.

The National Measurement Laboratory bears a large part of the responsibility for fulfilling this mission. The Laboratory was created in 1978 as a result of a major NBS reorganization. The following major objectives have been established to guide its programs.

1. Provide the central basis, within the United States of a complete and consistent set of physical and chemical measurements.

2. Provide reference measurement methods and reference materials so that measurements performed in diverse locations for industrial, commercial, or regulatory applications are consistent.

3. Assure that technological development is not hindered by a lack of accurate physical or chemical information.

4. Apply NML capabilities in the physical sciences and measurement technology to solving specific problems of national concern.

5. Provide outstanding comprehension and competence in selected fields of advanced scientific research with long-term relevance to areas of critical importance to NBS and the Nation.

To meet these objectives, the laboratory is managed in a matrix form, with five centers organized generally along disciplinary lines and a number of offices that direct the scientific programs by drawing on the competences in the centers and divisions. The centers cover absolute physical quantities, radiation research, thermodynamic and molecular science, analytical chemistry and materials science.

The cross-cutting programs are nondestructive evaluation, environmental measurements, standard reference materials, standard reference data, nuclear technology, recycled materials, and measurement services. These centers and programs will be described in more detail later.

NML has a staff of 1400. Approximately 80 percent are scientists and engineers, of which approximately 60 percent have earned doctorate degrees. The NML has a total fiscal year 1980 budget obligation of $75.4 million of which $45.8 million is directly appropriated fund (STRS money), $29.6 million is in return for technical services rendered.

One of the most important events for NBS in recent years was the recognition by the Office of Management and Budget and the Congress of the need to widen the Bureau's scientific base (competence building). The National Measurement Laboratory has invested almost $3 million in new programs in a variety of disciplines. In the area of surface science, a program has begun to characterize the structures and reactions of atoms and molecules adsorbed on surfaces. This area will also investigate other surface phenomena, such as catalysis. In electrochemistry, a study has begun of the mechanisms and kinetics of complex electrochemical oxidation reduction processes involving organic compounds. The electrochemistry program will also develop methodologies and detector systems for analyzing selected organic and organo-metallic compounds.

A small angle neutron scattering system has been funded for the NBS reactor. This facility will be used to study the structure and properties of polymers and magnetic and biological materials. Methods will also be developed to probe bulk microstructures for inhomogeneities affecting materials performance. Another new

ompetence area will investigate fundamental mechanisms of chemical and physical processes induced by interaction of ionizing radiation with matter. The results of his research will be used to develop a sound basis for dosimetry measurements and assist those concerned with he problem of the effects of ionizing radiation on biological systems.

A new program involving offsite work by NML scientists is the use of the National Synchrotron Light Source at Brookhaven. In a joint effort with the U.S. Naval Research Laboratory, Bureau scientists will begin real-time in situ studies on materials transformation, analysis of crystal structure, and studies of material properties and phase transitions via electronic bonding properties of atoms and molecules in condensed matter. A new competence area has also been funded to develop a state-of-the-art picosecond pulse laser for studying effects of ionizing radiation, structure of liquids, surface science, chemical kinetics, and molecular and atomic spectroscopy.

In addition to these new competence areas, NML has received Congressional funding for a materials durability program. The need for this research was established by a 1978 NBS-sponsored study on the economic effect of metallic corrosion in the United States. Areas to be emphasized include localized corrosion, elastic plastic fracture, and wear.

The center and program overviews will give more details on these new research areas as well as their many existing programs. Following each of these overviews, members of the scientific staff will make brief technical presentations describing ongoing research efforts. While these presentations cannot give a complete description of NML activities, they do exhibit the far ranging breadth of its research, ranging from the theoretical studies of quarks to quantitative analysis of trace-level organic constituents in alternate fuels.
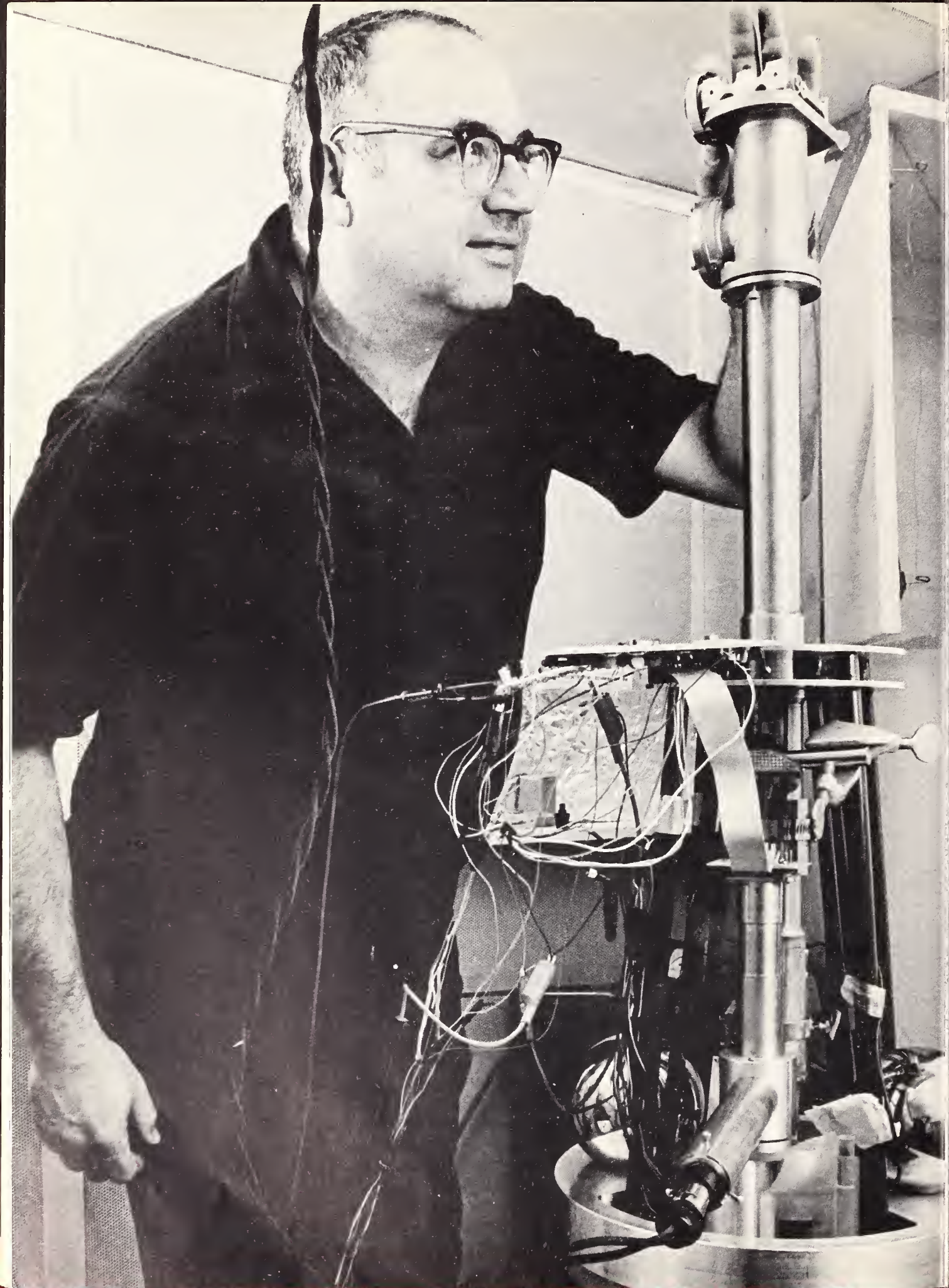
Center for
Absolute Physical Quantities

Karl G. Kessler
Ralph P. Hudson

John W. Cooper
Mary C. Cutkosky
Ugo Fano
Walter G. Schweitzer

Quantum Metrology
Richard D. Deslattes

Anthony J. Burek
Kenneth C. Harvey
Raymond W.
Hayward
Albert Henins
Helen K. Holt
Ernest G. Kessler, Jr.
Robert E. La Villa
Gabriel G. Luther
William C. Sauder
Thomas M. Shay*
James J. Snyder

**Electrical
Measurements and
Standards**
Barry N. Taylor

Norman B. Belecki
Marvin E. Cage
Giovanni
Costabile**
Robert D. Cutkosky
Raymond L.
Driscoll**
Ronald F. Dziuba
Woodward G. Eicke,
Jr.
Bruce F. Field
George M. Free
Forest K. Harris**
Louis B. Holdeman
Paul T. Olsen
William D. Phillips
John Q. Shields
June E. Sims
Jaan Toots
Thomas E. Wells
Earl S. Williams
Edwin R. Williams
Thomas J. Witt**

**Temperature
Measurements and
Standards**
James F. Schooley

Vern E. Bean
Theodor H.
Benzinger**
William R. Bigge

George W. Burns
Michael J. Di Pirro*
Robert E. Edsinger
John P. Evans
George T. Furukawa
Sandra C. Greer**
Leslie A. Guildner
James T. Hall*
James Hines, Jr.
Harold J. Hoge**
James C. Houck
Wilbur S. Hurst
Richard W. Hyland
Robert S. Kaeser
Billy W. Mangum
Walter Markus
Harvey Marshak
Kenneth E.
McCulloh
Paul H. E. Meijer
Earl R. Pfeiffer
Harmon H. Plumb
Martin L. Reilly
John L. Riddle
Gregory J. Rosasco
Margaret G. Scroger
Robert J. Soulen, Jr.
Donald D. Thornton
Charles R. Tilford
Craig T. Van
Degrift
Deborah Van
Vechten*
Bernard E. Welch
Sharrill D. Wood

**Length and Mass
Measurements and
Standards**
Ralph P. Hudson

Richard S. Davis
Marvin Kroll
Howard P. Layer
James E. Taylor

Time and Frequency
James A. Barnes

David W. Allan
Richard L. Barger
Roger E. Beehler
James C. Bergquist*
Joseph V. Cateora
George J. Collins
John Cooper
Dicky D. Davis
Robert E. Drullinger
Lyman B. Elwell
Kenneth M. Evenson
Mark Feldman

David J. Glaze
James E. Gray
Noboru Hironaka
David A. Howe
Wayne M. Itano*
Stephen Jarvis, Jr.
Donald A. Jennings
James L. Jespersen
George Kamas
Gregory M. Kielian
Judah Levine
Lindon L. Lewis
Howard E. Machlan
Robert J. Mahler
Charles H. Manney
Emma Mendez-
Quinones
John B. Milton
Karl B. Persson
F. Russell Petersen
Allan S. Risley
Hugh G. Robinson
Earl W. Smith
Samuel R. Stein
Charles L.
Trembath, Jr.
Fred L. Walls
Marc A. Weiss
Joseph S. Wells
David J. Wineland

Quantum Physics
Gordon H. Dunn

Steven L. Baughcum*
Earl C. Beaty
Peter L. Bender
James E. Faller
Alan C. Gallagher
Katharine B. Gebbie
Sydney Geltman
John E. M.
Goldsmith*
John L. Hall
David G. Hummer
Stephen R. Leone
Jeffrey L. Linsky
Frank Magnotta*
Earl R. Mosburg, Jr.
David W. Norcross
Arthur V. Phelps
Patricia L.
Ruttenberg
Stephen J. Smith
David A. Van Baak*
Richard T. Weppner

*Post Doctoral Staff
**Research Associates
  and Guest Workers

*Gabriel Luther readies the apparatus for measuring the
Newtonian gravitational constant. The change in the period
of a torsion pendulum is caused by the gravitational attraction
of two spherical tungsten masses located near the bottom of
the picture.*

The NBS Center for Absolute Physical Quantities is
responsible for maintaining the consistency and integrity
of the United States' legal physical measurement stand-
ards and for assuring that they are compatible with
international standards. The Center's central mission is
to carry out this responsibility in accord with the needs
of this Nation. The demands of our highly technical
society for measurement accuracy can no longer be met
entirely with artifact primary standards such as meter
bars and kilogram masses. Consequently, as a result of
research to which NBS has made important contributions,
most basic standards of measurement are or soon may be
based not on artifacts but on properties of nature such as
atomic transitions or the speed of light.

As standards have become more sophisticated, the
requirements for improved measurement methods have
intensified and our understanding of the physical world
has deepened. Our physical measurement system is
bound together by the laws of physics, a detailed under-
standing of which is necessary to maintain an accurate,
consistent system, and conversely subjecting these laws
to test.

In order to meet its primary mission, the Center con-
ducts a research program at the forefront of physics.
That program involves measurements of increasingly
high accuracy, made possible by capabilities developed
through the determination of important physical con-
stants and the study of fundamental physical phenomena.
Frequently the measurement expertise of the Center is
applied to important problems relating to other national
issues, such as those involved in the development of
advanced energy systems.

The most strongly mission-oriented programs of the
Center are concerned with measurement standards for
mass, length, time and frequency, temperature, and elec-
trical quantities. They are multifaceted efforts requiring:
basic research; development of sensors, instrumentation,
and methodology; critical evaluation and documentation
of data; international comparison of standards; and nu-
merous measurement services to the public, including
training sessions in measurement procedures, measure-
ment assurance programs (MAPs), and instrument
calibrations. Other programs, which concentrate on ex-
ploratory research into the basic properties of matter,
focus on areas such as atomic and nuclear spectroscopy,

areas that presently offer the best prospects for advancing our metrological capabilities.

Recently, in response to some difficult measurement challenges, the Center has: provided frequency standards stable to 1 part in 10^{13} for navigation, lunar ranging, and military targeting; developed relatively simple but accurate thermometer calibration devices for improving the reliability of clinical and medical diagnostics throughout the country; harmonized optical x-ray and γ-ray wavelength standards to help resolve a discord in muonic physics experiments; used state-of-the-art laser technology to test the validity of Einstein's theory of special relativity; and more accurately measured the gyromagnetic ratio of the proton and the fine-structure constant.

Research to improve our measurement capability and extend our knowledge of fundamental constants and processes is underway or planned in a variety of areas. Frequency, the physical quantity that can be measured with the highest accuracy, can now define our time scale to within 1 part in 10^{13}. However, further improvement is required for modern global navigation systems and for measurement of movements of the earth's crust. Researchers in the Time and Frequency Division are exploring new ideas for improved frequency standards and for methods to coordinate time worldwide at an accuracy of a few billionths of a second.

Recent work in the Center has established an accurate wavelength scale for x-ray and gamma-ray measurements. That work is being extended to both lower energies and higher energies, with potential applications to atomic and nuclear spectroscopy. Until now, the main applications of this new scale have been redeterminations of the scales for muonic and pionic x-ray spectra. Other work in the Center has led to a proposed NBS/Naval Research Laboratory research program using the synchrotron light source now under construction at Brookhaven. This effort will emphasize application of the synchrotron source to descriptive materials science while also providing opportunities for further studies in scattering and spectroscopy.

In the temperature measurement area, current work is establishing a firm foundation for the International Practical Temperature Scale. The improvements in that scale and its extension to lower temperatures have been to a large extent the result of NBS efforts. The future NBS program in thermometry will concentrate on the development of methods for dynamic measurements on transient, non-equilibrium systems such as those encountered in new energy system.

The laser will continue to be an important tool fo standards research. Work is underway to improve stable high-accuracy laser systems and to utilize laser systems i studying atomic and molecular properties and in investi gating the details of molecular interaction processes. A new technique developed by NBS, laser magnetic reso nance, has yielded high resolution information on th structure of excited molecules. Further development o this technique will, for the first time, allow studies o absorption properties of molecules in excited states.

Pioneering NBS work on the measurement of very hig frequencies is leading to the redefinition of the meter i terms of the speed of light. The technique of frequenc measurement has now been extended by NBS scientist working in collaboration with scientists at the Nationa Research Council of Canada, into the visible regio where the measured frequency of light is 5×10^{14} hertz Since the length of a light wave is equal to the speed o light divided by the frequency of the waves, a very precis length scale can be established by measuring the fre quency of a stabilized laser source. Because a value fo the speed of light is agreed upon, accurate frequenc measurements can be used to define the fundamenta unit of length, the meter, in terms of the speed of light.

A fundamental phenomenon of physics, the Josephso effect, has been used by the Electrical Measurements an Standards Division to establish a new basis for accurat voltage measurement. Based on the Josephson effect voltage can be measured in terms of frequency. Smal devices incorporating this capability are now used in NB laboratories to maintain the U.S. legal volt. They replac banks of standard cells used in the past. Development now under way will make these devices, called Josephso junctions, more widely applicable, especially in industry

Modern instrumentation capable of high accurac measurements must not only be automated, but fre quently must also be capable of internal calibration Studies planned in the Center will investigate basic physi cal phenomena that can be utilized to develop self-cali brating devices. Such devices, when perfected, will mak it possible to maintain maximum accuracy in field meas uring instruments without frequent calibrations by NBS

The thrust of all Center programs is to build a stronger more accurate foundation for physical measurements an to improve understanding of the basic phenomena o which our physical measurement standards are based.

Rydberg Values for X- and γ-Rays

Richard D. Deslattes and Ernest G. Kessler, Jr.
Quantum Metrology Group

We have significantly improved the accuracy with which x-ray and γ-ray transitions are known in terms of the Rydberg constant, R_∞. These improved connections have sharpened critical comparisons between theory and experiment for both normal and exotic atoms. In the case of x-ray spectra from normal atoms, our measurements have helped reveal provocatively simple regularities in the departures of experimental results from the predictions of relativistic self-consistent field calculations. Our γ-ray measurements contribute indirect information on the atomic x-ray problem just mentioned but, perhaps more importantly, serve to renormalize many spectra from muonic, pionic, and kaonic atoms. These measurements have yielded enhanced tests of quantum electrodynamics in muonic spectra and improved particle masses in the case of certain pionic and kaonic x-ray spectra.

Our strategy in this work followed the pattern of establishing secondary spectroscopic standards, well known in other spectroscopic regions. Although the measurement chain we developed links the γ-ray and x-ray transitions to the base units of wavelength and frequency quite well, the main scientific interest derives from their linkage to the Rydberg constant, R_∞. Specifically, one extracts from the theory of the hydrogen atom a description of the visible Balmer α spectroscopic complex. Since the theoretical term differences are proportional to R_∞, R_∞ might be said to set the scale of the H-atom were it otherwise known or R_∞ may be derived from the scale of the H-atom as is presently the case. All other atomic calculations are also homogeneous in R_∞, hence the manifest importance of R_∞,

using it as an invariant basis for the establishment of secondary standards.

Today's best knowledge of the Balmer α region of atomic hydrogen is derived from linking (by means of Doppler-free spectroscopy) its non-overlapping components to certain Doppler-free absorption lines in molecular iodine. Of particular interest are those measurements carried out with respect to I_2 absorption features within the 633 nm HeNe laser gain curve. (Subsequent improvement in precision of measurement with respect to I_2 absorption in another region is not of significance for the present effort in view of limitations which are, for the most part, intrinsic.)

Our work therefore took as a token for R_∞ a visible 633 nm HeNe laser locked to an I_2 absorption feature closely related to that used in the Balmer α spectroscopy mentioned above. We used this source to establish a scale with respect to which the spatial period of an almost perfect silicon crystal was determined using x-ray interferometry along a [110] lattice direction. This procedure produced a more accurate (~ 0.1 ppm) local standard in the 0.2 nm (2 Å) region than is otherwise available via classical x-ray methods.

FIGURE 1. Schematic features of the measurement chain established for linking visible and γ-ray (or x-ray) wavelengths. Part a shows the x-ray/optical interferometer used to determine a particular lattice spacing relative to a visible standard (see text). Part b suggests the principle involved in comparing lattice spacings of various specimens so as to reduce the effect of x-ray line uncertainty on the comparison. Part c is a diagram of a classical transmission two-crystal instrument for x-ray and γ-ray wavelength measurement. Our realization of this system provides for absolute angle measurement with high precision thereby establishing (through parts b and a) direct connection to certain visible reference wavelengths and through these to R_∞.
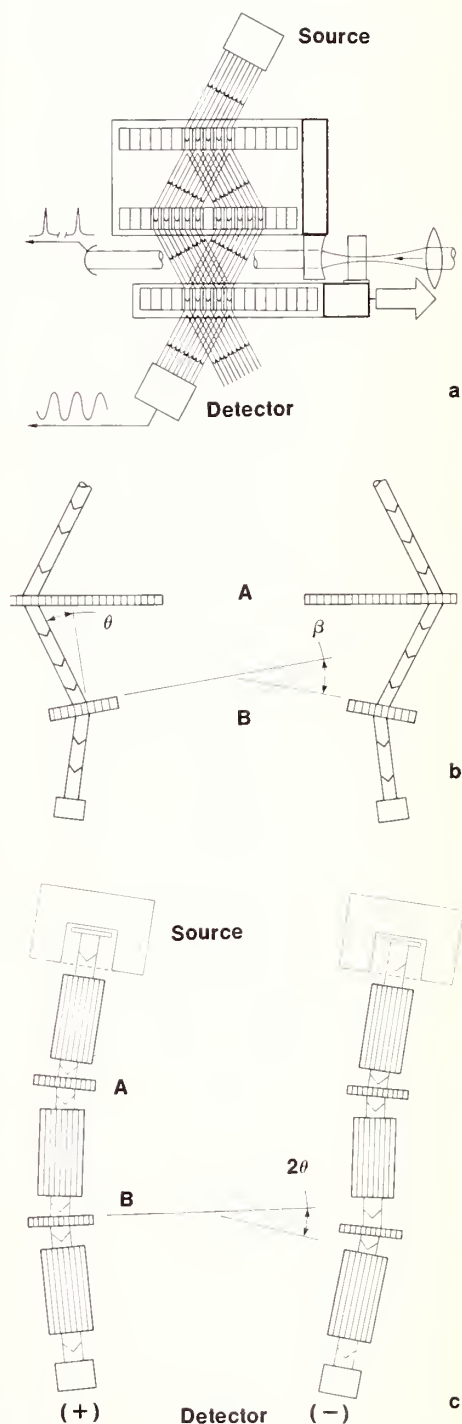
Figure 1

By utilizing non-dispersive techniques we were able to transfer the above calibration to other crystals of Si and Ge having appropriate shapes and orientation for x-ray and γ-ray diffraction measurements. The non-dispersive (or slightly-dispersive) character of these transfer measurements insured that the results were not degraded due to the width and shape of x-ray line sources used. Finally, pairs of crystals calibrated in this way were used in double-crystal x-ray and γ-ray spectrometers with accurate means for diffraction angle measurement. These three steps then relate in a rather direct way the x-ray and/or γ-ray lines measured in the last part to the I_2 stabilized HeNe lasers used in the first part and through them to the fundamental scale unit, $R\infty$. We proceed at this point to comment briefly on the three-step process.

The overall measurement chain is suggested by the three diagrams of figure 1. Figure 1a shows a diagram of the combined x-ray and optical interferometry of the Si 220 repeat distance. Our procedure yielded (by means of observations at a set of optical lock points) an effective number of x-ray intervals transited in a scan of approximately 100 optical half-wavelengths. For the particular Si specimen used, the summary of several hundred measurements was d_{220}(Si, 25 °C) = 192.01707 pm (0.1 ppm). An adjacent specimen was then used in a geometry such as that illustrated in figure 1b to calibrate other specimens and, indeed, other crystal types. Evidently, the procedure suggested in figure 1b gives a null result when standard and unknown crystals agree, independent of x-ray wavelength. In the case of a small difference, one can adopt a perturbation type approach in which it becomes rapidly evident that properties of the x-ray line used are

less crucial to the quality of inter-crystal comparisons than they would be in the case that we had to use fully dispersive techniques. It is also clear that the accuracy required of angle measurement schemes is significantly less in this approach than it would be in a fully dispersive area. This step is not a limiting one at the 0.1 ppm level.

Most recent work has focused on the third step, figure 1c, wherein pairs of crystals calibrated as just described are placed in the symmetrical transmission geometry shown. The interval between the two diffraction conditions indicated is twice the Bragg angle, θ, where the wavelength to crystal-spacing ratio, λ/d is simply $2\sin\theta$. Evidently, accuracy available for λ follows that associated with d, provided measurement precision is adequate and provided the scale for θ is established on an absolute basis. Measurement precision has been obtained by means of polarization encoded angle interferometry which yields a typical sensitivity of 0.05 milli arcsec for ranges of

± 2.5° and ± 15° in first and second generation instruments respectively. Perfect crystal resolutions, typically 20 to 50 ppm, provide a basis for adequate pointing precision provided statistically required source strengths (∼ 10 to 100 Ci) are available. Accuracy, on the other hand, requires that the interferometric angle be calibrated in terms of fractions of the cyclic angle, 2π. To this end, we have employed optical polygons and sensitive nulling autocollimators which furnish indexing precision well below 1 milli arc-sec. Angles between all adjacent face pairs of a polygon sum to 2π regardless of the polygon's in-plane errors and with calculable (small) effects from out-of-plane errors. The process of marking all external angles constitutes a calibration; such calibrations have been established with a precision of about 0.05 ppm but require periodic repetitions to track secular changes in interferometer geometry. Thus the calibration constant operant during a particular γ-ray or x-ray diffraction measurement is in-
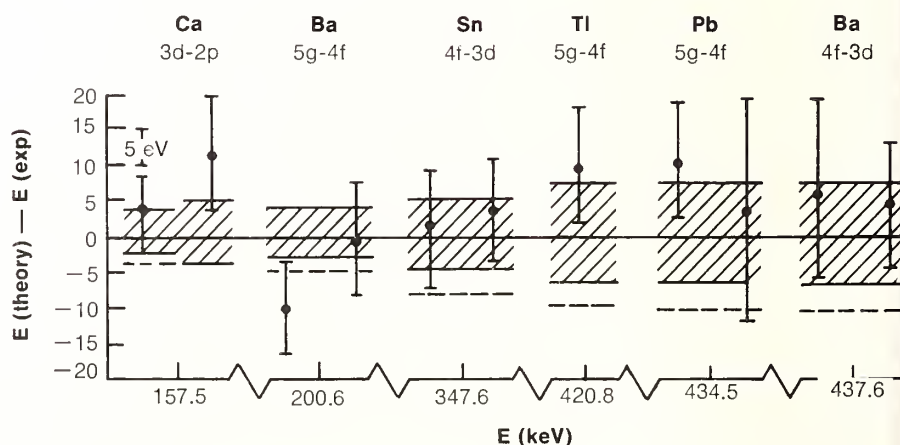
FIGURE 2. Comparison between theory and experiment for a class of outer orbit muonic x-ray transitions. Hatched bands represent estimates of theoretical uncertainties and data have been renormalized as required by new γ-ray data arising from the measurement chain of figure 1. In the absence of this revised energy scale, hatched bands would have centered on horizontal dashed line segments shown. The resulting discrepancy pattern would have been small but significant.

terpolated from a "curve of growth" including prior and subsequent calibration results. We feel that this process may be carried out with errors not greater than 0.1 ppm.

The above-described procedures have been by now applied to frequently used γ-ray secondary standards available from the isotopes ^{198}Au and ^{192}Ir [1] along with those from ^{170}Tm and ^{169}Yb [2]. In separate exercises the same technology has been applied to the W $K\alpha_1$ x-ray line [3], while related procedures were previously applied to Cu $K\alpha_1$ and Mo $K\alpha_1$ [4]. By also utilizing otherwise available high precision results on ratios of K-series x-ray lines to a γ-ray reference [5] together with our measurement of the γ-ray reference [1], it has been possible to appreciably expand this atomic x-ray data base [6]. In general, our x-ray results are significantly poorer owing to the great spectral widths of these lines. On the other hand, both direct and indirect measurements of these lines have permitted us to approach the 1 ppm level.

Two examples illustrating applications of this work are shown in figures 2 and 3. In figure 2 we show a comparison between theory and experiment for a class of muonic x-ray transitions in moderate-to-high Z elements. This comparison is a significant test of quantum electrodynamics, especially the vacuum polarization terms, which had previously shown significant discrepancies [7]. Such a comparison is naturally sensitive to the numerical values of the γ-ray scale [8]. Were we to neglect the scale change then the comparison points would lie on the horizontal segments appearing in figure 2. These results are satisfying in two ways: evidently we have now agreement between theory and experiment in an area of some significance; and,
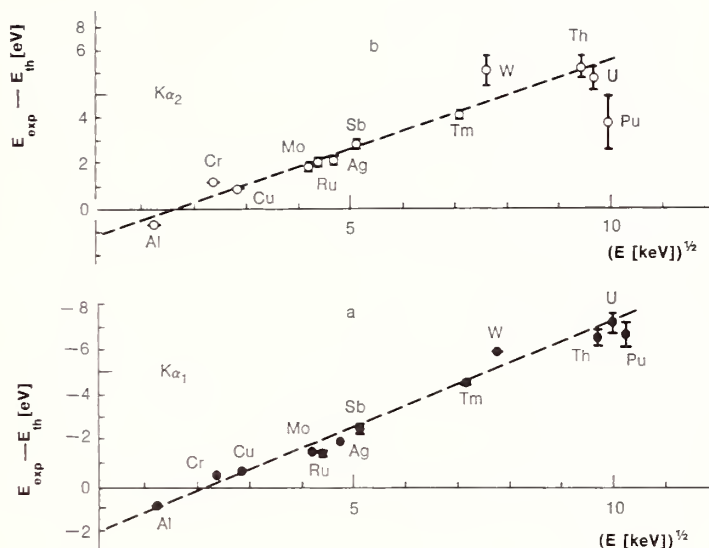
FIGURE 3. Comparison of experimental data as obtained or modified by our work with relativistic self-consistent field calculations in the relaxed orbital limit. Part a of this figure shows results for $K\alpha_1$ lines while part b shows those for $K\alpha_2$. Further results presently being accumulated show similar patterns for the case of more prominent $K\beta$ lines.

the quality of this comparison is no longer limited by lack of knowledge of the reference γ-ray lines.

As a second application area, we turn to x-ray spectra of normal atoms. Over the past several years. relativistic self-consistent field calculations have become available [9]. These have been applied to the case of single inner shell vacancies in the relaxed-orbital limit [10]. When such "term-value" calculations are available with sufficient precision, predictions of emission transitions follow from subtraction of terms. Comparisons between theory and experiment for the $K\alpha$ lines of several elements are shown in figure 3 [11]. The systematic discrepancies shown (which are evidently linear in Z) were not evident in previous data because of their lesser precision. Efforts toward understanding this situation have begun on the theoretical side while, at the

same time, we have undertaken to broaden the available data base by a systematic study of these discrepancies as functions of principal and orbital quantum numbers as well as Z.

Several avenues suggest themselves for future work. These will be pursued as resources permit. Obviously, one wishes to extend the optically controlled scale to higher energies. This is particularly interesting as it becomes possible to reckon a γ-ray cascade summing to the order of $\Delta E = 10$ MeV. In this case, the corresponding mass decrement, ΔM is measurable to ~ 1 ppm. This combination of ΔE and the associated ΔM is sufficient [12] to establish a value for Faraday's constant which is manifestly independent of chemical procedures. Significant nuclear spectroscopy near 2 MeV awaits application of the high resolution capabilities of our instrumentation. A precision measurement of the electron-positron annihilation radiation has been largely developed but remains to be executed. Finally, the progress to date in atomic x-ray spectra suggests the utility and interest of considerably expanding their study which we propose to undertake.

References

A more complete description of this work is in press, Annals of Physics (1980).

[1] Kessler, E. G., Jr., Deslattes, R. D., Henins, A., and Sauder, W. C., *Phys. Rev. Lett. 40*, 171 (1978).

[2] Kessler, E. G., Jr., Jacobs, L., Schwitz, W., and Deslattes, R. D., *Nucl. Instr. and Meth. 160*, 435 (1979).

[3] Kessler, E. G., Jr., Deslattes, R. D., and Henins, A., *Phys. Rev. A 19*, 215 (1979).

[4] Deslattes, R. D., and Henins, A., *Phys. Rev. Lett. 31*, 972 (1973).

[5] Borchert, G. L., *Z. Naturforsch. 31a*, 102 (1976).

[6] Deslattes, R. D., Kessler, E. G., Jr., Jacobs, L., and Schwitz, W., *Phys. Lett. 71A*, 411 (1979).

[7] Rafelski, J., Müller, B., Soffard, G., and Greiner, W., *Ann. Phys. 88*, 412 (1974); Watson, P. J. S., and Sundaresan, M. K., *Canad. J. Phys. 52*, 2037 (1974).

[8] Hargrove, C. K., Hincks, E. P., McKee, R. J., Mes, H., Carter, A. L., Dixit, M. S., Kessler, D., Wadden, J. S., Anderson, H. L., and Zehnder, A., *Phys. Rev. Lett. 39*, 307 (1977); Dubler, T., Kaeser, K., Robert-Tissot, B., Schaller, L. A., Schellenberg, L., and Schneuwly, H., *Nucl. Phys. A 294*, 397 (1978).

[9] Desclaux, J. P., *Atomic Data and Nuclear Data Tables 12*, 311 (1973).

[10] Huang, K-N., Aoyagi, M., Chen, M. H., Crasemann, B., and Mark, H., *Atomic Data and Nuclear Data Tables 18*, 243 (1976).

[11] Deslattes, R. D., Jacobs, L., Kessler, E. G., Jr., and Schwitz, W., Comparison of Relativistic Atomic SCF Calculations with Improved Experimental Data (volume of papers done in honor of Professor Y. Cauchois upon her retirement).

[12] Deslattes, R. D., and Kessler, E. G., Jr., Precision Gamma- and X-ray Energies (to be published in Proceedings of Sixth International Conference on Atomic Masses (AMCO-6) held September 18-20, 1979, in East Lansing, Michigan).

Laser Cooling of Stored Ions

David J. Wineland,
Time and Frequency Division

We have been able to reduce the temperature of a sample of Mg^+ ions to a value < 0.5 K by using radiation pressure. This technique will allow us to reduce in a fundamental way the present limits to accuracy in frequency standards and precision spectroscopy, namely those imposed by the first and second order Doppler shifts. When combined with first-order Doppler cancellation schemes, the method should yield orders of magnitude improvement over present techniques.

In spite of the great accuracy and stability achieved by today's frequency standards, the need for improved standards continues to grow in both the pure and applied sciences. The present uncertainty in the cesium beam frequency standard which defines the length of the second is about 1 part in 10^{13}. Interesting tests of various gravitational theories require clocks which are several orders of magnitude more accurate. In addition, substantially better clocks are needed, for example, in long baseline interferometry and in various navigation systems.

Doppler shifts are the dominant cause of uncertainty in the cesium standard and other existing or proposed frequency standards. When interrogating the frequency of an atomic transition (which provides the basis for the standard) we must use some method to cancel first-order Doppler shifts. However, our ability to do so is limited, and residual shifts always occur. More importantly, we are always required to account for the second-order Doppler effect, or relativistic time dilation shift of the moving atoms. In the Time and Frequency Division, a group including J. C. Bergquist, R. E. Drullinger, Wayne M. Itano, F. L. Walls, and D. J. Wineland has attacked the Doppler shift problem in a fundamental way—by substantially lowering the temperature of atoms.

The "atoms" in our experiments were actually atomic Mg ions confined in a room temperature electromagnetic "trap" which in turn was contained in a high vacuum. (The use of ion traps has another significant advantage in that the confining forces are benign and do not cause significant frequency shifts ($< 10^{-15}$)). The cooling principle can be understood by first noting that the ions are harmonically bound to the center of the trap, hence they oscillate back and forth with an amplitude and velocity governed by the temperature. We can irradiate the Mg ions with monochromatic light from a frequency-doubled dye laser whose frequency is tuned lower than the ion rest frequency but within the Doppler profile. The ions will preferentially scatter photons when they are moving toward the laser, and hence Doppler shift it into resonance. For each scattering event, the momentum of the ion is changed by the momentum of the absorbed photon. After about 10^4 scattering events, substantial cooling below room temperature can be achieved. Figure 1 shows a plot of temperature versus time. The temperature was monitored by observing the induced currents in the trap electrodes. This experiment showed that, although cooling could be obtained, resolution was limited by noise in the detection electronics. A more sensitive measure of temperature could be obtained if we monitored the Doppler width of the optical transition. This was complicated because under the optimum cooling conditions that were used (small compact ion cloud, focused laser beam) cooling rates and heating rates (as the laser was tuned through resonance) could be as high as 1000 K/s. Hence a second, fixed-frequency laser was used to keep the ions cold while the scattered light from

FIGURE 1. Ion temperature versus time when laser cooling is applied for fixed detuning of about 2 GHz. The ions were initially heated above equilibrium temperature with the laser. Laser cooling was then applied for a fixed time until a temperature approaching 0 K was achieved. After the laser is turned off, the ions rethermalize to the ambient temperature owing to collisions with background gas.

the frequency-swept laser was monitored. Figure 2 shows a resulting trace where the ion temperature was about 2.5 K. Similar traces now indicate that temperatures < 0.5 K can be obtained.

The limit on temperature achievable by this method is governed by the effects of recoil. For example, if the ion comes to rest when the "last" photon is absorbed, it will attain the recoil energy of the photon upon re-emission. We have studied this problem theoretically and find that, for Mg^+ ions, where the electric dipole transition is fully allowed, the limit on temperature is about 1 mK. The cooling limit on less strongly allowed transitions, however, can be $<< 1 \mu K$. Even with the presently-attainable temperature, we should be able to reduce the second-order Doppler shift correction in very high resolution studies (e.g., frequency standard) by about three orders of magnitude. The extremely weak relaxation of cold ions in a trap will produce line-widths that are limited only by the natural lifetime, implying $Q > 10^{15}$. Used in conjunction with established techniques (confinement to dimensions less than a wavelength, 2 photon Doppler-free spectroscopy, saturated absorption, etc.) uncertain-

ties in atomic clocks should be eventually lowered by several orders of magnitude.
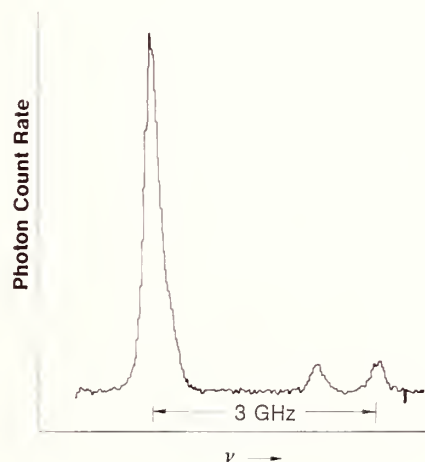
FIGURE 2. Photon scatter rate versus laser frequency showing the three isotopes of Mg^+ in the trap. The sample is maintained cold during the scan by irradiating the low frequency side of the strong line with a second laser. From left to right the three lines are due to the

$$(3s^2S_{1/2}, M_J = -1/2) \longleftrightarrow$$
$$(3p^2P_{3/2}, M_J = -3/2)$$

transitions in the ^{24}Mg, ^{25}Mg, and ^{26}Mg isotopes. At 300 K the Doppler width is approximately equal to the spacing between the ^{24}Mg and ^{26}Mg isotopes ($\cong$ 3 GHz).

Observation of Pure Rotational Transitions in the HBr⁺ Molecular Ion with Laser Magnetic Resonance

Richard J. Saykally[1] *and Kenneth M. Evenson,*
Time and Frequency Division

Molecular ions are extremely important in the upper atmosphere and are thought to dominate the chemical dynamics of the more dense gas clouds found in the interstellar medium. To study ions in these environments by spectroscopic methods, such as radio or far-infrared astronomy, accurate laboratory spectra must first be obtained. Although optical emission spectra have been observed for a fairly large number of molecular ions, the high-resolution techniques required to yield the desired level of accuracy (e.g., microwave spectroscopy, EPR, rf-optical double resonance and, recently, Doppler-tuned laser spectroscopy) have been successfully applied to these species in only a few cases. The difficulty is simply that of producing a detectable number of ions by a means compatible with the respective detection systems. We have recently observed the pure rotational spectrum of a molecular ion—HBr⁺— by the technique of laser magnetic resonance (LMR). This first detection of an ion by LMR is significant because it makes the entire class of paramagnetic ions amenable to study.

Within the last few years, LMR has emerged as a powerful technique for the study of pure rotational spectra of transient species in the gas phase. It exhibits a considerably higher sensitivity than that of competing techniques, such as microwave spectroscopy and EPR, while the resolution attainable is roughly the same. The LMR method itself is intimately related to gas-phase EPR. The appropriate paramagnetic energy levels of an absorbing sample are tuned by a dc magnetic field until their difference frequency equals that of a fixed-frequency source. The prin-
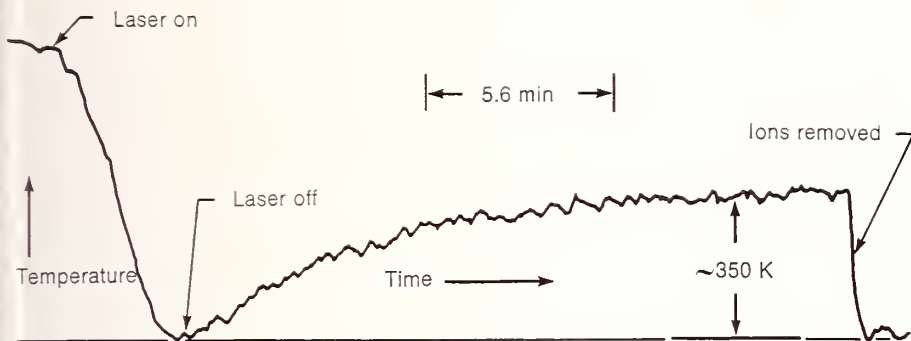
cipal distinction between these two methods is: in EPR the relevant transition is between different magnetic sublevels (M_J) of the same angular momentum state (J), typically occurring in the microwave region for normally accessible laboratory magnetic fields (2 tesla); in LMR the relevant transitions are between rotational states (in molecules) or fine-structure levels (in atoms), and occur in the far-infrared (FIR). In both techniques, the sample is contained inside a resonant cavity. The increased sensitivity of LMR is mainly derived from operating at freqencies about 100 times higher than the microwaves normally used in EPR, and from the fact that absorption coefficients typically vary with the square or cube of frequency in this region. Detection limits for OH radicals are roughly as follows: LMR: 1×10^6 cm^{-3} and EPR: 2×10^{12} cm^{-3}.

A schematic diagram of an optically-pumped FIR laser magnetic resonance spectrometer is shown in figure 1. In this system, a tunable CO_2 laser operating single-mode with a power output near 50 W transversely pumps the gain cell of a FIR laser. The FIR radiation oscillates in the optical cavity defined by a fixed mirror at one end and a movable mirror attached to a micrometer drive at the other. The detection volume of the cavity is separated from the gain cell by a thin polypropylene window set at the Brewster angle. A fraction of the FIR laser power is coupled out of the cavity and into a liquid-helium cooled germanium bolometer by an adjustable 45° coupling mirror.

In the apparatus shown in figure 1, the detection volume is centered between the pole faces of a 38 cm electromagnet. The magnetic field is modulated at frequencies near 5 kHz, and phase-sensitive detection is employed, resulting in a first-derivative line-shape.

Until very recently, all of the species observed by LMR had been produced in various types of atomic and molecular flames reacting inside the detection volume. These flames were generated by using a concentric flow tube mounted on the laser system per-

A = -79.494 THz
B = 0.23845 THz

FIGURE 2. Energy level diagram for the $^2\Pi$ ground state of HBr$^+$. The small lambda doubling in the $\Omega = 3/2$ state (case A notation) is multiplied by 100; that in the diamagnetic $\Omega = 1/2$ state is to scale.

pendicular to the plane of the diagram. In the new spectrometer used to observe HBr$^+$, the flame has been replaced with the positive column of a glow discharge, and the magnetic field is instead produced by a 5-cm diameter by 33-cm-long liquid nitrogen cooled solenoid magnet, which can generate fields up to 0.6 T (6 kG). This new configuration provides for an increased detection volume, and the axial symmetry readily accommodates the electrical discharge. With this apparatus, we have succeeded in detecting several short-lived species, including ground-state oxygen atoms and metastable excited electronic states of O_2 and CO, as well as the HBr$^+$ ion.

HBr$^+$ was generated in a discharge through 1 percent HBr in helium at 133 Pa total pressure and near-ambient temperatures. We observed the two lowest rotational transitions in the $\Omega = 3/2$ spin-component of its $^2\Pi$ ground electronic state, for which the enegy-levels are shown in figure 2. Bromine occurs in nature with nearly equal abundances of the 79 and 81

FIGURE 1. Schematic diagram of an optically-pumped laser magnetic resonance spectrometer.

Extension of Absolute Frequency Measurements to the Visible

Donald A. Jennings, F. Russell Petersen, and Kenneth M. Evenson, Time and Frequency Division

T he direct frequency measurement of visible light was achieved by D. A. Jennings, F. R. Petersen, and K. M. Evenson of the National Bureau of Standards and K. M. Baird and G. Hanes of the National Research Council, Ottawa, Canada. This experiment paves the way for frequency-based spectroscopic investigations in the important visible spectral region which are potentially a thousand times more accurate than measurements of wavelength. In addition, this experiment may eventually lead to a new definition of the meter.

H (Tesla)

FIGURE 3. The laser magnetic resonance spectrum of the $J = 3/2 \rightarrow 5/2$ transition of HBr^+ observed at 251.1 μm (CH_3OH). This spectrum was recorded on a single scan with a 0.1 s time constant. The positions of the eight doublets represent the hyperfine splitting in the $M_J = -3/2 \rightarrow -1/2$ Zeeman transition. The doublet splitting is due to the lambda doubling.

mass isotopes, and the reduced masses of these two forms of HBr^+ are nearly identical; thus we observe both isotopes simultaneously. Since each Br isotope has a nuclear spin of 3/2, we find a pattern of two sets of four lines, additionally split into doublets by the small "lambda-doubling" interaction. The additional hyperfine splitting from the proton is too small to resolve. This pattern is shown in figure 3.

When completed, the analysis of these LMR spectra will produce the first information on the hyperfine

structure of HBr^+, as well as precise values for the rotational constants and lambda doubling parameters. These, in turn, can be used to deduce spin densities, charge distributions, and accurate bond lengths for the molecule. It will be very interesting and informative to observe the effects of the net positive charge on these properties by comparing them with properties of corresponding neutral molecules. More exciting, however, is the prospect of detecting other similar ions by the same method. In particular, HCl^+ may be of considerable astrophysical interest. Measurement of LMR spectra of this and other ionic species will provide the accurate rest frequencies required to perform astronomical searches for these molecules in interstellar clouds.

[1] Department of Chemistry, University of California, Berkeley, California 94720.

Visible frequency measurements were achieved by a laser frequency synthesis chain, shown in a very simplified way in figure 1. This experiment links the cesium frequency standard directly with the frequencies of 10 hyperfine lines of $^{127}I_2$ at the frequency of the second harmonic of the 260 THz He-Ne laser. The measurements were made in seven steps from cesium to iodine by using only frequency counting techniques. Actually, 14 lasers and 6 klystrons were used in the heterodyning experiments, finally culminating in the 520 THz visible frequency. The measurements of the first six steps were made at NBS and the final one at NRC. (The NBS 260 THz laser was transported to Ottawa for comparison with NRC's 260/520 THz composite laser in the final step.) The schematic illustrating step 7 is shown in figure 2.

The NRC composite laser contained the iodine cell, the lithium niobate doubling crystal, and the 260 THz gain tube. The 260 THz frequency was stabilized to hyperfine components of the P(62) 17-1 transition in $^{127}I_2$ by using saturated absorption techniques, and the 520 THz radiation generated from the 260 THz by the doubling

13

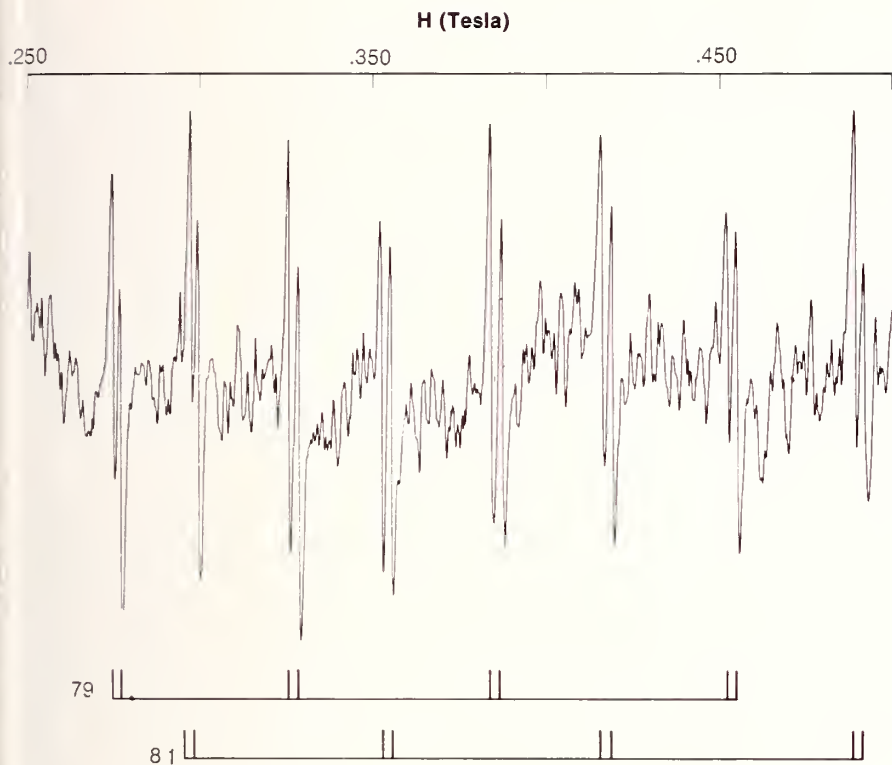# Fine Structure Constant Determined to an Accuracy of 1 in 10⁷

P. Thomas Olsen and
Edwin R. Williams,
Electrical Measurements and
Standards Division

A value for the fine-structure constant accurate to 1 in 10⁷ has been obtained from a new determination of the proton gyromagnetic ratio. This achievement has helped test one of modern physics' most fundamental theories: quantum electrodynamics (QED). QED is believed to provide an exact description of all atomic phenomena which do not directly involve nuclear forces, weak interactions, or gravitation.

The key to obtaining the new value was our development of a unique magnetic technique to measure accurately the relative positions of each of 1000 turns of wire on a single-layered precision solenoid. This new method allowed us to determine directly the proton gyromagnetic ratio, γ_p' (where the prime indicates that the protons are in a spherical sample of pure H_2O at 25 °C). We then obtained an order of magnitude improved value for the fine-structure constant, α, by combining our result for γ_p' with the values of other already well-known constants, such as the speed of light in vacuum, c, and the Rydberg constant for infinite mass, R. The fine-structure constant is the fundamental expansion parameter of QED and therefore must be accurately known in order to compare critically the calculated values of various QED-dependent quantities with their experimentally determined values. Indeed, with the new value of α, QED is able to predict the value of the electron g factor, g_e, with an uncertainty of only about 3 in 10¹⁰. This theoretical result may then be compared with the experimental result obtained from the electron magnetic moment anomaly, $a_e = (g_e - 2)/2$, as obtained in a recent experiment at the University of Wash-
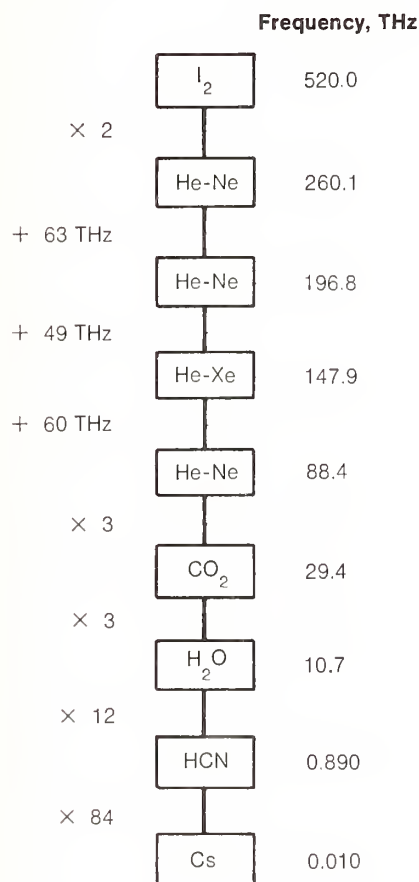
FIGURE 1. A block diagram of the laser frequency synthesis chain connecting the Cs frequency standard with the visible.

crystal. The visible frequency measurements were made simply by combining the 260 THz beams from the two lasers on a high-speed photodiode. The beat frequency was displayed on a spectrum analyzer and measured with an adjustable marker oscillator and counter. The estimated error in the beat frequency measurement is ± 0.5 MHz, and the overall error is ± 60 MHz—a result of the free running nature of two lasers in the frequency synthesis chain. The frequency of the O - hyperfine component (nearest the center of the second harmonic output at 520 THz) is $t_0 = 520,206,837 \pm 60$ MHz.

Work is in progress to reduce the large uncertainty.

The redefinition of the meter in terms of the second is now a real possibility. In fact the CCDM (Consultative Committee for the Definition of the Meter) at its meeting in June 1979 has proposed that:

"The meter is the length equal to the distance travelled in a time interval of 1/299 792 458 of a second by plane electromagnetic waves in a vacuum."

The era of speed of light measurements may cease as the value for the speed of light becomes fixed in the redefinition of the meter.

The measurement of this iodine line with frequency measurement technology some 50 years after this line was first measured by wavelength techniques represents a truly exciting advancement in the science of measurement.
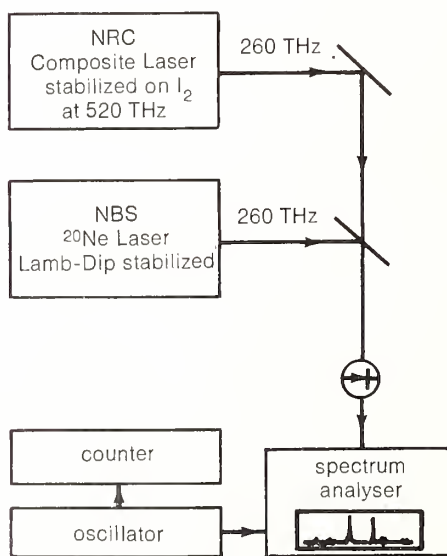
FIGURE 2. A block diagram showing how the last step to the visible in the frequency synthesis chain was accomplished.

ngton. The agreement found is deemed
acceptable in view of the incomplete
nature of the theoretical calculations.

The quantity γ_p' is an atomic constant
which relates the angular frequency,
ω_p', with which the proton precesses
when placed in a magnetic field, B, to
the value of the field: $\gamma_p' = \omega_p'/B$.
Thus, the experimental determination
of γ_p' requires the measurement of both
the proton precession frequency and
the magnetic field which produces the
precession. Determining the precession
frequency is relatively straightforward
when nuclear magnetic resonance
(NMR) techniques are used. More
challenging is the critical problem of
making an accurate dimensional mea-
surement of the precision solenoid so
that the magnetic field produced by a
known current can be calculated.

In our experiment, the solenoid was
single layered and wound on a hand
lapped, fused silica form. Its critical
dimensions were measured by a mag-
netic induction technique which located
the current in the windings. Coils A
and A' in figure 1 formed a linear
differential transformer which located
the axial position of the current injected
into selected turns of the solenoid.
Coils A and A' were connected so that
their output voltages cancel when cen-
tered on the activated turns of the sole-
noid. A servo system locked the coil
assembly to the null point with a pre-
cision of better than 0.05 μm. A mirror
(corner cube, M') located in the center
of the coil assembly was part of a
laser-interferometer system, with the
reference mirror (M) connected to the
end of the solenoid. Thus, with the aid
of a computer-automated system, the
relative position of successive turns
could be recorded. We chose to acti-
vate 10 turns at one time, and then
move the current injector to successive
10 turns until information about all
1000 turns of the solenoid was ob-
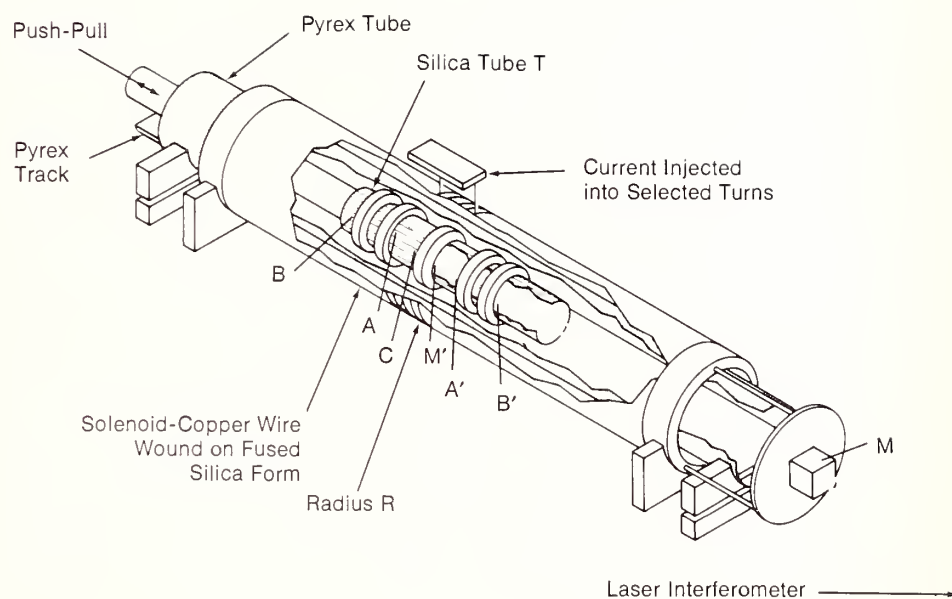
FIGURE 1. Solenoid dimensional measurement system used to determine the axial position
and radial variations of the wires. The five coils A, A', B, B', and C are attached to a
silica tube T and can be pushed or pulled along the axis of the solenoid. Coils A and A'
locate the axial position of the injected current and coils B, B', and C form a diameter-to-
voltage transducer. Mirrors M and M' are part of a linear interferometer. The Pyrex
tube is evacuated.

tained. Coils B, B', and C formed a
radius-to-voltage transducer which
measured the variations in the radius of
the injected current. The voltage in-
duced in coil C was inversely propor-
tional to the radius of the activated
turns of the solenoid. To detect small
changes we first "bucked out" most of
the voltage in coil C by using the two
coils, B and B'. At the same time that
we were bucking out the voltage in
coil C, we were also increasing the
sensitivity of this three-coil system to
changes in the radius R of the solenoid
because the voltage in coils B and B'
increased when the radius R increased.
This three-coil radius-to-voltage trans-
ducer was then calibrated by having a
few turns of wire on both ends of the
solenoid that were 25 μm larger at one
end and 25 μm smaller at the other end.
With this system, the axial position and
the radius variations of the turns of the

solenoid were measured to an accuracy
of 0.05 μm. No turn deviated from that
expected of a perfect solenoid by more
than 2 μm.

These improved dimensional meas-
urements along with other refinements
in the experiment provided a 0.21 ppm
(parts per million) value for γ_p', which
in turn yielded for the fine-structure
constant $\alpha^{-1} = 137.035963(15)$ (0.11
ppm). This value of α^{-1} is (0.33 $\pm$
0.14) ppm less than the value of α^{-1} de-
rived from measurements of the anom-
alous magnetic moment of the elec-
tron and its current best QED estimate.
The 0.14 ppm uncertainty in this com-
parison represents a test of QED which
is a factor of ten more precise than all
previous tests. The small, 0.33 ppm
remaining discrepancy has the follow-
ing possible explanations: (1) it could
be purely statistical, about a 2 per-
cent probability by chance; (2) the

Superconducting Thermometric Fixed Point Devices

Robert J. Soulen, Jr. and James F. Schooley, Temperature Measurements and Standards Division

QED numerical calculations of a_e are not yet complete and in addition, are sufficiently complex so that they could easily be in error; (3) one or more of the five fundamental constants required to obtain α^{-1} from γ_p', γ_p' itself, and/or the experimental value of a_e could have unknown systematic errors; or (4) there could be something wrong with the basic physics, i.e., quantum electro-dynamics. We are now working to extend this test of QED to yet another decimal point by carrying out a new γ_p' experiment with an accuracy of a few parts in 10^8. It is expected that by the time this new effort is finished, the theoretical calculations of a_e as well as its experimental determination will also be completed and that an unequivocal test of a QED prediction to an accuracy of a few parts in 10^8 will be possible.

The narrow and highly reproducible superconductive transitions of 10 materials have been shown to be useful as reference temperatures (fixed points) for definition of temperature scales which are being developed in the region of 0.01 to 20 K. Two devices incorporating these 10 superconductors are now available through the Office of Standard Reference Materials.

One of the cornerstones of the International Practical Temperature Scale (IPTS)—the lingua franca for thermometry—is a set of reference temperatures, or fixed points. These well delineated and reproducible points are defined by the change in physical state of selected materials. Their stability is used to hold the temperature scale and to check temperature calibrations. Notable examples are the melting point of gold, the triple point of water, and the boiling point of oxygen. When the IPTS was last formulated (1968), it was not extended downwards, partly because few conventional fixed points were available below 13.8 K. Traditional phase transitions (boiling points, melting points, triple points) of all materials except ^{3}He and ^{4}He take place at higher temperatures. Therefore, fixed points needed for this region must be found in phase transitions occurring *within the solid state*. A program was started at the NBS in 1968 with assistance from the NBS Office of Standard Reference Materials[1] to develop cryogenic fixed points based on the phenomenon of superconductivity. There now exist ten such points be-

tween 0.015 K and 7.2 K, five of which have been incorporated in a new provisional temperature scale, EPT-76, which extends the IPTS-68 down to 0.5 K.

The fixed points are provided by two devices, Standard Reference Material (SRM) 767 and (SRM) 768, which are produced at NBS and distributed by the Office of Standard Reference Materials. Each unit contains five very pure, well characterized materials for which the phase transitions into the superconductive state occur over a temperature region of
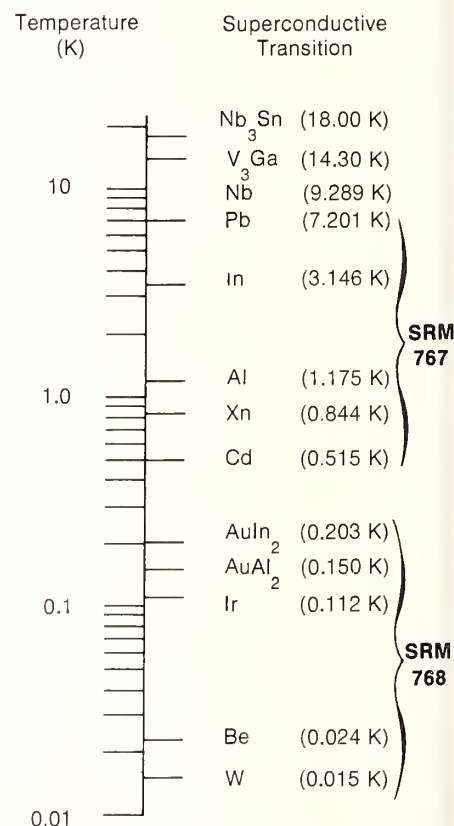
FIGURE 1. Superconductive transition temperatures of several materials. The 10 materials included in the Standard Reference Material units are shown together with materials at higher temperatures which are being examined as candidates for fixed points.

---

[1]Standard Reference Materials are well characterized materials or simple artifacts with special chemical or physical properties certified by NBS.

about 0.001 K and for which the reproducibility of the observed transition temperature, designated T_c, is $\pm$ 0.001 K or less. The materials used in the two devices and the assigned T_c's are shown in figure 1.

Observation of the phase change is based on the fact that in the normal state above T_c the electrons exhibit a very weak magnetic response to an impressed alternating magnetic field, while in the superconducting state the electrons respond with perfect diamagnetism. This very strong effect is easily registered as a change in mutual inductance in two coils surrounding the material. A typical transition is shown in

figure 2, in this case for the element indium which is used in SRM 767. Provided that the ambient magnetic field as well as the measuring field are less than 1 μT (0.01 Gauss), some of the transitions have been found to reproduce to within $\pm$ 0.0001 K.

Referring to figure 1, we see that the materials included in the SRM units do not cover the full temperature range over which superconductivity is known to exist. We are, therefore, conducting research to produce satisfactory samples of Nb and Nb_3Sn to extend the region covered by superconducting fixed points to a full three decades in temperature.
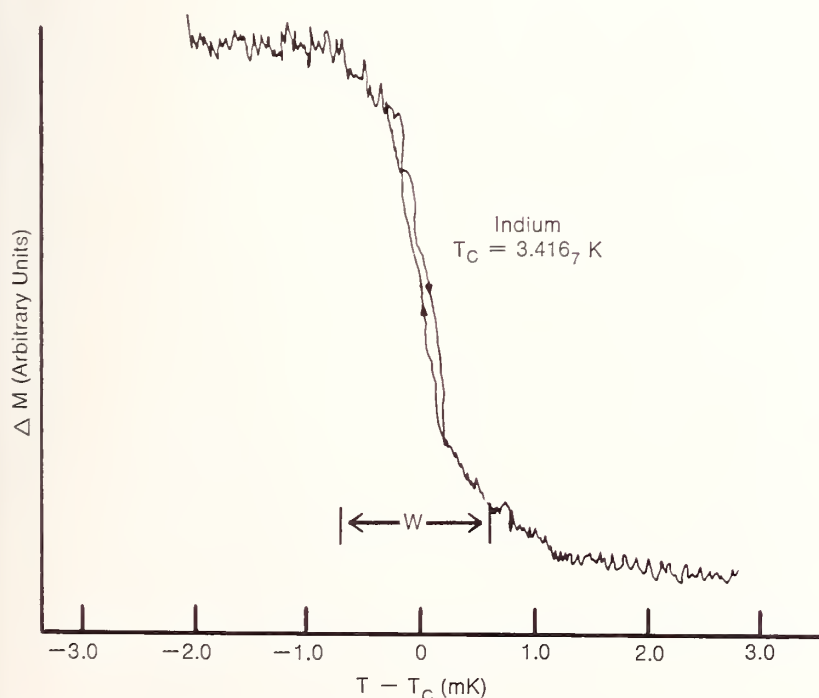
FIGURE 2. Indium phase transition. The change in mutual inductance, ΔM, in a set of coils surrounding the In sample is plotted versus the output of an ac resistance bridge monitoring a calibrated germanium resistance thermometer. The transition temperature is chosen as the mid-point of the transition, while the width W of the transition is defined as the temperature interval, centered about T_c, corresponding to 80 percent of the change ΔM.

Improved Laser Test of the Isotropy of Space

John L. Hall, Quantum Physics Division, for himself and Alain Brillet, Joint Institute for Laboratory Astrophysics

We report the application of stabilized laser techniques to the precision test of one of the fundamental concepts of Relativity Theory. These measurements confirmed the isotropy of space to $\pm$ 2.5 parts in 10^{15}, and represent a 4000-fold improvement over the best previous test.

One of the most meaningful and significant human activities might be called "guessing with inspiration." Indeed, we daily are called upon to invent an "outside reality" with only clues and shards of evidence for input. But I am thinking here of the kind of scientific guessing, or concept synthesis, that occurs in a field perhaps only a dozen times a century. This year we celebrate the 100th birthday of the genius that made three such contributions in a single year.

Einstein's inspired guesses and their consequences must surely have been troublesome to conventionalists at the time. In explaining why Michelson and Morley had failed to see a few tenths of a wavelength shift when their apparatus rotated, Einstein gave up such reasonable physical ideas as simultaneity, absolute time, and absolute motion. New and unfamiliar ideas were introduced such as the equivalence (for discussion of physical effects) of all intertial reference frames, the physical equivalence of mass and energy, a kind of symmetry between time and length, and certain group properties of frame transformations. Outrageous and deeply troubling paradoxes were identified, such as the "twins" paradox. Other "unphysical" effects were predicted, such as the shrinking of a physical bar along the direction of its motion. This shocking physical theory is still of fundamental interest to us now 74 years

later since these remarkable counter-intuitive predictions are found to be in perfect agreement with every experiment performed up to now. Indeed, a major industry is based on the conversion of a bit of the binding energy of the uranium nucleus into commercial amounts of heat energy. Synchrotrons sweep their frequency as the accelerated particles gain mass. Time dilation of the muon's internal decay clock gives a distance range in the CERN laboratory some 29 times the distance that light could travel in one (proper) decay time.

It is not surprising that experimentalists have found this special theory of relativity a powerful stimulus to the invention of precision experiments against which to test the theory. In the 1950's and 60's, high resolution techniques based on the Mössbauer effect provided some major advances to confirm our knowledge of the validity of special relativity (the so-called interaction of local clocks with distant matter and "anisotropy of inertia" experiments). The other new experimental tool, lasers, provided a first glimpse in 1964 of the dramatic enhancement of measurement sensitivity that lay ahead.

This first important experiment was performed in a special isolated laboratory near MIT by Charles Townes, Ali Javan, and their coworkers. They pointed out for the first time the gain in sensitivity possible through the use of frequency techniques to measure small length changes. Unfortunately, their laser experiment was troubled by systematic noise sources, probably inertial forces arising from the periodic motion, and the attained sensitivity was only somewhat better than that obtained in the 1930's by G. Joos using Michelson's original techniques. Thus, a large amount of technical development of laser techniques has been a necessary preliminary to testing rela-

tivity theory with lasers. It is probably fair to say that the first really meaningful laser test of special relativity was only recently completed. In this measurement, Alain Brillet (from the Laboratoire de l'Horloge Atomique, in Orsay) and I, using appropriate laser techniques, repeated the famous Michelson-Morley "Isotropy of Space" experiment of 1887. Impressively enough, one still finds a null result, in agreement with Einstein's postulate, even with a measurement sensitivity 4000-fold improved over the best previous experiment (the 1964 experiment of Charles Townes et al.).

Our experiment is timely in three ways. First (and trivially), it is appropriate to do an improved relativity experiment in an Einstein celebration year. Secondly, laser techniques have been developed to the point that they permit a really major advance in sensitivity. Thirdly, it is probably true that all physical laws are approximate statements: As the measurements become more refined and sensitive, a larger and larger fraction of "outside reality" needs to be taken into account in describing the system under study. Ultimately then, one might expect some image of the cosmic status in the microscopic physics which we can probe. Recently, several lines of investigation, but most notably radio noise thermometry done from above the earth's atmosphere, lead to the conclusion that we are probably moving at speed ~ 400 km/s relative to the 3 K blackbody background radiation remaining from the primordial "big bang". Thus it is interesting to see whether the supposed small lack of isotropy in physics "in the large" will have an ultimately observable effect on extremely sensitive laboratory experiments which test some kind of local isotropy. (Honesty compels me to note that the experimental basis for this third, philosophical point

did not even exist when the experiment was first undertaken. Basically we had developed new measurement techniques that appeared useful for several fundamental experiments, and the NBS management supported the work on these completely adequate and reasonable grounds.)

Our experiment was designed to be highly sensitive, clear in its physical interpretation, and free of problems involving spurious effects. Its basic concept can be understood by considering figure 1. Fundamentally, we were comparing the laser frequency defined by an etalon of length with the laser frequency defined by an optical frequency standard. As depicted in figure 1, a 3.39 μm laser was servostabilized to the standing wave condition in an isolated and stable passive Fabry-Perot etalon. The laser, Fabry-Perot interferometer, and associated electronics were mounted on a large granite slab on a table which could be slowly rotated around a vertical axis. Information about the length of the interferometer was implicitly carried by the wavelength (frequency) of the portion of the laser beam which left the table along its rotation axis and which was directed over to another table to be optically heterodyned with an "isolation" laser. This laser was frequency-stabilized relative to another 3.39 μm laser which was in turn frequency-stabilized relative to the saturated absorption peak in CH_4. In following Javan and Townes, we had thus prepared a highly sensitive readout of the optical length of the Fabry-Perot etalon through the use of frequency measurement techniques. To see whether there was a measurable spatial anisotropy in our laboratory, the laser and Fabry-Perot etalon part of the apparatus was rotated slowly and we looked for a change synchronized with this rotation. It is natural—perhaps inevitable when
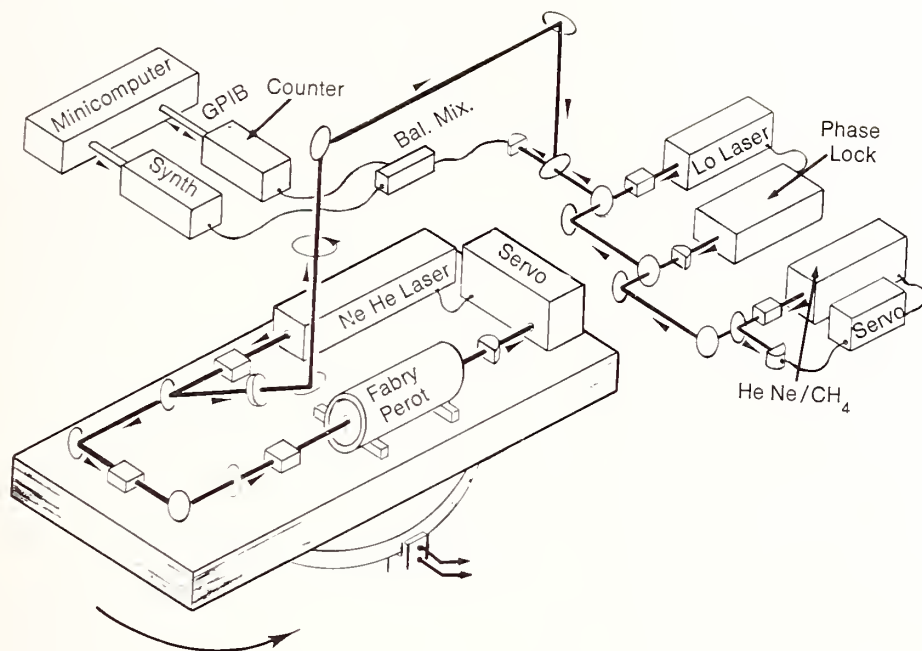
FIGURE 1. Schematic of isotropy-of-space experiment. A He-Ne laser (3.39 μm) is servostabilized to a transmission fringe of an isolated and highly stable Fabry-Perot resonator, with provision being made to rotate this whole system. A small portion of the laser beam is diverted along the table rotation axis to read out the cavity length via optical heterodyne with an "isolation laser", which is stabilized relative to a CH_4-stabilized reference laser. The beat frequency is shifted and counted under minicomputer control, these frequency measurements being synchronized and stored relative to the table's angular position. After 30 minutes of signal averaging, the data are Fourier-transformed and printed out, and the experiment is repeated.

the sensitivity is sufficiently high—that some such synchronous perturbation will be observed. We saw a signal at the table rotation frequency of some 200 Hz excursion, representing a 2×10^{-12} length change of our Fabry-Perot etalon. Its origin is now understood as a gravitational stretching of the interferometer which occurred because of residual asymmetry in the mounting of the reference etalon when there was a slight misalignment of the rotation axis from the vertical. A 10-fold smaller signal was observed at the double frequency of the table rotation, which is the spectral location expected for a genuine anisotropy signal. However, considering that the laboratory axes were rotated relative to the hypothetical "preferred direction in space" by the earth's rotation, a true cosmic anisotropy signal would show a further modulation every 12 sidereal hours.

We observed that the spurious signal at the double rotation frequency was essentially fixed in the laboratory coordinate system, and so averaging over a few days in 12 or 24 sidereal hour blocks reduced our spurious signal essentially to zero. This null result represented a fractional synchronous length variation below 2.5 parts in 10^{15}, and this limit represents a 4000-fold improvement over the MIT laser experiment. Further, if it is supposed that the earth's inferred velocity of ~ 400 km/s is the relevant one to be used in the coordinate frame transformation, this "laserized" Michelson-Morley experiment represents the most demanding test yet of the Einstein-Lorentz transformation.

As mentioned above, the laser heterodyne techniques provided a very high sensitivity in these experiments. If the spurious background signal could be reduced or eliminated, a factor of at least 1000 further improvement would be possible. In this domain, general relativistic effects (the earth's gravitation) would cause a vertical spatial anisotropy of the type we can detect, $\frac{1}{2}$ (GM/R) $(1/c^2)$ $(1/R) \sim 3 \times 10^{-17}$. Unfortunately, such a vertical experiment would be hopelessly contaminated by gravitational distortion of the Fabry-Perot etalon itself. A more promising direction for growth is to redo the Kennedy-Thorndike measurement that shows the equivalence of the transformation of length and time. Extreme care would be necessary to avoid drifts, since the only modulation in this experiment arises from the earth's motion. For example, a temperature stability of 50 μK for 1 month and creep rate noise below 10^{-11} per day^2 would allow a 20-fold improvement on the original experiment of Kennedy and Thorndike.
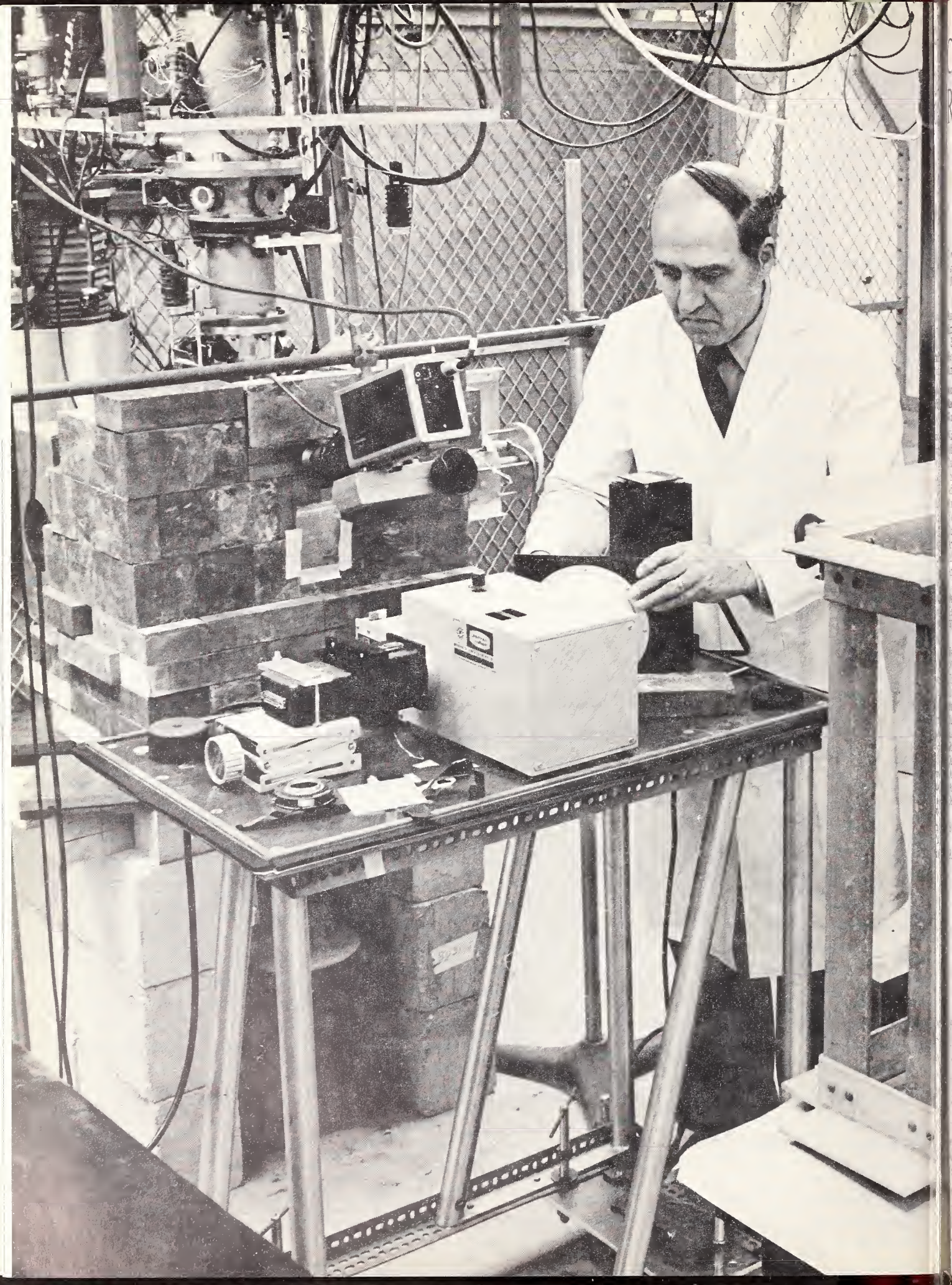
Center for Radiation Research

Chris E. Kuyatt
Wayne A. Cassatt, Jr.

Ronald Colle
Elmer H. Eisenhower, Jr.
Henry T. Heaton, II
James S. O'Connell

Atomic and Plasma Radiation
Wolfgang L. Wiese

Nicolo Acquista
John M. Bridges
David G. Cooper
Charles H. Corliss
Jeffrey R. Fuhr
Ronald L. Greene*
Victor Kaufman
Daniel E. Kelleher
Arthur K. Kerman
Jules Z. Klose
Andrea M. Malvezzi**
Oscar Manley**
Georgia A. Martin
William C. Martin, Jr.
Tsu-Jye A. Nee
William R. Ott
Timothy L. Pittman
Donald H. Priester**
Joseph Reader
James R. Roberts
Larry J. Roszman
Phillip M. Stone**
Jack Sugar
John Weiner
Andrew W. Weiss
Jean-Francois Wyart**
Stephen M. Younger*
Romuald Zalubas

Nuclear Radiation
Randall S. Caswell

Robert L. Ayres
Stephen M. Baloga
James W. Behrens
Charles D. Bowman
Patricia Burt**
Jacqueline M. Calhoun
Larry Cardman**
Allan D. Carlson
Lucy M. Cavallo
Bert M. Coursey
John J. Coyne
Hall Crannell**
John B. Czirr
Michael Danos
William R. Dodge
Kenneth C. Duvall
Charles M. Eisenhauer
Larry Fagg**
Everett G. Fuller
Henry M. Gerstenberg
David M. Gilliam
Daniel Golas**
James A. Grundl
Evans V. Hayward
Alan T. Hirshfeld
Dale D. Hoppes
John M. R. Hutchinson
Kenneth G. W. Inn
Ronald G. Johnson
Arthur K. Kerman
George P. Lamaze
John W. Lightbody, Jr.
Richard Lindgren**
Larry Lucas
Marcia D. Maltese

(Continued)

Robert Placious adjusts equipment for characterization of x-ray fluorescent intensifying screens. Measurements are made, on an absolute basis, of the total light output and spectral distribution of the x-ray excited fluorescence from radiographic intensifying screens. This unique facility utilizes mono-energetic x-ray production together with highly sensitive radiometric detection equipment. These screens are universally used in almost all medical, and in many industrial radiographic procedures to maintain good image quality while reducing x-ray exposure.

T he Center for Radiation Research has a unique mission. It provides high accuracy radiation measurement techniques and quantitative data about atomic and nuclear radiation processes. These outputs are required for the safe and effective use of radiation in key technologies. Center activities cover the electromagnetic spectrum starting at the infrared, through the visible, the ultraviolet, and vacuum ultraviolet, to x-ray and nuclear gamma rays. Particle radiations include electrons, positions, protons, deuterons and neutrons below 140 million electron volts. Our facilities include a 140 MeV electron linear accelerator, a 240 MeV electron storage ring for synchrotron light, many lower energy accelerators, a polarized electron source, plasma devices, and many sophisticated spectrometers with computer assisted data acquisition.

During the past year, CRR has directed special attention to several areas of growing national concern. One of these areas, ionizing radiation health and safety, has attracted a large amount of public and institutional concern. At the request of the Senate Committee on Commerce, Science and Transportation, the Center is cooperating with the Conference of State Radiation Control Program Directors. Together, we are reviewing the need for an intermediate level of calibration services such as regional facilities to better couple NBS laboratories with State and industrial needs. This review will contribute to an updated long-range plan and budget for ionizing radiation measurements.

CRR is working with the State of Illinois to set up a pilot regional calibration laboratory, with Florida to set up a calibration facility for low-level survey instruments, and with the University of Michigan on the testing of personnel dosimetry performance. Special measurements were made on dosimeters used near the Three-Mile Island nuclear power plant. Natural matrix radioactivity standards, such as human lung and liver, are being prepared for environmental monitoring. We are working on dosimetry measurements and standards for radiation sterilization, a process which replaces the use of carcinogenic ethylene oxide. Measurements of the response of x-ray screens are part of our work on the technology for reducing patient exposure. Because of the need for increased cooperation between the various agencies concerned with ionizing radiation, the Center is represented on two

Wilfrid B. Mann
Xavier K. Maruyama
Leonard C. Maximon
Emmert D. McGarry
Michael M. Meier
Sydney Meshkov
Vernon W. Myers
James R. Noyce
James O'Brien**
Gerald Peterson**
Mark Reeves**
Henry Rosenstock
Francis J. Schima
John C. Schleter
Roald A. Schrack
Ivan G. Schroder
Robert B. Schwartz
William E. Slater
Daniel Sober**
Valentine Spiegel, Jr.
William Stapor**
Richard D. Starr*
Michael P.
    Unterweger, Jr.
Oren A. Wasson
Elisa Wolynec**
Lungwen Yap**

Radiation Physics
Lewis V. Spencer

Martin J. Berger
L. Randall
    Canfield '
Robert Celotta
Barrett E. Cole
Randolph Culp**
Joseph Dehmer**
Charles E. Dick
Steve R. Domen
David L. Ederer
Margarete Ehrlich
Raymond L. Falge,
    Jr.
Annija D. Galejs
John C. Hamilton*
John H. Hubbell
Lanny R. Hughey
Jimmy C.
    Humphreys
Paul J. Lamperti
Donald R. Lehman**
Harry Levine**
Robert Loevinger
Thomas P. Loftus
Toh-Ming Lu**
Thomas B.
    Lucatorto
Robert P. Madden
William L.
    McLaughlin
Thomas J. McIlrath
Caroline Mehlman**
Stanley R.
    Mielczarek
Joseph W. Motz
John Noakes**
Hideo Onuki**
Rathindra Pal**

David R. Penn
Daniel T. Pierce
Robert C. Placious
Daniel Polansky
John S. Pruitt
Ronald W. Rendell*
Jack C. Rife**
Edward B. Saloman
Stephen M. Seltzer
Christopher G.
    Soares
Julian H. Sparrow
John Sutherland**
Nils Swanson
Peter Takacs**
Bernard J. Waclawski
Harold H. Walker
James T. Weaver, Jr.

Radiometric Physics
Jack L. Tech

Robert L. Booker,
    III
Robert J. Bruening
Kenneth L. Eckerle
Joel B. Fowler
Jon C. Geist
Warren K. Gladden
Jack J-G. Hsia
Henry J. Kostkowski
Ernest Lewis, Jr.
Donald A.
    McSparron
Fred E. Nicodemus
Charles H. Popenoe
Robert D. Saunders,
    Jr.
A. Russell Schaefer
John B. Shumaker,
    Jr.
James H. Walker
John F. Ward, III
William R. Waters,
    Jr.
Victor R. Weidner
Charles R. Yokley
Edward F. Zalewski

**Radiation Source
and Instrumentation**
Samuel Penner

John B. Broberg
Louis Costrell
Stephen C. Ebner
David C. Green
Eric R. Lindstrom
Isador J. Livant
Anthony B. Marella
Joseph Parrington**
George Rakowsky
John E. Rose
Julian K. Whittaker
Mark A. D. Wilson

*Post Doctoral Staff
**Research Associates
    and Guest Workers

recently formed interagency committees on ionizing radiation.

CRR is working to improve the state-of-the-art in optical radiation measurements. Better measurements are needed, for example, in solar and atmospheric monitoring and by the electro-optics and lighting industries. To make available to the lighting industry the new radiometric scale, which will eventually replace the current scale based on the candela, 175 lamps are being calibrated on both scales for simultaneous distribution. Progress toward the 0.1 percent radiometry needed in solar monitoring is being made through quantum-based calibrations of silicon photodiodes, by improved characterization of black body sources, and through intercomparisons of NBS radiometry standards. Improved measurements of UVR radiation are made possible by new source standards and by accurate measurements of spectroradiometer response. Provision of characterized detector packages on a rental basis enables users to measure the spectral response of their detectors and to test the performance of their measurement systems. New measurement assurance programs are being developed for diffuse reflectance and for retro-reflectance.

Several of our activities contribute to the Nation's energy programs. Measurement and calculation of the spectra of highly-ionized heavy ions are essential to the diagnostics of fusion-plasma devices. Ionization rate measurements now in progress will provide benchmark data for analyzing heavy ion impurities in Tokamak fusion devices. Vacuum ultraviolet radiometric calibrations and portable transfer source standards provide the measurement base for accurate measurements of radiation from fusion plasmas. Radiation phenomena, such as plasma line broadening and dielectronic recombination, are being investigated as possible new plasma diagnostic techniques. Resonance neutron radiography is being developed as a non-destructive method for obtaining accurate values for the total mass of fissionable isotopes. This method is expected to be useful in calibrating measurement devices for nuclear fuel rods as well as for waste and scrap from nuclear fuel reprocessing plants. Accurate measurements of neutron cross sections are being made for both fission and fusion reactions. Integral and differential neutron fields continue to be developed for

he calibration of neutron detectors used in fusion research, nuclear reactors, and personnel dosimetry.

The Center has a dedicated synchrotron radiation facility, SURF-II. This device produces electromagnetic radiation in a narrow, intense, highly-polarized beam with a continuous and accurately known spectrum from the infrared through the visible and into the extreme ultraviolet. This tunable, intense radiation is being applied to several new scientific and technical opportunities. Many of these activities involve collaboration with other Centers of NBS or with laboratories outside of NBS. Ultraviolet photodiode detectors are now being calibrated for photon energies up to 250 eV. This capability was used in a collaborative program with Los Alamos to measure photoemission yields of several promising cathode materials. Several calibrations were carried out on spectrometers for space experiments and fusion plasma diagnostics. A new spectrometer calibration facility, under construction with NASA funding, will give more accurate and convenient calibrations. During the past year our new high-flux normal-incidence monochromator came into full operation, and has been used to measure the angular distribution of photoemitted electrons from individual vibrational levels of highly excited molecules. This monochromator also has been used to study Stark mixing in high Rydberg autoionizing states of atoms and molecules. Further studies on excited state dynamics will utilize fluorescence measurements to investigate ion de-excitation processes. Using another monochromator, we have observed high pressure helium microbubbles in thin aluminum films by measuring the pressure-broadened helium resonance in absorption. Scientists from the Naval Research Laboratory are studying insulators by using reflection, photoemission and fluorescence. Scientists from Brookhaven National Laboratory are installing a circular dichroism apparatus for measurements of biomolecules. Apparatus is being built in collaboration with the Surface Science Division to study the photodesorption of ions from absorbates at surfaces. We do not have space to describe all of the activities at SURF-II, but these examples illustrate the wide range of activities being carried out with synchrotron radiation.

High energy photons and electrons are excellent probes of nuclear structure. The coupling of photons and electrons to charge, current, and magnetic moments of nuclear constituents is well known from quantum electrodynamics, and the flexibility of electron scattering allows energy and momentum transfer to the nuclear system to be varied independently. Using a high-current 140 MeV linear electron accelerator, CRR scientists have investigated nuclear structure using electron scattering, photon scattering. and electrodisintegration. Recent elastic photon scattering measurements from ^{12}C showed a surprisingly large electric quadrupole component. Similar measurements on ^{16}O will be of even greater theoretical interest. Elastic electron scattering has yielded an improved value for the ^{12}C nuclear radius which has become a world standard. Similar measurements on ^{4}He will provide a critical test of quantum electrodynamics.

In electron scattering, the cross section is measured as a function of energy and momentum transfer. In electrodisintegration, however, outgoing particles or induced radioactivies are integrated over all of the final states of the scattered electron. An entirely new type of experiment has recently been pioneered by CRR scientists in which the yield of particles is measured as a function of the incident energy. From analysis of such measurements it is possible to locate and measure the strength of the E1 and E2 giant resonances that result in proton and α particle emission. Results on ^{58}Ni, ^{60}Ni and ^{62}Ni show important E2 components in the α channel.

The ultimate experiment would detect both the scattered electron and outgoing particle in coincidence. Such experiments would require a 100 percent duty cycle (CW) electron accelerator and would be crucial in going beyond the classical description of nuclear structure and reactions in terms of elementary neutrons and protons; that is, in determining the effects of many-body correlations, virtual pions, and excited nuclear states on nuclear structure. These opportunities are so important that we have begun, with DOE funding, to develop a prototype 185 MeV room-temperature CW electron accelerator. In addition to demonstrating the feasibility of building a 1 to 2 GeV machine using the same technology, the prototype accelerator will be a powerful tool in its own right for nuclear physics.

These vignettes cover briefly only a fraction of the CRR programs. Some of these programs and others are described in more detail on the following pages.

Radioactivity Standardization

Wilfrid B. Mann
Nuclear Radiation Division

Radioactivity, like fire, has potential for both benefit and harm, and the increasing variety of its applications and public awareness of its hazards have brought challenges to the NBS Radioactivity Standardization group. We are meeting those challenges in a variety of ways. Nearly 2000 samples of some 50 different radionuclides were calibrated or issued as standard reference materials (SRMs) in 1978. Co-operative programs with nuclear-medicine and environmental-monitoring quality-control groups allowed the staff to assure correct instrument calibrations much beyond their ability to supply direct services.

Such cooperative measurements-assurance programs work to establish the traceability of radioactivity measurements to those of NBS. Why NBS? Because we are the legal promulgator of standards of the national radioactivity-measurements system. The term traceability may not be completely apt, but it is being used more and more by regulatory agencies to connote measurements that are demonstrably in agreement with those of the National Bureau of Standards.

Each year NBS must decide on those radionuclides for which standards are most urgently needed. Once those decisions are made, our work begins. In the last three years, an efficiency-extrapolation coincidence method employing a pressurized proportional counter and efficient gamma-ray spectrometers has been used to establish calibrations for ^{67}Ga, ^{99}Mo, ^{99m}Tc, ^{111}In, ^{123}I, ^{169}Yb, ^{195}Au, ^{201}Tl, and ^{203}Pb—all radionuclides now used in nuclear medicine. The same system was used to calibrate ^{145}Pm (used in a pressure measuring device) and ^{140}Ba-^{140}La (a significant monitor of nuclear-fuel burnup). Measuring the radionuclides released from the burning of coal required standards of several naturally occurring radionuclides. For example, a standard of flyash from the burning of Eastern United States coal was developed in which the sample is highly homogeneous and is certified for ^{226}Ra and ^{228}Ra content.

For some applications, preparing the SRM in the proper form and checking its uniformity offer more of a challenge than the basic calibration. Standards which are prepared to check the yields from chemical procedures are of this type. Such natural matrix standards of human lung and liver, soil from Rocky Flats, Irish Sea sediment, and river and lake sediments are being developed. Homogenization of these materials is a significant challenge which is being met partly by borrowing techniques from powder-mixing technology. Ultimately, not only the radioactivity of these materials will be measured, but the chemical forms will be examined. For example, we expect to tell users approximately how much of the plutonium in a sample is in the form of high-fired oxides.

Radioactivity calibrations are unique in that a value for a standard applies only for an instant. The radioactive decay law allows the standard to be used at a later time if accurate values for the half life and the associated uncertainty are known. For a number of years, the half lives of most radionuclides used as standards have been measured at NBS. The probability per decay for radiations is also required if their emission rate is to be deduced from the activity given for a standard. Well-calibrated germanium spectrometer systems have been used to measure gamma-ray probability-per-decay (P_γ) values for many recent standards.

Such spectrometer systems are used in monitoring at nuclear power plants, or wherever mixtures of radionuclides must be assayed, and special standards are prepared for calibrating the efficiency of these systems as a function of energy. A mixture of 9 radionuclides with well-established P_γ's was developed for this purpose, and commercial suppliers now submit samples of each batch of their standards of this mixture to NBS to establish explicit traceability. Longer-lived radionuclides, such as ^{133}Ba and ^{152}Eu, which emit gamma rays at several energies, are also now available from NBS as standards, and a mixture of ^{125}Sb, ^{154}Eu, and ^{155}Eu is being studied as a possible standard. For some common counting conditions, large errors can occur if the summing of coincident radiations is not taken into account, and computer programs are now being used to calculate these corrections for frequently encountered radionuclides.

Once a calibration has been established for any gamma-ray-emitting radionuclide, the response of NBS pressure ionization chambers to a known activity is measured relative to that of a ^{226}Ra source producing a comparable current. This preservation of what would otherwise be only a temporary calibration, in the case of short-lived radionuclides, eliminates the need for frequent direct recalibrations. Doing so allows the group to offer an efficient calibration service for many radionuclides for which the demand does not justify preparing SRMs.

The preservation of calibrations, and a comparison of them on an international scale, is also accomplished by the routine transmission of calibrated gamma-ray-emitting solution standards to the Bureau International des Poids et Mesures (BIPM) and to the International Atomic Energy Agency

(IAEA) for measurment on their ionization chambers. NBS calibration techniques are also checked by international intercomparisons of the radioactivity concentration of split samples of the same master solution. Such intercomparisons, arranged by BIPM, have recently taken place for ^{139}Ce, ^{134}Cs, ^{137}Cs, and ^{55}Fe. In the first two cases the agreement was quite good, with 22 laboratories agreeing to within 0.7 percent for the ^{134}Cs, but preliminary reports show a much greater spread for the more difficult ^{137}Cs and ^{55}Fe.

International cooperation on *applications* of radioactivity has been aided in the past few years by the International Committee for Radionuclide Metrology (ICRM), with active participation by NBS. The ICRM spectrometry group has organized comparisons of gamma-ray emission-rate measurements with germanium spectrometer systems for ^{152}Eu and ^{133}Ba; collected information on impurity searching, pertinent nuclear data, and germanium detector stability; and initiated, through IAEA, a study of random pile-up effects in gamma-ray spectrometry. Symposia were held by the low-level group to determine the need for specific natural-matrix standards of radioactivity, and the group has organized international cooperative projects for their production and distribution.

Any accurate radioactivity measurement requires good technique in addition to good standards, and several members of the NBS group have contributed to written standards for the use of ionization chambers, germanium and NaI (Tl) detectors and liquid scintillation counters. Much NBS effort went into the writing of the *Handbook of Radioactivity Measurement Procedures,* prepared as Report 58 by a group of experts for the National Council on Radiation Protection and Measure-

ment. It describes in detail many of the concepts and techniques mentioned here. Further, the NBS Radioactivity Standardization group has become known for its willingness to help those with radioactivity-measurements problems, through seminars or direct technical assistance. This attitude has brought them considerable satisfaction, and a very harried existence!

Spectra of Highly-Ionized Atoms

Joseph Reader,
Atomic and Plasma Radiation Division

T he development of controlled fusion reactors depends greatly on the ability to observe and understand the physical processes taking place in their very hot plasmas. One of the methods used to diagnose these plasmas is the observation of line spectra emitted by the various ionic species present. Such observations provide information about the temperature of the plasma, impurities, and spatial and temporal properties. For lighter ionic species much of the basic atomic data needed to interpret these observations are already on hand. However, for heavier ions, such as those with $Z \geqslant 20$, relatively few data are available. The problem is particularly acute for Tokamaks, because of their use of aperture limiters to prevent stray particles from striking the interior wall of the torus. Atoms from the limiter, which is usually made of a refractory metal such as molybdenum or tungsten, are sputtered into the discharge, where they become highly ionized and significantly affect the plasma conditions. Knowledge of the spectra of the ions of these heavy elements is therefore of great importance. By studying spectra of laser-produced plasmas our group has made progress during the past year toward providing new data about these highly ionized atoms. The work was done in collaboration with G. Luther and N. Acquista.

Data about highly ionized atoms were obtained in two separate experiments. First we focused the light from a 3 GW Nd/glass laser onto flat metallic targets to produce plasmas of various elements. The spectra were recorded on a 10.7 m grazing incidence spectrograph. Typical laser pulses were 15 J in 10 ns. By varying the energy and duration of the laser pulses we

FIGURE 1. Plot of the energy (in cm^{-1}) of the 5s configuration in the Cu isoelectronic sequence. Z_c is the net charge of the atomic core seen by the valence electron. Theoretical values are from Cheng and Kim (Ref. [1]).
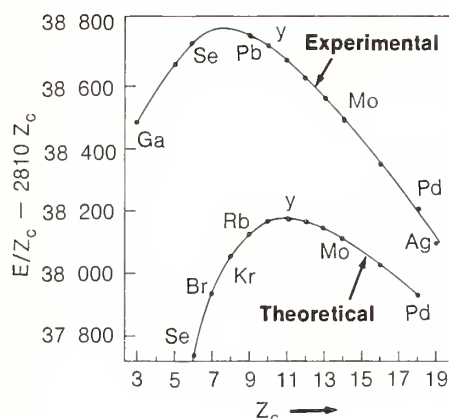
were able to distinguish spectra due to different ionization stages. Analysis of the data yielded the spectra, electronic energy levels, and ionization energies of ions in the zinc and copper isoelectronic sequences to Sb^{21+} and Sb^{22+}, including the important ions Mo^{12+} and Mo^{13+}. As an example of the re-

sults, figure 1 shows the energy of the 5s configuration in the Cu sequence, along with the values obtained in fully relativistic calculations [1]. The calculations predict the general variation of energy very well, although the absolute values are somewhat displaced. As the scale is greatly expanded here the absolute differences between the two curves are actually not large; for Mo the difference is only 0.5 percent.

In the second experiment we transported a 2.2 m spectrograph and target chamber to the Los Alamos Scientific Laboratory. There we used a very powerful (100 GW) Nd/glass laser to generate still higher stages of ionization. Spectra were recorded with laser pulses of 30 J in 300 ps. With these observations we extended the Zn and Cu isoelectronic sequences to W^{44+} and W^{45+}. These results represent the longest isoelectronic sequences ever observed as well as the highest stages of ionization recorded with diffraction gratings. Figure 2 shows an isoelectronic sequence plot for the 4s-4p resonance lines of Zn-like ions.

These experiments also produced significant results for molybdenum. Besides the resonance lines of Mo^{12+} and Mo^{13+}, two of the most important lines used in Tokamak diagnoses are the resonance lines of the Mg and Na-like ions, Mo^{30+} and Mo^{31+}. Until recently these lines had been observed only in Tokamaks. Confirmation of their proposed origins (ion and transition) were thus critically needed. Previous observations of laser-produced Mo plasmas [2] gave spectra that could not be interpreted unambiguously. In the present work we studied ions in the Mg and Na sequences from Sr^{27+} to Pd^{34+}.
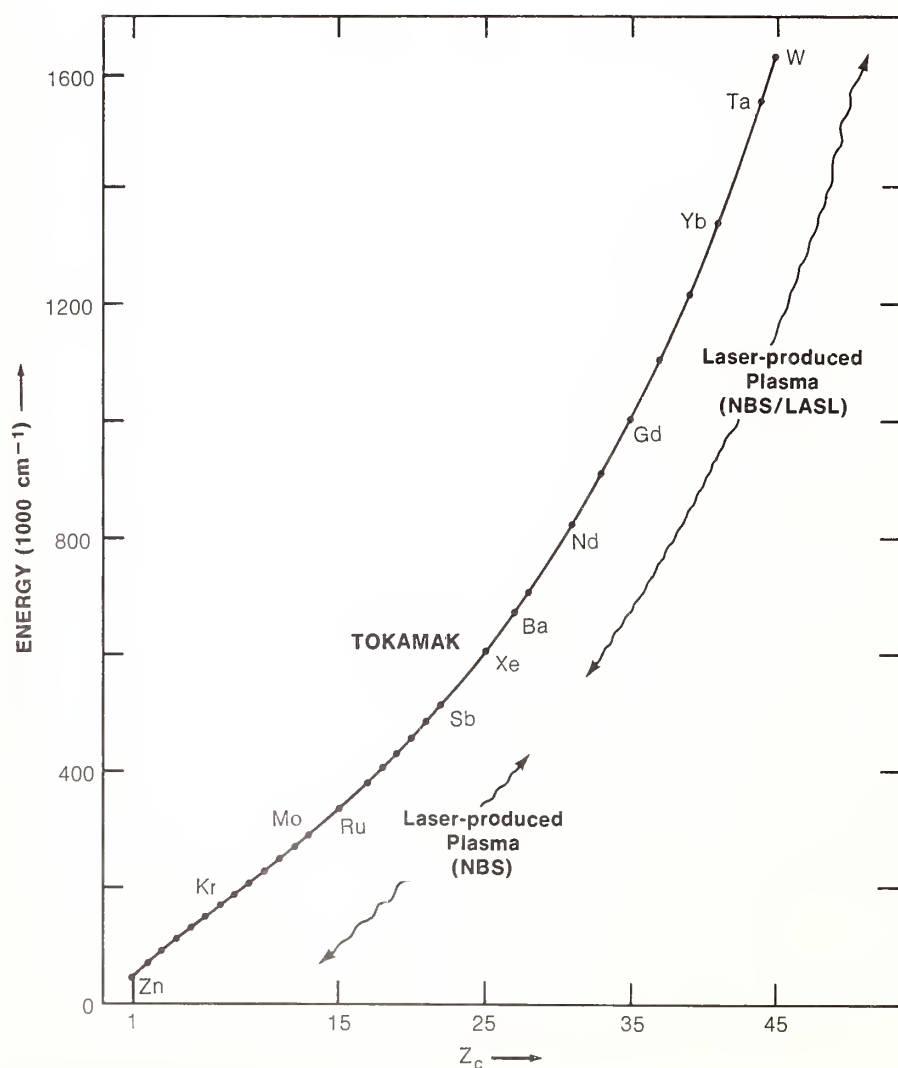
FIGURE 2. Isoelectronic comparison of the $4s^2$ $^1S_0$–$4s4p$ $^1P_1$ transitions in the Zn isoelectronic sequence.

Figure 3 shows a plot of two transitions in the Na sequence that are nearly coincident in Mo^{31+}. From the isoelectronic regularities we could identify the observed lines and correlate them with Tokamak observations. Wavelengths for Mo are compared in table I. For some lines the wavelengths agree well, confirming the proposed origins of the Tokamak lines. For other lines the wavelengths do not agree so well, suggesting a possible problem in the Tokamak measurements.

The results are also of interest for

FIGURE 3. Isoelectronic comparison of 3s-3p and 3p-3d transitions in the Na isoelectronic sequence.
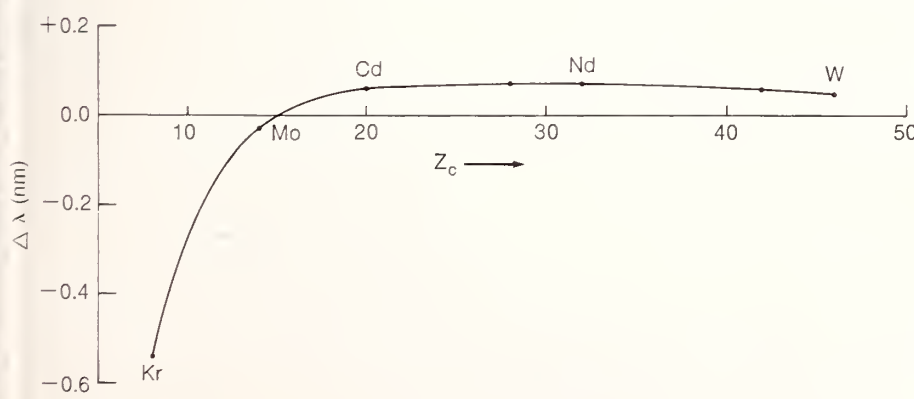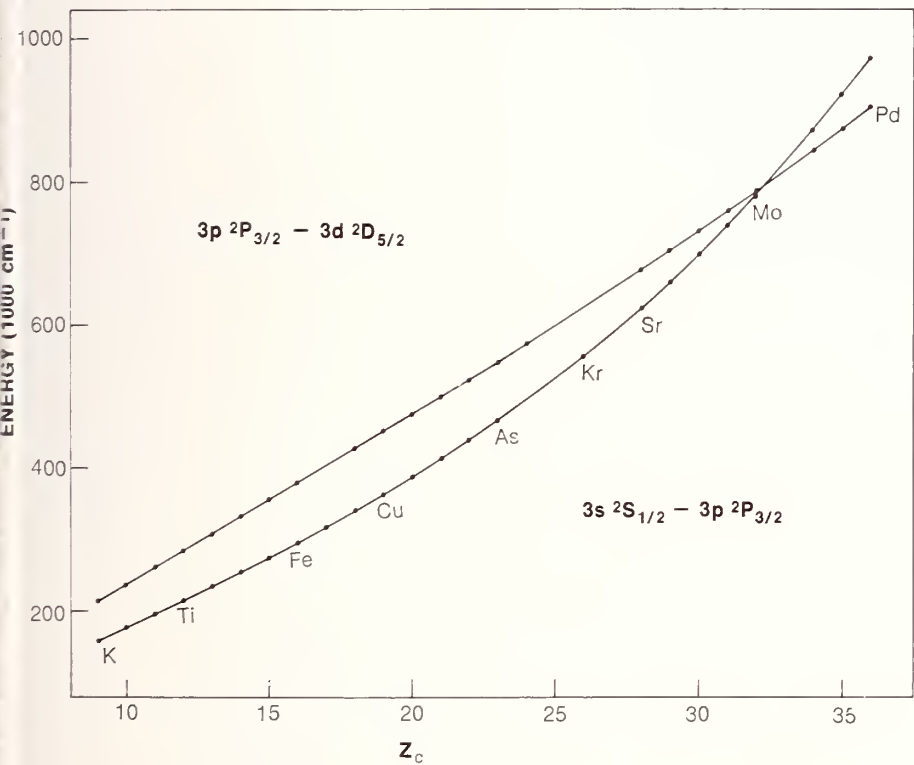
checking theoretical calculations of the properties of highly stripped ions in high temperature plasmas (energy levels, wavelengths, transition probabilities, cross sections for excitation and ionization by electron impact). In the domain of highly stripped ions, where relativistic effects are extremely important, the wavelengths predicted by the most accurate fully relativistic calculations agree with our experimental values to within about one percent (see fig. 4). As the predicted values are systematically low by this amount, the experiment reveals a possibly important effect not included in present theories.

Table 1. Present values of Mo wavelengths compared with Tokamak measurements of E. Hinnov, Phys. Rev. 14, 1533 (1976).

Ion	λ(PRESENT)-NM	λ(TOKAMAK)-NM
Mo^{12+}	34.0909(5)	34.10(5)
Mo^{13+}	37.3647(5)	37.38(5)
	42.3576(5)	42.35(5)
Mo^{30+}	11.596(1)	11.70(5)
Mo^{31+}	12.7814(5)	12.9(1)
	17.662(1)	17.7(1)

References

[1] Chen, K. T. and Kim, Y.-K., Energy Levels, Wavelengths, and Transition Probabilities for Cu-like Ions, *Atomic Data and Nuclear Data Tables 22*, 547-563 (1978).

[2] Burkhalter, P. G., Reader, J., and Cowan, R. D., Spectra of Mo XXX, XXXI, and XXXII from a laser-produced plasma, *J. Opt. Soc. Am.* 67, 1521-1529 (1977).

FIGURE 4. Comparison between observed and calculated wavelengths in the Cu isoelectronic sequence. Calculated values are from Cheng and Kim (Ref. [1]).

27

Polarized Low Energy Electron Diffraction (PLEED): A Technique to Study Surface Magnetism

Daniel T. Pierce and Robert J. Celotta, Radiation Physics Division

At the surface of a magnetic crystal, the lack of translational invariance perpendicular to the surface and the reduced number of neighbors of the surface atoms cause the magnetic properties to differ from those in the bulk. We have developed a new way to measure the magnetization of the outer few atomic layers of a single crystal surface based on polarized low energy electron diffraction (PLEED). [1]

Due to the exchange interaction, the diffracted intensities of electrons at the surface of a magnetic crystal depend on the relative orientation of the incident electron spin and the magnetization of the surface. The surface magnetization, its temperature dependence, and the transition temperature at the surface have been described by a number of theories which we now have a straightforward way to test experimentally. The increasing interest in lower dimensional magnetism and surface critical phenomena makes the development of our "surface magnetometer" especially timely.

We also expect the surface magnetometer to have technological applications. In the push to further miniaturize magnetic devices—by using thinner layers in magnetic storage media, for example—the magnetic properties of the outer few layers will become very important. Our technique provides a research tool to study, for instance, the magnetic changes at the surface of a recording head resulting from corrosion. Magnetic surfaces are also important in hydrogen storage and catalysis, such as in the coal gasification process. The surface magnetometer will allow the study of the role of the magnetic electrons in chemisorption on well characterized single crystal surfaces.

Electrons are widely used in surface analytical techniques (e.g., photoemis-

sion, LEED, Auger spectroscopy), because their strong interaction with the electrons in the material limits their probing to the outer few atomic layers. For example, in the Ni(110) surface which we studied, electrons with energy of about 100 eV can on the average penetrate and return through only two atomic layers without losing energy and being removed from the elastically scattered beam. Polarized electron scattering provides a way to study the surface of a well defined semi-infinite single crystal. The polarized electron probe is non-destructive and has potentially very high spatial resolution although we have not exploited it thus far. One can envision a magnetometer for surface microstructure which could display magnetic domains and bubbles.

The measurement of surface magnetization by polarized electron scattering is made possible by the polarized electron gun which we developed. The electron gun, which is based on photoemission from negative electron affinity GaAs, provides a constant intensity electron beam like an ordinary LEED gun, but the spin direction is modulated at a rapid rate. Since the incident electron beam intensity on the target crystal is constant, any ac component of the scattered intensity synchronous with

Figure 1. Measurement of S as a function of H showing hysteresis in the surface magnetization.

the polarization modulation must result from a spin dependent scattering. The scattered intensity for incident electron spin parallel to the net spin in the ferro-magnetic surface $I_{\uparrow\uparrow}$ is in general different from the scattered intensity when the spins are antiparallel $I_{\uparrow\downarrow}$. We measure a quantity S, which is this difference normalized to the spin averaged scattered intensity,

$$S = \frac{I_{\uparrow\uparrow} - I_{\uparrow\downarrow}}{I_{\uparrow\uparrow} + I_{\uparrow\downarrow}}$$

We also correct for the fact that the incident polarization is 43 percent rather than 100 percent.

Theoretically, S depends on the exchange potential $J(E,\theta)$ and the Coulomb potential $V(E,\theta)$ seen by the electron scattering at an energy E and an angle θ. It can be shown in the first Born approximation that S is proportional to the average magnetization M of the outer few layers of the surface. If multiple scattering is included there may be higher order terms proportional to M^n, where n is odd, but in Ni these are very small and may be neglected.

The apparatus [2] consists of the polarized electron gun attached to a conventional surface analysis chamber. We cleaned a Ni(110) crystal by successive Ar ion bombardment and annealing cycles. The surface cleanliness was checked by Auger spectroscopy using a cylindrical mirror analyzer. Generally, it is not straightforward to scatter low energy electrons from the surface of a ferromagnet because of the deflection of the electrons in stray magnetic fields. The stray magnetic fields have been minimized by making the Ni crystal the keeper of the small electromagnet that magnetically aligns the domains in the crystal.

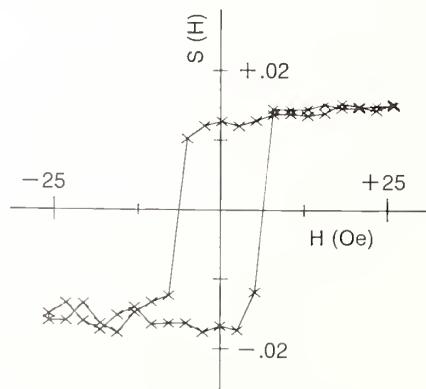We can measure S as a function of magnetic field to obtain a surface hys-

eresis curve S(H). Such a curve is shown in figure 1 for specular scattering at an angle of incidence of 12° and an energy of 125 eV. The maximum S in figure 1 is less than 0.02; this is a small signal but the noise level in this sensitive measurement technique is less than 0.001. Reversal of the magnetic field allows us to isolate any possible nonmagnetic contribution to the spin dependent scattering. We emphasize that figure 1 is a hysteresis curve representing the magnetization of the outer two atomic layers. Such a curve is very sensitive to surface contamination. In particular, segregation of sulfur to the surface decreases the magnetization to zero. Future measurements will study the effects of adsorbates on the surface magnetization. We will investigate the existence of magnetic dead layers at the surface (considered unlikely from these first measurements) and the role of the magnetic d-electrons in the bonding of adsorbed atoms.

We also explored the temperature dependence of the surface magnetiza-

FIGURE 2. Measurement of the temperature dependence of the surface magnetization showing a linear behavior as a function of temperature.

tion. There are definite predictions from theoretical scaling laws relating the surface and bulk behavior in the critical region near the Curie temperature T_c. We were able to measure S(T) from 0.5 to 0.8 T_c and found that the temperature dependence of the surface magnetization shows much less curvature than that of the bulk; in fact, it is approximately linear. Measurements were made by heating above T_c and cooling in applied magnetic fields of 18, 21, and 26 Oe as represented by the different points in figure 2. The cooling was too fast to allow measurement near T_c. In future measurements we will have crystal temperature control and will measure up to T_c, thereby providing a test of theories of surface critical phenomena. We plan also to extend the measurements to low temperature in order to normalize S(T) to the saturation magnetization.

In summary, this very powerful new technique may be compared to neutron scattering, which has been so successful in measuring bulk magnetic properties. We expect that analogous information will be obtained about surface magnetic properties using our new PLEED technique.

References

[1] Celotta, R. J., Pierce, D. T., Wang, G. -C., Bader, S. D., and Felcher, G. P., *Physical Review Letters 43,* 728-731 (1979).

[2] Wang, G. -C., Bunlap, B. I., Celotta, R. J., and Pierce, D. T., *Physical Review Letters 42,* 1349-1352 (1979).

X-Ray Image Information Theory

Joseph W. Motz and Michael Danos,
Radiation Physics Division

This study analyzes the dependence of image information content on x-ray exposure in medical diagnostic x-ray examinations. The results indicate that with the employment of image processing techniques and modified x-ray spectra, it is possible to significantly reduce these exposures without loss of the visual image information that is available to the radiologist.

Medical x-ray examinations provide the major source of radiation exposure to the population in this country. Therefore, any reduction in this exposure would have a large impact in reducing the adverse effects of radiation to the general health of the population.

Is it possible to reduce the exposure and still have the same diagnostic information that appears in visual form in present-day radiographs? We have carried out a theoretical study which concludes that this is indeed possible. This conclusion seems paradoxical, inasmuch as an exposure reduction is always accompanied by a loss of image information. However, our study indicates that only a fraction of the image information content in medical radiographs is visually detected by the radiologist. Accordingly, it is possible to reduce the exposure without loss of the visible information obtained previously, providing methods can be found to display all of the available image information. In fact, the exposure can be reduced to a theoretical minimum or threshold value without loss of the visible information on film. Such a lower limit exists because of the statistical noise introduced by the quantum nature of x-rays.

We have estimated the minimum exposures required for particular cases in diagnostic radiology from a theoretical relationship between the patient exposure and the image information con-

tent. The results for a few of these cases are shown in figures 1 and 2. Figure 1 shows the minimum exposures at different x-ray energies that are theoretically required for the detection with film of a tissue calcification sphere (0.5 mm diameter) which simulates the structure involved in the radiographic detection of breast cancer (mammography). Present day mammography exposures are in the region of 1 roentgen, primarily because the high film densities produced by such an exposure are necessary to obtain optimum image visibility. However, the data in figure 1 indicate that it may be possible to obtain the same visible image information with exposures that are one to two orders of magnitude smaller than 1 roentgen, provided that the x-ray spectrum is confined to an energy band (± 10 keV) in the region of 30 keV. Figure 2 shows our estimates of the exposure reductions that are possible in chest and abdominal x-ray examinations. These data show that for chest and abdominal x-ray exams with respective 1 mm and 0.5 mm diameter spatial resolutions, the corresponding exposures may be reduced respectively from approximately 20 to 4 milliroent-

gens and from approximately 500 to 3 milliroentgens.

The effect of reducing the exposure in this manner is to produce a very low-density, low-contrast radiograph which provides a poor image on direct visual inspection. However, with commercially available image processing techniques, it is expected that contrast and density of the image can be suitably enhanced, essentially restoring image information previously observed. This procedure assumes that a suitable screen-film combination can be found to store *all* of the image information provided with a given x-ray exposure.

In this discussion, we used as an example the screen-film system. However, any type of x-ray imaging system with adequate sensitivity, dynamic range, and linearity can be used to obtain the described exposure reductions. An example of such a system is the x-ray image intensifier optically coupled to a TV camera. The video signal passes to an analog-to-digital converter and is then stored on a disc. With such a system, the stored image can be displayed on a TV monitor with any desired type of image processing such as contrast or edge enhancement.

The application of these new systems to radiology requires data on the information content and the correspond-

FIGURE 1. Minimum x-ray exposure theoretically required in mammography for the detection of a tissue calcification sphere (0.5 mm diameter) embedded in 5 cm tissue.
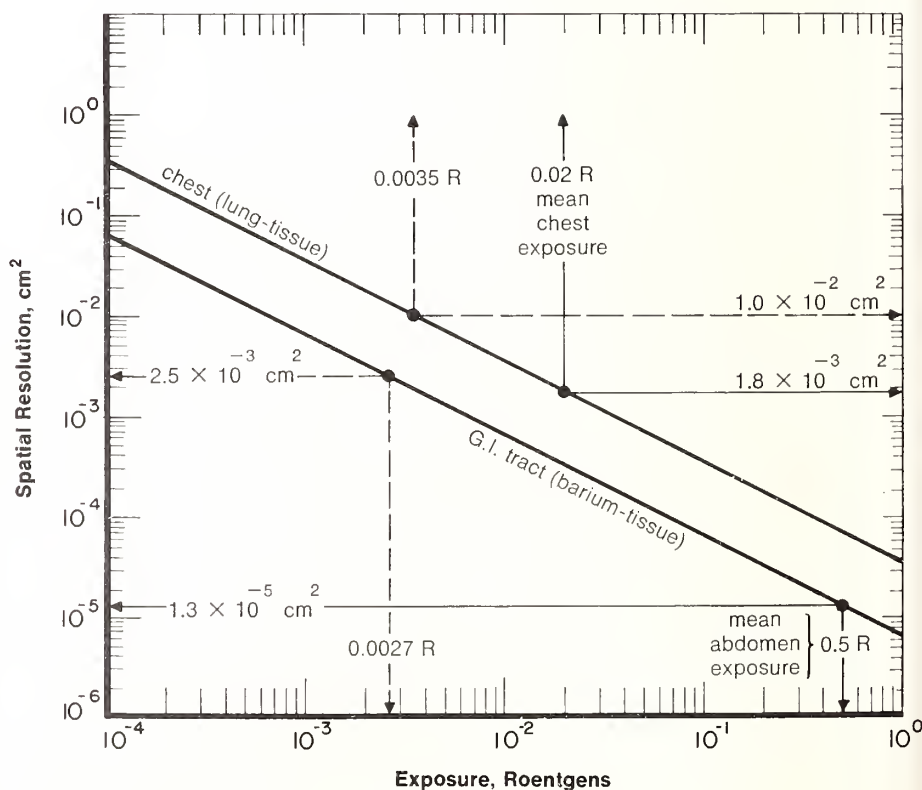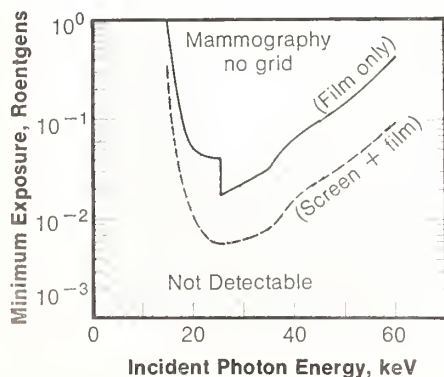
FIGURE 2. Dependence of the attainable area (cm²) of the spatial resolution element on the patient exposure for chest and abdominal (G.I. tract) x-ray examinations for body structures described in Table II of paper by J. W. Motz and M. Danos, *Medical Physics* 5, 8 (1978).

New Studies of Electric Quadruple (EZ) Excitation in Nuclei Using Electromagnetic Probes

William R. Dodge,
Nuclear Radiation Division

The (e,p) and (e,α) cross sections for targets of ^{58}Ni, ^{60}Ni, and ^{62}Ni have been measured in the electron energy range 16 to 100 MeV. They have been analyzed using the DWBA E1 and E2 virtual photon spectra. Protons are emitted primarily following E1 absorption but α emission results from a combination of E1 and E2 absorption.

ing image storage requirements for x-ray pictures. As shown in figure 3, we have determined the maximum number of bits per cm² required for the storage of x-ray images as a function of the x-ray exposure and the desired spatial resolution at two x-ray energies (20 and 50 keV) that are in the energy region used in medical radiology. We expect that these data will provide the basis for developing improved radiological systems that will permit either extracting more image information for a given x-ray exposure or reducing x-ray exposure for a given image information content.
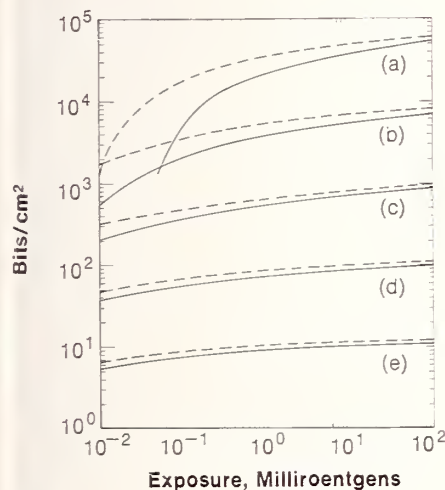
FIGURE 3. Dependence on the number of bits per cm² on the x-ray exposure at the image plane for x-ray energies of 20 and 50 keV, and for different spatial resolutions where the area α of the spatial resolution element is equal to (a) 10^{-4}, (b) 10^{-3}, (c) 10^{-2}, (d) 10^{-1}, and (e) 10^0 cm².

Since the early days of Fermi, the idea that the effects of the electron's electromagnetic field in electron-nuclear scattering could be related to the real photon cross section has intrigued nuclear physicists. As early as 1934 Bethe and Peierls had computed the electric-dipole electrodisintegration cross section of the deuteron and had compared the result with the photodisintegration cross section. In the next few years electrodisintegration cross sections for magnetic dipole, electric quadrupole and octopole transitions were calculated. These cross sections were enhanced relative to the electric dipole cross sections. The enhancement was understood on the basis of the strong momentum dependence of these cross sections and of the greater linear momentum which an electron can deliver to the nucleus compared to a photon. However, while all of these predictions were based on Dirac electron theory, they did not include Coulomb distortion effects (i.e., they did not allow the incident or scattered electron to change energy and momentum by exchanging longitudinal photons with the nuclear Coulomb field). Consequently, these early cross section estimates were grossly inadequate for all but the lightest target nuclei.

Faced with these technical difficulties, electrodisintegration experiments only played a minor role in mapping out the properties of the first nuclear normal oscillation or resonance to be discovered, the giant electric dipole resonance, GDR. Rather, the GDR was established and studied through photonuclear reactions. (As a point of interest many of the most important early experimental and theoretical studies of the GDR were done at NBS).

However, during the past seven years, normal oscillations of the nucleus other than dipole oscillations have been experimentally observed. Unlike the GDR, these new giant resonances were discovered and studied almost exclusively through inelastic scattering of medium energy hadrons and electrons.

Figure 1 shows a pictorial view of the monopole, dipole, and quadrupole oscillations of the nucleus ($\lambda = 0, 1, 2$, respectively). Normal oscillations which do not involve a nucleon spin flip are labeled $\Delta S = 0$ while those which do are labeled $\Delta S = 1$. Giant resonances, which are internal collective nuclear motions involving all nucleons, are important because they involve basic parameters of nuclear matter such as compressibility, polarizability, and the effects of the in-phase (isoscalar, $\Delta T = 0$) or out-of-phase (isovector, $\Delta T = 1$) motions of protons and neutrons. In addition to the normal oscillations shown in figure 1, the giant isoscalar octopole resonance has been reported in the literature.

While the new multipole resonances (NMR) are commonly called giant multipole resonances they are in fact less intense than the GDR. Because of the relatively small intensity of the NMR some method either to suppress the isovector GDR or enhance the NMR is needed to facilitate the study of the NMR. In hadron excitation of the isoscalar NMR, the method is to use an isoscalar projectile, thus suppressing excitation of the isovector

GDR. In electron scattering or electro-disintegration the method is to enhance the NMR excitation through the strong momentum transfer dependence of the cross section in the manner alluded to earlier.

Fortunately, almost simultaneously with the discovery of the NMR, a theory which provided a solution of the Dirac equation in a point Coulomb field with no kinematic restraints such as characterized earlier theories became available. This theory, called a distorted wave Born approximation—DWBA theory in the trade—showed that Coulomb distortion of the electron wave function greatly enhanced the "virtual photon" intensity spectra, especially for E2 and higher electric multipoles.

The virtual photon spectra are those functions involving only electron kinematics which relate photo- and electro-disintegration cross sections. Figure 2 shows E1 and E2 DWBA virtual photon intensity spectra for Ni. The large difference between E1 and E2 virtual photon intensity spectra make it relatively easy to separate transitions involving E1 and E2 excitations in an electrodisintegration experiment.

The upper half of figure 3 illustrates the conventional photoproduction experiment, in which bremsstrahlung produced by electrons of energy E_0 strikes a radiator of high atomic number. The real photons—with intensity spectrum, $N_\gamma (E_0, \omega)$, which of course does not depend on multipolarity of the reaction which the photons will induce—are absorbed by the target nucleus, which then emits particle x. The yield of x for real photons is given by

$$Y_{(\gamma,x)}(E_0) = \qquad (1)$$
$$\sum_L \int_{thres}^{E_0 - m_e} \frac{N_\gamma (E_0, \omega)}{\omega} \sigma^L_{(\gamma,x)}(\omega)\,d\omega$$

where $\sigma^L (\gamma,x)$ is the photodisintegration cross section for the Lth multipole and ω is the excitation energy.

The lower half of figure 3 shows schematically an electrodisintegration experiment in which the electrons strike the target nuclei directly. The electroproduction yield, $Y_{(e,x)}$, is given by an expression similar to $Y_{(\gamma,x)}$, except that the spectrum of virtual photons seen by the target nucleus now depends on the multipolarity L of the nuclear transition. In this case

$$Y_{(e,x)}(E_0) = \qquad (2)$$
$$\sum_L \int_{thres}^{E_0 - m_e} \frac{N^L_e(E_0, \omega)}{\omega} \sigma_{(\gamma,x)}(\omega)\,d\omega$$
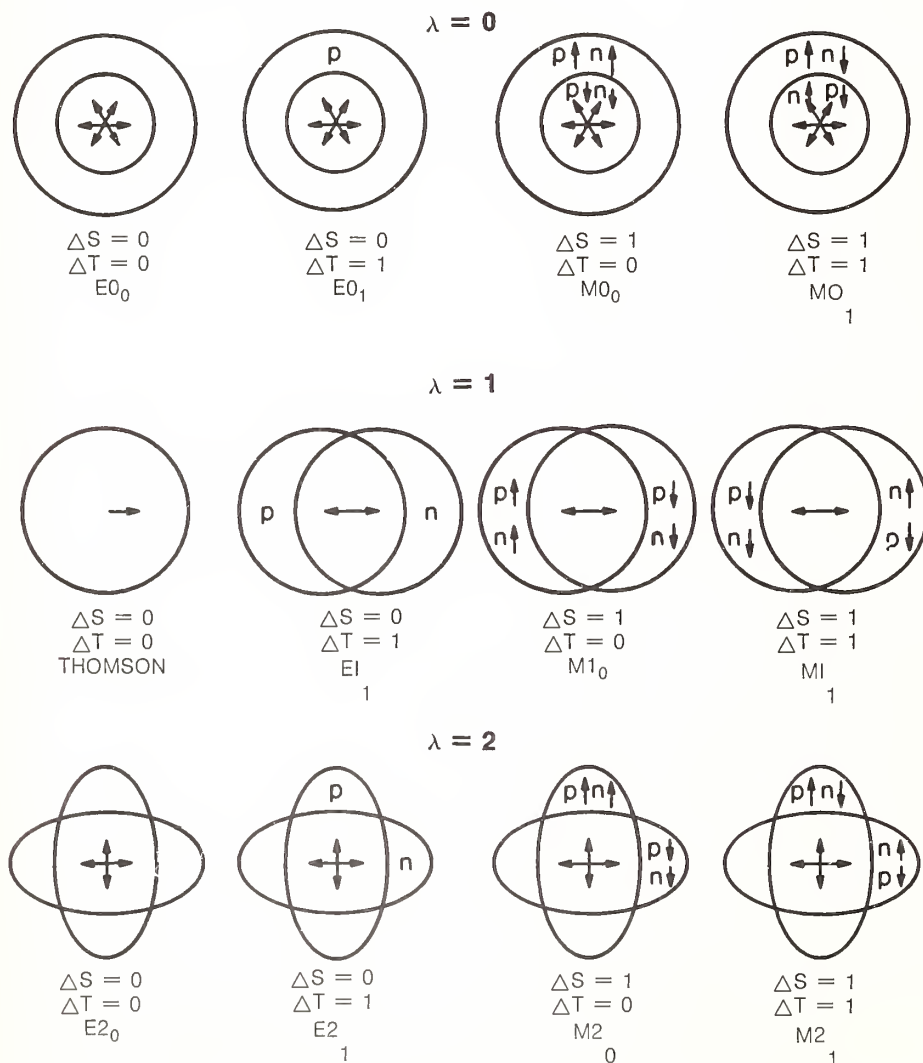
FIGURE 1. The giant monopole, dipole, and quadrupole ($\lambda = 0$, 1, and 2, respectively) oscillations of the nucleus. Normal oscillations not involving nucleon spin flips are labeled $\Delta S = 0$ while those which do are labeled $\Delta S = 1$. Normal oscillations which involve in-phase motions of protons and neutrons are labeled $\Delta T = 0$ while those which involve out-of-phase motions are labeled $\Delta T = 1$.
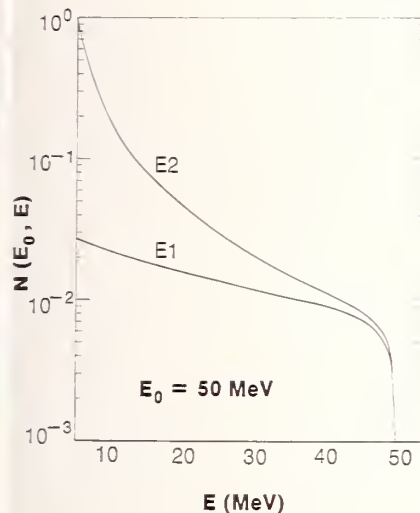
FIGURE 2. Virtual photon spectra for E1 and E2 transitions calculated in the distorted wave Born approximation for Ni (Z = 28).
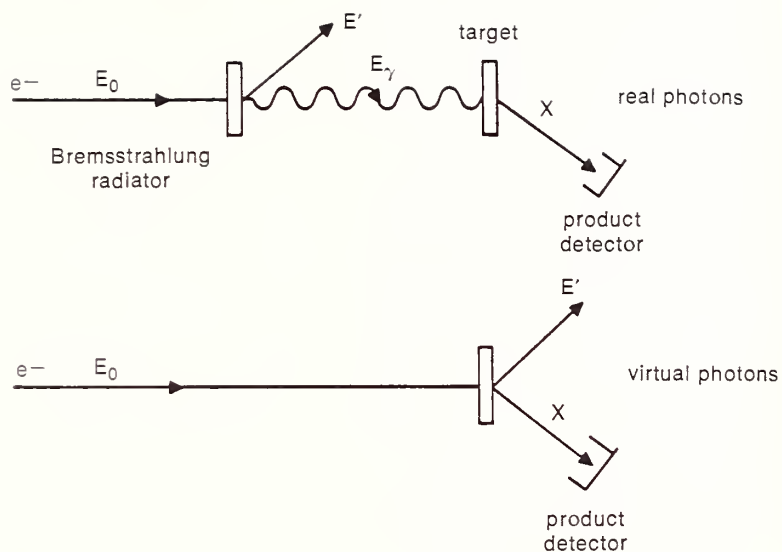
FIGURE 3. Schematic diagram of a typical photodisintegration experiment (top) and of a typical electrodisintegration experiment (bottom).

Since $N_e^L(E_0,\omega)$ rapidly increases as L increases for a given E_0 and ω electrodisintegration yields are very sensitive to the multipolarity of the transition.

Thus armed with a good virtual photon theory the discovery of the NMR by inelastic hadron scattering experiments, and the arrival of an energetic guest worker, E. Wolynec, from the University of Sao Paulo, we set about trying to exploit these developments.

For our initial experiments, we selected targes of ^{58}Ni, ^{60}Ni, and ^{62}Ni. Our measurements were made with electrons in the energy interval between 16 and 100 MeV provided by the NBS linac and with a magnetic spectrometer capable of separating the many charged particle groups (such as protons, deuterons, tritons, and alphas) which can be copiously produced in a nuclear disintegration. At each of several spectrometer-incident-electron-beam angles we measured proton and alpha particle energy spectra as a func-
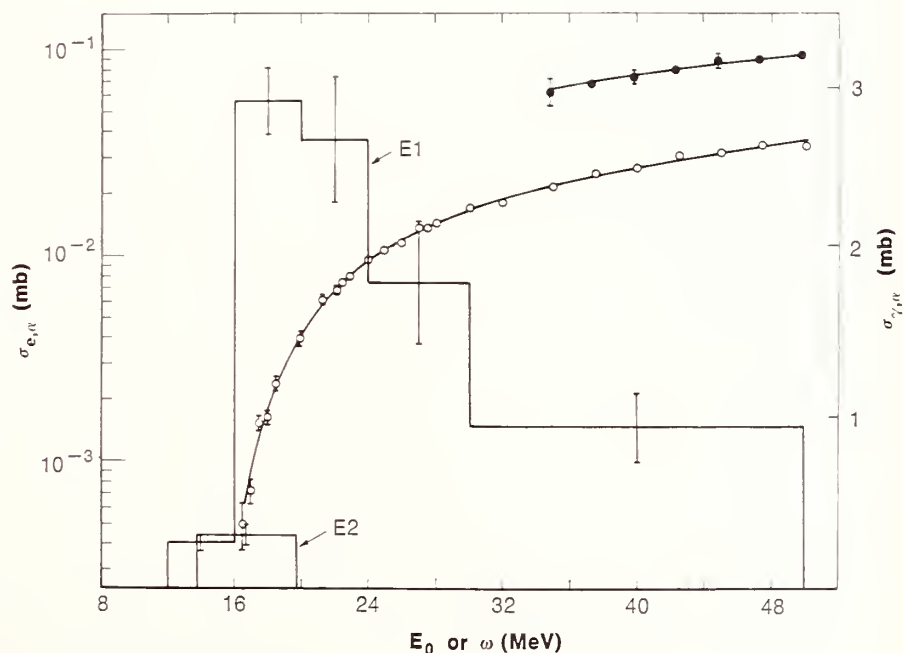
FIGURE 4. The ^{58}Ni (e,α) and (e+γ,α) excitation functions. The open circles are the results for pure electroproduction and the filled circles are the results for electroproduction plus photoproduction. The histograms are E1 and E2 cross sections deduced from these excitation functions. E_0 is the incident electron energy and ω is the excitation energy.

tion of the incident electron energy, E_0. These energy spectra were integrated over all particle energies and then the resulting angular distributions integrated over all angles to obtain $Y_{(e,x)}$ and $Y_{(\gamma,p)}$ (E_0). The yields $Y_{(\gamma,p)}(E_0)$ and $Y_{(e,p)}(E_0)$ were both accounted for when the previously measured $\sigma_{(\gamma,p)}(\omega)$ was inserted in eqs. (1) and (2) using the electric-dipole virtual photon spectrum for $E_0=16$ to 50 MeV. These results confirmed the expectation that photon emission from the Ni isotopes was a predominately E1 process near 20 MeV.

On the other hand, the measurement of the (γ,α) and (e,α) yields showed that a sizable fraction of the α emission comes from the giant isoscalar quadrupole resonance near 16 MeV. Figure 4 shows our ^{58}Ni(e,α) excitation function. The open circles are the results for pure electroproduction and the filled circles are the results for electroproduction plus photoproduction when a 0.217-g/cm² Ta radiator is inserted in the electron beam. The histograms labeled E1 and E2 are the cross sections which produce the best fit to both the electroproduction and the electroproduction plus photoproduction excitation functions. Note that attempts to fit the excitation data wih pure E1 or pure E2 cross sections were not satisfactory.

The striking result of our measurements is that the alpha decay mode of the isoscalar E2 resonance exceeds statistical estimates by a factor of 4. Said another way the alpha decay channel accounts for 25 percent of the E2 isoscalar-energy-weighted sum rule value. Similar conclusions regarding the decay of the oxygen isoscalar E2 resonance have been reached by the Heidelberg-Jülich group on the basis of a ^{16}O$(\alpha,\alpha'\alpha'')$ coincidence measurement. Theorists have long speculated

that alpha clusters might be continually forming and dissolving in the nuclear surface. A quadrupole oscillation might preferentially shake off these conjectured alphas. At the present time these are only speculations and no theoretical explanation of our results is available.

Glueballs and Quark States

Sydney Meshkov,
Nuclear Radiation Division

A systematic enumeration of the glueball spectrum of QCD and other SU(n) gauge theories yields $J^{PC} =$ odd^{-+}, even^{+-}, and 0^{--} states in addition to the usual quark model states. The properties of these new states are discussed.

Quantum Chromodynamics (QCD), our present theory of the strong interactions, describes hadrons as being composed of colored quarks and antiquarks. Color is a new degree of freedom associated with the strong interaction. All single quarks have color. So far all observed hadrons are colorless. The strong force between quarks and antiquarks is mediated by the exchange of massless colored gluons, just as the electrical force between electrons and between electrons and positrons is mediated by the exchange of massless photons. Convincing manifestations of the existence of the gluon have been displayed in recent e^+e^- annihilation experiments at 27 and 31.6 GeV. QCD implies that glueballs (gluonia) should exist [1]. These are mesons which are composed entirely of gluons; they contain no quarks and have no color. A current activity of the NBS Elementary Particle Program is the study of gluonium, i.e., to set criteria for its existence, and to understand how to distinguish gluonic states from the usual quark states experimentally.

Understanding the formation, structure, and decay of gluonic systems requires a full knowledge of the spectroscopy of "quarkful" mesons, i.e., those described in the usual way as quarks and antiquarks moving with a relative orbital angular momentum L. Fortunately, the latter is a major component of high energy activity of NBS as manifested by work on charmonium and other "onium" spectroscopy (2).

Some of the simplest differences be-

Quantum Basis for Visible Region Radiometric Standards

Jon Geist, Edward Zalewski, and A. Russell Schaefer, Radiometric Physics Division

Silicon photodiodes are the detectors most widely used for radiation measurements in the visible region of the electromagnetic spectrum. When employed in this capacity, their calibration is based on the thermal physics of either electrical substitution radiometers or the blackbodies. The possibility of basing these calibrations directly on the quantum physics of the internal photoelectric effect in silicon has been suggested frequently. Recently, we demonstrated a quantum-based calibration that is accurate to within ±0.3 percent. This uncertainty compares favorably with that currently available from the best thermal based calibrations, and, for silicon photodiodes, the new procedure is more convenient as well.

In a study of the radiometric properties of several high quality (high resistivity, shallow junction) silicon photodiodes, we found that the quantum efficiency, after correcting for reflectance losses, was within 1 percent of unity in the red region of the spectrum. The range of internal quantum efficiencies for five photodiodes along with their measured absorptance is shown in figure 1. At wavelengths longer than 650 nm the internal quantum efficiency is 0.99 or greater. Because it is so close to unity, there are less stringent requirements on the accuracy of the theoretical model used to predict this small difference.

Photon energies in the wavelength region longer than 530 nm are less than twice the band gap, so that for every photon absorbed only one electron-hole pair is created. (Photons absorbed by the free carriers in the conduction band are a negligible fraction of the total absorption.) Photons that penetrate to the vicinity of the p-n junction before absorption have a quantum efficiency of one because the minority carrier thus generated is immediately swept by the electric field through the depletion region. It is only in the regions away from the p-n junction that recombination or trapping

The left column charmonium text

tween the two spectroscopies are simple, i.e., in the quantum numbers J^{PC} (J=total angular momentum, P=parity, C=charge conjugation). The quantum number assignments depend on whether the glueballs are made of two, three, or more gluons, and whether the quark systems with which they are compared are simple quark-antiquark systems, or are multiquark composites. For example, states with $J^{PC}=0^{--}$, $0^{--}, 2^{--}$ occur in the 3 gluon system but cannot be made with either 2 gluons or the usual $q\bar{q}$ systems. Other possible distinguishing factors such as modes of production and decay are also currently being investigated.

The charmonium quark structure work has continued with emphasis on the existence and masses of the pseudoscalar $c\bar{c}$ state n_c and its radial excitation n'_c. A reanalysis [3] of the German e^-e^- annihilation data which had led them to claim the existence of the n_c at 2.83 GeV led to the conclusion that the claimed state was at most a 2-3 standard deviation effect. Recent experimental searches at the Stanford colliding electron-positron ring have found no state at 2.83 GeV, but strong indications of a state at 2.98 GeV which may well be the n_c. Work is continuing on the properties of the n_c and n'_c.

References

[1] Bjorken, J. D. Electron-Positron Annihilation. Talk given at European Physical Society High Energy Physics Conference, Geneva, Switzerland, June 27-July 4, 1979. SLAC-PUB-2366.

[2] Fishbane, Paul M., Horn, David and Meshkov, Sydney, Spin forces in charmonium spectroscopy, *Phys. Rev.* D19, 288 (1979).

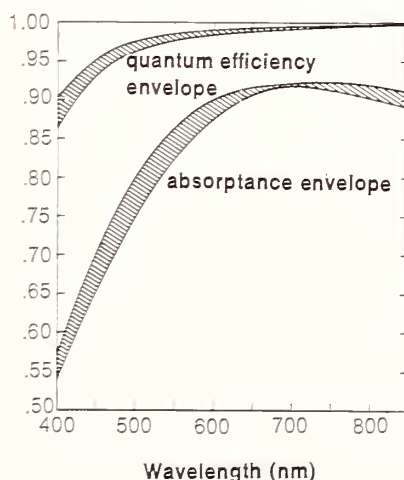[3] Samios, N. P. and Meshkov, Sydney (BNL 25926) 1979.

FIGURE 1. The absorptance (one minus the reflectance) and the internal quantum efficiency for five silicon photodiodes.
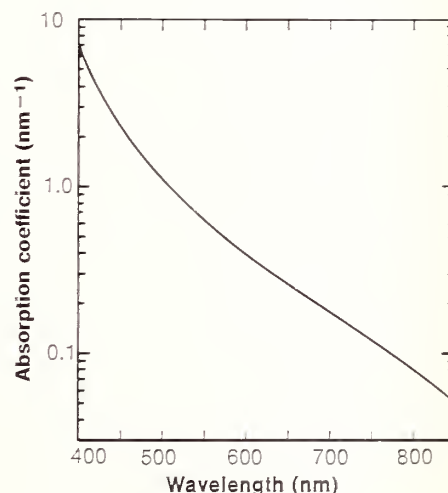

FIGURE 2. Variation of the absorption coefficient of silicon in the visible region of the spectrum.

can be expected to decrease the quantum efficiency.

Figure 2 shows the variation of the silicon absorption coefficient with wavelength. The absorbance is high in the blue region, decreasing by about two orders of magnitude toward the red. Therefore, in the blue region the majority of the photons are absorbed near the front surface. Here the recombination probability, 1-P, where P is the collection efficiency, is significant because of the large density of majority carriers and possible surface effects. One might expect that $P(x)$ would be a complicated function of distance, x, into the diode; however, we have found that a model which postulates a layer of constant recombination probability followed by a region of zero recombination probability fits our data quite well. An example of the quality of the fit of this model to the data for one of the silicon photodiodes is shown in figure 3. Other more physically significant models for the recombination probability distribution function were also fit to these data. They only affected the shape

FIGURE 3. The curve obtained from the model of the internal quantum efficiency of silicon (equation 1) and the data for a typical photodiode.

of the function at wavelengths shorter than 400 nm.

In the long wavelength region of the spectrum the photons can penetrate beyond the junction into the bulk region of the diode before being absorbed. Because the region between the junction and the rear of the diode has a low concentration of impurities and defects, the lifetime of the electron-hole pair is long relative to the diffusion rate back to the junction. Therefore, recombination in the bulk region also has a very small effect on the quantum efficiency.

The simplest mathematical model which fits our data is of the form

$$\epsilon = K \left[P + (1-P) \exp(-\alpha(\lambda)J) - \frac{B}{\alpha(\lambda)L^2} \right] \qquad (1)$$

Here ϵ is the internal quantum efficiency, P is the collection efficiency, $\alpha(\lambda)$ is the spectral absorption coefficient of silicon, J is the junction depth, B is the thickness of the bulk region and L is the minority carrier diffusion length. The coefficient K can be interpreted as the calibration factor of the electrical substitution radiometer used to determine the external quantum efficiency. From our data the values obtained for K ranged from 0.9987 to 1.0033. These results are consistent with the estimated accuracy of the electrical substitution radiometer we used and the assumption that absorption of a visible photon in silicon produces one electron-hole pair.

Equation 1 can now be used as the basis of an absolute calibration of a spectrally non-selective radiometer. In order to do this, the internal quantum efficiency of a silicon photodiode is measured in the blue and near infrared spectral regions relative to that in the red. These data plus the published

values of $\alpha(\lambda)$ at the appropriate wavelengths can then be used to obtain K from eq. (1). The types of measurements involved in this procedure, except for the current from the photodiode, are all relative as opposed to absolute measurements. That is, the reflectance, absorption coefficient and relative spectral response all involve a ratio of similar measurements—no absolute radiometric measurements are required.

This research has demonstrated the feasibility of adopting a new measurement basis for absolute radiometry based on quantum physics instead of thermal physics. High quality silicon photodiodes can now be used for measurement of visible radiant power with an accuracy comparable to that of standards presently available. It is expected that improvements in the measured values of the absorption coefficient of silicon plus a more complete knowledge of the physics of these devices will yield more accurate and convenient radiometric standards. The long term goal of future work in this area would be the development of photodiodes whose radiometric properties could be accurately determined from a knowledge of their structure and physical properties instead of the relative radiometric measurements now used. Possible approaches are electronic test structures built into the photodiode and calculations based on device fabrication history.
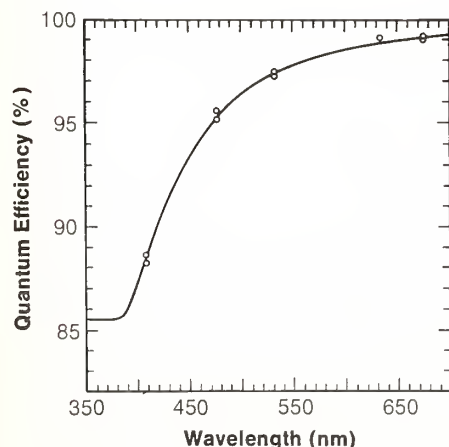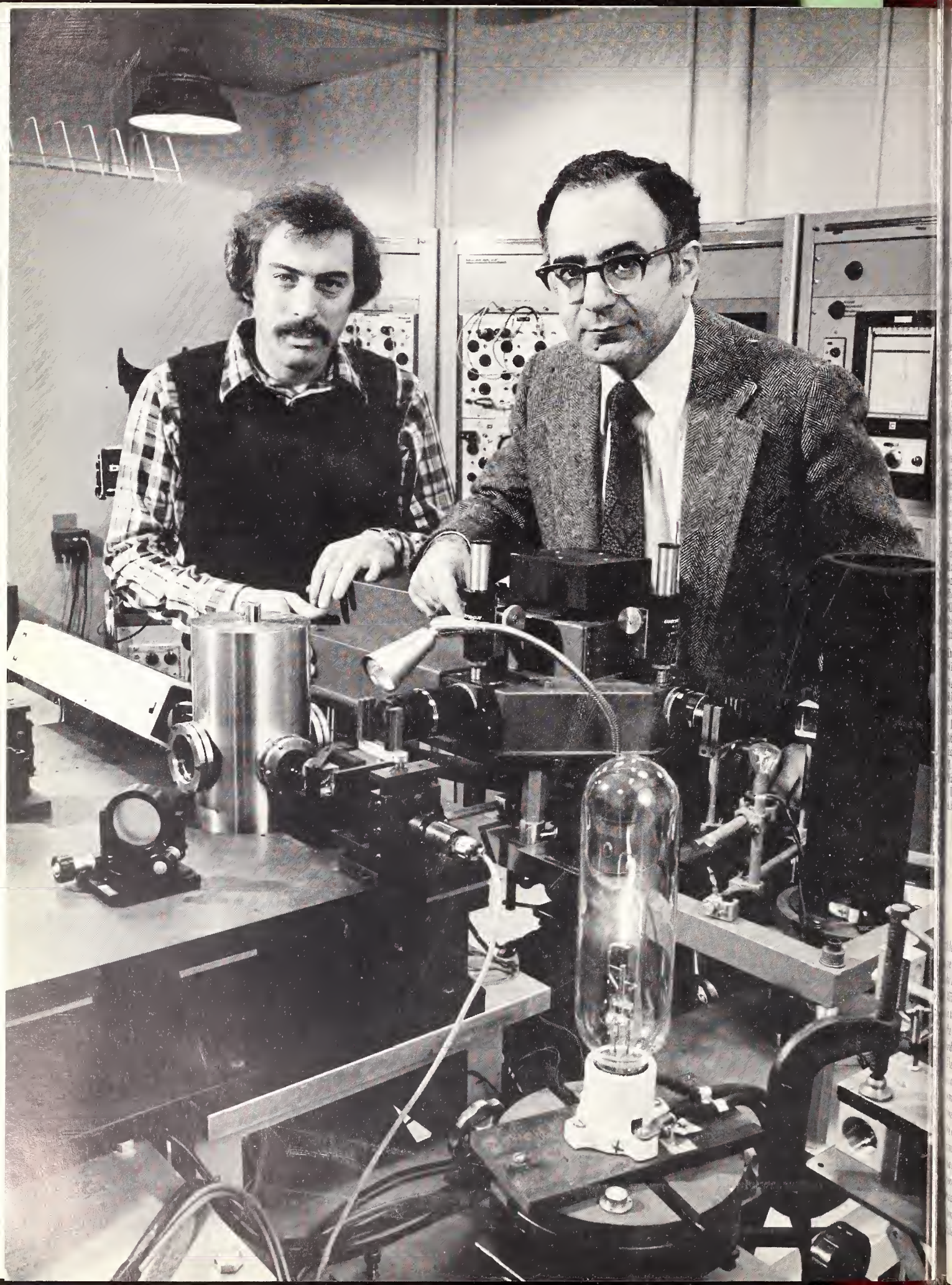
Center for Thermodynamics and Molecular Science

Peter L. M.
  Heydemann
Ralph Klein
Albert E. Ledford,
  Jr.

Surface Science
Cedric J. Powell
James J. Carroll
Richard R.
  Cavanagh*
William L. Clinton**
William F. Egelhoff,
  Jr.
Joseph Fine
John W. Gadzuk
Steven M. Girvin
David W. Goodman
Gregory L. Griffin*
David K. Hoffman**
Jack E. Houston**
Terrence J. Jach
Richard D. Kelley
Sam H. Kim**
Theodore E. Madey
Allan J. Melmed
Roger L. Stockbauer
John T. Yates, Jr.

Chemical Kinetics
Wing Tsang
Walter Braun
Robert L. Brown
Robert F. Hampson,
  Jr.
John T. Herron
Tadahiro Ishii**
M. Odo Klais**
Michael J. Kurylo,
  III
Allan H. Laufer

Richard I. Martinez
Norman C. Peterson
James A. Walker
Francis Westley
Robert E. Huie, III

**Chemical
Thermodynamics**
David Garvin

Stanley Abramowitz
George T. Armstrong
Pierre J. Ausloos
Kenneth L. Churney
Jennifer C. Colbert
Howard J. DeVoe**
David A. Ditmars
Eugene S. Domalski
Robert N. Goldberg
Thomas L. Jobe, Jr.
Duane R. Kirklin
Sharon G. Lias
Michael Mautner
George W. A.
  Milne**
Ralph L. Nuttall
Vivian B. Parker
Edward J. Prosen
Richard E.
  Rebbert
Richard H. Schumm
Frederick P.
  Schwarz
Lewis W. Sieck
Bert R. Staples
Donald D. Wagman
Jin T. Wang**
Stanley P. Wasik
William J. Webb
Harry D.
  Youmans**
(Continued)

Selected thermophysical properties of metals are measured with millisecond time resolution by Ared Cezairliyan (foreground) and Archie Müller. The metal sample is heated electrically in the metal cylinder shown near the center of the photograph. Measurements are made either under vacuum or in selected inert atmospheres. The temperature of the sample is measured with an optical pyrometer seen to the right of the sample container. The large lamp in the foreground is a tungsten filament lamp used for the calibration of the optical pyrometer. The pyrometer, designed specifically for the project, is a unique instrument, capable of millisecond resolution. The laser pulse interferometer which measures, with millisecond resolution, the thermal expansion of the sample is on the table around the sample container.

T he Center for Thermodynamics and Molecular Science (CTMS) provides the scientific community with the means to measure, interpret, and control accurately the behavior of complex chemical systems. Examples of such systems, whether manmade or natural, are ubiquitous: heat engines, lasers, chemical reactors, distillation columns, catalytic processes, the oceans, even biological systems.

To researchers in this Center, these systems represent mixtures of chemical substances in one or more phases, either in equilibrium or in the process of approaching equilibrium and interacting with both radiation and the containment surface.

The problems CTMS scientists address are often solved generically, with the result that the solutions are applicable to a variety of specific practical questions. For example, the quantification of the behavior of fluids can be applied to the development of standards for pressure measurement and to the provision of the values of those properties of steam needed in the design of electric power plants. Methods used to calculate the electronic properties of transient species in the atmosphere are applicable to transient species in chemical lasers. Procedures for measuring of the rates of chemical reactions relate equally well to atmospheric chemistry or to combustion kinetics. Methods developed to measure the heat evolved in chemical or physical transformations can be applied to study biological cell metabolism or to determine the stability of oil in the simulated environment of an internal combustion engine. Accurate spectroscopic data can be used to calculate the concentration of atmospheric pollutants; such data can also serve as a basis for calibrating laser frequencies or identifying molecular species in interstellar clouds.

A brief review of recent work within CTMS will illustrate the broad applicability of CTMS research and development.

Researchers involved in surface science are concerned with developing accurate methods to characterize the physical and chemical properties of surfaces. Surface science has been a rapidly developing field over the past 10 years, with important applications in corrosion, catalysis, air pollution, and integrated circuit technology. This

Thermophysics
Harold J. Raveche

Francis W. Balfour**
Anita Calcatelli**
Ared Cezairliyan
Ren-Fang Chang
Jack H. Colwell
Theodore D. Doiron*
Nils E. Erickson
Vincent J. Fratello*
John S. Gallagher
Robert W. Gammon
Lester Haar
John R. Hastings
Richard F. Kayser, Jr.
John M. Kincaid
Max Klein
James W. Little
Rosemary A. Mac Donald
John L. McClure
James B. Mehl
Archie P. Miiller
Michael R. Moldover
Malcolm S. Morse
Raymond D. Mountain
E. Gordon Powell**
Jan V. Sengers
Johanna M. Sengers
G. Bruce Taggart**
Donald H-N. Tsai
Meyer Waxman
Arnold Wexler**
Harold W. Woolley**

Molecular Spectroscopy
Merrill M. Hessel

Stephen E. Bialkowski*
Arthur J. Grimley*
Jon T. Hougen
Marilyn E. Jacox
Paul S. Julienne
David S. King
Morris Krauss
Walter J. Lafferty
Frank J. Lovas
Arthur G. Maki, Jr.
Frederick H. Mies
David B. Neumann
Hideo Okabe
William B. Olson
John C. Stephenson
Walter J. Stevens
Lawrence L. Strow**
Richard D. Suenram
Alfons Weber
Richard F. Wormsbecher*

*Post Doctoral Staff
**Research Associates and Guest Workers

growth has resulted largely from the development of su face characterization techniques and instrumentation greatly improved specificity and sensitivity, from an i creased understanding of surface properties and prc esses on a microscopic scale, and from the successf application of modern measurement methods and the retical concepts to a wide variety of scientific and tec nical problems.

Yet, in spite of the growth in this area, serious mea urement-related problems and limitations remain. T Surface Science Division works to develop quantitati understanding of the details of the measurement proce as they relate to surface science and to apply this know edge to the development of new and improved measur ment methods and standards. Surface properties such composition, atomic structure, electronic structure, atomic motions are being probed through a great varie of techniques, usually involving the interactions of ene getic particles (ions, electrons, atoms) or the interactio of radiation with surfaces. Understanding of these pro esses on an atomic or molecular scale is critical to tl development of reliable, quantitative measureme methods.

Researchers are engaged in work on electron stimi lated desorption of molecules from surfaces, the surfac characterization of certain catalytic processes, the appl cation of infrared spectroscopy to the characterizatic of molecules absorbed on surfaces, field ion microscop ion sputtering, the application of auger spectroscopy the analysis of airborne particulates, and the develoj ment of theories for describing the interaction of photor or charged particles with atoms and molecules.

In chemical kinetics, our scientists develop methoc to measure the rates of chemical reactions and to dete mine the mechanisms of reacting systems. They also pr vide evaluated kinetics data and measure particular rat constants when data of sufficient accuracy are not avai able elsewhere. In the chemistry of the atmosphere or i combustion, dozens of reactions often occur simultane ously, with intermediate products of a transient natur playing a significant role. Frequently, knowledge of th nature of these intermediate products is purely specula tive. The possible reactions they undergo must be cor sidered in any quantitative description of a chemica

rocess if the behavior of the system over time is to be adequately characterized.

Programs in the Chemical Kinetics Division are concerned with the intermediates that occur in the atmospheric oxidation of olefins, the upper atmospheric chemistry of fluorocarbons, the processes that occur in planetary atmospheres, and the high temperature decomposition of hydrocarbons. Important intermediates and their reactions are being characterized. New methods for identifying species are being investigated and new methods for initiating chemical reactions, such as laser induced decomposition, are under study. Computer codes for modeling these systems are also being developed. Indeed, the linking of computer models and laboratory measurements will characterize the activities of the Chemical Kinetics Division in the future. The evaluated rate constants and related kinetics data provided by this Division are used in large scale computer models of upper atmospheric chemistry.

In the area of chemical thermodynamics, we provide accurate chemical thermodynamics data and standards. Scientists develop state-of-the-art instruments for measuring thermochemical properties. In support of the NBS Recycled Materials Program, researchers are designing the world's largest combustion calorimeter. It will be capable of measuring the heat evolved during the combustion of multi-kilogram-sized samples. Although the principal purpose of this calorimeter will be to determine the calorific value of refuse-derived fuel, it will serve as part of a general research facility for studying combustion processes. At the other extreme, microcalorimeters capable of measuring the heat evolved during metabolic processes have already been designed and built. Laboratories throughout the world use microcalorimeters based on the NBS designs.

Other efforts include work in determining equilibrium constants associated with ionic properties, high accuracy bomb calorimetric measurements for certifying heat-constant Standard Reference Materials (SRM's), the development of SRM's to serve as standards for the calorimetric assay of radioactive plutonium, and the calculation of the high temperature thermodynamic properties of refractory compounds from molecular properties. Also, Division scientists are studying the heterogeneous

and homogeneous decomposition of halocarbons and nitrous oxide (contributing to models of the ozone layer in the stratosphere) and developing a new mass spectrometric technique for characterizing fossil fuels. A major effort of the Chemical Thermodynamics Division continues to be evaluating and publishing of selected values of thermodynamic properties under the auspices of the National Standard Reference Data System.[1]

Whereas the Chemical Thermodynamics Division is concerned primarily with the chemical properties of substances, the Thermophysics Division concentrates on the physical properties of substances. The Dynamic Measurements Program involves the measurement of such properties as thermal diffusivity, thermal expansion, heats of fusion, and heat capacities under conditions requiring an extremely rapid response. At present, a millisecond system is operational and a microsecond facility is under development. The capability now exists to measure both equilibrium and nonequilibrium properties at elevated temperatures.

The equation of state program is concerned with: the accurate measurement of the temperature, volume, and pressure relationships in fluids and complex fluid mixtures, the measurement of such properties as dielectric constants near critical points, the development of quantitative theories to explain the behavior of these properties in the vicinity of critical points, the development of new measurement techniques to measure these properties more accurately, and, the development of mathematical correlation models for the properties of a variety of fluids used in energy generation.

These correlation models have been used, for example, to calculate accurately the properties of steam over wide ranges of temperature and pressure. A spherical acoustic resonator has been designed to accurately measure of the velocity of sound in gases, from which thermophysical properties can be calculated. A laser light scattering instrument has been constructed to measure transport and equilibrium properties with the greatest accuracy currently achievable. In the future, properties of complex mixtures of polar and nonpolar compounds will be measured and interpreted. Such compounds are

---

[1] See pages 99 to 114 for a discussion of the NSRD program.

found, for example, in systems for tertiary oil recovery.

The Thermophysics Division provides methods and standards for the measurement of pressure. Pressure measurements in industrial and government laboratories are made traceable to NBS standards through measurement assurance programs developed and maintained by division scientists. One current program consists of measurement assurance services (i.e., transfer standards consultation, round robin intercomparisons) for aircraft altimetry measurements. Highly accurate pressure measurements also find application in materials properties research. For example, a new high pressure phase of CCl_4 has recently been discovered which shows that a substance can have dual melting curves.

To meet the demands for static and dynamic properties data, a theoretical capability for prediction is required for systems not accessible with existing measurement methods. In response to this need, the Thermophysics Division has a statistical physics program in which models based on molecular properties are being developed to predict the behavior of bulk matter.

The work includes computer simulation of the behavior of properties and development of analytical theories. Both equilibrium phenomena and such nonequilibrium phenomena as metastability are being studied. Recent measurements of anomalously high values of solid heat capacities at high temperatures are being thoroughly investigated by the computer simulation of the bulk properties of solids taking into account the effects of large amplitude, anharmonic lattice vibrations. Theoretical work is also underway to predict the behavior of systems as they undergo phase transitions and to predict behavior under conditions of intense pressure and high temperature.

In molecular spectroscopy, scientists are concerned with the electronic properties of molecules and their interactions with electromagnetic radiation. The laser-high resolution spectroscopy group devises new measurement techniques for generating highly accurate spectra and computer models for interpreting and extrapolating the values of molecular properties obtained from the spectra. A laser diode spectrometer for measuring and analyzing infrared spectra of atmospheric constituents is being developed. The group is also engaged in providing wave-

length standards that will be two orders of magnitude more accurate than those presently available. This effort is a response to requests from the instrumentation industry, industrial and government laboratories, and standards groups. This group also uses nozzle-beam and single-moded laser techniques to determine the electronic structure of molecules and to improve the resolution and sensitivity of molecular electronic spectra measurements.

The microwave spectroscopy group furnishes accurate microwave spectra to astronomers for use in studying the chemistry of interstellar clouds. Researchers determine the structure of small, unstable molecular intermediates in atmospheric or combustion processes through analysis of the microwave spectra. NBS scientists have discovered new compounds such as ethylenimine and dioxirane in these studies.

The laser chemistry and photochemistry groups have as their objective the quantitative understanding of the chemistry of molecules when they interact with high power laser radiation. The quantum chemistry group develops and evaluates methods for calculating from first principles the electronic, structural, and chemical properties of molecules. Transient species in such systems as lasers play a critical role in the functioning of the system but, because of their very small concentration, cannot be observed experimentally. The quantum chemistry group calculates reliable values for the molecular properties of species encountered in applied problems ranging from upper atmospheric chemistry to laser development for defense and energy purposes.

This brief description touches on the activities of the approximately 100 scientists who contribute to the programs of the Center for Thermodynamics and Molecular Science. Each year, CTMS researchers publish approximately 300 technical papers and reports and present 250 papers at national and international meetings. They cooperate extensively with scientists in universities, industry, and other Government agencies and participate in national and international standards activities.

The technical highlights that follow have been chosen to illustrate in more detail the breadth of the Center activities. They represent work which is new or particularly exciting, but they by no means include all that has been significant or new during the past year.

Bond Energies and Chemical Reactivity

Wing Tsang
Chemical Kinetics Division

Bond energies are the essential ingredients for understanding chemical reactivity. Recent studies at NBS suggest that many long accepted values are in error. It is demonstrated that the new bond energies provide a sound basis for understanding cis-trans isomerization and small ring decyclization processes.

The course of any chemical reaction is marked by breaking and forming chemical bonds. For a quantitative understanding of chemical kinetics, a knowledge of the appropriate bond energies is necessary. Chemical kineticists usually define the bond dissociation energy as the enthalpy of reaction for the process AB → A+B at 298 K, where A and B are molecular fragments. Note that this is a thermodynamic quantity and is directly related to the enthalpies of the molecule and fragments. However, since A and B are frequently unstable, direct determinations through heat of combustion measurements are not feasible. Indirect techniques must therefore be used, and for all except the smallest fragments, this means kinetic methods. Thus, one selects a reaction involving the unstable species in question and measures the rate of the reaction in both directions. Detailed balancing yields an equilibrium constant which can then be converted to heats of reaction if structural information for all species is known. Alternatively, a heat of reaction can be calculated from the temperature dependence of the equilibrium constant as measured across a range of temperatures. For all these measurements the instability of the molecular fragments introduces severe uncertainties and the heats of formation or bond energies so determined are necessarily fraught with assumptions. Nevertheless, for bond energies to play

a role in predictive theories, accuracy requirements are extremely stringent.

For example, in the cases where the bond energy is directly reflected in the rates for a particular process, an error of 6 kJs will result in an order of magnitude deviation in rate at 298 K and a factor of 2 at 1000 K.

The history of gas kinetics has been marked by repeated determinations of bond energies and, as new techniques and understandings have developed, by continual revisions of what had been thought to be well established numbers. Recent work at NBS has led to new insights on such measurements. The validity of this work is suggested by the self-consistency of the results as derived from a wide variety of measurements. Specifically, the NBS studies have concentrated on the reactions

$$A_2 \underset{k_b}{\overset{k_f}{\rightleftharpoons}} 2A$$
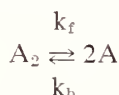
(where A = ethyl, isopropyl and t-butyl radicals), and have shown that high temperature determinations for k_f at 1100 K (carried out at NBS) and a reinterpretation of low temperature measurements, are completely consistent with existing results on the reverse reaction k_b. These combined studies cover a range of rate constants of 35 orders of magnitude. Thus, for these "over-determined" systems we arrive at a consistent set of thermal properties for the unstable species A. Furthermore, the calculated entropies agree with present day ideas on the molecular structure of the species involved. The enthalpies are, however, significantly different from those determined by scattered measurements of the type described earlier. The NBS results are thought to be more reliable due to the larger data base and consistency of determinations. Generalizing from these results, we arrive at the

values for the heat of formation of simple organic radicals presented in table 1. Also included for comparative purposes are previously recommended values. It should be noted that the general trend of the new data is towards increasing bond energies. In other words, most aliphatic hydrocarbons are much more stable than previously assumed.

An interesting consequence of these findings, which serves to illustrate the use of bond energies as a predictive tool, deals with the isomerization of small ring hydrocarbons. This is a subject of great current interest for which a considerable volume of data exists. The study of such highly strained systems pushes chemical theory to its limits. The simplest way of visualizing such processes is to postulate a biradical intermediate formed from the

Table 1. Comparison between old and new values for carbon-hydrogen dissociation energies.

Compound	New NBS values (kJ/mol)	Previous recommended values (kJ/mol)
Ethyl-H	420	412
Isopropyl-H	407	395
N-Propyl-H	420	409
S-Butyl-H	407	398
I-Butyl-H	422	417
T-Butyl-H	404	387
T-Amyl-H	405	
Cyclohexyl-H	416	395
Allyl-H	377	369
Isobutenyl-H	373	
1-Methylallyl-H	375	355
Propargyl-H	384	393
3-Methylpro-pargyl-H	385	
Benzyl-H	372	352

Table 2. Comparison between predicted and experimental activation energies for ring opening reactions.

Compound	Experimental (kJ/mol)	From NBS bond energies (kJ/mol)	Previous results (kJ/mol)
Ethylene (2-membered ring)	275	272	255
Cyclopropane	268	255	238
1,2 Dimethylcyclopropane	259	263	250
1,1,2,2, Tetramethylcyclopropane	228	232	188
1,2 Dimethylcyclobutane	257	251	230
Vinycyclopropane	208	208	108

breaking of the highly strained C-C bond, followed by appropriate rotations and finally recyclization. The activation energy for the isomerization is therefore: $E = \Delta H_T$ (ring opening) $+$ RT and ΔH_T (ring opening) $= 2D_T$ (C-H)-D_T (H-H) $+ \Delta H_T$ (hydrogenation) where D_T is the bond dissociation energy at temperature T and the heat of hydrogenation refers to the conversion of the cyclane to the appropriate aliphatic compound. Since the last two terms are accurately known, the dependence of the activation energy on the bond dissociation energy is quite clear. Such calculations performed using the older bond dissociation energies have always resulted in values approximately 20 to 40 kJ lower than ex-

perimentally measured. As a result, it has been necessary to postulate a 20 to 40 kJ activation barrier for recyclization or rotation. Structural and quantum mechanical considerations are however at variance with the assumption of such a barrier, making this subject quite controversial. With the new bond energies, we obtain the activation energy results summarized in table 2. It can be seen that the deficit has been almost completely removed and in most cases is probably within the experimental uncertainty. Thus, it is now clear that the biradical mechanism does provide an accurate quantitative basis for predicting the activation energy for the isomerization of small ring compounds.

Dynamic Thermophysical Measurements

Ared Cezairliyan, Thermophysics Division

Research has been carried out to explore, by dynamical means, the thermophysical behavior of solids and fluids under extreme conditions of rapid heating. In addition to studying properties of materials of interest in the areas of high temperature sciences and technologies, we have attempted to:

- clarify the anomalous behavior of the heat capacity of metals at high temperatures (fig. 1),
- determine the effect of dynamic heating conditions on vacancy generation and migration,
- study superheating in phase transitions, and
- investigate the non-linear contributions to the transport phenomena under large thermal and electrical gradients.

Because of limitations in the conventional steady state techniques at high temperatures (above 2000 K), we have developed a dynamic technique for conducting the research. For convenience, our activities may be divided into
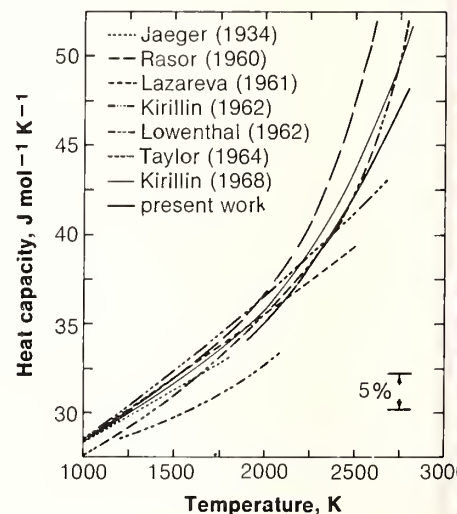
FIGURE 1. Heat capacity of molybdenum. The results indicate considerably higher values at high temperatures than the classical value of 3R (about 25 J mol^{-1} K^{-1}).

two categories, namely "millisecond" and "microsecond" systems—terms indicative of the speed of the dynamic experimentation. In either case, the technique is based on rapid resistive self-heating of a specimen by an electrical current pulse and on measuring the pertinent experimental quantities with appropriate time resolution.

In the millisecond system, we undertook two types of activities: (1) measuring selected thermophysical properties of new materials with the facility developed earlier in this program, and (2) developing new capabilities to enable the measurement of additional properties. In the microsecond system, we continued to develop a facility for extending accurate measurements to temperatures above the melting points of materials and up to 6000 K. Some of the highlights are given below.

With the "millisecond" system, we measured heat capacity, electrical resistivity, and thermal emittance of a graphite composite used as a high temperature material in aerospace applications. Similar measurements, in addition to its melting point, were also performed on palladium. It should be noted that the melting point of palladium is a reference point on the International Practical Temperature Scale and that its value is based on measurements performed over 40 years ago. New developments, as additions to the millisecond system, include a capability to measure thermal expansion simultaneously with other properties. We designed, developed, and performed a feasibility study of a laser pulse interferometer for this purpose (fig. 2). Another addition was a technique for measuring heat of fusion of metallic materials in experiments of subsecond duration. To check the technique, we performed measurements on niobium. Other new areas that we
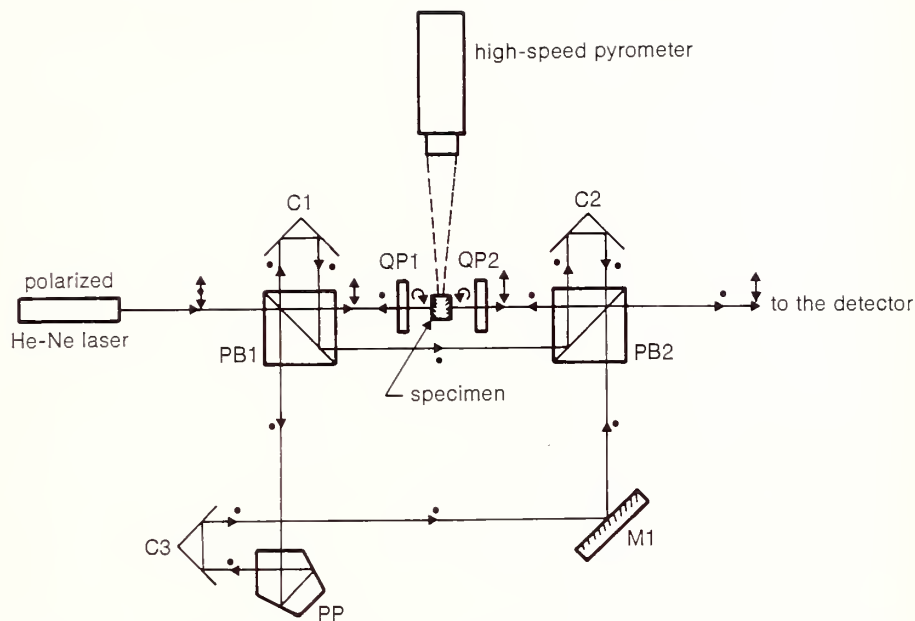
FIGURE 2. Schematic diagram of the laser pulse interferometer for rapid measurement of thermal expansion.
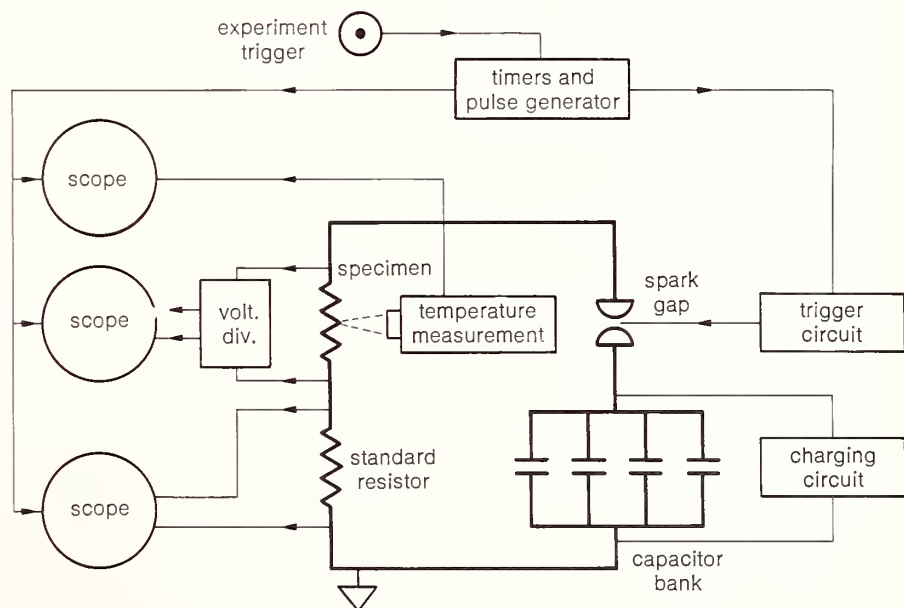
FIGURE 3. Functional diagram of a dynamic (microsecond-resolution) thermophysical measurements system.

Pressure as a Probe of Molecular Interactions

Vern E. Bean, Thermophysics Division

The use of pressure as a variable parameter is a valuable tool for studying molecular interactions. We have recently used differential thermocouple analysis to explore the phase transitions in carbon tetrachloride (CCl_4). Our measurements demonstrate that CCl_4 has dual melting curves up to a pressure of 100 MPa.

embarked on include (in conjunction with S. Block's group, Center for Materials Science) developing a measurement technique under combined conditions of high temperatures and high pressures. Research is presently underway to assess the feasibility of pulse heating specimens in a diamond anvil high pressure cell. The objective is to determine the melting temperature of materials as a function of pressure (up to above 10 GPa).

As an important step in developing an accurate microsecond resolution thermophysical measurement system (fig. 3), we designed and constructed a prototype pyrometer which incorporates a digital data acquisition system. The pyrometer has the capability of measuring the temperature of a rapidly heating specimen every one microsecond with a resolution of about 0.1 percent.

We have also advanced the state-of-the-art in electrical power measurements of high-voltage, high-current discharges. We plan to use this very fast system to obtain thermophysical properties data on solids and liquids up to 6000 K and to conduct studies on the behavior of materials under rapid dynamic heating conditions.

There are four phases in CCl_4 in the temperature/pressure region investigated: liquid, a face-centered cubic phase (denoted as Ia), a rhombohedral phase (Ib), and a monoclinic phase (II). Both Ia and Ib are plastic crystals. The interest is in the relationship between the liquid, Ia, and Ib. When CCl_4 is cooled at atmospheric pressure, it solidifies into Ia at about 245 K and with further cooling transforms to Ib. When heated, Ib melts around 250 K without passing back through the Ia phase. Should the cooling be limited

so that only Ia is formed, then Ia melts around 245 K. Thus, at atmospheric pressure, CCl_4 has two melting points some 5 degrees apart. We have studied these phase changes as a function of hydrostatic pressure up to 350 MPa and over the temperature range of 210 to 330 K with the following results:

1. Between atmospheric pressure and 100 MPa, CCl_4 has dual melting curves, one for Ia, and, a few degrees higher, one for Ib, as shown in figure 1. Above 100 MPa, there is only one melting curve, that of Ib. These two curves diverge with increasing pressure. Above 273 K and 100 MPa, it was not possible to detect the formation of the Ia phase.

2. The Ia-Ib phase boundary is metastable. It is vibration sensitive and pressure rate dependent. The Ib phase will abruptly and spontaneously form from the Ia under a variety of conditions. Ib will also form from the liquid without passing through the Ia phase.

FIGURE 1. Melting curves for the Ia and Ib phases and the II→Ib transition curve for CCl_4.

3. There is no liquid-Ia-Ib triple point.

4. Liquid CCl_4 will superpress (which is analogous to supercooling in an isobaric experiment) forming a band in the T/P plane where the metastable fluid exists. The width of this metastable band increases with pressure.

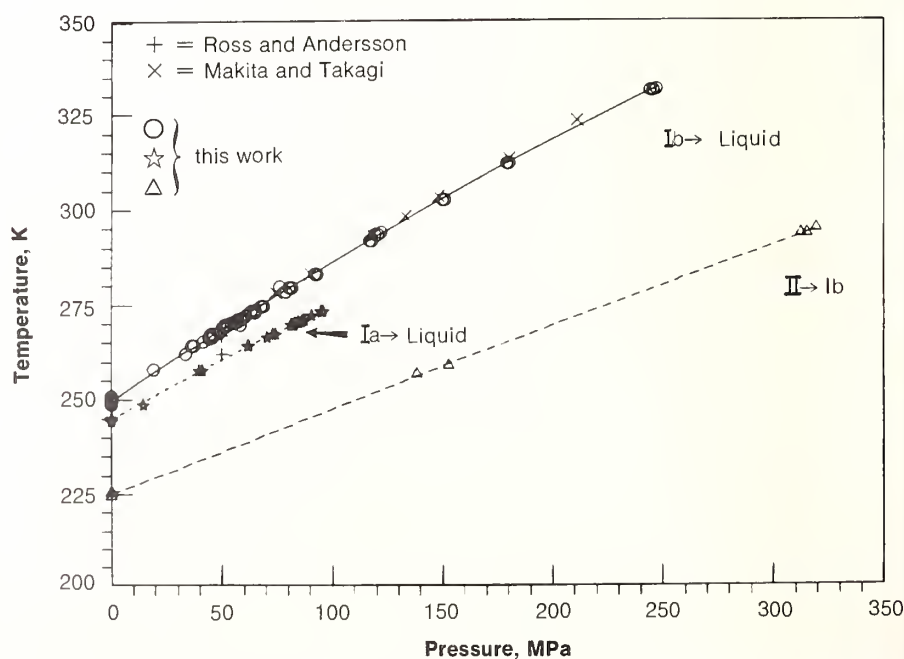A number of other experiments where pressure is an independent variable are either underway or are being developed. They include:

1. Light scattering measurements on fluids at high pressure through use of photon correlation spectroscopy for highly viscous liquids, and Brillouin scattering for less viscous liquids Such measurements will yield: (a) the mean time for structural relaxation, (b) a measure of the distribution of relaxation times about the mean, and (c) a measure of the elastic response of the liquids to high frequency disturbances. Based on these data, researchers will initiate a program to develop theories which relate the rearrangement dynamics to the mechanisms which lead to viscosity and connect these mechanisms with the ease with which metastable states can be realized.

2. Isothermal compressibility measurements in fluids which use the precision of ultrasonic interferometry. The technique involves making ultrasonic measurements on two samples of the same fluid in the same pressure vessel. One sample has a constant ultrasonic path length, the other a constant mass. From the data, one obtains the speed of sound in the fluid as a function of pressure and the isothermal compressibility without going through the usual adiabatic to isothermal conversion.

This capability will be used to: (a) look for density anomalies in the metastable liquid region of CCl_4, (b) obtain compressibility data on fluids having nearly spherical molecules (to be used with change of the index of refraction with pressure data, obtained by K. Vedam of Pennsylvania State University, in a critical evaluation of equations of state of fluids), and (c) obtain compressibility data to be used in conjunction with dielectric relaxation measurements in an attempt to apply activation volume concepts to metastability in fluids.

3. Capacitance measurements on fluids as a function of pressure, temperature, and frequency for the dielectric relaxation studies mentioned above.

The Catalytic Methanation Reaction: A Source of Synthetic Natural Gas

John T. Yates, Jr., David W. Goodman, Richard D. Kelley, and Theodore E. Madey, Surface Science Division

Synthetic methane, CH_4 produced from coal, will become a major component of the Nation's natural gas supply after 1990. Heterogeneous catalysts will certainly play a significant role in achieving this objective. We have been studying the fundamental mechanism of the key catalytic reaction involved in the synthesis of methane. Using modern surface measurement methods, we have determined the chemical mechanism for the catalytic hydrogenation of carbon monoxide, CO, over nickel catalysts, and certain mechanisms of catalyst poisoning have been thoroughly investigated. This understanding of catalytic processes should provide a conceptual basis for optimizing the efficient use of catalysts in what promises to become a multibillion dollar national enterprise.

All proposed routes from coal to high-BTU methane involve the initial gasification of coal using steam and air or oxygen and yielding coal gas, a mixture of CO, H_2, and CH_4. While this mixture will burn, its BTU content is too low (150 to 500 BTU per standard cubic foot) for economical transport through the Nation's pipeline system. Therefore, the coal gas mixture must be catalytically converted to pure methane (1000 BTU per standard cubic foot). Although the catalytic synthesis of methane from CO and H_2 has been studied for the last 50 years [1, 2], until recently the mechanism by which the reaction occurs had not been definitely determined. We have been successful in focusing modern surface measurement techniques on this reaction to learn how it works and how to maintain efficient catalyst operation.

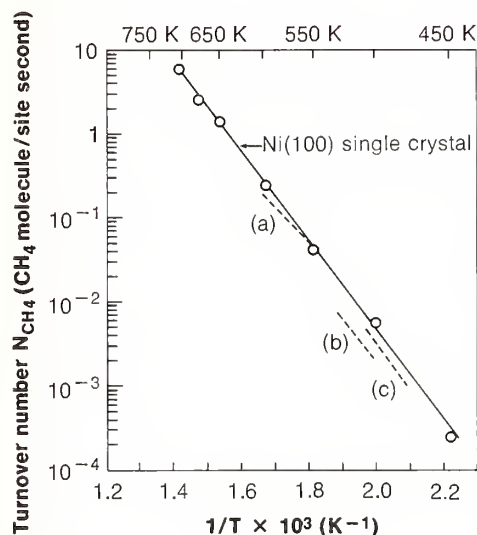Carbon monoxide is the most strongly bound molecule known. The

FIGURE 1. Arrhenius plot of rate of CH_4 synthesis (N_{CH_4}) over different Ni catalysts in various temperature regimes. Ni(100) present work; $P_{H_2} = 96$ Torr, $P_{CO} = 24$ Torr (0.85 cm², $E_a = 103$ kJ/mol); (a) 25-50% Ni/Al$_2$O$_3$, $E_a = 84$ kJ/mol; (b) 5% Ni/Al$_2$O$_3$, $E_a = 105$ kJ/mol; (c) 8.8% Ni/Al$_2$O$_3$, $E_a = 109$ KJ mol.

energy required to dissociate the carbon-oxygen bond is 1070 kJ/mol^{-1}. Because of this basic fact, it is necessary to use a catalyst surface to achieve a suitable chemical pathway leading to: (a) to CO dissociation and (b) to hydrogenation of the fragments to produce CH_4 and H_2O. The catalyst must be able to carry out both reaction steps (a) and (b) with suitable efficiency and with the desired selectivity. In other words, it must produce pure CH_4 efficiently without significant production of other undesired products. A number of transition metal catalysts are suitable, but Ni is, by a large margin, the most inexpensive catalyst currently employed in laboratory and pilot plant CH_4 synthesis studies.

We have employed a Ni single crystal (1 cm² surface area) as a model catalyst for our investigations of the reac-

tion mechanism [3]. Use of the crystal permits us to utilize modern surface spectroscopy techniques for studying the reaction. However, it was first necessary to show that the Ni crystal behaved similarly to actual Ni catalysts having about 10⁶ cm² surface area per gram. A spectacular result was obtained, as shown in figure 1, where the rate of CH_4 synthesis (turnover number) over the Ni(100) single crystal is plotted against 1/T as an Arrhenius plot. Two important conclusions are apparent: (a) linear Arrhenius behavior is observed over a very wide dynamic range (5 orders of magnitude), giving an activation energy of 103 kJ/mol^{-1} (~ 10 percent of the C-O kJ/mol dissociation energy), and (b) The agreement of the rate measured for the single.crystal with rates and activation energies measured on Al$_2$O$_3$-supported high-area Ni catalysts is excellent. The single crystal may be used over a wider temperature range than the technical catalysts, giving more confidence that true activation energies are being determined.

We have directly shown that the single crystal is a good model catalyst [3, 4], and that results obtained on the single crystal are transferable to the real world.

Auger electron spectroscopy was then used to study the chemical com-

position of the surface of the Ni crystal following methane synthesis. We were able to show that a fraction of a monolayer of "carbidic" carbon always exists during the catalytic reaction. It originates from CO dissociation on the Ni surface: the rate of dissociation of the CO is closely related to the rate of CH_4 production [5]. If either the H_2/CO ratio or the temperature falls outside an optimal range, a graphite layer forms on the surface; this graphite layer is a poison which deactivates the Ni catalyst. Such poisoning is a principal problem in methane synthesis over technical catalysts. It was also found that extremely small traces of gaseous $Fe(CO)_5$ present in many sources of unpurified CO produced by coal gasification will decompose to yield an Fe-covered Ni surface which immediately produces the graphite poison, shortening the catalyst lifetime.

The mechanistic details which we have inferred are that both CO and hydrogen dissociate on the Ni surface. The carbon atoms form an active "carbide" layer on the Ni; the carbide species react with absorbed H to form –CH_x intermediates. Further hydrogenation of these intermediates results in the formation of CH_4 product. A simplified view of the mechanism for the reaction of CO and H_2 over Ni catalysts to yield CH_4 is schematically
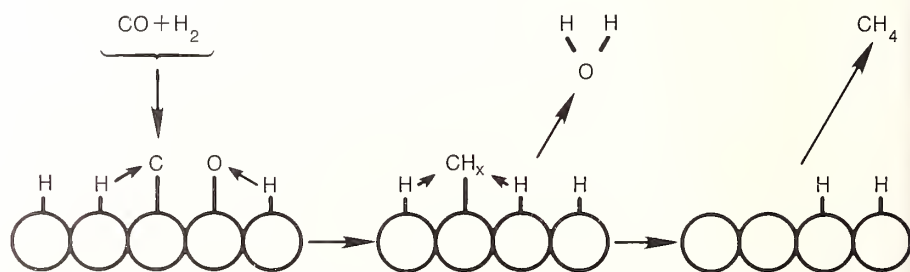

FIGURE 2. Schematic representation of methane synthesis over Ni. The open circles represent the top layer of Ni atoms.

48

Multiphoton Chemistry

John C. Stephenson, Molecular Spectroscopy Division

F undamental studies of how intense infrared laser light causes chemical reactions are described. Time-resolved in situ spectroscopy is used to detect reaction rates, product energy states, and isotope enrichment factors, as functions of laser wavelength, fluence, intensity, and gas pressure. The data is compared to a comprehensive model, yielding new conclusions about the dynamics of excited molecules.
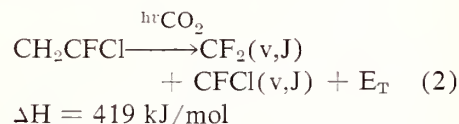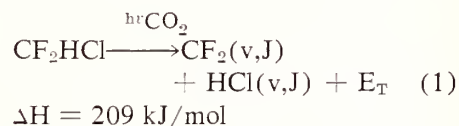
Radiation from powerful and efficient infrared (IR) lasers may directly induce chemical reactions such as molecular isomerizations and dissociations [1]. Since the energy required to break a chemical bond (e.g., 20 000 to 40 000 cm^{-1}) is substantially greater than the energy of an IR laser photon (e.g., the energy of a CO_2 photon is 1000 cm^{-1}), a molecule must absorb many IR laser photons to react. For this reason, such chemical reactions are called "infrared multiphoton reactions" or IRMR. This IR laser radiation selectively excites particular chemical bonds in a molecule, unlike ordinary thermal reactions in which energy in the reactant molecules is distributed randomly. Chemists have hoped that particularly efficient or unique reactions could be effected through laser induced "bond specific chemistry."

An enormous amount of research on laser-induced chemistry is now being done at universities, U.S. and foreign national laboratories, and at several leading corporations. Potential applications of IRMR include separation of stable and fissionable isotopes. Our research here at NBS has focused on developing the basic understanding of how IR laser excitation causes such reactions.

Most experiments in IRMR have been done with CO_2 TEA laser pulses focused into bulbs of gas at high pressures and have relied on chemical analysis of the final stable end products. Such high pressure conditions may be necessary for potential commercially practical processes. However, it may be difficult to relate the results of such experiments to the basic questions of how IRMR occurs. This difficulty arises from complicating factors related to collisions between highly excited molecules, radical chain reactions, reactions on cell walls, secondary photolysis of initially formed products, and undefined or inhomogeneous laser fluence (energy/unit area) or intensity (fluence/unit time).

Our experimental approach [2-6] has been to use a CO_2 laser pulse (about 10^{-7} second duration) to cause an IRMR in a very low pressure gas, such as:

$$CF_2HCl \xrightarrow{h\nu CO_2} CF_2(v,J) + HCl(v,J) + E_T \quad (1)$$

$$\Delta H = 209 \text{ kJ/mol}$$

$$CH_2CFCl \xrightarrow{h\nu CO_2} CF_2(v,J) + CFCl(v,J) + E_T \quad (2)$$

$$\Delta H = 419 \text{ kJ/mol}$$

We then use a weak visible or uv probe laser pulse (5 ns duration) to detect in real time before collisions occur (10 ns resolution) the rate [3, 4] at which products are formed. This technique lets us probe primary processes resulting from the coupling of isolated molecules to the radiation field, before the complicating effects mentioned above have occurred. We probe a region of constant, known CO_2 laser fluence to determine the vibrational (V), rotational (J) and translational energy (E_T) of the products, [2, 6] and the isotopic enrichment [5] (e.g., $^{13}C/^{12}C$) in the products.

Illustrated in figure 2. Efforts are underway to study directly the molecular nature of the postulated CH_4 surface intermediates. We are using neutron energy loss spectroscopy to investigate these species [6]. Also, we plan to study the details of sulfur poisoning of Ni single crystal catalysts; it is known that this will be a major technical problem in the industrial process because sulfur is a major impurity of coal.

A general conclusion from this work is that modern surface measurement tools may be applied successfully to unravel the secrets of catalytic chemistry and to provide new and useful concepts applicable to practical catalytic chemistry.

References

[1] Chemical and Engineering News, *57*, 20-28 (1979). "Synfuels: Uncertain and Costly Fuel Option," by Ward Worthy.

[2] Mills, G. A. and Steffgen, F. W., *Catalysis Reviews, Science and Engineering, 8*, 159 (1973).

[3] Goodman, D. W., Kelley, R. D., Madey, T. E., and Yates, J. T. Jr., Kinetics of hydrogenation of CO over a single crystal Ni catalyst, *J. Catalysis* (in press).

[4] Goodman, D. W., Kelley, R. D., Madey, T. E., and Yates, J. T. Jr., in, *Hydrocarbon Synthesis from Carbon Monoxide and Hydrogen,* E. L. Kugler and F. W. Steffgen, eds., pp. 1-6, *Advances in Chemistry Series 178* (Am. Chem. Soc., Washington, D.C., 1979).

[5] Goodman, D. W., Kelley, R. D., Madey, T. E., and White, J. M., Measurement of carbide buildup and removal kinetics on Ni(100), *J. Catalysis* (in press).

[6] Kelley, R. D., Rush, J. J., and Madey, T. E., *Chem. Phys. Letters, 66*, 159-164 (1979).

We have measured all these factors and determined their dependence on the intensity, fluence, and wavelength of the IR laser. Another important experiment is underway to measure these parameters under conditions in which the reactants are extremely dilute (e.g., 1 part in 10^6) in a high pressure bath of Ar atoms. Under these circumstances, the reactants undergo many collisions with bath molecules during the laser excitation process.
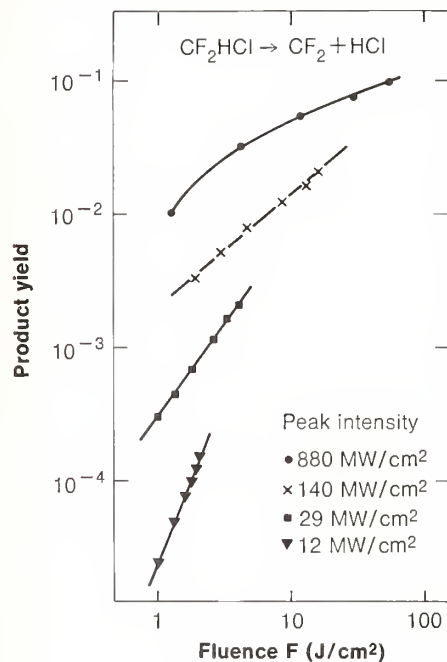

FIGURE 1. Intensity dependence in the IRMR of CF_2HCl. Absolute product yields from the dissociation of CF_2HCl (9.3 μm R(32) CO_2 laser transition of 1086 cm^{-1}) for non-modelocked laser pulses for four different total energies. The pulses all exhibited identical temporal envelopes and are labeled according to the peak intensity. The data given for each different pulse represent the yield of CF_2 observed at various times τ_D, during the IR laser pulse plotted against the

$$\text{fluence } F(\tau_D) = \int_0^{\tau_D} I(t)dt \text{ for that time}$$

and laser pulse. The total pulse energies were 2, 5, 25, and 150 mJ, respectively, for the 12, 29, 140, and 880 MW/cm² pulses.

Any consistent theory of IRMR must explain product yields, formation rates, isotope enrichment, and the energy content of the products as a function of pressure and laser intensity. We are making progress in developing a comprehensive theory.

Some specific results on reaction (1) are shown in figures 1 and 2. In figure 1, the collision-free reaction yield [4] is shown as a function of laser fluence F for CO_2 laser pulses of different peak intensity, I. One popular theoretical model [7, 8] of IRMR, used to explain many results on larger reactant molecules such as SF_6, predicts that the reaction yield depends only on F and is *independent* of I. This is dramatically not true for CF_2HCl, where for laser pulses of constant F, the yield increased by a factor of 400 as the average intensity I increased by only a
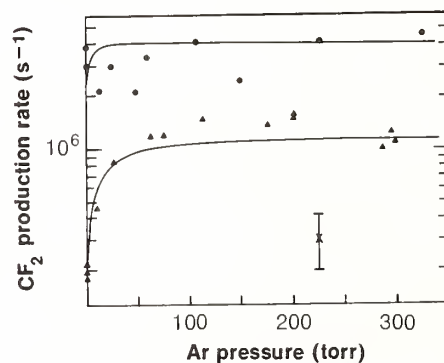
FIGURE 2. Rates of production of XCF_2 during the dissociation of CF_2HCl by CO_2 laser pulses, determined for CF_2HCl very dilute in Ar at the indicated Ar pressures (1 Torr = 133.3 N/m²). The pressure dependence was measured for two experimental conditions: (O), CO_2 laser operating on the R(32) transition at 1086 cm^{-1} which is resonant with the CF_2HCl one-photon absorption, peak laser intensity of 150 MW/cm²; ($\triangle$), R(32) laser energy reduced by a factor of 10. The curved lines drawn through the data points are the theoretically calculated results, based on the model described in ref. [3]. The isolated point shows the magnitude of the ($\pm$ 35%) associated with each experimental datum.

factor of 6. This result shows that for CF_2HCl, coherent excitation of the molecule is important, and that a significant barrier to laser excitation occurs in the discrete lower vibration-rotation levels of this molecule. In figure 2, the absolute rate [3] at which CF_2HCl molecules decompose is shown as a function of Ar pressure, for CO_2 laser pulses of two different intensities. The initial rise in reaction rate with increasing Ar pressure is due to collision-induced rotational relaxation, i.e., CF_2HCl collisions with Ar atoms result in rotational equilibration within the absorber pump mode, allowing the pumping of molecules which were originally in rotational states outside the power broadened line. The fact that there is no *downturn* in rate at high Ar pressure shows that vibrational deactivation of excited CF_2HCl reactant molecules is not as efficient as theories [3, 8] had predicted.

By using a comprehensive model to understand data like that in figures 1 and 2, we can make predictions or draw conclusions about molecular dynamics that are very difficult to measure directly. Figures 3 and 4 show such predictions [3, 8] based on the model which fits the data for figure 2. In figure 3, the distribution of vibrational energy in the laser excited reactant (solid line) is shown at time (1, 2, and 50 ns) during the laser pulse when the average reactant had absorbed 5, 10, and 15 photons, respectively. For comparison, the dashed lines show thermal distributions of the same average energy. Note that the laser-driven distribution always differs from a thermal distribution. Figure 4 shows the absorption cross section for a CF_2HCl reactant to absorb CO radiation as a function of the amount of energy the CF_2HCl has absorbed. Note that the absorption cross section

ecreases rapidly as the energy in-
reases. This decrease is due to very
apid intramolecular dephasing rates
short T_2 times) caused by anharmonic
ouplings. The result is a "smearing
ut" of oscillator strength over a very
road spectral region.

The field of IRMR is extremely ac-
ve. Questions related to coherent vs.
ncoherent excitation, T_1 and T_2 times,
nd the feasibility of "bond specific
hemistry" are still controversial, as
re questions regarding the commer-
ial practicality of IRMR processes.
However, these experimental and the-
retical IRMR studies are creating new

and detailed understanding useful in
all areas of gas phase chemistry and
molecular dynamics.

References

[1] Cantrell, C. D., Freund, S. M., and
Lyman, J. L., Laser Induced Chemi-
cal Reactions and Isotope Separation,
in *Laser Handbook,* Vol. II (North-
Holland, Amsterdam, 1978).

[2] Stephenson, J. C. and King, D. S.,
J. Chem. Phys. 69, 1485-1492 (1978).

[3] Stephenson, J. C., King, D. S., Good-
man, M. F., and Stone, J., *J. Chem.
Phys. 70,* 4496-4508 (1979).

[4] King, D. S. and Stephenson, J. C.,
Chem. Phys. Letters 66, 33-38 (1979).

[5] King, D. S. and Stephenson, J. C.,
J. Am. Chem. Soc. 100, 7151-7155
(1978).

[6] Stephenson, J. C., Bialkowski, S. E.,
and King, D. S., Energy Partitioning
in CO_2 Laser Induced Multiphoton
Dissociations: Energy of XCF_2 and X
CFCl from CF_2CFCl, *J. Chem. Phys.
80,* (1980).

[7] Bloembergen, N., Yablonoviach, E.,
Physics Today 31, 23-30 (May 1978).

[8] Goodman, M. F., Stone, J., and
Thiele, E., Laser-Induced Decomposi-
tion of Polyatomic Molecules: A
Comparison of Theory with Experi-
ment, in *Multiple Photon Excitation
and Dissociation of Polyatomic Mole-
cules, Topics in Current Physics,* C.
D. Cantrell, ed. (Springer-Verlag,
New York 1979), and op. cit. therein.
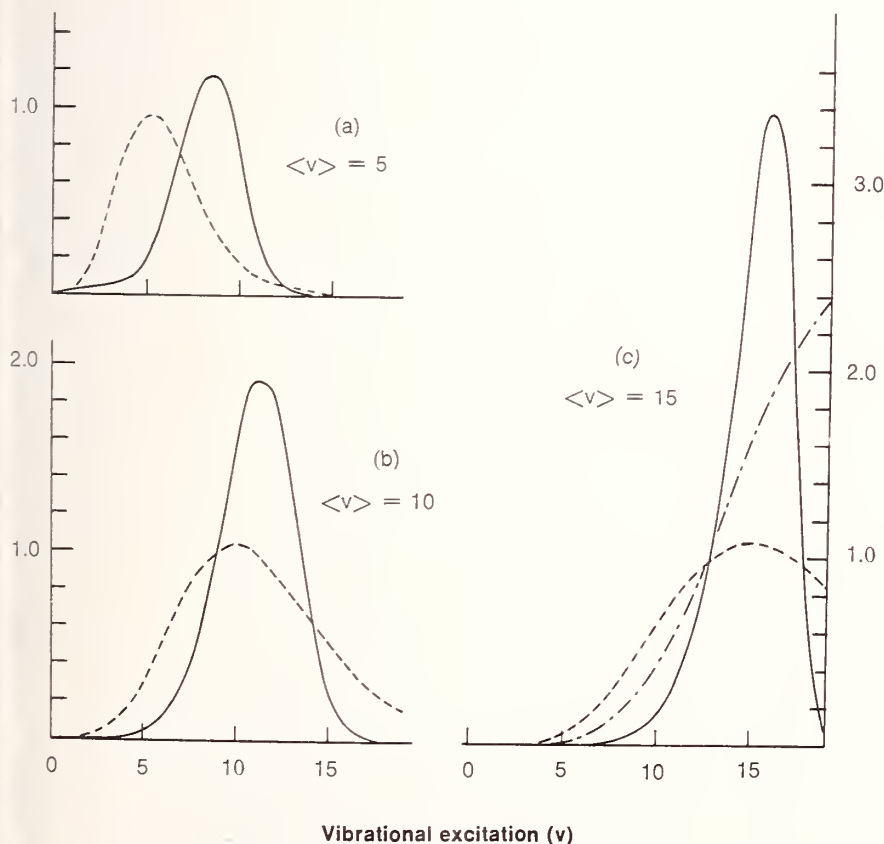
FIGURE 3. Laser excited distributions (—) compared with thermal distributions (- - -):
a) average energy (v) = 5; (b) average energy (v) = 10; and (c) average energy (v)
= 15. The extra curve (—.—) in (c) for (v) = 15 is the thermal distribution for a
molecule arbitrarily truncated at 20 levels. These model predictions are for a CO_2 laser
intensity of 150 MW and 300 Torr Ar.
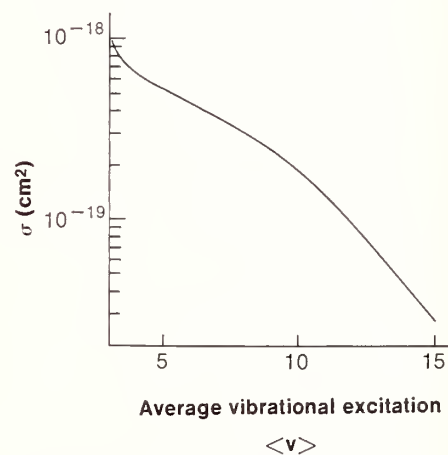
FIGURE 4. CF_2HCl absorbtion cross section
calculated for various values of energy ab-
sorbed (v). These average absorptions were
achieved by varying the time of irradiation
at an intensity of 150 MW/cm² and a pres-
sure of 300 Torr Ar.

Quantum Calculations of Excimer Molecules

Morris Krauss, Molecular Spectropy Division

Quantum chemical calculations are being performed to identify and analyze the potential of candidate electronic laser systems for the Department of Energy and Defense Advanced Research Projects Agency-sponsored programs for generating high power laser beams. The net gain of a candidate system must be known. Experimental determination of this property is difficult for exciplex or excimer systems. Calculation of the spectroscopic behavior of excimer and continuum-continuum systems has proved to be an important source of information.

We have calculated the spectroscopic properties of important molecules in the following classes of laser candidates: Group VI-rare gas, rare gas-halide, Group IIb-Group IIa and b dimers, Group IV-rare gas, and rare gas-rare gas.

Ab initio molecule calculation for evaluating energies and spectroscopic properties can be done for small molecules containing low Z atoms using all-electron multi-configuration variational techniques. Considerable experience has been accumulated on dealing with the calculation of the correlation energy involved in bonding interactions over the entire range of internuclear separations. Of particular importance for excimer systems is the recent development of techniques for calculating van der Waals interactions into distances where the overlap of the charge distributions is no longer negligible. We have shown that the modification of the usual inverse power series expansion by a damping function $\chi(R)$,

$$E(vdw) = -\sum_{l,L} C(l,L) \; \chi(l,L,R) \, R^{-2(l+L+1)}$$

can be applied to all the systems mentioned above.

All the molecules of a class are of interest; thus the all-electron techniques have been extended by introducing pseudo-potentials to replace the core electrons. Both non-relativistic and relativistic effective core potentials (ECP) have been generated and used as necessary to treat high Z atoms. Calculations of the electronic properties of ion-pair molecules using ECP have compared favorably with all-electron results, although more research is still needed on the use of the ECP. Using the pseudo potentials, we have considered molecules containing elements as heavy as Hg and Pb. The ECP take the relativistic contraction of the core into account, but at the present time the spin-orbit interaction in the valence shell is treated as a perturbation.

The transition moments and energies have been calculated for the X-A bound to continuum transition in HgCl. The photodissociation cross section is illustrated in figure 1 as a function of the transition energy and temperature. The laser energy for the B-X transition is close to the peak energy, and a significant absorption will result from a buildup in the concentration of X state HgCl in the course of exciting the laser media. This absorption could explain the low extraction efficiency observed for certain types of HgCl lasers.

Self-absorption in Cd_2 is also predicted by ab initio calculations for the excimer transition. From the energy curves shown in figure 2, we see there is strong bound-bound, $^3II_g \rightarrow {}^3II_u$ absorption near 470 nm. Absorption was also predicted earlier for the 335 nm emission from Hg_2 from the reservoir metastable excited states.

The Group VI-rare gas laser transition is a collision-induced electric dipole transition between electronic states that correlate to the valence states of the Group VI atom and the ground state of the rare gas atom. We have determined that, with the exception of XeO, the transistions are dominantly continuum-continuum. Calculation of the transition line shape is found to require a multichannel coupling among all states arising from the valence asymptotes. The line-shape for the Ar-O(^{1}D) - Ar-O(^{1}S) transition has been calculated in reasonable agreement with an experimental determination.

Pb vapor is now being explored as a Raman scattering media for producing highpower backward scattered pulse from an XeCl laser pulse. Rare gas buffers are used to enhance the backward scattering cross section over the forward. Collision-induced absorption at either the pump or Stokes frequency would reduce the efficiency of the process. A calculation of Pb-He and Pb-Xe energy curves and transition moment reveals that collision-induced absorption is not significant at the frequencies of interest.

The rare gas halide diatomic and triatomic excimer spectroscopy owe a great deal to theoretical calculation. Not all of the relevant states have been observed directly by experiment and assignments of some transitions are still not definitive. The relative ener-
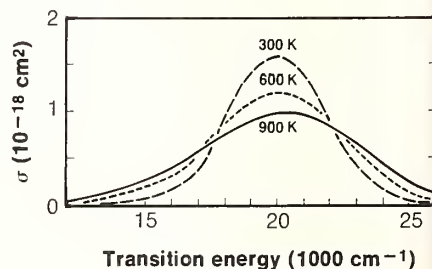
FIGURE 1. Photodissociation cross section for the $X^2\Sigma - A^2II$ transition in HgCl as a function of transition energy and temperature.

ies of the B and C states in the
iatomic system are of present interest.
Ve are now comparing our calculations
ith the interpretations of the experi-
iental data. We agree with previous
heoretical all-electron calculations that
he B state is lower in energy than the
. for XeF and XeCl.

Theoretical calculations have proved
to be a fast, accurate way to obtain the
spectroscopic data needed in modelling
laser media. We are continuing our
studies of the rare gas halide lasers by
examining photodissociation of bottle-
necked states in XeF and the likelihood
of positive gain for the Xe_2Cl system.

New Development in the Evaluation of Thermochemical Data

D. D. Wagman, David Garvin, Vivian
B. Parker, Richard H. Schumm, and
J. Brian Pedley[1], Chemical Thermo-
dynamics Division

A comprehensive, up-to-date
compilation of evaluated thermochem-
ical data has been completed by the
NBS Chemical Thermodynamics Data
Center. The compilation is called
Selected Values of Chemical Thermo-
dynamic Properties. It covers the peri-
odic table except for some of the
actinide elements and includes over
12,000 inorganic and low molecular
weight organic compounds. These
include pure substances in the gaseous,
liquid, and solid phase as well as many
binary solutions.

The properties tabulated in the com-
pilation are the enthalpy of formation,
$\Delta_f H°$, Gibbs energy of formation,
$\Delta_f G°$, entropy, $S°$, and heat capacity,
$C_p°$, all at the temperature 298.15 K
(25 °C). In addition, values are pro-
vided for the enthalpy of formation at
0 K, $\Delta_f H° (0)$, and the enthalpy
difference $H° (298) - H° (0)$. The
values are based almost entirely on
experimental measurements and statis-
tical calculations. Approximately 20,-
000 property values are included. Well
over half of these are enthalpies of
formation. The next two most numer-
ous entries are for Gibbs energies of
formation and entropies.

These tables are designed for use in
chemical engineering, chemical and
biochemical research, rocketry, plasma
studies, environmental control, energy
conservation, and other related tech-
nological fields. Thermodynamic prop-
erties are essential for calculating the
energetics of chemical processes and
optimizing of equilibrium yields. They
are widely used in interpreting physico-
chemical research.

The numerical values in the tables
resulted from critical analysis and eval-
uation of many different types of

FIGURE 2. Excited state energy curves for the Cd_2 molecule calculated with multi-configura-
on self-consistent-field variational techniques.

[1] University of Sussex, England.

physico-chemical measurement. Various calorimetric reaction enthalpies can be combined to yield values for the enthalpy of formation of particular substances. High temperature equilibrium studies may be combined with values of the thermal functions for the individual species in the reaction to yield desired values. Calculating thermal functions of gases by statistical-mechanical methods requires a knowledge of molecular structure parameters (bond lengths and angles) and vibrational frequencies; the calculation for a substance in the condensed phase requires values for the enthalpy content as a function of temperature and enthalpies of phase transitions. Low temperature (298 to 0 K) $C_p°$ measurements are used to obtain the third law $S°$ (298 K)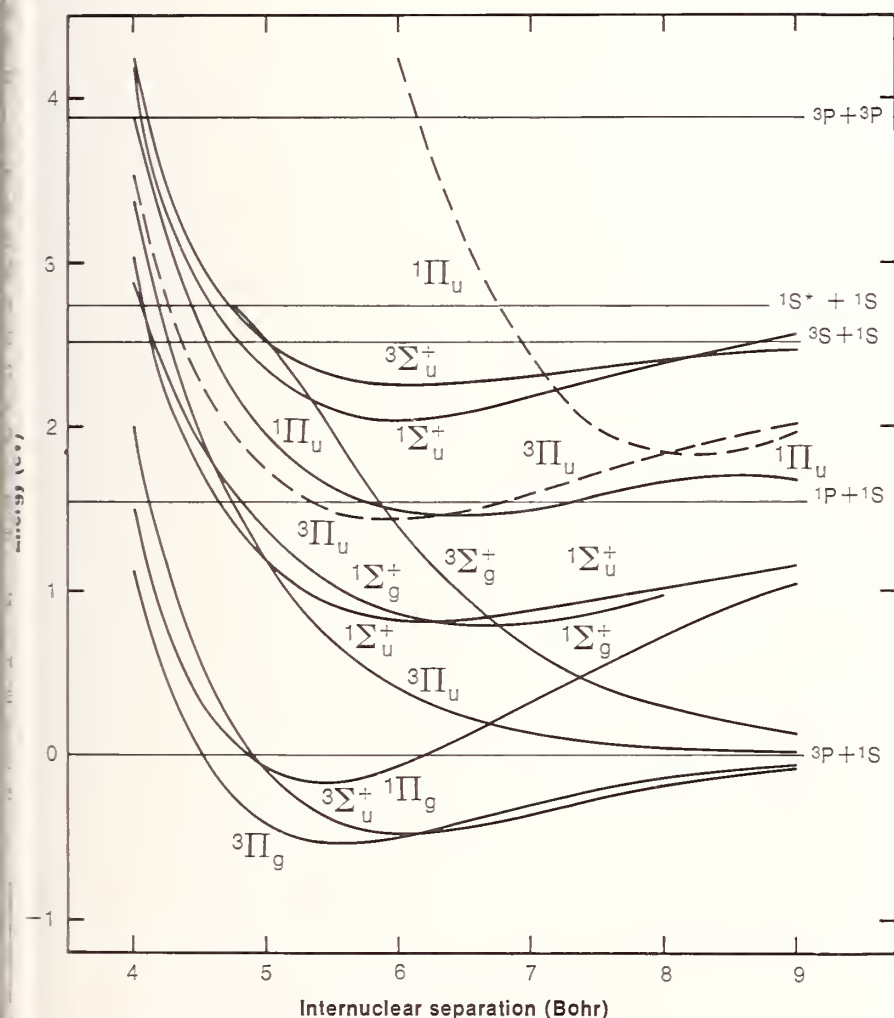. Similarly, data on solubility, activity and osmotic coefficients, vapor pressures, and enthalpies of solution and dilution are required for the proper evaluation of measurements on solutions. Enthalpies of combustion, hydrogenation, and halogenation are used in the calculation of thermodynamic properties for organic molecules.

To do the above evaluations, we have amassed a reference file of numerical data abstracted from more than 40,000 articles describing over 200,000 measurements made since 1848 on individual chemical substances. Each year, an annotated bibliographic reference list of all material added to the Data Center files is published in the Bulletin of Chemical Thermodynamics. This list, arranged by chemical formula of the substance measured, indicates the type of measurement made as well as the full bibliographic citation.

Construction of these reference data tables is an exercise in the art of data evaluation. Often the properties of a substance can be determined by using
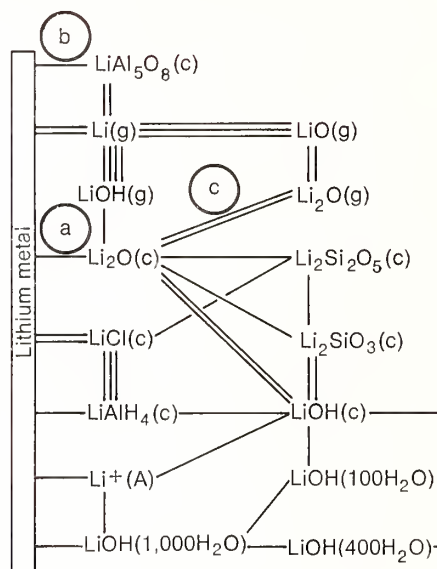
FIGURE 1. Loops of 5 members or less, containing reaction ⓐ ; each line between substances represents one reaction between lithium compounds; processes ⓑ and ⓒ appear to contribute large errors.

several different measurement paths. The interconnections among the paths may be seen in figure 1. The results obtained from the various paths usually do not agree. Choices must be made in establishing the "best" values.

There are two fundamental components in this evaluation process. The first is the heart of the process and must be done by an expert. It is necessary to determine, for each measurement, in the light of present knowledge, whether or not the interpretation of the chemistry was correct and whether the technique was suitable. Reinterpretation, recalculation, and correction of the data often are necessary. A consistent set of auxiliary data is used in reducing the measurements, e.g., physical constants and properties of ubiquitous substances. Accuracies of the measurements must be assigned.

The second component is the combination of the accepted measurements to produce the final, recommended

values for the substances. The following criteria are required for this component: (1) The recommended values must reproduce well those measurements considered to be reliable. (2) The values selected must be thermodynamically consistent throughout the tables and be in reasonable accord with physico-chemical correlations (similar substances should have similar properties).

Recently, this second component has been automated. More than 1,000 measurements involving 600 or more substances may be involved in a particular problem. Computer techniques are ideal for manipulating such large masses of data. In addition, a systematic fit of the data is obtained with an analysis of the network. This fit is used as a guide to the strategy of data evaluation and to indicate the importance of various substances. Rapid updating of the recommendation is possible when new and significant measurements become available because these evaluated measurements are stored in reusable form. The network solutions combining the measurements are done in an iterative process in which linear programming is used to locate the most highly consistent set of measurements and weight them accordingly, prior to a least squares solution. This two-step approach has been shown to mimic the decisions made by data analysts when they combine the measurements in the traditional "by-hand" solution. It results in a solution from which the user may combine any set of values in the data bank to predict with confidence the thermochemistry of a process.

Automation has been an important factor in the development of the data bank. The selected values are stored in a machine-readable file. Tables can be printed in any system of units
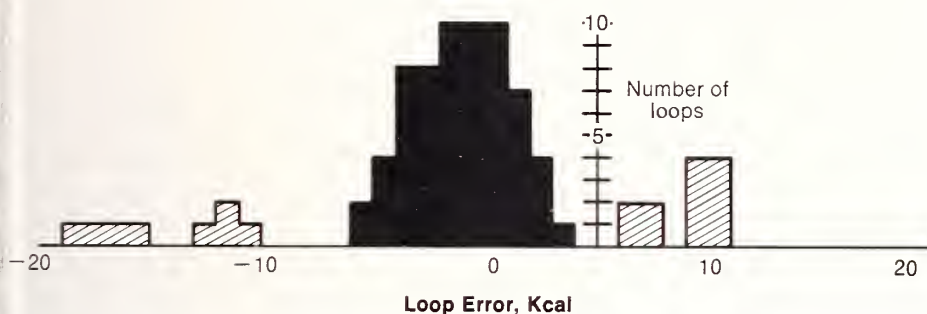
FIGURE 2. Errors in loops containing up to 5 members, and containing reaction (a) ; shaded portions are deleted when reactions (b) and (c) are discarded.

(Publication in SI and in "caloric units" is planned.) A machine-readable catalog of the accepted measurements is being developed—both to document the tables and for direct use in applications. In a cooperative program with the University of Sussex, England, automated quality control, network solution, and graphic display techniques have been developed. These simplify and speed up the routine parts of the task. These quality controls assure that thermodynamic consistency is maintained.

A recent development is "loop analysis". In this analysis, measurements are summed over every closed path in the loosely connected network. Conservation laws require zero sums, but experimental inaccuracies produce errors of closure. An analysis of the loop errors shows which measurements are highly inconsistent. As an example, figure 1 shows a network involving enthalpy measurements for 16 lithium compounds. It shows all 5 membered (or fewer) closed paths involving process a (there are 84 of these). The distribution of errors of closure is shown in figure 2. The mean error is close to zero, indicating that process a probably is acceptable. But the distribution is distinctly nonnormal. Processes b and c account for all extreme values and therefore are of doubtful accuracy.

This technique holds the promise of becoming a very rapid technique for preliminary analysis of thermochemical data and may play an important role in future data evaluation strategies.

Center for Analytical Chemistry

Curt W. Reimann

Lucy B. Hagan
John K. Taylor

Instrument Development
James R. DeVoe

Thomas C. O'Haver
Willmer C. Ruegg
Robert L. Sams
Donald W. Shideler
Richard K. Simon, Jr.*
John C. Travis
Gregory C. Turk

Inorganic Analytical Research
Ernest L. Garner

John Alienkoff**
John R. Baldwin
L. Lynus Barnes, Jr.
Ellyn S. Beary
James M. Blackman**
William A. Bowman, III
David E. Brown
Robert W. Burke
L. Stephen Carpenter
Isabell Casar**
Erle R. Deardorff
Barry I. Diamondstone
Lura P. Dunstan
Michael S. Epstein
John D. Fassett
Donald F. Fleming
Thomas E. Gills
John W. Gramlich
Robert R. Greenberg
Jose Guerrero**
Shigeki Hanamura
Joe M. Harris**
Wally H. Harrison
Emerson F. Heald
William R. Kelly
Howard M. Kingston, Jr.
William F. Koch
James Koskoris

Richard M. Lindstrom
George J. Lutz
Lawrence A. Machlan
E. June Maienthal
George Marinenko
Radu Mavrodineanu
Jerry D. Messman
Klaus D. Mielenz
J. Mitchell**
John R. Moody
Pedro A. Morales**
Thomas J. Murphy
John A. Norris
Paul J. Paulsen
Theodore C. Rains
Robert L. Watters, Jr.
Tadashi Yamamoto**
Rolf L. Zeisler

Organic Analytical Research
Harry S. Hertz

Robert E. Botto**
Jeanice M. Brown
Stephen N. Chesler
Richard G. Christensen
Alex Cohen
Bruce Coxon
Lawrence M. Doane*
Richard A. Durst
Delmo P. Enagonio
Rafael Espinosa-Leniz**
Alexander J. Fatiadi
Mary L. Fultz
Franklin R. Guenther
Diane Hancock
Laurence R. Hilpert
Barbara F. Howell
Pamela L. Konash
William A. MacCrehan
Sam A. Margolis
Willie E. May
Reenie M. Parris
Dennis J. Reeder

Kristy L. Richie
Robert Schaffer
Lorna T. Sniegoski
William J. Sonnefeld**
Pietr VanDerLijn**
Rance A. Velapoldi
Michael J. Welch**
Edward White, V
Patricia A. White**
Stephen A. Wise
William T. Yap

Gas and Particulate Science
Harry L. Rook

Arnold M. Bass
Adville A. Bell
John J. Blaha
David S. Bright
Barry C. Cadoff
R. Casciani**
Ilan S. Chabay
Lloyd A. Currie
William D. Dorko
James W. Elkins
Edgar S. Etz
Charles Fiori**
Robert A. Fletcher
Alan Fried
Jimmie A. Hodgeson
Ernest E. Hughes
Robert H. Kagann
George A. Klouda
Edwin C. Kuehner
Ryna B. Marinenko
Raymond L. McKenzie
W. R. Miller**
Robert L. Myklebust
Dale E. Newbury
Richard Paur**
Peter A. Pella
William P. Schmidt
John R. Sieber
David S. Simons
Gerald A. Sleater
John A. Small
Eric B. Steel
W. Thorn**

*Post Doctoral Staff
**Research Associates and Guest Workers

Raman spectra from individual micrometer-size particles are obtained with the Raman microprobe, developed at NBS. The molecular identity of the constituent chemical species in the sample can be determined. Local environment and crystallinity of the microsample can also be inferred in many cases. This rapid nondestructive technique requires no special sample treatment or special conditions such as vacuum. It complements other microanalytical probe (electron- or ion-beam) techniques which furnish primarily elemental data. John Blaha (rear) and Edgar Etz identify the composition of airborne dusts and submicrometer atmospheric aerosols. The mineralization process of teeth and bone, the characterization of environmental trace organic materials and the study of fluid and gaseous inclusions in minerals which are related to geological processes are also studied.

T he Center for Analytical Chemistry maintains expertise in analytical measurement to support activities in this Nation's industrial, clinical, environmental, and research laboratories. The results of analytical measurements often form the basis for regulatory, medical, and industrial decisions. It is essential that they be reliable.

The Center serves as the reference laboratory for assuring this reliability. For example, methods of high accuracy are developed for identifying substances and for quantifying the chemical composition of materials. Materials standards of known composition and stability are prepared for aiding in quality control of measurement procedures and for determining the reliability of data.

The National Bureau of Standards uses several means to transfer to others the Center's analytical methods, standards, and research results. These means include publications, seminars, consultation, cooperative programs, and the direct distribution of materials standards through the NBS Standard Reference Materials Program.

The diversity of materials standards produced in the Center reflects the ubiquity of analytical measurements in this society. These standards include samples used in the metals industries (e.g., steel, aluminum, copper), chemical industries, and clinical and environmental laboratories. To carry out the research underlying each of the several hundred gas standards, the Center must maintain a level of expertise not achieved in any other single analytical laboratory in the world. Moreover, standards become increasingly complex, and technical requirements for their development become more demanding. These factors create needs for new methods of measurement. The Center works to achieve a balance between provision of currently needed standards and research in new analytical methods.

The technical activities of the Center focus on sample and compound types (analytes)—organic, inorganic, gas, and particles. For each analyte, researchers in several disciplines take part in an integrated measurements standards program.

The Center has developed more than 80 gas standards. Though initially stimulated by the need for reliable measurement of air pollutants, such standards are becoming increasingly important in occupational health and safety, technology applications (e.g., evaluation of en-

gine performance), and atmospheric monitoring and research. Requirements for increasing accuracy, measurements of trace amounts of constituents, and determination of a greater variety of gases and toxic vapors necessitate research and development in the area of highly sensitive spectroscopic methods—those involving the use of lasers as well as mass spectroscopic techniques.

Organic compound analysis is often called a new frontier in analytical chemistry in recognition of two facts: hundreds of thousands of organic compounds occur in nature or are produced commercially; yet methods of measurement of complex mixtures are just now beginning to emerge. Moreover, the basis for standardization of methods is in a very early stage of development. The importance of methods for the detection and quantitative determination of organic molecules is evident in the potential applications: measurement of health-related constituents, including therapeutic drugs, in body fluids; measurement of nutrients and contaminants in foods; measurement of carcinogenic compounds in water, in air, on particles emitted with pollutant gases by factories and in synthetic fuels. Though the Center has been involved in organic analysis for a relatively short time, it has made a number of significant contributions: development of the first standard for trace organic analysis (antiepilepsy drugs in serum); development of quantitative methods of measurement of polynuclear aromatic hydrocarbons in recycled oil, and development of definitive methods for clinical chemistry. Research plans include the development of sophisticated chromatographic separation schemes and the linking of separation systems with novel spectroscopic, electrochemical, and mass spectrometric quantitative measurement systems.

The largest research activity in the Center is in inorganic analysis. Studies in this area have led to hundreds of materials standards, ranging from trace metals in food materials and blood to samples used at all stages in the production of metals—steels, cast iron, aluminum, and copper. In addition, high precision and high accuracy mass spectrometry on isotopic composition has led to the redetermination of atomic weights accepted as international standards. In the future, efforts will focus more on measurements of high technology materials and very complex matrices such as hazardous wastes. These endeavors will require the development of very sensitive techniques, with emphasis on improving the accuracy of multielement methods involving the use of lasers, neutron radiation, electroanalytical techniques, and mass spectrometry.

Research in microanalysis is an important activity in the Center. Work in this area has emphasized understanding the fundamentals of electron, photon, and ion interactions with matter so that more quantitative information may be derived from microprobes. Most existing electron microprobes now use one of a series of quantitative x-ray emission data reduction programs developed in the Center. The most recent development, a computer program called FRAME-α, has yielded promising improvements in the ability to determine quantitative elemental compositional information on micron size particles. These basic studies have aided in research to develop improved techniques in particle analysis, including a major effort to standardize the analysis of asbestos in air and water.

The field of analytical chemistry is undergoing a rapid growth and an increase in scientific complexity. This "evolution" is stimulated by the growing application of analytical chemistry to areas of public concern. Also, advances in analytical chemistry are helping to promote scientific advancement in other fields. As analytical measurements become more sensitive, they are increasingly valuable in areas such as materials science, climate research, health research, and nutrition research. Thus, the Center for Analytical Chemistry faces a dual challenge, to keep pace with the growing demand for standards to support current analytical applications and to take part in the advance of analytical chemistry itself.

Laser Enhanced Ionization in Flames

John C. Travis, Gregory C. Turk,
James R. DeVoe, and
Peter K. Schenck [1]
Instrument Development Group and
Chemical Stability and Corrosion
Division (CMS)

From its inception in the summer of 1976 [1], until today, laser enhanced ionization (LEI) has held the promise of unprecedented sensitivity and accuracy in atomic flame spectrometry. It is characterized in a recently awarded U.S. patent No. 4-148,586) [2] as part of a general phenomenon called the "opto-galvanic effect" (OGE). Understanding the underlying mechanisms of LEI has been a significant step in establishing a solid foundation for the atomic spectrometric method.

Laser enhanced ionization occurs when a tunable dye laser is used to selectively populate a particular excited state of an atomic species present in a flame. Since the laser-prepared excited atoms have a lower effective ionization potential than they did prior to excitation, the rate of ionization of these atoms by thermal collisions increases significantly. This ionization enhancement can be easily monitored by drawing a current through the flame and by observing changes in the current that are synchronous with pulsed or chopped laser illumination. As shown in figure 1, the laser-induced ac component of the flame current is separated from the dc background current by an RC filter. It is then amplified and signal averaged by gated integration.

The analytical application of LEI comes from the well established technique of using a flame as an atom "reservoir". It requires a liquid solution of the sample to be "nebulized" into the oxidant supply as a fine mist, carried through the fuel/oxidant mixing chamber, and finally into the flame.
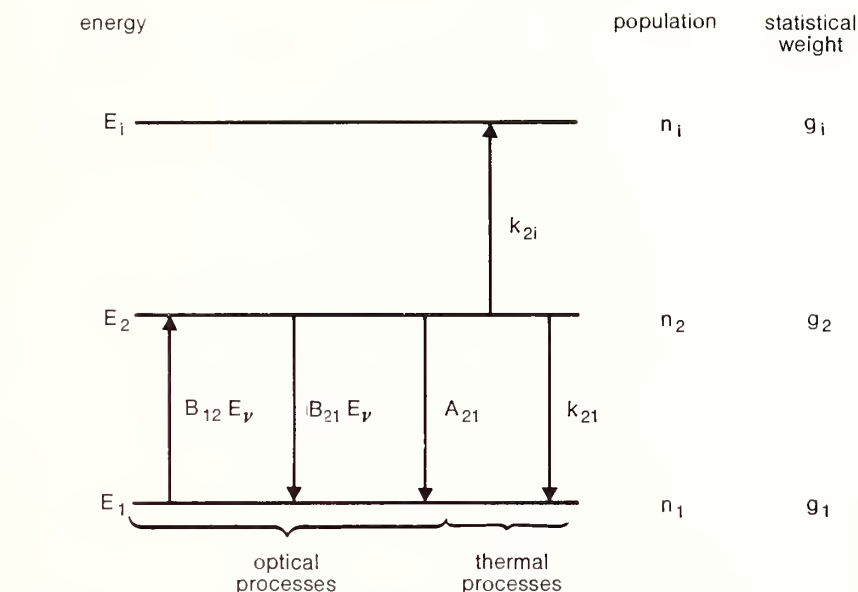
FIGURE 1. Energy level diagram showing the radiational and collisional processes used to model laser enhanced ionization.

The flame rapidly evaporates the solvent, while most trace metals present in the solution are left as free atoms. Quantitation is achieved by comparing spectrometric signals from unknown sample solutions to those from "calibrated" solutions.

Calibration curves exist for a number of elements detected by LEI. They yield "limits of detection" (LOD) often less than 1 part per billion (ng/mL) for aqueous solutions, as shown in table 1 [3]. These data show that the technique compares favorably with the others listed. Conspicuously absent from the table are any elements having high (≥ 7.5 eV) ionization potentials. The role of the ionization potential, as well as other pertinent parameters, can now be explained on the basis of a model using the simplified energy level/rate constant scheme of figure 2. Several processes with relatively slow rates are neglected, for simplicity, including the "recombination" rates from the ionization level to the neutral

levels. Recombination is insignificant because the applied electric field lowers the electron density and thus the recombination rate.

For example, consider the population of level 2 (n_2) to be negligible in the absence of laser irradiation. Then the LEI signal current is taken to be proportional to $k_{2i}n_2$ during the pulse, with level 2 being totally populated by the laser (see fig. 2). Assuming a square laser pulse which maintains a fraction $R(\leq [g_2/(g_1 + g_2)])$ of the neutral atom density ($n_1 + n_2$) in level 2 during the pulse, the LEI current should go as $k_{2i}R(n_1 + n_2)$, where R is determined by the rate constants of figure 2 and the laser spectral irradiance, E_ν. Since the total number density, n_T, is given by $n_T = n_1 + n_2 + n_i$, the final enhanced ionization rate becomes

$$(dn_i/dT) \approx k_{2i} R (n_T - n_i) \; \alpha \; \text{signal current.} \qquad (1)$$

The effect of the ionization potential

Table 1. Comparison of detection limits[a] (ng/ml).

Element	LEI[b]	FAA[c]	FAE[d]	FAF[e]	Laser FAF[f]
Ag	1	1	2	0.1	4
Ba	0.2	20	1	—	8
Bi	2	50	20000	5	3
Ca	0.1	1	1.1	20	0.08
Cr	2	2	2	5	1
Cu	100	1	0.1	0.5	1
Fe	2	4	5	8	30
Ga	0.07	50	10	10	0.9
In	0.006	30	0.4	100	0.2
K	1	3[g]	0.05[g]	—	—
Li	0.001	1	0.02	—	0.5
Mg	0.1	0.1	5	0.1	0.2
Mn	0.3	0.8	1	1	0.4
Na	0.05	0.8	0.1	—	0.1
Ni	8	5	20	3	2
Pb	0.6	10	100	10	13
Sn	2	20[h]	100[g]	50[g]	—
Tl	0.09	20	20	8	4

a Detection limits for comparison taken from S. J. Weeks, H. Haraguchi, and J. D. Winefordner, *Anal. Chem. 50,* 360 (1978), unless otherwise noted.
b Ref. 3, laser enhanced ionization in flames.
c Flame atomic absorption.
d Flame atomic emission.
e Flame atomic flourescence, conventional light sources.
f Laser induced flame atomic flourescence.
g Taken from J. D. Winefordner, J. J. Fitzgerald, and N. Omenetto, *Appl. Spectrocs. 29,* 369 (1975).
h Taken from V. A. Fassel and R. N. Knisely, *Anal. Chem. 46,* 1110A (1974).

comes from the excited state rate constant

$$k_{2i} \approx \alpha \exp \left[-(E_i - E_2)/kT\right], \quad (2)$$

where k is Boltzmann's constant, and T the flame temperature. Equations (1) and (2) indicate an inverse exponential dependence of signal current on ionization potential. However, semi-log plots have yielded slopes differing from a realistic $1/kT$ value by ≥ 50 percent, and, therefore, an improvement of the model was required.

Re-examining equation (1) reveals that a possible explanation to the problem might arise from the depletion of the neutral atom pool $(n_T - n_i)$ by ionization during the laser pulse. Thus,

at any time after the beginning of the pulse (for which $n_i \approx 0$), although the LEI current is favored in k_{2i} for low ionization potential elements, it is penalized by the factor $(n_T - n_i)$ representing depletion of neutrals. Since real laser pulses are not "square", but have a finite risetime, the population fraction R is building up in time as the neutral atom density $n_T - n_i$ is diminishing and thus, a complex solution is expected for the maximum value of dn_i/dt.

Such a solution has been obtained for a laser pulse shape approximating that used in these experiments. The resulting expression agrees with ex-

perimental sensitivities for 23 transitions within 17 elements using an air/acetelyne flame [4]. This expression, as recently reported in Analytical Chemistry [4], can be used to predict sensitivities for observed transitions and elements, utilizing conventional spectroscopic cross sections.

Two additional areas of study are in process: (1) the relative insensitivity of high ionization potential atoms, and (2) the characterization of the mechanism of electron/ion collection. The first problem is being approached through sequential—or "stepwise"—excitation to high energy levels using two tunable lasers, and satisfactory results have already been published [5]. The second area of study is being approached both experimentally and theoretically. The experimental work involves measuring a number of variables, including signal strengths, flame potentials, and flame background currents as a function of other variables, such as electrode geometry, applied potential, flame composition, and aspirated solution composition. The theoretical studies will involve obtaining numerical solutions of Poisson's equation in a flame subjected to an applied field, with realistic electrode configurations and flame conditions.

The outlook is promising for LEI in flames to become established as a major method for quantitative spectroscopic analysis.

References

[1] Green, R. B., Keller, R. A., Schenck, P. K., Travis, J. C., and Luther, G., Opto-Galvanic detection of species in flames, *J. Am. Chem. Soc. 98,* 8517-8518 (1976).

[2] Green, R. B., Keller, R. A., Luther, G. G., Schenck, P. K., and Travis, J. C., Apparatus for Galvanic Detection of Optical Absorptions, U.S. Patent No. 4,148,586, April 10, 1979.

Measurement of Trace Elements in Solar-Cell Silicon

Richard M. Lindstrom, Ronald F. Fleming, and Paul J. Paulsen, Inorganic Analytical Research Division

[3] Turk, G. C., Travis, J. C., DeVoe, J. R., and O'Haver, T. C., Laser enhanced ionization spectrometry in analytical flames, *Anal. Chem. 51,* 1890-1896 (1979).

[4] Travis, J. C., Schenck, P. K., Turk, G. C., and Mallard, W. G., Effect of selective laser excitation on the ionization of atomic species in flames, *Anal. Chem. 51,* 1516-1520 (1979).

[5] Turk, G. C., Mallard, W. G., Schenck, P. K., and Smyth, K. C., Improved sensitivity for laser enhanced ionization spectrometry in flames by stepwise excitation, *Anal. Chem. 51,* 2408 (1979).

Large quantities of pure silicon will be required in the 1980's as solar photovotaic electricity becomes an important energy source. Accurate measurements of trace impurities help to define the optimum balance between purity and cost.
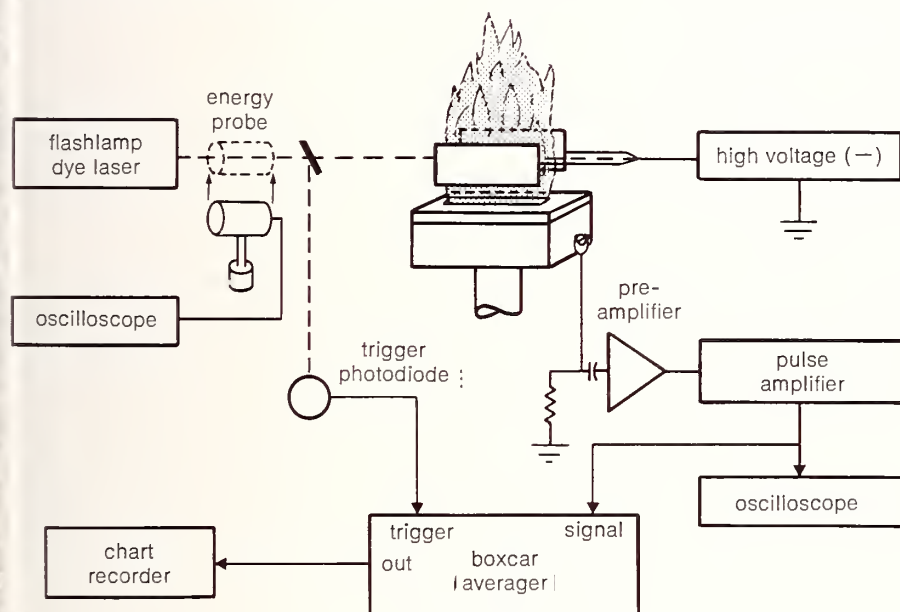
FIGURE 2. Block diagram of the laser enhanced ionization apparatus.

The Low-Cost Solar Array project, managed by Jet Propulsion Laboratory (JPL) for the Department of Energy, has as its goal the generation of electrical power from the sun at a cost comparable to that charged by electric utilities. Reaching this target requires a massive increase in the scale of operations of the solar-cell industry. This increase is expected to cause a dramatic drop in the price of solar cells, their structural supports, and the power-conditioning equipment required for a large distributed activity.

It now appears that the targets set at the beginning of the project in 1975 can be met by more than one combination of methods. The most mature technology is that of flat-plate, single-crystal silicon arrays, which were developed primarily for space applications. For such applications, the quantity of cells produced was small and the cost was relatively high. The cells were made by slicing disks, one by one, from large single-crystal ingots of semiconductor-grade silicon, the purest material produced in multi-ton quantities in commerce today.

For generation of electrical power, much greater quantities of silicon will be required in the 1980's. Current estimates are that photovolatics will require tens of thousands to hundreds of thousands of tons of silicon to be produced per year by 1990.

This quantity of silicon must be produced without an unacceptable degradation of cell quality, at a price no

greater than one-fifth the current price of semiconductor grade silicon. It is the quality of this "solar grade" silicon that our work addresses through trace element characterization.

Workers at Westinghouse, Dow Corning, and Monsanto are studying the effects upon solar-cell performance caused by adding specific impurities to silicon. These studies will define "solar grade" silicon. Measuring cell efficiency as a function of concentration requires that the concentration be known; however, for some impurity elements, the concentration at which the cell degradation begins is less than 1 part in 10^9 (1 ppb). Such low concentrations cannot be measured by most methods of trace analysis. In those cases where sufficiently sensitive analytical techniques are unavailable, the concentration in a doped crystal must be inferred from that in the melt from which it is grown. This requires a knowledge of the liquid-solid distribution coefficient, which is difficult to measure because of the great tendency of crystallizing silicon to exclude certain impurities from its crystal lattice.

Related difficulties must be faced by chemical engineers who design large-scale production processes for solar silicon. Since impurity concentrations of interest are very low chemical analysis performed by most service laboratories will have low accuracy. Therefore, an engineer will have difficulty in constructing an impurity mass balance that would assure with high confidence that some sensitive contaminant will not concentrate in the final product.

To this set of problems analytical chemists at NBS have applied two sensitive methods of trace analysis that have been shown to be reliable in the past by repeated agreement in the certification of Standard Reference Materials. These two techniques are neutron activation analysis (NAA) and isotope dilution spark-source mass spectrometry (IDSSMS). In NAA, packaging and handling methods have been established and detection limits have been caluculated and verified by measurement of blank silicon samples. Nearly all elements of interest can be determined quantitatively at concentrations where changes in electrical properties begin to be visible. Two notable exceptions are titanium and vanadium, which we are still unable to measure at sub-ppb concentrations in silicon. In IDSSMS, the laboratory blank sample and instrument sensitivity are roughly equally important limits to the minimum quantity of impurity that can be observed, which is generally in the region of a few nanograms for the elements of primary interest.

The results of our measurements, when compared with those made by other investigators, show the difficulty of the measurement problem. For forty percent of the samples compared, the discrepancy is greater than a factor of two. The problem is most extreme for copper (see table 1). Our measurements in some cases differ by three orders of magnitude from those reported by other analysts. Systematic errors in our NAA determinations are not likely since excellent agreement was found in an analysis of the same sample by both IDSSMS and NAA. Measurements of concentrations of other elements in samples also show large discrepancies when NBS measurements were compared with others.

Experience in geochemical trace element measurements has shown how discrepancies of this kind can be resolved. The method used is an analysis of a common lot of materials in different laboratories by different techniques. If disagreement in results exists, the process is repeated, with improvements in methods, until agreement is reached. To aid in such comparisons of analyses, a silicon Research Material is in the process of being prepared.

Table 1.   Comparison of copper analyses (10^{15} atoms/cm^3).

	Sample	W-007-Cu	W-017-Cu	W-051-Cu/Ti	W-056-Cu
Other Workers	Mass Spec	1.80	32	4	70
	NAA	1.65	25	NA	—
	"Best Estimate"	1.7	17	1.7	42
NBS	NAA	0.050 0.065 $\Big\} \pm 0.01$	11.2 10.9 $\Big\} \pm 0.5$	0.002 ± 0.002	45.3 ± 0.8
	IDSSMS	—	—	—	42.2

Quantitative Analysis of Individual Trace-Level Organic Constituents in Alternate Fuels

Willie E. May and Stephen N. Chesler, Organic Analytical Research Division

Increasing energy demand in the United States, coupled with increasing reliance on foreign sources of petroleum, has caused national concern that has resulted in a program for developing new sources of energy. The conversion of coal to gaseous or liquid fuels and the utilization of oil shale and tar sands appears to be some of the promising new energy sources. However, a serious though largely unknown complication of developing these alternate fuels is their potentially deleterious effect on man and the environment. Of particular concern are the numerous compounds (for example, those identified on EPA's priority pollutant list) which result from processing alternate fuels, and which may eventually be transported into the environment as gaseous or liquid effluents. To evaluate the potential environmental effects, the alternate fuels base source, its industrial processing, and its resultant effluents must be analyzed. Results of these analyses cannot be assessed adequately without knowing the accuracy of the analytical techniques and data obtained.

We have in the past conducted several collaborative studies aimed at assessing the accuracy of data obtained from various trace organic analytical methodologies. The results of a recent comparison of the determination of hydrocarbons, and N- heterocyclics by several laboratories under contract to the Department of Energy, are given in Table 1. The variance among results reported by these laboratories document the current state of measurement in this area. One well-documented method of increasing the accuracy of analytical measurments involves the uses of quality assurance standards, or Standard Reference Materials (SRM's). However, until recently, SRM's for environmental trace organic

Table 1. Interlaboratory comparison of shale oil analysis (mg/kg).

Compound	NBS	2[a]	3	4	5	6	7	8	9
pyrene	107	155	360	150	168	212	141	620	185
flouranthene	61	102	220	80	108	104	112	380	115
benzo(a)pyrene	22	—	117	—	—	—	3.3	—	—
benzo(e)pyrene		21	—	—	—	—	— 1.3	—	—
phenol	394	392	180	—	—	—	399	—	310
o-cresol	338	350	150	—	—	—	381	2400	328

[a] Numbers indicate another laboratory's determination.

Table 2. Shale analysis (mg/kg, 95 percent confidence level).

Compound	HPLC extraction with quantitation by			Acid/Base extraction with quantitation by		No extraction with quantitation by
	LC	GC	GC/MS	GC	GC/MS	GC/MS
pyrene	108±16	101± 4	102± 9	94±10		104±8
fluoranthene	53± 6	55± 6	62± 6	75± 5		58±5
benzo(a)pyrene	20± 3		21± 5		24± 2	
benzo(a)pyrene			20± 6		22± 5	
phenol	383±50	387±26	416±28		334±63	
o-cresol	330±34	334±86	350±16		322±45	

analyses did not exist because they require for certification a determination by a minimum of two totally independent methods. During the past year, we have developed the requisite methods for certifying a Shale Oil SRM.

The methodology used in the certification of shale oil was developed over an 18 month period. Initially, we focused our efforts on the evaluation of techniques for extracting the compounds of interest from shale oil matrix. A classical acid-base extraction scheme and a high performance liquid chromatographic fractionation procedure, which was developed in this laboratory, served as independent methods for isolating the analytes from the sample. Next, we investigated the use of gas chromatographic (GC), gas chromatographic-

mass spectrometric (GC/MS), and high performance liquid chromatographic (HPLC) methods for identifying and quantifying the compounds of interest in the various fractions obtained from the isolation procedures. Direct analysis by GC/MS was also used when possible.

These data, given in table 2, show that the overall agreement between the various methods of extraction and quantitation was good up to the 95 percent confidence level. This excellent agreement between these results compared to those obtained in the interlaboratory collaborative study provided the basis for establishing state-of-the-art methods for trace organic analyses.

The specimen of shale oil being cer-

Computer-Controlled Electrochemical System for Electrode Kinetics Research

Lawrence M. Doane and Richard A. Durst, Organic Analytical Research Division

tified is from a 150-ton retort for in-situ simulated combustion operated by the Laramie Energy Technology Center, Laramie, Wyoming. The shale is from the Mahogany Zone of the Colorado Green River formation. The stock of shale oil being certified was obtained from Dr. Bruce R. Clark at Oak Ridge National Laboratory, Oak Ridge, Tennessee. It has undergone centrifugation to separate water ($\sim$ 40 percent) and sludge from the oil prior to shipment to NBS.

This SRM, having the concentrations of phenol, *o*-cresol, fluoranthene, pyrene, benzo(e)pyrene, and benzo(a)-pyrene certified, will be issued in early 1980. Its use should greatly improve the accuracy of related environmental measurements. Accurate measurements will assist scientists in correctly relating health effects to levels of individual pollutants, engineers in correctly assessing effectiveness of control technologies, regulatory agencies in relating levels of pollution emissions with ambient air and water quality, and the Federal Government in correctly making policy decisions on cost-benefit trade offs concerning environmental protection, energy conservation, and economic health.

This work represents efforts by the staff of the NBS Organic Analytical Division who have expertise in gas chromatography, liquid chromatography, and mass spectrometry.

Modern electrochemical research often requires measurements of fast electrode kinetics and transient intermediates. Since commercial electrochemical equipment generally do not meet these rate requirements, a state-of-the-art, computer-controlled system capable of data acquisition at a rate of 100 kHz is in the final stages of development. A specially designed potentiostat, with dynamic and nearly complete compensation of the cell resistance, will be incorporated into this system. Fourier transform experiments can be implemented, since this system can sample two inputs simultaneously at a rate of 50 kHz. The system has been designed for maximum data acquisition throughput and versatility, and simplified control.**

The recent emphasis on finding energy-efficient processes has stimulated a resurgent interest in electrochemistry and electrochemically related fields. Since maximizing the efficiency of electrochemical processes will involve the elucidation of electrode reaction mechanisms it is necessary that fundamental investigations of these processes and their associated elecrode kinetics be undertaken. Commercially available electrochemical instruments are generally not versatile enough to be useful in many of these types of investigations. We are therefore constructing a computer-controlled electrochemical system (CCES) that can generate complex waveforms, apply these waveforms to an electrochemical cell, and then acquire data at a high rate. A system similar to this is used in single-drop square wave polargraphy and will serve as a model for evaluation of the CCES. In the single-drop experiment, the potential range of interest is scanned at

the end of the mercury drop lifetime, so that several polarographic problems can be minimized, e.g., electrode charging current and solution agitation. In addition, the potential is applied as a square wave while sampling the resulting current at the end of each potential change and adding together the two sampled currents. Thus, this method gives an increased current signal over that obtained from the linear ramp experiment. This system is obviously applicable for trace metal analysis, and such an analysis will be used to evaluate the CCES.

We have designed the CCES around the relatively low-cost central processing units (CPU) that are now commercially available. The CPU is a Zilog Z80A microprocessor, operated at a clock rate of 4 MHz, in which the fastest instruction cycle takes place in 1 μs. Memory consists of 64 kilobytes (K) of random-access memory (RAM) and 240 K dual-drive disk memory. A block diagram of CCES is shown in figure 1. The CCES acquires the electrochemical signals via two modes: mode A uses fast commercial potentiostats (an electronic instrument used to control the potential of an electrochemical cell) from which analog signals are converted to digital format in the com-
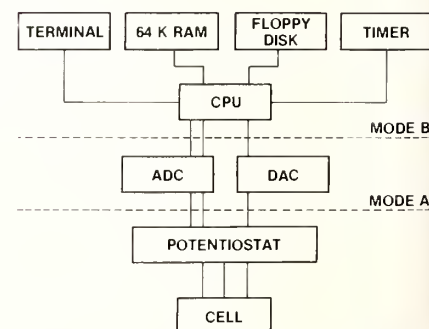

FIGURE 1. Block diagram of the computer controlled electrochemical system (CCES)

uter; mode B uses a laboratory-constructed potentiostat which digitizes he electrochemical signals before entering them into the computer. There . a five-fold difference in signal acqui-tion rate between the two modes: 20 s for mode B versus 100 μs for mode A.

In mode A, the analog electrochemi-al signals are digitized by two analog-o-digital converter boards (ADC) esiding in the computer. The conver-ion can occur at a maximum rate of 0 kHz (i.e., one data point every 33 s). however, execution of the pro-ram to input and store the data equires an additional 30 to 60 μs, epending on whether or not an analog ignal is being sent to the potentiostat. herefore, the overall throughput could e restricted to no less than 100 μs. Although the two data words are stored equentially, the two converters operate n a master/slave relationship so that he two electrochemical signals (current nd potential) are sampled simulta-ieously.

We have built a fast potentiostat in vhich two ADC's and a digital inter-ace have been included to minimize he software required to operate the CES (fig. 2). In this scheme, the computer loads a group of parallel reg-isters with the parameters of the electrochemical signal to be outputted by the potentiostat. When this function is finished. the computer reverts to an input sequence that sends the digitized data to the computer upon signal from the ADC's. One input sequence can occur during the conversion of the next analog signal; however, when two signals are converted simultaneously, the second datum input to memory will add an additional 10 μs to the overall throughput. i.e., 20 μs are required to perform one complete two-data input. The registers can be reloaded during an outputting sequence so that the output can be dynamically altered in a manner dependent on the format of the program.

Currently. we are developing software for this system. We have chosen to write our program in FORTRAN and use assembly language subroutines to input the data. This allows us to operate CCES at the maximum possible computer-controlled speed. In addition to the gain in speed, the RAM memory space which a BASIC interpreter would normally occupy is now available for data storage. However, a direct memory access (DMA) controller is being designed to directly input the data to memory (bypassing the CPU). By using the DMA, the CCES speed will depend only on the ADC conversion rate, freeing the CPU for other tasks.

Following an evaluation of the CCES, its application will be broadened to include: (a) electrode kinetics experiments via Fourier transform of AC voltammetry, a technique providing high-precision measurements of faradaic admittance vs potential or frequency; (b) rapid scanning detectors for high performance liquid chromatography, where the dynamic resistance compensation and rate of data acquisition will permit the real-time identi-fication of eluting species; (c) signal enhancement by ensemble averaging techniques employing newly developed pulse and relaxation methods, e.g., the square wave experiment described above. There also exists excellent opportunities in data retrieval and pattern recognition, two operations which have been underutilized in electrochemistry. Such operations would be useful for the identification of specific compounds in complex mixtures (deconvolution) and in the elucidation of electrode kinetics and mechanisms by comparison of acquired data with theoretical curves generated by digital simulation of coupled chemical-eletrochemical reactions.
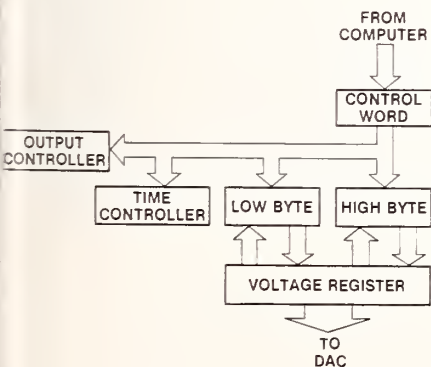
FIGURE 2. Block diagram of data flow through interface.

High Resistance Junction Formation in House Wiring Circuits With Aluminum Conductors

Dale E. Newbury, Gas and Particulate Science Division

The mechanism of high resistance junction formation in aluminum-wire iron screw connections is shown to be the generation of iron-aluminum intermetallic compounds during arcing.

In the period 1968-1972, many new homes built in the United States were equipped with aluminum wiring and conventional brass-coated iron junctions. In laboratory experiments, these aluminum-iron junctions have been observed to undergo a glow-arcing phenomenon accompanied by severe overheating which could lead to the initiation of a fire [1]. The origin of the overheating, which involves two normally satisfactory electrical conductors, has not been previously explained. Electron probe microanalysis of the microstructures of circuit components which have undergone such failures has revealed the probable mechanism of the glow phenomenon [2].

Previous laboratory investigation of the glow phenomenon revealed that glowing began when the aluminum wire-iron screw junction became mechanically loose [1]. As a starting point for this study, conducted in cooperation with the NBS Center for Consumer Product Technology (CCPT) a loose connection between an aluminum wire and an iron screw was simulated in a circuit carrying 15 amperes of current. When the components were separated by a small gap, an arc was created that led to the glow phenomenon. Scanning electron microscopy and x-ray microanalysis of the regions damaged by the arc revealed evidence of significant material transport across the arc and of high temperatures at the surface of the components (see figs. 1 and 2). Iron and a minor amount of
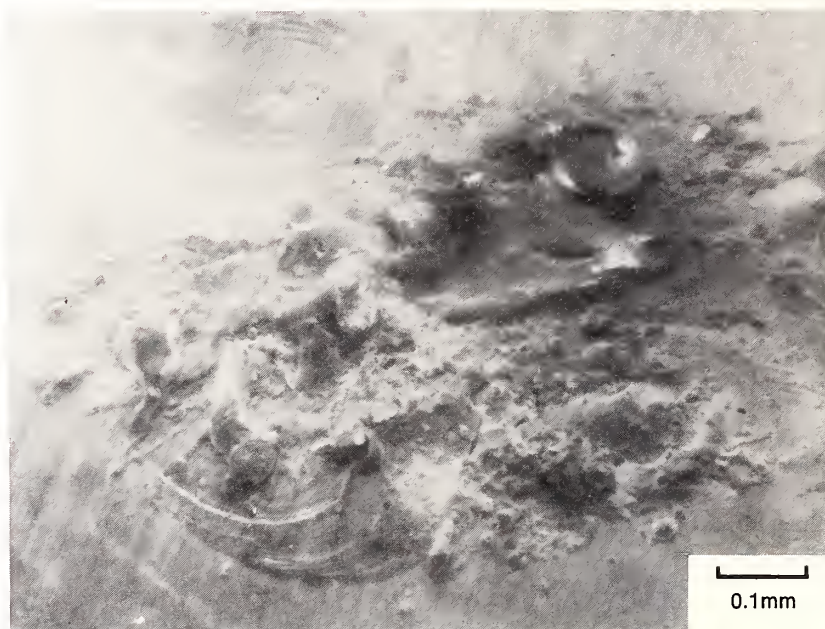
FIGURE 1. SEM image of an arc-damage crater.
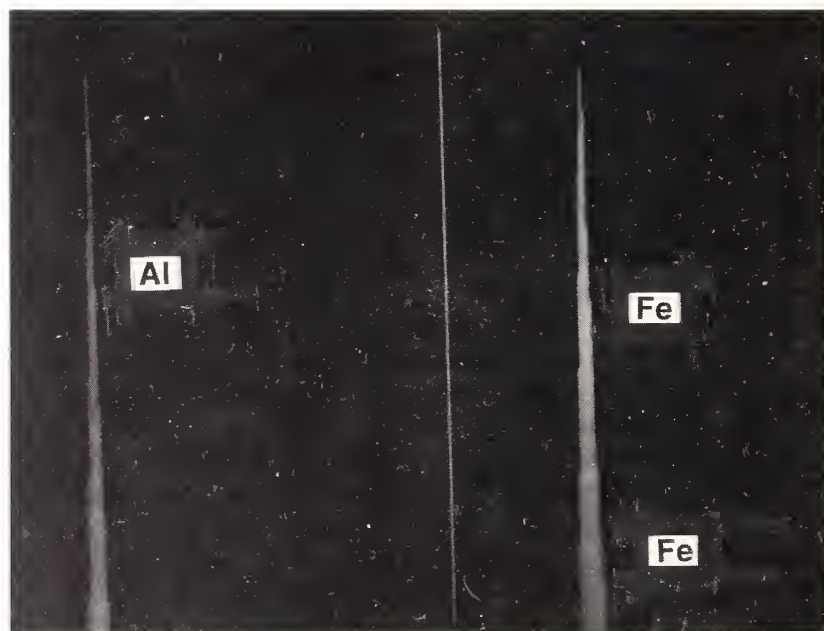
FIGURE 2. X-ray spectrum of a region of a crater.

copper were transported to the surface of the aluminum wire, and aluminum was transported to the iron screw apparently in the vapor phase. The zinc component of the brass was not detected and was probably lost by evaporation. Temperatures in excess of 1500 °C were suggested by the observation of solidification structures of nearly pure iron at the periphery of the crater on the screw.

This combination of high temperatures and intimate mixing of the metals suggested the possible formation of intermetallic compounds. A section through the damage crater revealed the presence of such a compound, Fe_3Al, as determined by x-ray microanalysis. The existence of the intermetallic compound at the current-transmitting interface is of special significance since its resistivity is generally a factor of 10 to 100 times greater than that of either of the pure metals.

In order to confirm that this phenomenon occurs in actual junction boxes wired with aluminum, a second series of experiments was carried out in cooperation with CCPT. Typical household junction boxes wired with aluminum were subjected to high current cycling until glow failure was induced. In the process large portions of the assembly reached temperatures of 400 to 500°C [1]. Samples for metallographic examination were prepared from a section through the wire screw contact; a typical section through a contact is shown in figure 3. A thick reaction zone spanning the entire region of contact between the wire and screw can be seen in the optical micrograph (figure 3). An electron microscope image of this region, Figure 4, reveals that the zone is composed of two layers. X-ray microanalysis with the NBS theoretical matrix correction procedure FRAME C indicates (1) that the layer

FIGURE 3. Cross section of aluminum wire through a damage crater.

FIGURE 4. SEM (backscattered electron) image of the same region.

adjacent to the aluminum corresponds to the intermetallic compound $FeAl_3$ and (2) that the outermost layer consists of Fe_2Al_3 with 0.5 percent copper. Examination of samples taken at various stages in the glow process suggests that initially intermetallic compounds are either iron-rich or aluminum-rich depending on the major constituent present. With continued reaction, intermetallic compounds containing roughly the same quantities of each element are formed [3]. All of the intermetallic compounds containing aluminum and iron have resistivities 20-200 times greater than aluminum or iron [4].

The observation of the development of thick intermetallic layers in the current carrying region during the glow failure suggests the following chain of events: (1) an arc occurs in an initially loose connection, causing local heating and material transport in the vapor phase; (2) on both the wire and the screw, the metallic elements react in the high temperature environment, forming intermetallic compounds; (3) the high resistivity of the intermetallic compounds leads to sharply increased I^2R heating at the interface; and (4) the heat produced leads to enhanced material transport, first as a vapor and perhaps eventually as a liquid, which then promotes rapid reaction to form even more intermetallic material, resulting in an unstable, runaway process. Knowledge of this basic mechanism for glow failure of electrical junctions provides important information which could lead to the design of safer circuit connections.

References
[1] Meese, W. J. and Beausoliel, R. W., Exploratory Study of Glowing Electrical Connections, NBS Building Science Series 103 (NTIS, Washington, D.C. 1977).
[2] Newbury, D. E., Investigation of the Mechanism of the Formation of Resistive Junctions in Aluminum Wire, Report of Analysis 78-96, Center for Analytical Chemistry, Gas and Particulate Science Division, National Bureau of Standards (1978).
[3] Hansen, M., *Constitution of Binary Alloys,* (McGraw-Hill, New York, 1958) pp. 90-95.
[4] Vol, A. E., *Handbook of Binary Metallic Systems,* Vol. 1 (U.S. Dept. of Commerce Washington, D.C., 1966) pp. 136-149.

Discrimination of Natural From Anthropogenic Carbonaceous Pollutants Through Mini-Radiocarbon Measurements

Lloyd A. Currie and George A. Klouda, Gas and Particulate Science Division

Radiocarbon dating rests on the fact that living matter is in isotopic equilibrium with cosmic ray-produced ^{14}C; death breaks the photosynthetic chain, leading to reduction of the isotopic ratio $^{14}C/^{12}C$ in accordance with the physical half-life of 5730 years. We have taken advantage of this natural phenomenon to develop a method for quantitatively discriminating between biogenic ("living") and fossil ("dead") carbonaceous contaminants in the environment [1] (see fig. 1).

The importance of distinguishing biogenic from fossil carbon arises from the effects of both natural and anthropogenic carbonaceous species on health, stratospheric ozone, and climate. In order to plan responsible control strategies, it is therefore vital to determine the relative contribution of man's activities to atmospheric hydrocarbons, halocarbons, carbon monoxide, and primary and secondary carbonaceous particles. Although natural emissions of hydrocarbons far exceed those originating from man's use of fossil fuel [2], for example, there remain very significant questions concerning the sources of hydrocarbons contributing to rural pollution episodes as well as the influence of natural forest emissions on urban air pollution [3]. Longer-lived tropospheric species, such as methane, may lead to depletion of stratospheric ozone; and trace gases and particles may influence the earth's radiation balance directly through "greenhouse" and albedo effects or indirectly through cloud nucleation [4]. It is worth noting that radiocarbon is the only unique biogenic/fossil discriminator. Chemical composition and

stable isotope measurements ($^{13}C/^{12}C$) are frequently helpful but the former is indirect and subject to interference and the latter exhibits large natural variations.

Because of the small atmospheric concentrations of many of the species of interest (table 1), it has been necessary to advance the state of the measurement art by a factor of a thousand. That is, measurements must be practicable for samples containing just a few milligrams of carbon—rather than having gram-size samples which are typical of conventional Radiocarbon

Table 1. Tropospheric concentrations (mg-C/m³).

	Range	Air quality standard
CO_2	180. +	—
CH_4	0.76 ± 0.03	—
CO*	0.06 - 20.	17.
HC	<10⁻³ - 2.00	0.14
CCl_4, C_2H_6 a	10⁻⁵ - 10⁻³	—
Particles	<10⁻³ - 0.10	0.052
Dissolved (rain) Organic Carbon	2 - 10 (mg/l)	—

a N-S asymmetry.

Dating.[1] This requisite sensitivity was achieved through the design of a high purity, miniature gas proportional counter which is linked with a two-parameter low-level counting system, described in the following section.

Measurement System

Following collection and separation according to size or chemical characteristics, environmental samples containing 5 to 15 mg carbon are converted quantitatively to CO_2 for radiocarbon measurement. Prior to counting of the ^{14}C, the sample-CO_2 must be rigorously purified—a few ppm of electronegative impurities interfere with counting—and cryogenically transferred to a high-purity quartz counting tube. Measurement of the radiocarbon takes place over a period of several days using a special low background system incorporating massive shielding, electronic anticoincidence cancellation of cosmic ray muons, and two-dimen-

[1] The required sample size is given by the fact that 10 mg of contemporary carbon yields a net counting rate of about 0.15 cpm which results in a 10 percent uncertainty (Poisson relative standard deviation) after about one day of counting. The corresponding air sample size would be 100. m³ for a substance whose concentration is 0.1 mg-C/m³ [1].

RADIOCARBON

Production: Cosmic Rays (p) ⟶ n $\xrightarrow[\text{(atmosphere)}]{^{14}N}$ $^{14}C \xrightarrow{O_2} CO_2$ (Biosphere)

Dating: $A = A_0 e^{-t/\tau}$ [10 g, 1%]

Pollutant Source: $A = f \cdot A_0 + (1-f) \cdot 0$ [10 mg, 15%]

FIGURE 1. Radiocarbon production by cosmic rays, and its application to dating and pollutant source identification. (f equals the fraction of contemporary or living carbon in an environmental sample; A_0 represents the equilibrium $^{14}C/^{12}C$ isotope ratio in living matter. Typical sample sizes and Poisson Standard deviations are given in brackets.)

sional spectroscopy according to pulse amplitude and risetime. Special features of the system, which includes an on-line computer, provide for rejection of spurious electronic pulses and long-term monitoring of stability. As a result of the attention given to materials' radio-purity plus active (timing, spectroscopy) and passive background reduction, our residual background is comparable to the signal ($\sim$ 0.1 cpm). This is equivalent to a "noise" attenuation (with reference to the unshielded counter) of more than a factor of two hundred.

Figure 2 is a photograph of our 15 mL quartz counter and the internal shield of high purity copper. This counter is used for samples containing up to 30 mg-carbon; a second counter having an internal volume of 5 mL and operated up to 4 atmospheres CO_2 is used for samples having ≤10 mg-carbon. (The residual background rate for the 5 mL counter is remarkable: a recent measurement in the underground counting laboratory at the University of Bern yielded a mean interval of 25 minutes between counts.) A display of the two dimensional spectrum, for an air particulate sample collected in Salt Lake City, is given in figure 3. Valid pulses lie below the dashed line, and eight (rejected) spurious events are seen above. Further details concerning the sample preparation and purification system, and a brief description of the counting system may be found in References 5 and 6, respectively

Experimental Evidence of Man's Activities

Our research, whose objective is to use radiocarbon to discern man's perturbations of environmental carbonaceous matter, has been directed toward three classes of samples: atmospheric
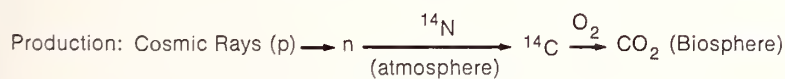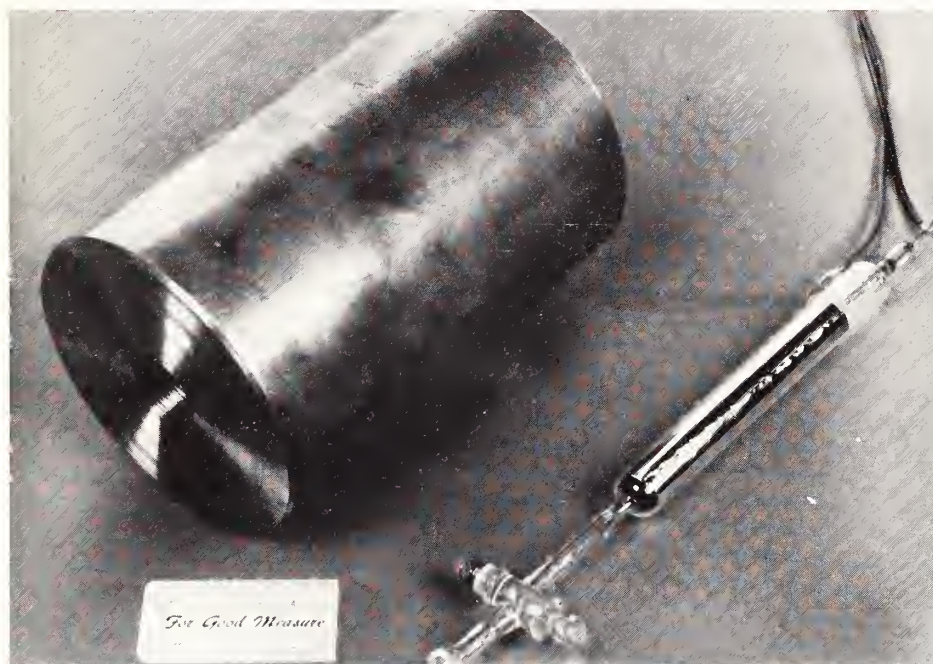
FIGURE 2. Photograph of the small quartz counter (15 mL volume) and associated shield. The shield, along with the inner wall of the counter, is constructed of OFHC copper.

Table 2. Radiocarbon in aerosols and sediment.

	Mass-Carbon (mg)	Percent contemporary $[^{14}C/^{12}C]$ ($\pm$1 S.D.)	Supporting data
Ambient particles [a]			
Los Angeles	7.8	23 $\pm$ 15	Organic
Salt Lake City	5.3	28 $\pm$ 13	(insoluble)
Utah Desert	10.2	88 $\pm$ 16	composition
Impact particles ($<3\ \mu m$)[b]			
Portland, OR.	5.1 - 10.7	62. - 107.	Inorganic composition
Sediment [c]			
Puget Sound, WA. { FA 60.		86 $\pm$ 21	Isotopic
{ PAH 14.		19 $\pm$ 21	($^{13}C/^{12}C$) composition

[a] Ref. 5.
[b] Ref. 8.
[c] Ref. 9 (FA = Fatty acid fraction, PAH = Polycyclic aromatic hydrocarbon fraction).

gases, atmospheric particles, and organic matter in "recording" media, such as sediment and ice cores. Study of the first two categories yields information on the significance of current activities, while the third provides the historical record and a link to the global carbon cycle. Work with atmospheric gases is still at an early stage; we have just begun sampling atmospheric methane, and suitable apparatus for the collection of mg-quantities of non-methane hydrocarbons and carbon monoxide is under development. In cooperation with University groups, however, we have carried out a number of measurements of radiocarbon concentrations in atmospheric particles and in sediment. The results are summarized in Table 2.

The first point to be noted in Table 2 is that, with the exception of one sample, all samples consisted of only about 10 mg of carbon. This is the amount which was available with normal, daily operation of a HiVol air sampler or with the chemical processing of about 600 grams of surface sediment. The only two previous studies of radiocarbon in urban aerosols involved a thousand times as much carbon and required a week of sampling [7]. (Similarly, conventional radiocarbon measurements of PAH in sediment would have required extraction of a metric ton of material.) Aside from the increased ease of sampling and time resolution, the ability to measure very small samples is essential in terms of selectivity. That is, miniradiocarbon counting makes it possible to derive reliable information on individual chemical or size fractions—especially fine particles which may be free from local contaminants, such as resuspended waste or spores.

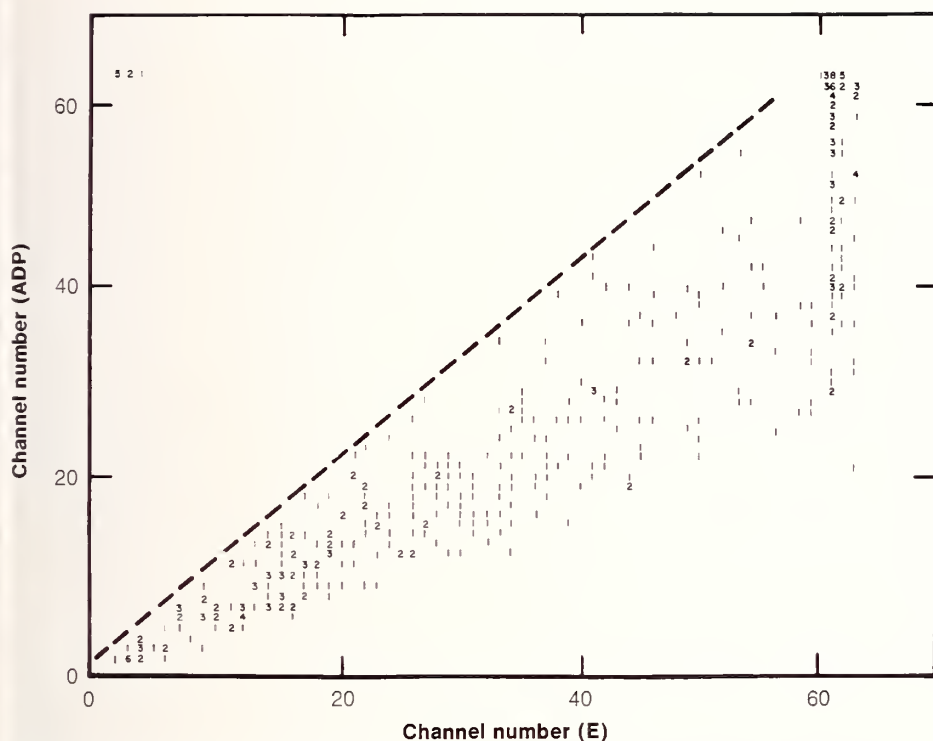The ambient particles (table 2), studied in collaboration with the Uni-

FIGURE 3. Two-parameter proportional-counter spectrum for the Salt Lake City sample. Abscissa represents pulse energy (E); ordinate, pulse shape (ADP). Spurious pulses appear above the 45° dashed line.

FIGURE 4. Comparison of observed with expected vegetative burn impact (fine particles). Dashed line represents the idealized situation for a pure source. The numbered box [3] indicates the median and 1σ is shown only on #4 for clarity. Abscissa locations (A, B, C, D) are derived from the atmospheric radiocarbon input function and the ages (t) of the material burned.

versity of Utah Research Institute and the University of Utah [5], confirmed what is generally expected; that is, the urban particles consisted largely of fossil carbon while the rural (desert) particles indicated a biogenic source. Supporting studies on the composition of the insoluble carbonaceous component (soot) also pointed to an anthropogenic (fossil) source for the urban samples. Pyrolysis-gas chromatography-mass spectrometry revealed several cyclic and substituted aromatic compounds which have also been observed in vehicular exhaust.

Collaborative work with the Oregon Graduate Center was designed to assess the impact of vegetative burning (by man) on urban (Portland) air particulate pollution [8]. The results of that study, indicated in table 2 and summarized in figure 4, demonstrated that on high impact days, contemporary carbon from vegetative burn sources such as field and slash burning and space heating with wood contributed between 27 and 51 percent of the fine particulate mass, and up to 35 percent of the total suspended particulate material collected in the Portland and Eugene, Oregon, airsheds. The radiocarbon analyses of filters selected for high impact from residential wood combustion suggested that this source is currently significant and could become one of the most significant seasonal sources of respirable particulates in the future, unless steps are taken to improve combustion efficiency and/or emission control. Chemical Mass Bal-

ance, based on the inorganic composition of the particles, tended to corroborate the radiocarbon data, but it could not provide the same degree of unique source identification. (Note that the "anthropogenic" carbon in the Portland study was contemporary—i.e., biogenic, whereas it was fossil in the Los Angeles and Salt Lake City study.)

One of the most interesting areas of investigation is the record of man's past impacts on the environment. This was the stimulus for the last study [9] included in table 2, the measurement of the chemical and isotopic record in organic matter in a sediment core from Puget Sound, taken midway between urban North Seattle and the rural Olympic Peninsula. The initial results, which apply to the top 10 cm sediment

layer or material deposited during the last two to three decades, show that different organic species are far from isotopic equilibrium. The high radiocarbon content (86 ± 21 percent contemporary) of the fatty acid fraction, indicating a biogenic origin, is consistent with the premise that this fraction originated from recently-living planktonic matter. The Polycyclic Aromatic Hydrocarbon (PAH) fraction on the other hand, was found to contain little or no radiocarbon, indicating that it was primarily of fossil origin, presumably associated with man's use of fossil fuel. Stable isotope measurements ($^{13}C/^{12}C$) of the PAH did not clearly discriminate between coal and petroleum, but they did rule out waste oil as a primary source. These findings support the contention [10] that PAH in the surface sediment comes mostly from fossil fuel combustion rather than from natural forest fires. (PAH, which contains known carcinogens and mutagens, is a common product of incomplete combustion, and it is generally associated with the particulate emissions.) Further studies, at increased depths in the sediments, should yield the historical record for both fossil and vegetative combustion.

Future Directions

Our immediate plans call for expanding the miniradiocarbon counting system to accommodate up to twenty or more simultaneous counting channels, such that sample throughput need not be limited by the relatively long counting times associated with individual measurements. Information on the global methane cycle and assessment of the fossil contribution to urban and rural non-methane hydrocarbons will follow from our current work on atmospheric gas sampling.

Within the past few months, in cooperation with the University of Rochester, we have begun also to explore a new measurement technique which promises to extend our sensitivity by an additional factor of 10^2 to 10^3. Through the use of Accelerator Mass Spectrometry (AMS), in which individual radioactive atoms (rather than their disintegrations) are counted in a nuclear accelerator, we have succeeded in measuring the radiocarbon concentration in just 40 μg of a contemporary radiocarbon sample [6, 11]. The relationship between decay counting (llc) and atom counting (AMS) as well as the main features of our exploratory experiments are sketched in figure 5. Considerable work remains to be done, particularly in the areas of ion source sample preparation and fast and reproducible beam switching, before AMS will be established as a reliable and accurate technique; and

machine availability and cost make it currently somewhat less attractive than llc if 5 to 10 mg of environmental carbon samples are available. However, its incredible sensitivity—literally a million-fold better than conventional radiocarbon dating—promises to make practicable hitherto impossible experiments. We can anticipate the use of radiocarbon to determine the origin of the rarer atmospheric species (e.g., halocarbons), and we should be able to greatly increase our knowledge of environmental sources and transformations through the examination of individual organic compounds found in ocean sediment, polar ice cores, and atmospheric particles.

References

[1] Currie, L. A., Noakes, J., and Breiter, D., Measurement of Small Radiocarbon Samples: Power of Alternative Methods for Tracing

Accelerator Mass Spectrometry

$$A = -dN/_{dt} = \lambda N = N/_\tau$$

$\underline{llc}$: $n = A \cdot \epsilon \cdot \triangle t$ $\underline{AMS}$: $n' = A \cdot \epsilon' \cdot T$

Exploratory Experiment

(Rochester, July 1979)

OBJECTIVES

- Environmental sample preparation/dilution [particulate SRM]
- Electromagnetic isotope enrichment/implantation [CO_2]
- Minimum sample size [new radiocarbon dating SRM]

PRELIMINARY RESULT
(dating SRM)

$$40 \ \mu g - C \rightarrow {}^{14}C/{}^{12}C = (1.41 \pm 0.04) \times 10^{-12}$$

FIGURE 5. Accelerator Mass Spectrometry (AMS) Exploratory Experiment at the Microgram Level. (*llc* represents low-level counting; *n*, number of counts; *A*, disintegration rate; ϵ, detection efficiency; $\triangle$t, *llc* counting time; $\tau = 1/\lambda$, the mean life of radiocarbon; N, the number of atoms of radiocarbon.

Atmospheric Hydrocarbons, *9th Internatl. Radiocarbon Conf.,* R. Berger and H. Suess, eds., Univ. of Calif., Los Angeles and San Diego, June 1976; Currie, L. A. and Murphy, R. B., Origin and Residence Times of Atmospheric Pollutants: Application of C^{14}, in *Methods and Standards for Environmental Measurement,* W. H. Kirchhoff, ed., NBS Special Pub. 464, 439-447 (U.S. Government Printing Office, Washington, D.C. 1977).

[2] Covert, D. A., Charlson, R. J., Rasmussen, R., and Harrison, H., Atmospheric chemistry and air quality, *Review of Geophysics and Space Physics, 13,* 765-771 (1975).

[3] Maugh, T. H., II., Air pollution: where do hydrocarbons come from? *Science, 189,* 277-278 (1975).

[4] Geophysics Study Committee, *Energy and Climate,* NRC Geophysics Research Board, National Academy of Sciences, Washington, D.C. (1977).

[5] Currie, L. A., Kunen, S. M., Voorhees, K. J., Murphy, R. B., and Koch, W. F., Analysis of Carbonaceous Particulates and Characterization of Their Sources by Low-Level Radiocarbon Counting and Pyrolysis/Gas Chromatography/Mass Spectrometry, in *Proc. of the Conference on Carbonaceous Particles in the Atmosphere,* T. Novakov, ed., Lawrence Berkeley Laboratory, Berkeley, California (1978).

[6] Currie, L. A., Environmental Radiocarbon Measurements, in *Proceedings of First Conference on Radiocarbon Dating with Accelerators,* H. Gove, ed., pp. 372-390 (University of Rochester, New York, 1978).

[7] Clayton, G. D., Arnold, J. R., and Patty, F. A., Determination of sources of particulate atmospheric carbon, *Science 122,* 751-753 (1955); Lodge, J. P., Jr., Bien, G. S., and Suess, H. E., Carbon-14 content of urban airborne particulate matter, *Intl. J. Air Poll. 2* 309-312 (1960).

[8] Cooper, J. A., Currie, L. A., and Klouda, G. A., Application of carbon-1 measurements to impact assessment of contemporary carbon sources on urban air quality, (to be published in *Environmental Science & Technology,* 1979).

[9] Swanson, J., Fairhall, A., and Currie, L. A., Carbon Isotope Analysis of Sedimentary Polycyclic Aromatic Hydrocarbons (submitted to *Nature,* 1979).

[10] Hites, R. A., Laflamme, R. E. and Farrington, J. W., Sedimentary polycyclic aromatic hydrocarbons: the historical record, *Science 198,* 828-381 (1977).

[11] Currie, L. A., Klouda, G. A., Elmore, D., and Gove, H., Accelerator mass spectrometry and electromagnetic isotope separation for the determination of natural radiocarbon at the microgram level (to be submitted to *Science,* 1979).
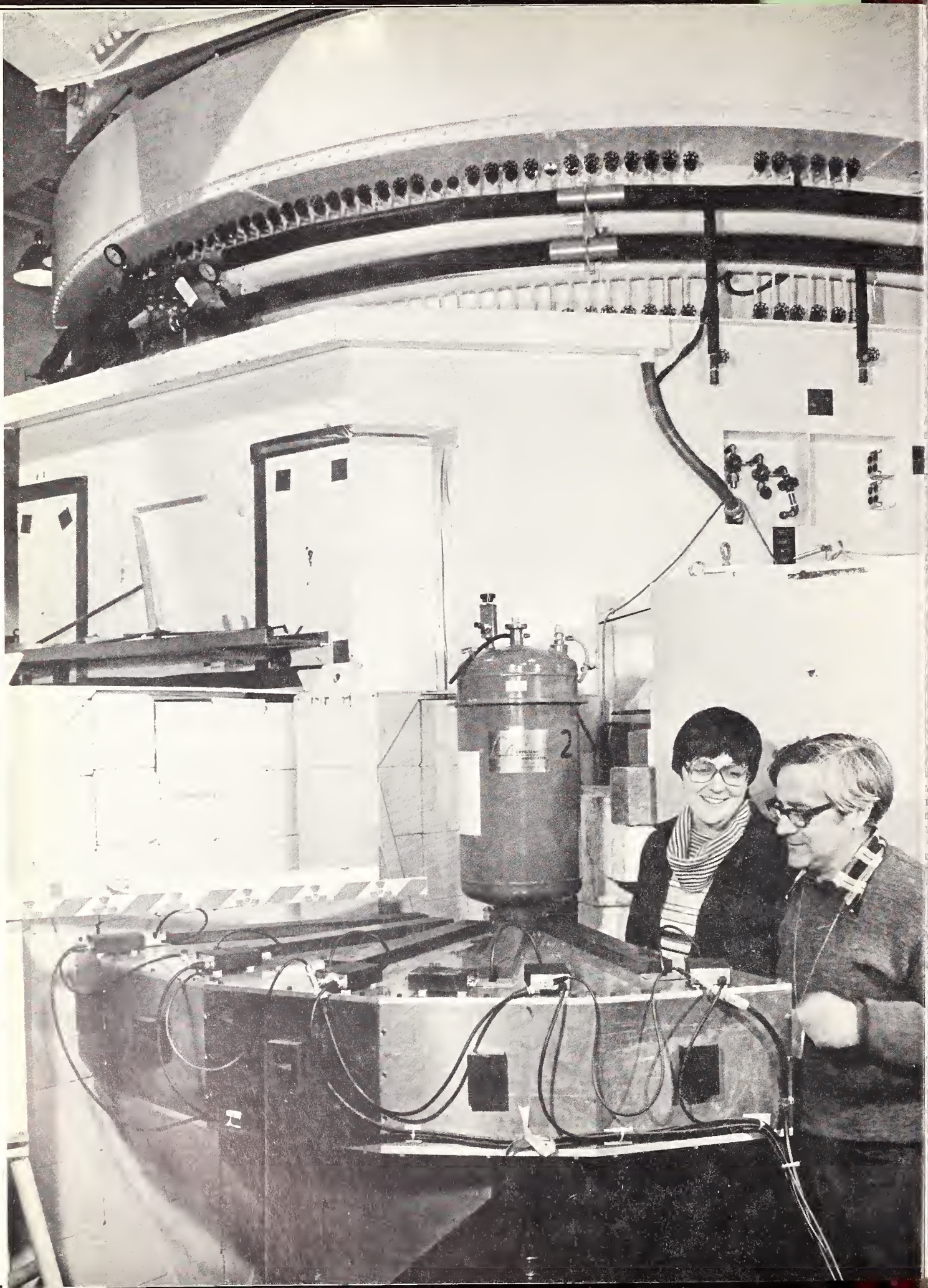
Center for Materials Science

John B. Wachtman,
Jr.
Darrell H. Reneker

John G. Abbott
Harvey J. Anderson
David B. Blanchard
John W. Cahn
Donald G. Fletcher
Fred Gornick
Melvin Linzer
John D. McKinley,
Jr.
Stephen J. Norton
Stephen I. Parks
Samuel J. Schneider,
Jr.
Bruce W. Steiner
Robb M. Thomson
Claudia F. Vosbeck
Melvin R. Wallace
M. Katheryn
Wharton
Gerry N. Wixson

**Chemical Stability
and Corrosion**
Thomas D. Coyle

Ugo Bertocci
James R. Bethin
William R. Blair
David W. Bonnell
Frederick E.
Brinckman, Jr.
Henrietta J. Brown
Chwan-Kang
Chiang
John J. Comeford
Richard G. Crumley
Arthur L. Cummings
Alan L. Dragoo
Edward Escalante
Alan D. Franklin
Richard S. Gates
William F. Gerhold
Ludwig H. Grabner
John W. Hastie
William S. Horton
Stephen M. Hsu
Satoshi Ito**
Warren P. Iverson

Jo-Anne A. Jackson
Kenneth L. Jewett
Rolf B. Johannesen
Jerome Kruger
Chia-Soon Ku
David S. Lashmore
Jasper L. Mullen
Fielding Ogburn
Gregory J. Olson*
Edwin J. Parks
Patrick T-S. Pei
Ernest R. Plante
Edison N. Pugh
Joseph J. Ritter
Benjamin T.
Sanderson
Peter K. Schenck
Joseph H.
Simmons**
Jacob Smit
Stephan J. Weeks
John P. Young

**Fracture and
Deformation**
Richard P. Reed

John M. Arvidson
Mark W. Austin
Betty A. Beck
Elliot L. Brown
Bruce W. Christ
Leon Chuck
Roland deWit
Ronald C. Dobbyn
James G. Early, Jr.
John W. Elmer
Richard J. Fields
Stephen W. Freiman
Edwin R. Fuller, Jr.
Arthur H. Heuer
George E. Hicho
Bernard J. Hockey
Charles G. Interrante
Maurice B. Kasen
Ralph F. Krause, Jr.
Ronald D. Kriz*
Hassell M. Ledbetter
Samuel R. Low, III
Clyde L. McDaniel
Harry I. McHenry
Terry A. Michalske*
Robert S. Polvani

David T. Read
D. Ellis Roberts
Raymond E.
Schramm
Thomas R. Shives
John H. Smith
Nancy J. Tighe
Ralph L. Tobler
Thomas A. Whipple
Sheldon M.
Wiederhorn
William A. Willard

**Polymer Science and
Standards**
Ronald K. Eby

Joseph M. Antonucci
Harold Argentar**
John D. Barnes
Gary M.
Beaudreau**
Barry Bernstein
Leonard H. Bolz
Rayphel L. Bowen**
Gerhard M. Brauer
Martin G.
Broadhurst
Daniel W. Brown
Walter E. Brown**
Anthony J. Bur
James M. Cassel
Shu-Sing Chang
Tzeng Chen**
Lawrence C. Chow**
Edward S. Clark
James P. Colson
John M. Crissman
George T. Davis
Ronald E. Dehl
Aime S. Dereggi
Brian Dickens
James G. Dillon**
Seymour Edelman
Bruno M. Fanconi
Barry L. Farmer
Lewis J. Fetters
Roland E. Florin
Joseph H. Flynn
Edmond L.
Graminski
Warren H. Grant
(Continued)

The National Bureau of Standards has had a continuing involvement in materials research and development since its founding in 1901. Today, more than ever, NBS is committed to a strong program in the materials sciences, and has focused most of such research in the Center for Materials Science.

This Center's program is geared towards providing technical support to private organizations and government agencies to enhance more effective use of materials. Further, we believe that a strong base of materials science at NBS is an essential foundation for U.S. industry in developing new products, increasing productivity and assuring future economic competitiveness. Accordingly, the Center conducts major research activities in polymers, metals, ceramics, and glasses focus on areas where measurement services and data are especially needed.

Our materials research program addresses major phases of the materials cycle, from processing through design, manufacture, and assembly, to use and finally to recycle or discard. The Center's research program covers three major aspects of materials science: transformation science, structure/property science and durability science. Transformation science is the basic science which underlies materials processing research, for it deals with the changes in state or microstructure of materials. It seeks to predict the microstructure which results from variables of composition, temperature gradients, pressure, and mechanical stresses. Those same variables are of importance in industrial processing. Structure/property science addresses how to measure structures and how chemical and physical properties depend upon structure. Durability science deals with the changes which cause deterioration in service, such as corrosion, wear and fracture.

Center activities are formulated partly on the basis of materials' trends and problems, such as those identified by the National Academy of Science. We find it especially effective, however, to plan our efforts through direct contact with the users of our services, frequently by working in cooperation with our many "clients" in industry and government. Thus, our assessment of the needs for materials' standards is aided by having members of our staff participate in more than 120 engineering standards committees concerned with measurements needed for effective use of materials. We are helped both in pro-

View of the counter arm of the five-counter diffractometer. Antonio Santoro and Kay Hardman are investigating a material at low temperature; the sample is enclosed in the cryostat shown standing in the central part of the picture. The neutron beams diffracted by the powdered material are intercepted and measured by the counters in the horizontal plane of the instrument. There are five such counters, placed 20° apart, so that different regions of the pattern can be measured simultaneously. Visible in the picture are also the catcher of the primary beam (on the left), and shielding walls, necessary to reduce background.

Robert E. Green
Thomas M.
    Gregory**
Stephen S. Hass**
Charles C-C. Han
Gerald R. Harris**
William P. Harris
Harley L. Heaton**
Ture Heline**
Elliot A. Kearsley
James M. Kenney
Freddy A. Khoury
David E. Kranbuehl
Samuel J. Kryder
William V.
    Loebenstein
David J. Lohse*
Robert E. Lowry
Curtis P. Mabie**
Cyrus G.
    Malmberg**
Gordon M. Martin
Robert M. Marvin**
Arthur A. Maryott**
Mathai Mathew**
John R. Maurey
Jacob Mazur
Frank L. McCrackin
Donald McIntyre
Gregory B.
    McKenna
John E. McKinney
Daniel L. Menis**
Dennis B. Minor
Dwarika N. Misra**
Frederick I. Mopsik
George C.
    Paffenbarger**
Robert W. Penn
Anton Peterlin
Joseph C. Phillips
Walter J. Pummer
Darrell H. Reneker
Steven C. Roth
Robert J. Rubin
Nelson W. Rupp**
Isaac C. Sanchez
Charles P. Saylor**
George A. Senich
Jack C. Smith
Leslie E. Smith
Jeffrey W. Stansbury
Shozo Takagi**
John A. Tesk
Elizabeth E. Toth
Ming S. Tung**
David L.
    VanderHart
Peter H. Verdier
Gerald L. Vogel**
Herman L. Wagner
Francis W. Wang
Richard M.
    Waterstrat**
James J. Weeks, Jr.
Eric P. Whitenton**
Richard P.
    Whitlock**
William K. Wilson**

Lawrence A.
    Wood**
Wen-Li Wu
Hyuk Yu
Louis J. Zapas

Metallurgy
Robert Mehrabian

David B. Ballard
Cletus J. Bechtoldt
Lawrence H. Bennett
Francis S.
    Biancaniello
Peter J. Blau
William J.
    Boettinger
Harry C. Burnett, Jr.
Daniel B.
    Butrymowicz
Roger B. Clough
Gabrielle G. Cohen
Sam R. Coriell
John R. Cuthill
Billy J. Evans
Steven E. Fick
Anna C. Fraker
Stephen C. Hardy
M. Ashraf Imam**
Lewis K. Ives
Daniel J. Kahan
Masao Kuriyama
Kenneth C. Ludema
John R. Manning
Thaddeus B.
    Massalski
George J. Mattamal
Archie J. McAlister
Simon C. Moss
Joanne L. Murray
Lucien A. Nedzi**
Robert L. Parker
Michael E. Read
Robert C. Reno
Steven T. Ridder
Arthur W. Ruff, Jr.
Robert J. Schaefer
Robert F. Sekerka
Robert D. Shull
John A. Simmons
Gregory B.
    Stephenson
Pei Sung**
Lydon J.
    Swartzendruber
Ann C. Van Orden
Richard E. Watson
Morgan L. Williams

**Ceramics, Glass,
and Solid State
Science**
*Hans P. R.
    Frederikse*

Michelle C. Austin
Michael I. Bell
Rebecca A. Bird
Douglas H.
    Blackburn
Stanley Block

William S. Brower,
    Jr.
Simon J. Carmel
Mario J. Cellarosi
Given W. Cleek**
Martin I. Cohen
Lawrence P. Cook
David J. Cronin
Marilyn J. Dodge
Louis P.
    Dominquez**
Eloise H. Evans**
Edward N.
    Farabaugh
Albert Feldman
Thomas A. Hahn
Wolfgang K. Haller
Vicky L. Himes
William R. Hosler
Camden R. Hubbard
Arnold H. Kahn
Michael J. Lynch**
Floyd A. Mauer
Howard F.
    McMurdie**
Alan D. Mighell
Marlene E. Morris**
Ronald G. Munro
Taki Negas
Craig D. Olson
Helen M. Ondik
Boris Paretzkin**
Harry S. Parker
Alvin Perloff
Gasper J.
    Piermarini
Carl R. Robbins
Robert S. Roth
David M. Sanders
Richard D. Spal
Judith K. Stalick
Jon L. Waring
Roy M. Waxler
John T. Wenzel
Grady S. White

Reactor Radiation
Robert S. Carter

Norman F. Berk
Russell C. Casella
Yu-Tarng Cheng
Donald A. Garrett
Charles J. Glinka
V. Kay Hardman*
Jeffrey W. Lynn
Bernard Mozer
John H. Nicklas
Edward Prince
Tawfik M. Raby
James J. Rhyne
J. Michael Rowe
John J. Rush
Antonio Santoro
James F. Torrence
Alexander Wlodawer

*Post Doctoral Staff
**Research Associates
    and Guest Workers

gram design and execution by 22 industry-supported Research Associates who work with our staff. In addition, we have attracted 54 guest workers from industry and universities. We also work closely with other government agencies. In fact, the Center currently provides technical assistance to approximately 60 different organizations within the Federal Government. About 40 percent of our materials program is carried out to provide direct support to other government agencies. In addition, we sponsor or co-sponsor national or international conferences, symposia, and workshops.

The technical activities of the Center are carried out by six divisions: Chemical Stability and Corrosion; Fracture and Deformation; Polymers Science and Standards; Metallurgy; Ceramics, Glass and Solid State Science; and Reactor Radiation. These divisions vary considerably in their balance between theory and experiment, between direct standards work and research, and in their orientation toward industrial needs and the needs of other components of the scientific and technological community.

For instance, to meet the needs of the metals processing and manufacturing industries for data required to develop durable, high performance alloys, the Center carries out theoretical, experimental, and data-analysis activities on alloy phase stability. The needs for accurate phase diagram information on new alloy systems have been addressed frequently in recent years, and a joint effort with the American Society of Metals (ASM) on phase diagrams is now underway. In this joint program, the Center provides overall guidance to the program to assure reliability of the data evaluations, to maintain coordination among participating phase diagram centers (most of which are in the private sector), and to develop techniques for the graphic presentation of phase diagram data. ASM will serve as a direct interface with the metals industry so that needs and priorities can be properly determined. An international council involving 70 members from nine countries will advise us on this effort. Two significant features of this joint effort are the publication of a new bulletin for rapid information transfer and the availability to industry of evaluated data directly from ASM.

One unique feature of our structure/property science work is the 10-megawatt research reactor located at our

aithersburg site. The low energy thermal neutrons emitted by the reactor are used in the structural analysis of complex and sophisticated materials. Researchers involved in such analyses come from a variety of government agencies, universities, and industrial organizations. Working with our staff, these investigators have studied many materials and material transformations—among them cements, magnetic materials, and battery materials. Most recently, they have carried out fundamental studies of the chemistry of ceramics by neutron diffraction profile analysis, which promises to be a powerful new tool for crystal structure analysis.

We are constructing a special facility at the reactor for small angle neutron scattering, to be used, for example, in the study of polymer structures. Next year, we will develop an additional facility at Brookhaven Laboratory for the application of synchrotron radiation to materials. This application, we feel, is to be the next generation of x-ray techniques for structural studies of crystalline materials.

Similarly, we are broadening our research on the structure of noncrystalline materials through new studies in glassy materials which are formed by deposition from the vapor phase. Under construction is a film deposition apparatus which allows the simultaneous codeposition from separately controlled molecular beam sources. Deposition rates will be monitored during observation of optical properties of the forming films. In addition, the deposition facility will be coupled to a diagnostic facility, allowing in vacuo transfer and analysis by several electron and particle emissive techniques. When operative, the facility will be used for the production of reflective and antireflective optical coatings and flat configuration waveguides, and in such fundamental studies as molecular cluster formation in glassy films, the determination of accommodation coefficients in multi-component amorphous structures, and in the simulation of amorphous oxide films found on corrosion-resistant metals.

Additional work on structure/property relationships involves investigations to define the molecular mechanisms in polymers associated with deformation and fracture. For polyethylene, these mechanisms are elucidated through comparisons between Fourier transform infrared (FTIR) spectra of undeformed and fractured specimens. Small variations in the concentrations of carbon-carbon

double bonds, methyl groups, and carbonyl groups result from rupture of carbon-carbon backbone bonds and subsequent free radical reactions. These concentration changes can be detected in difference spectra obtained through subtraction of the digital FTIR data. The detectability of small concentration variations is enhanced by the superior sensitivity of the FTIR method over conventional dispersive infrared spectroscopy. In addition, the FTIR method has potential application in the study of polymer matrix composites, a group of new materials of interest to Center scientists. These materials are finding increasing use as structural parts in the transportation industry because they can be fabricated into lightweight structural components.

The anticipated durability of materials and products in service is a central consideration in their selection and use. Thus, a major aspect of the Center's materials program concerns corrosion abatement as well as other aspects of materials durability including wear, which is the primary cause of materials degradation in operating machinery; fracture, which is the cause of catastrophic failure of structural components; and the migration of plastic stabilizers, which is one of the principal causes of failure in plastics.

One example of our research in measurement and corrosion science is localized corrosion wherein a metal is attacked at specific sites instead of being dissolved generally, leading to pitting, stress corrosion, and crevice corrosion. When it happens, failure can result even when most of the metal is relatively unattacked. In fact, localized corrosion accounts for the majority of corrosion failures. This form of corrosion is the most difficult to detect, since the total amount of metal dissolved prior to failure may be small. We consider localized corrosion to be a major technical challenge and are working on several approaches to help understand and control it. In particular, Center scientists are developing measurement methods to determine the susceptibility of a variety of metals to localized corrosion. This information is essential for developing standard methods of assessing the suitability of a metal for service in a given environment and for the developing of new, corrosion-resistant alloys.

Another and a very important aspect of materials durability is fracture control. Improved fracture control methodologies depend upon predictive models. In fact,

predictive models coupled with nondestructive evaluation techniques are becoming increasingly important in developing materials performance codes and standards, including those for metals. For example, in 1976, Alyeska Pipeline Service Company requested waivers from the Department of Transportation (DOT) for a number of buried girth welds. The welds contained radiographically detected defects which appeared to be not in conformance with DOT regulation. The waiver was based on a fracture mechanics analysis.

In anticipation of the waiver, DOT requested assistance from NBS in evaluating the fracture mechanics analysis and the nondestructive evaluation methods used to detect and determine the dimensions of specific girth weld defects. In large part because of the analysis provided by Center scientists, DOT did eventually conclude that under some circumstances, exemptions from existing standards could be granted if warranted on the basis of fracture mechanics test results. Thus, more petitions for exemptions can be anticipated. The Center is working with DOT now to establish a technical framework for ruling on these waiver requests—a framework which would minimize the need for subjective judgments and thus obviate a tendency toward overly conservative design.

The breadth, scope, and accomplishments of the Center's technical program are comprehensively reflected in the more than 420 articles by Center scientists published in 1979 in numerous professional journals, books and conference proceedings. The following brief reports highlight some current work of particular interest.

Erosion of Brittle Materials by Solid Particle Impact

Sheldon M. Wiederhorn, Bernard J. Hockey, A. William Ruff and Lewis K. Ives, Fracture and Deformation Division

In an effort to provide a better understanding of the micro-mechanics of erosion and other impact-related processes, the detailed nature of damage produced in ceramics and metals by impingement with solid particles has been investigated. Results obtained by scanning and transmission electron microscopy clearly specify the elastic-plastic nature of the impact. This has led to the development of models which incorporate the concept of elastic-plastic fracture in describing the erosive wear of brittle materials.

Erosion is a major cause of material degradation in both civilian and military applications. It is caused by the high velocity impact of solid particles or liquid droplets against solids. Although each impact causes only a minute amount of damage, the cumulative effect of millions of impacts can result in appreciable loss of material from structural components. Furthermore, even the minute damage caused by the impact of a single particle often can significantly reduce the strength of brittle materials.

In many military applications, erosion shortens the lifetime and increases the cost of replacement of mechanical components. The operation of gas turbines in dusty terrains, for example, reduces turbine lifetime to one-tenth the normal value. As a result of this shortened lifetime, the cost of replacing turbines in helicopters used in Southeast Asia amounted to $150 million in 1970 alone. Other examples of component degradation include: the erosion of radomes by water, ice, and dust; the damage of optical components such as laser windows by rain and dust; the damage of turbine and rocket components by combustion products; and the erosive thinning of helicopter rotor tips by dust.

Because of their outstanding erosion behavior, ceramic materials are often used in applications where erosion resistance is required. Thus, castable refractories have largely replaced metals in certain high wear areas of oil refineries and are being considered for use for similar applications in coal gasification plants. In another application, ceramics have been usefully employed as nozzle vanes in experimental radial-flow gas turbines, where they have exhibited a pronounced superiority over the standard metallic vanes in resisting erosion. Ceramics are also used in a number of applications where other properties are important, but where erosion is a factor in limiting reliability. In windscreens and radomes for example, ceramics are used because of their transparency to electromagnetic radiation, but must also be able to resist erosion to maintain their integrity. Similarly, in turbine nozzles and vanes, ceramics must withstand both high temperatures and erosion from combustion products and dust.

The few examples given above underline the need for improved erosion resistant ceramics, the development of which could, in principle, be assisted through a better understanding of the erosion process. Studies have been conducted primarily through the use of the scanning and transmission electron microscopes. Erosion rate measurements have also been made in a variety of chemical environments, and at temperatures ranging from room temperature to 1000 °C. The combination of techniques employed on this project has led to the development of
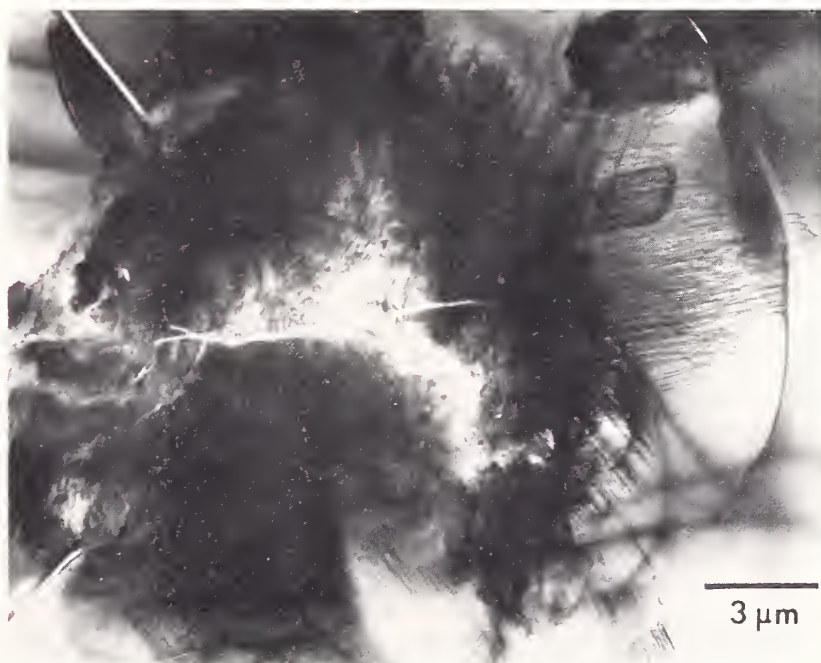

FIGURE 1. Impact site in SiC produced by 150 μm SiC particles at a velocity of 94 m/s, and an impact angle of 90°.

a deeper understanding of the erosion process, and to the development of new elastic/plastic models of erosion that are particularly applicable to brittle materials. These models are based on the observation that all erosion of ceramic materials, no matter how brittle, is accompanied by plastic deformation.

The earliest indication of plastic deformation during erosion of hard brittle materials, such as Al_2O_3, SiC and Si, came from examination of individual impact sites by light microscopy. Residual plastic impressions were found to be associated with cracks that formed as a result of the impact. The damage resulting from impact is, in fact, very similar to that produced during hardness testing using Vickers or Knoop diamond indentors. For soft materials such as LiF or MgO, etch-pit techniques have been used to show that dislocation slip-bands are associated with impact damage or hardness impressions. These observations naturally suggest that similar deformation accounts for impact impressions in hard materials such as Si, Al_2O_3 and SiC. However, direct evidence for plastic flow in these materials was difficult to obtain, because the dislocations produced by impact are closely confined to the impact site. This close proximity of the dislocations to the plastic deformation was observed for all materials studied (Ge, Si, Al_2O_3, SiC, MgO), but the extent of deformation and the morphology of the cracks associated with the deformation was dependent on the crystal structure. MgO, an ionic crystal, exhibited the most extensive deformation at impact sites; cracks that formed (on 110 planes) in this crystal were always confined within the zone of plastic deformation. Quite the opposite behavior was observed for Si and Ge, which are covalent materials and more

brittle than MgO. For these materials, plastic deformation was confined to the near vicinity of the impact site, while cracks propagated relatively large distances into the crystal. The behavior of SiC and Al_2O_3 was somewhat intermediate, the extent of deformation being approximately twice the size of the residual impact impressions. Cracks in SiC and Al_2O_3 propagated beyond the deformation zone and were arrested in materials that was free of dislocations.

A qualitative comparison of this type of erosion damage with that occurring in metals indicates a great similarity for both types of materials with regard to the density and extent of dislocation formation at the impact site (figure 2). For both types of materials, the density of dislocations at the contact site is so high that the crystal structure is severely strained; fruitful examination by transmission electron microscopy is not feasible. Dense

tangles of dislocations result in complete scattering of the transmitted electron beam. At the edge of the impact site, the dislocation density drops abruptly to the density characteristic of the undamaged crystal. Ceramics and metals differ in appearance because metals are able to accommodate the mechanical strains resulting from the impacting particle, whereas ceramic materials crack when subjected to high strains. As a consequence, crack formation is normally observed during the erosion of ceramics. In fact, it is this crack formation that normally accounts for material loss during the erosion of ceramics.

Investigations of impact damage by light microscopy and by scanning electron microscopy are useful for revealing the relative extents of fracture and plastic flow. Plastic deformation in ceramic materials is enhanced when particles strike target surfaces at low angles of impingement. Scan-
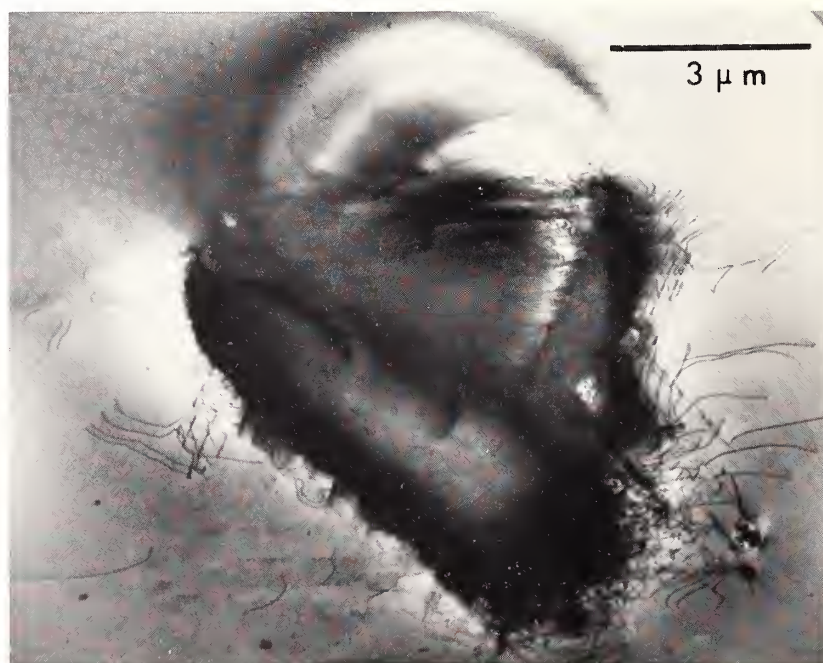

FIGURE 2. Impact crater in 310 stainless steel produced by 50 μm Al_2O_3 particles at 59 m/s, impact angle 90°.

ning electron micrographs of the damage surface suggest extensive plowing as a consequence of the particle impact (figure 3). At low impact angles, fracture during contact is greatly reduced. The damage sites are often free of cracks, and plastic deformation appears to be the primary mode of material removal. These observations are confirmed by transmission electron microscopy studies, which show that crack-free plastic indentations are frequently obtained in brittle materials for small angles of impact.

Based on scanning and transmission electron microscopy data obtained on ceramic materials, several models of erosion have been developed recently which incorporate concepts of elastic-plastic fracture into erosive wear. The formation and growth of plastic zones during the impact process determine the types of cracks that are formed and hence, the amount of strength degrada-

tion and material loss from brittle materials during erosion. These theories are currently being tested in the Center for Materials Science in order to develop a body of knowledge that can be used to model the lifetime of ceramic components in environments where erosion is important. Studies suggest that the hardness, H, and the critical stress intensity factor, K_C, are the two materials properties that control erosion: a strong dependence of erosion rate on K_C, but a weak dependence on H, is observed. Although the available experimental data supports the view that K_C and H (measured using dynamic loading) are independent of temperature, additional research is needed to confirm this conclusion. Consequently, future research in the Center for Materials Science will concentrate on the dependence of erosion on K_C and H, and on the effect of temperature on these parameters.

Atomistic Theories of Crack Growth and Fracture

Edwin R. Fuller, Jr., Robb M. Thomson, and Brian R. Lawn [1]

A structural component that fails by a brittle fracture mode generally involves the growth of an intrinsic flaw, or crack under sustained load until it attains some critical size.

The desire to understand this crack growth and fracture from a fundamental level has provided considerable impetus to the atomistic modeling of crack tips and crack-tip processes. While these models are usually overly simplistic in relation to real structures and materials, they demonstrate the connection between microscopic processes in the crack-tip region and macroscopic fracture parameters; they thereby provide a qualitative framework for considering the complicated phenomena of crack growth and fracture. Only through this fundamental understanding can more realistic models be developed and more quantitative calculations be performed that permit an assessment of crack growth behavior, and accordingly, of component reliability from more fundamental principles.

Our studies in the Center for Materials Science have been to develop atomistic models of a cracked solid, which minimize the mathematical complications that necessitate elaborate computer calculations, yet which contain the essential elements of the fracture process and do not preclude general conclusions. Reconsidering an earlier model of Thomson et al [1], we were able to decouple effectively the nonlinear interatomic interactions in the crack-tip region from the linear elastic interactions in the bulk of the solid [2,3]. This stratagem provides a mechanics model within which the influence of the crack-tip interaction can
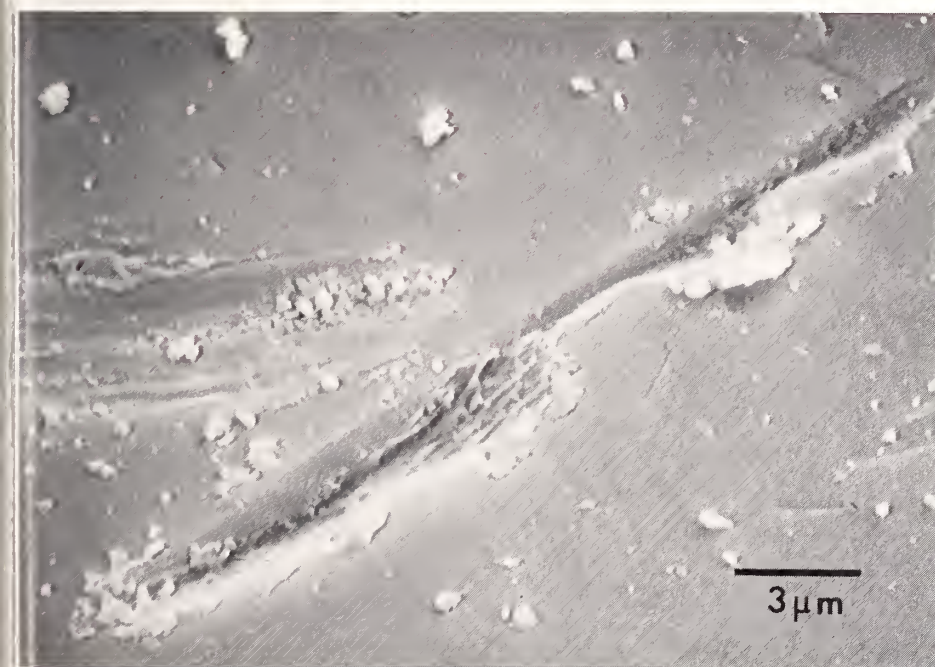

FIGURE 3. Impact crater in dense Al_2O_3, 3-5 μm grain size, caused by 150 μm SiC particles at a velocity of 90 m/s and an impingement angle of 15°.

[1] On study leave from University of New South Wales, Australia.

be explored. It was into this framework that we were able to incorporate, again in a simplified manner, the molecular interaction of a gaseous species with the crack-tip atoms to obtain a theory of chemically assisted crack propagation [4,5].

In the following section we describe the lattice model of a crack we have considered, and indicate how the atomisticity of the problem leads to a number of mechanically stable crack configurations ("lattice trapping"), from which the crack can advance by activation. The final section discusses how a molecular chemical reaction can be incorporated into this mechanics model to give a qualitative model of chemically assisted bond rupture.

Intrinsic Bond Rupture. Our atomistic model of a crack in a quasi-one-dimensional solid is shown in figure 1. It consists of two semi-infinite chains of atoms that maintain their rigidity by means of an interatomic interaction. This interaction is modeled as a flexural spring element with force constant β. The chains of atoms are bonded together by a series of cohesive interactions between the chains, modeled as stretchable spring elements between the atom pairs. To form a crack, we suppose that the first n stretchable elements are ruptured, or stretched beyond their assumed finite range of interaction. We assume further that the remaining cohesive spring elements are
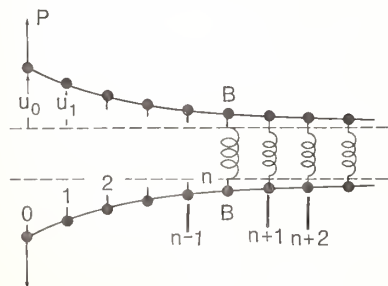

FIGURE 1. Atomistic model of a crack in a quasi-one-dimensional solid.

in the linear regime of their force-displacement response with spring constant α. The one exception is the crack-tip interaction which, by the necessity that it must rupture to advance the crack, must be allowed to be in the nonlinear regime of its response. Transverse opening forces P are applied to the end atoms of each chain to force open the crack.

The total potential energy of this crack system is given by [3]

$$U = -2Pu_0 + \beta \sum_{j=1}^{\infty} [u_{j+1} - 2u_j + u_{j-1}]^2 + nU_{BB} + U_b(2u_n) + \tfrac{1}{2} \alpha \sum_{j=n+1}^{\infty} [2u_j]^2, \qquad (1)$$

where the first term on the right hand side is the potential energy of the loading system; the second term is the strain energy stored in the flexural bonds; and the remaining terms are the contributions from the cohesive bonds across the crack. These cohesive contributions are, respectively, the total bond energy from the n ruptured bonds, the bond energy of the nonlinearly strained bond at the crack tip, and the linear-elastic strain energy of the remaining cohesive bonds. From a fracture mechanics viewpoint, this potential provides both the driving force for fracture and the resistance force to fracture. The crack driving force is derived from the stored elastic strain energy which is released upon crack advance; whereas, the resistance to fracture is contained in the cohesive bond energy of the crack-tip bonds that must be ruptured to advance the crack.

In contrast to a Griffith continuum analysis, where the fracture resistance is provided by the average cohesive energy required to form the new element of surface, the atomistic treatment reveals a fine structure in this process through the discrete nature of the bond rupture event. To illustrate this atomistic influence, we examine

the variation of the system potential energy as the crack-tip bond ruptures. We require, however, that for each crack-tip bond displacement the remaining atoms of the solid are in an equilibrium configuration with respect to this displacement. Necessary conditions for these equilibrium configurations are

$$[\partial U/\partial(2u_j)] = 0, \qquad \text{for } j \neq n, \quad (2)$$

which correspond to an infinite set of fourth-order difference equations. Analytical solutions of these equations are obtainable[3] in the functional form $u_j(P, n, u_n)$. Substitution of these equilibrium-displacement solutions into Eq. (1) accordingly reduces the system potential energy to an explicit function of both the applied fracture mechanics parameters (load and crack length) and the crack-tip bond displacement

$$\delta_n = 2u_n:$$
$$U(P, n, \delta_n) = nU_{BB} - (P^2/6\beta)(2n^3 + 3n^2\xi + n) - K\delta_n + U_b(\delta_n) + \tfrac{1}{2} \alpha (\frac{\xi - 1}{2})\delta_n^2, \qquad (3)$$

where ξ is an elastic coefficient defined by $\xi^2(\xi^2 - 1) = (2\beta/\alpha)$, and $K = (P/\xi)(n + \xi)$ is an effective one dimensional "stress intensity factor".

This expression is particularly useful for demonstrating the origin of the atomistic energy barrier to intrinsic bond rupture and crack advance. Focusing our attention on the nth bond, the first two terms on the right hand side of Eq. (3) are constant for a given applied force and will not be considered further. The next term, $-K\delta_n$, corresponds to the reduction in potential energy that results from the applied fracture driving force as the crack-tip bond ruptures. The two remaining terms represent the resistance of the system to the rupture of the crack-tip bond. The first of these resistance

terms, $U_b(\delta_n)$, corresponds simply to the interatomic interaction between the

term, $\frac{1}{2} \alpha (\frac{\xi-1}{2})\delta_n^2$, is more subtle

crack-tip atoms; whereas the second and corresponds to the harmonic restoring potential exerted on the crack-tip atoms by the remainder of the (linear elastic) structure. It is the balance between these last three terms that determines the atomistic energy barrier, as illustrated graphically in figure 2. The individual terms are plotted in figure 2a and their sum is shown in figure 2b. Clearly, the stress intensity factor term, $-K\delta_n$, biases the bond rupture to make the final state the more stable configuration in this example.

Chemically-Assisted Bond Rupture.
An important part of the above construction was that the interatomic potential between the crack-tip atoms was effectively decoupled from the interactions of the remainder of the solid. Accordingly, this construction provides a mechanics model whereby an arbitrary bond-rupture reaction can be studied in an equivalent linear elastic continuum of crack-tip stiffness $\alpha (\frac{\xi-1}{2})$. An appropriate crack-tip reaction to consider is a bimolecular chemical reaction. It provides a qualitative model for understanding stress corrosion cracking in a gaseous environment.

We begin by reviewing the energy surface for a bimolecular chemical reaction of two free molecules (similar to Lawn and Wilshaw [6]. Consider the reaction depicted in figure 3 where a gaseous molecular A_2 interacts with the crack-tip bond $-B-B-$ to form the product molecule $A-B-$. Several possible potential energy surfaces for this four-atom complex are depicted in figure 4 as a function of the $B-B$ bond
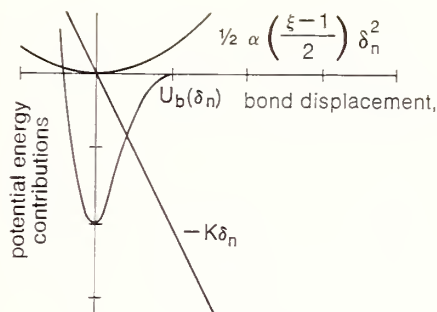

FIGURE 2. System potential energy as an explicit function of the crack-tip bond displacement, δ_n: (a) Individual contributions; and (b) Sum of these contributions, illustrating the stable initial and final configurations (i) and (f) respectively, and the activation state (i^*) through which the system passes to rupture the crack-tip bond. ΔU_+ is the activation energy barrier to this intrinsic bond rupture, and ΔU_- is the energy barrier to the activated healing of this bond.
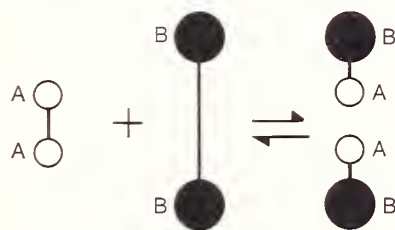

FIGURE 3. Schematic of a bimolecular chemical reaction to rupture the crack-tip bond. A gaseous A_2 molecule reacts with the crack-tip bond $-B-B-$ to produce the "terminal" surface species $A-B-$.
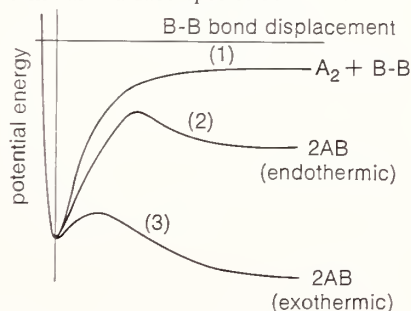

FIGURE 4. Possible potential energy surfaces for the bimolecular chemical reaction illustrated in figure 3. The chemical reaction reduces the bond-rupture energy or thermodynamic surface [curves (2) or (3)] compared to the nonreacted surface [curve (1)].

displacement. We assume that the $A-A$ atoms arrange themselves in the most energetically favorable position for each value of the $B-B$ bond displacement. Comparison of curve (1) with curves (2) or (3) show that the presence of the A_2 molecule makes it easier to dissociate the B atoms. Generally this reaction occurs with an activation energy barrier that could result, for example, from the repulsive interaction of the polar component of the AB molecule. If the reaction is endothermic, the final state of 2AB is metastable with respect to that of $A_2 + BB$, and the reverse is true for exothermic reactions.

The procedure for inserting this chemical reaction, via a modified cohesive force law, into the constraint of a lattice crack is the same as that used in the construction of figure 2b. The initial and final equilibrium configurations now correspond to nonreacted and reacted (adsorption) states of the bond, respectively. The unstable configuration relates to the activated complex of the reaction. The exact influence of the chemical reaction on the rupture of the crack-tip bond depends on the details of the chemical reaction and its activation barrier. Various possibilities have been considered in a recent manuscript [7]. The main effect of the chemical reaction is to further bias the intrinsic activation energy barrier and to allow crack growth to occur at a lower applied stress. Another important conclusion is that the thermo-dynamic surface energy, which determines the thermodynamic condition for crack propagation, is also lowered to that of the chemically reacted surface.

References

[1] Thomson, R. M., Hsieh, C., and Rana, V., Lattice Trapping of Frac-

Neutron Diffraction Profile Analysis and the Structures of Electronic Ceramics

Antonio Santoro and Robert S. Roth, Reactor Radiation Division

ture Cracks, *J. Appl. Phys. 42*, 3154-3160 (1971).

[2] Fuller, E. R., Jr. and Thomson, R. M., Nonlinear Lattice Theory of Fracture, in *Fracture 1977*, D. M. R. Taplin, ed. Vol. 3, pp 387-394 (Univ. of Waterloo Press, Canada, 1977).

[3] Fuller, E. R., Jr. and Thomson, R. M., Lattice Theories of Fracture, in *Fracture Mechanics of Ceramics*, R. C. Bradt, D. P. H. Hasselman and F. F. Lange, eds. Vol. 4, pp 507-548 (Plenum Publishing Corporation, 1978).

[4] Fuller, E. R., Jr. and Thomson, R. M., Theory of Chemically Assisted Fracture, in Proceedings of the Third International Conference on *Mechanical Behavior of Materials*, K. J. Miller and R. F. Smith, eds. Vol. 2, pp 485-494 (Pergamon Press).

[5] Fuller, E. R., Jr. and Thomson, R. M., Atmosphere Assisted Fracture: II. Atomic Models of Crack Growth", (*J. Matl. Sci.*, in press).

[6] Lawn, B. R. and Wilshaw, T. R., *Fracture of Brittle Solids*, Section 7.5 (Cambridge University Press, Cambridge, 1975).

[7] Fuller, E. R., Jr., Lawn, B. R. and Thomson, R. M., Atomic Modelling of Crack-Tip Chemistry (to be submitted to *Acta. Met*).

In recent years it has become evident that certain crystalline phases allow cations and anions to move through the crystal structure of which they are part much more quickly than had previously been believed possible. Such materials, which include, for example, sodium β-alumina and cubic stabilized zirconia, are often called "super-ionic conductors." In an effort to better understand the mechanisms involved in super-ionic conductivity, the phase equilibria, crystal chemistry, and crystal structure of these materials are being examined in laboratories throughout the world. In fact, only a thorough understanding of the possible mechanisms of conduction in different types of conductors will enable a more accurate prediction of properties and allow the researchers to tailor-make solid ionic conductors for specific applications in batteries, fuel cells, etc.

The two most promising classes of possible ionic conductors have O^{-2} and Li^+ ions as the mobile species. Conventional oxygen ion conductors have the fluorite-type structure with oxygen vacancies, and the conduction involves some type of hopping mechanism through the vacancies. However, it has been found that a new group of compounds based on the scheelite- and $BaMnF_4$-type structures may accommodate oxygen ions in interstitial positions which then become the vehicle for the ionic conduction. On the other hand, the Li^+ containing materials have structures with channels sufficiently large to permit the motion of the conducting ions.

A problem associated with the study of compounds of the type mentioned is related to the fact that heavy and light atoms are present simultaneously in the structures. It follows that x ray diffraction cannot lead to an accurate knowledge of the atomic distribution, and neutron methods are the only alternative. In addition, many of the materials of interest cannot be prepared as single crystals of sufficiently large size for single-crystal work and have to be analyzed by powder diffraction. Because of the random orientation of the crystallites in a powder,
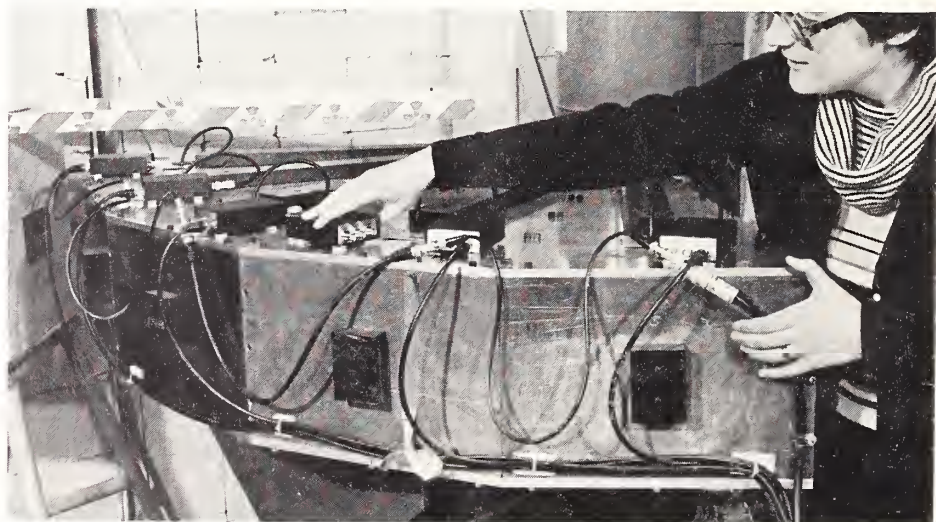

FIGURE 1. View from the top of the counter arm of the five-counter diffractometer. The counters are placed 20° apart and simultaneously measure different regions of the pattern. The sample is located at the geometrical center of the diffractometer.

the three-dimensionally diffracted intensities are collapsed into a monodimensional distribution, which results in a loss of information about the spatial properties of the crystal, and, if overlapping of the diffracted lines occurs, about the intensities associated with each set of crystallographic planes. The lost information can be partially recovered if the powder patterns are measured with diffractometers of high resolution, and if, instead of using integrated intensities in structural refinements, one fits the entire observed profile with one calculated in terms of a plausible model of the structure ("Rietveld Method," or "Profile Analysis").

Not surprisingly, the application of the method of profile analysis in the U.S. and in foreign laboratories has become increasingly important in the study of a wide class of polycrystalline materials, and numerous improvements of both the experimental techniques and data refinement methods have been proposed or applied. In the past few years, scientists and technicians at the NBS reactor have established the forefront capability in the U.S. in the methods and applications of neutron diffraction-profile analysis and have developed a new multidetector high res-

olution diffractometer for profile analysis studies.

With this facility, illustrated in figure 1, five counters are used simultaneously. The resulting gain in intensity may be used to reach an instrumental resolution such that the natural broadening due to the physical conditions of the sample becomes observable and constitutes the predominant factor in determining the width of the diffracted lines.

At the NBS reactor, studies of possible ionic conductors are underway as part of a collaborative effort between scientists of the Reactor Radiation Division and the Ceramics, Glass, and Solid State Science Division. Compounds with both O^{-2} and Li^+ ions have been, or are being, examined with powder neutron diffraction. The structures of $CeNbO_4$, $CeTaO_4$, and $NdTaO_4$ have been well refined so that reasonable conjectures can be made about the relationship between the stiochiometric and the oxygen-rich phases obtainable by oxidation of some of these compounds. Similarly, the structures of $LiNb_3O_8$, $M-LiTa_3O_8$, and Ta_2WO_8 have been accurately measured as part of an attempt to determine the still unknown positions of the Li^+ ions in

the structure of $H-LiTa_3O_8$. As an example of the results obtained in these studies, the calculated and observed profiles for the structure of $LiNb_3O_8$ are compared in figure 2.

More recently, it has become apparent that the structures of many ionic conductors are modulated. Modulation, for example, has been clearly established in $CeNbO_{4.08}$, and there are good reasons to believe that it is also present in $H-LiTa_3O_8$. Little is known about modulated structures, and even their definition is still being debated. We may define modulation from a strictly crystallographic point of view in the following way:

We may say that a structure is "modulated" when it has one or more structural "features" having a periodicity which is "inconsistent" with, or "incommensurate" with respect to, the periodicity of the bulk of the structure. When this condition occurs, the ratio of the two periods is not a rational number (perhaps, we should say that this ratio is not "a simple" rational number). The "features" which cause the modulation may be: 1) positional in nature (i.e., shifts from the positions that one or more atomic species would have if the structure were unmodul-
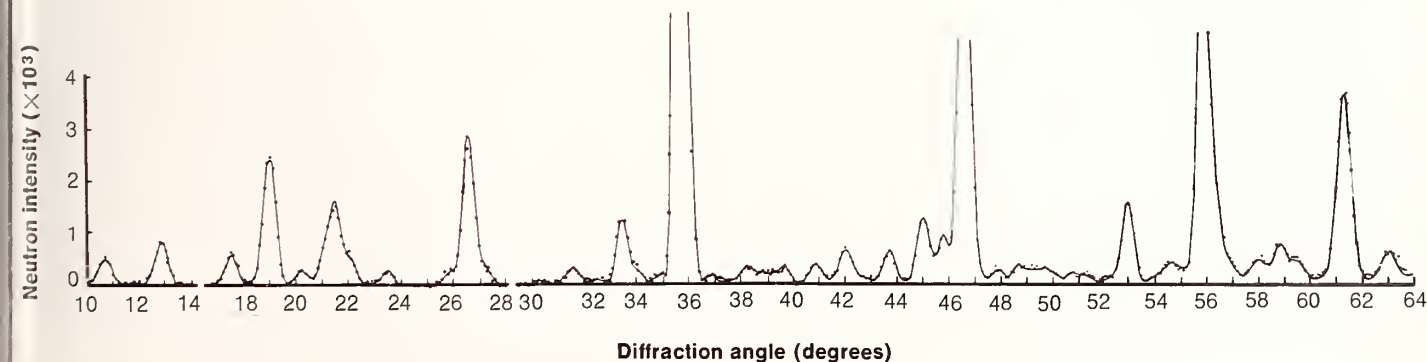

FIGURE 2. Calculated profile (continuous line) and observed data (dots) in the powder pattern of $LiNb_3O_8$. The close agreement between theoretical prediction and experimental data, shown, in the diagram, indicates that the refined structure is highly accurate.

Recent NBS Advances in Physical Properties Measurements at Ultra High Pressures

Stanley Block, Ronald G. Munro, and Gasper J. Piermarini

ated), 2) substitutional (i.e., one or more sets of positions, which would be crystallographically equivalent if the structure were unmodulated, have variable occupancies), or 3) a combination of the two.

The diffraction patterns of such structures contain reflections corresponding to the periodicity of the bulk of the structure ("main" reflections) and reflections which are inconsistent with, or incommensurate with respect to, those of the first type ("satellite" reflections). These definitions are necessarily provisional and may well be modified when more information is gained about modulated structures.

The solution of structures of this sort requires the development of new techniques for the interpretation and processing of the experimental data. Along this line, we are at present developing methods for indexing powder patterns in which the presence of satellite reflections is suspected or ascertained. At the same time, least-squares fitting programs are being, or have been, modified so that the intensities of satellites can be taken into account, and so that background and thermal motions of the atoms are properly treated. This last development should be particularly useful in the study of nonstoichiometric phases, in which one or more sets of equivalent positions are partially occupied.

We hope the NBS program to combine advanced profile refinement methods, high-resolution neutron diffraction, and new approaches to dealing with and predicting incommensurate features in complex diffraction patterns will lead to a significant improvement of our understanding of structure and properties of ionic conductors and broad classes of other crystalline materials.

Pressure is beginning to take its rightful place beside temperature as an important research variable in the quest to understand the nature and behavior of matter. Two developments at NBS are chiefly responsible for the recent blossoming of high pressure science: (1) the capability to generate very large static pressure and (2) the capability to measure it. As a result of these two milestones, the discovery of new phases and properties of materials, new insights into the physics of condensed matter systems, the synthesis of new materials, and the opportunity to test experimentally theories which previously could be considered little more than interesting conjectures have all become possible. A steady flow of refinements and new applications are now being developed in our laboratory. Other developments can be found in the current scientific literature.

In the past, the direct generation of pressures by applying a known force to a known area required the costly construction of a large apparatus and a considerable effort to operate it successfully. The development of the diamond anvil pressure cell (DAPC) at the National Bureau of Standards surmounted these difficulties. The NBS pressure device obtains large pressures by using small areas. The substance to be studied is placed between two diamonds (see figure 1). When the diamonds are squeezed together with a moderate force, a large pressure is transmitted to the substance because of the small area presented by the faces of the diamonds. The resulting apparatus (see figure 2) is compact, small enough to be held in one hand, relatively inexpensive, easy to operate, and readily adaptable to existing measurement equipment. Furthermore, the diamonds provide optical and x-ray access to the stressed sample. The result has
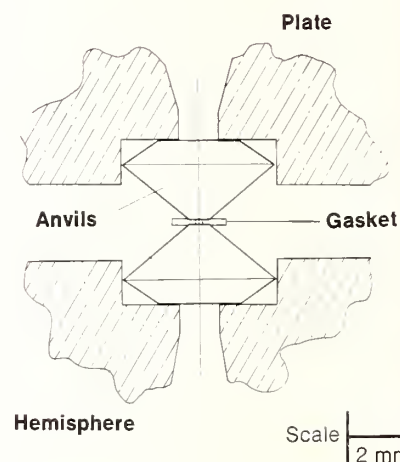
FIGURE 1. Schematic cross-section of the Diamond-Anvil assembly of the NBS pressure cell. Two gem diamonds roughly 1/3 of a carat in size act as opposed anvils. The sample is contained in a small hole (approximately 0.5 mm in diameter) in the gasket located between the anvil faces. The diamonds also act as windows for 180° and EPI optical access.

been an increase in the number of experiments that can be performed at high pressure. Previously, work was restricted primarily to compressibility studies, pressure-volume-temperature relations, and electrical resistance measurements. The DAPC adds microscopic observations, infrared spectroscopy, x-ray studies, and, most recently, viscosity measurements.

Quantitative use of pressure in research requires both a means to generate the pressure and a means to measure it. Pressure is force per unit area, and hence if a known force is applied to a known area, the pressure is easily computed. This direct method of pressure determination was the basis of early pressure devices, but severe problems in accuracy develop above about 3.0 GPa. Consequently, secondary pressure standards are required for most of the work at high pressure.

Fortunately, a very useful, rapid,

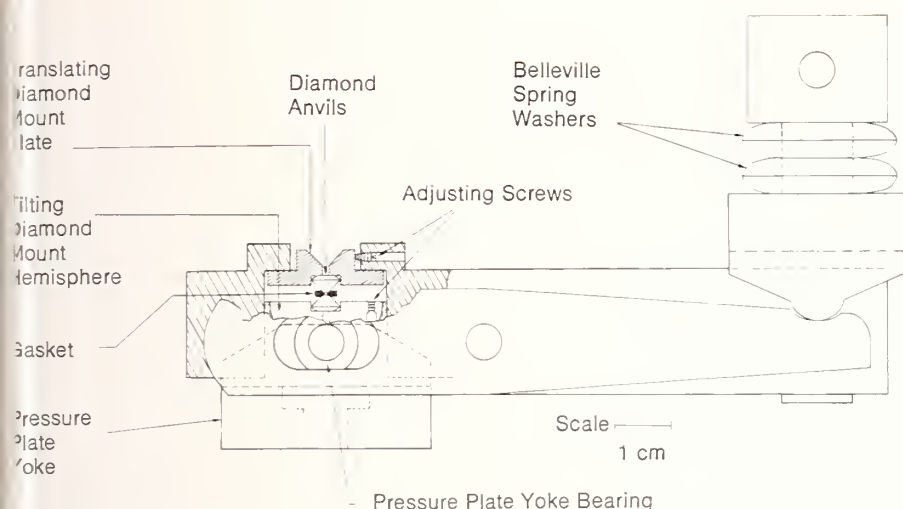FIGURE 2. The mechanism for generating force consists of a spring loaded lever-arm assembly shown in cross section above. Belleville spring washers are compressed by the simple rotation of a screw. The force generated is transmitted through the lever arms to the pressure plate yoke which loads the piston containing one of the anvils.

FIGURE 3. The chart shows the intensity of research activity with the diamond cell relative to the year 1972—the year that the ruby pressure sensor was introduced by NBS. The chart is based on results from a recent literature survey.

convenient, and versatile pressure scale as developed at NBS using the fluorescence spectra of ruby. The famous red color of ruby is produced by chromium impurities in the host material, aluminum oxide, and the red fluorescence lines known as the sharp R-lines occur at well defined wavelengths. The pressure dependence of the R_1-line was calibrated at NBS as a pressure scale. With the original calibration, pressures up to 30 GPa can be determined accurately. With increased use of the ruby method, work to extend the scale to 100 GPa has been reported by others recently. The temperature dependence of the scale has also been examined in other laboratories over the range in 4.2 K to 358 K; and it has been found that the rate at which the wavelength of the R_1-line changes with pressure is nearly constant over the entire range. As a result of its convenience and its large range of utility, the ruby fluorescence technique is the most widely used pressure scale presently available for pressures above 1 GPa.

The impact of the ruby scale on high pressure research with the diamond anvil cell is indicated in figure 3. The curve is the result of a survey we made of the scientific literature from 1960 through 1978. After the introduction of the DAPC in 1959, activity increased slowly for a few years, but without a quantitative knowledge of the pressure, interest was limited. However, after the introduction of the ruby pressure scale in 1972 and its calibration in 1975, a dramatic increase occurred in research activity which has not yet reached its peak.

Among the recent advances associated with the increasing activity have been the applications of x-ray energy dispersive and single crystal techniques. We have, for example, carried out with F. Mauer of NBS a detailed study of factors affecting intensity and resolution in energy dispersive powder diffraction in order to optimize the experimental conditions for obtaining x-ray diffraction data with the diamond anvil cell. The factors studied included size and intensity distribution of the white radiation source, absorption in the diamonds, beam divergence and particle size of the sample, as well as collimator and slit system design. Improvements in equipment and techniques have led to obtaining better data in less time, and thus have enhanced NBS capabilities for high pressure crystallographic studies.
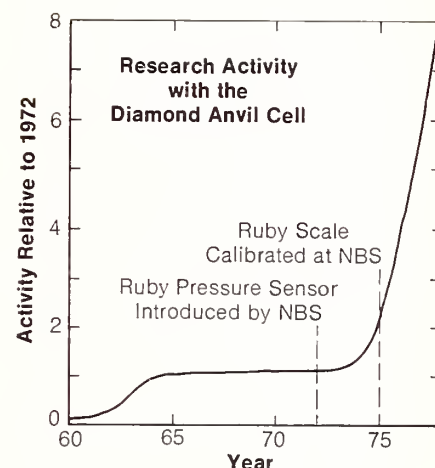
As examples, we discuss our results on CuCl, CdS, and ice VII. The behavior of CuCl under pressure has received much attention recently, prompted by the reports that it undergoes a transition to a metallic state at about 4.0 GPa. Further, anomalies in compressibility, resistivity and magnetic susceptibility in the pressure range of 4.0 GPa and in the temperature range 4.2 K to 300 K have been reported, and the existence of superconductivity has been postulated for the anomalous diamagnetic behavior.

The pressure dependence of the electrical resistance of CuCl to pressures up 14.0 GPa was measured using our recently developed two-probe method adapted to the diamond anvil

high pressure cell. The results of our electrical measurements, which were made on four samples of CuCl prepared by different methods, do not show any evidence for a "metallic" IIa Phase even after repeated cycling. We also considered the possibility of a photo-conduction effect in the CuCl samples. The electrical measurements were performed in the absence of light, in dim red light, and in white light, and no significant photo-effect was observed. In additional experiments done in collaboration with A. Jayaraman, et al., at Bell Telephone Laboratories with a piston cylinder device, no large resistance drop was observed in the range of 0.1 to 5.0 GPa, which is in agreement with our diamond cell results.

We have also performed x-ray measurements on CuCl. We used both film techniques with ungasketed CuCl samples and gasketed samples with our newly developed energy dispersive method mentioned previously. Our results confirm the transitions from zincblende to tetragonal structures at 4.4 GPa and from tetragonal to the NaCl type structure at about 8.0 GPa. Our x-ray pattern of the black opaque phase taken in an ungasketed diamond anvil consists of NaCl-type lines. We therefore believe that in the NaCl phase of CuCl, a disproportionation reaction sets in, in the presence of large shear stress. In summary, we found no evidence for a dielectric-transition in CuCl.

In collaboration with G. E. Walrafen of Howard University, we have carried out high pressure Raman and x-ray diffraction experiments on ice VII. The group at Howard University did Raman studies in a diamond anvil cell. They determined that the O-H vibrational frequencies of ice VII shifts downward with pressure and they expected that the shift would correlate

with 0-0 distances. We carried out x-ray powder diffraction studies using wavelength dispersive film and energy dispersive counter techniques. We found that the cell dimensions changed from 33.55 nm at 2.36 GPa to 30.35 nm at 20.2 GPa indicating a $\Delta V/V_0$ of 26 percent and a shortening of the O-O bond distance from 29.06 nm to 26.38 nm. There is a sharp break in the compressibility at approximately 15.86 GPa with very little change in A_0 (30.52 to 30.35 nm). This probably indicates that the repulsive forces become highly significant.

At the request of Watervleit Arsenal we are studying the electrical and structural properties of CdS as a function of pressure and temperature. The semiconductor-conductor transition has been measured electrically, by energy dispersive x-ray diffraction, and observed microscopically. The transition is dependent on particle size purity. Single crystals transform at 2.65 GPa, while powders transform at 3.25 GPa. Interestingly, the slope $\Delta P/\Delta P_{trans}$ is negative. At 100°C, the transition occurs at 2.49 GPa and at −44°C, the transition is at 3.24 GPa. All measurements were performed in a 4:1 methanol-ethanol solution and were therefore hydrostatic.

We also made x-ray diffraction measurements above and below the CdS transition. The transition is from the zincblende structure where each atom is tetrahedrally coordinated to the sodium chloride structure where each atom is octahedrally coordinated. Preliminary results indicate that the low pressure phase has a volume compression of − 3.1 percent to the transition and an additional − 19.3 percent upon transforming to the high pressure form.

The compressibility of S_4N_4 was studied with J. K. Stalick of NBS to a pressure of 4.2 GPa through use of a
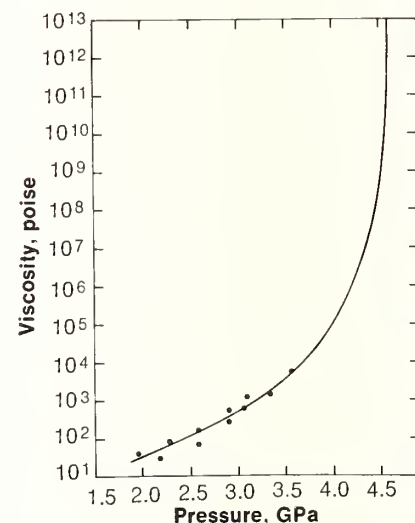
FIGURE 4. Viscosity of n-butyl chloride as function pressure at 20 °C. The equilibrium freezing pressure is 2.3 GPa; above this pressure, the liquid is metastable (super pressed).

new type of diamond anvil pressure cell designed for single-crystal x-ray studies. A single crystal of S_4N_4 was first mounted on a glass fiber and the unit cell determined by centering 15 reflections on the Syntex diffractometer. The cell parameters of the monoclinic unit cell (a = 87.91(1), b = 71.73 (13), c = 87.06(1) nm; β = 92.47(1)° numbers in parentheses represent uncertainty in the values) agree with those obtained from a single crystal placed within the pressure cell with no external pressure applied. Unit cell data were also determined at pressure of 1.3, 3.0, 3.7, and 4.2 GPa. At 4.2 GPa, the cell parameters decrease to a = 81.56(21), b = 66.67(5), c = 81.62(8) nm; α = 89.93(7), β = 91.74(16), γ = 89.90(15)°. The volume of the unit cell decreases from 5.481(2)$\times 10^5$ nm^3 to 4.437(13)$\times 10$ nm^3, a reduction of 19 percent, while the a and c axial lengths become equal within the accuracy of the measurements. The monoclinic metric symmetry is retained to 4.2 GPa.

Since the diamond anvil cell places severe restrictions on the acquisition of data, especially with respect to angle, a theoretical investigation is being conducted to examine the consequences of these limitations for radial distribution function analysis. The method of investigation is to form a comparison of the reliability of various computational procedures and to construct the comparison as a function of the degree of data limitation. An exact set of data having an exactly known radial distribution function is used so that the absolute error can be determined in each case.

The recently developed diamond anvil cell falling-sphere viscometer has been utilized to measure the pressure dependence of the viscosity of stable and metastable n-butyl chloride (see figure 4). This substance was chosen as suitable for a cooperative intra-NBS investigation of metastable states of matter. The equilibrium freezing pressure (2.3 GPa) and the glass transition pressure (4.2 GPa) were determined at room temperature by separate measurements to identify the region of metastability ($2.3 \ \text{GPa} \leq p \geq 4.2 \ \text{GPa}$) (see figure 5). The viscosity was then obtained by starting at a pressure of 1.94 GPa. This transport property was found to vary smoothly through the transition from the stable to the metastable state.

The viscosity results for n-butyl chloride were also used in conjunction with the critical point viscosity model,

$$\eta = A(1-P/P_g)^{-\nu}$$

where η is the viscosity, P_g is the glass transition pressure, and A and ν are other parameters. Use of the model makes it possible to obtain a reasonable estimate of the glass transition pressure if the viscosity as a function of pressure is known for sufficiently high pressures. Values of P_g have thus been
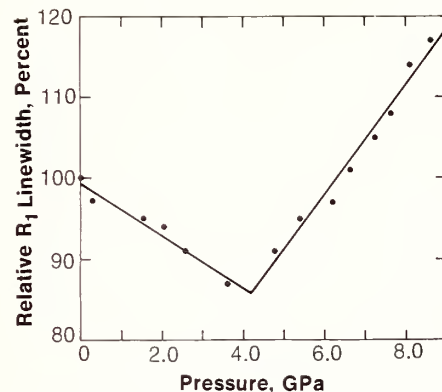

FIGURE 5. Line width of the ruby R_1 fluorescence relative to the one atmosphere value, as a function of pressure at 20 °C when n-butyl chloride is used as the pressure transitting medium. Glass transition pressure = 4.2 GPa.

determined for n-butyl chloride, 4:1 methanol-ethanol, and isopropyl alcohol, and the results have been used to confirm the ruby line-broadening method of determining glass transition pressures. For the noted liquids, the model yields, respectively, 4.6, 10.2, and 5.1 GPa for P_g, and the ruby method yields 4.2, 10.4, and 4.5 GPa.

In addition to confirming the line-broadening method of finding P_g, the viscosity model might prove to be useful for describing the properties of lubricants. Since lubricants are used under conditions of widely varying stresses, the value of the exponent in the viscosity model could be important for evaluating the ability of a lubricant to respond to the changes in the stress. The unusual magnitude of the critical exponent also presents a challenge to theoreticians in this field.

The temperature dependence of the glass transition in 4:1 methanol-ethanol was determined by the ruby line broadening method. At − 48 °C the glass transition is 5.65 GPa yielding $\Delta P_g/\Delta T = 0.68$ GPa per degrees. This value agrees with values obtained at lower pressures for other alcohols.

Piezoelectricity and Pyroelectricity in Poly(vinylidene fluoride)

Martin G. Broadhurst and George T. Davis, Polymer Science and Standards Division

I n the past ten years polymer transducers made of poly(vinylidene fluoride) (PVDF) have been discovered and accepted as reliable, practical and unique measurement devices. NBS was involved in early developments in this field and demonstrated a variety of applications such as intrusion and fire detectors, laser beam profile measurement devices, absolute radiometers, hydrophones, etc. NBS work has stimulated commercial development of transducer devices and their application to measurement problems throughout government.

During this period, we were particularly involved in establishing a broad description of the basis of piezoelectricity and related phenomena in PVDF. This knowledge was needed to guide optimization of the effects and define reasonable limits on how much could be expected from these devices. In the following, we present a general description of the molecular structure of PVDF, show how a simple piezoelectric model was developed and successfully tested, and describe the important consequences of this development.

Microscopic Details of PVDF

PVDF crystallizes from the melt into spherulitic structures. Figure 1 is a photomicrograph of a melt-crystallized PVDF film taken between crossed polaroids. The volume fraction of crystalline material is typically about 50 percent, depending on thermal history. Most of the uncrystallized molecules are in a metastable supercooled liquid phase. The glass transition temperature for this liquid phase is around −50 °C.

We assume, as shown in figure 2, that the spherulites consist of stacks of lamellae which grow outward from the center of the spherulite. These lamellae

89

are typically 10-20 nm thick, depending on crystallization conditions. The molecular chains are approximately normal to the large lamellae surfaces and to the radii of the spherulites. Much of the liquid material is probably located between the crystalline lamellae. That is, a typical region (figure 2) consists of parallel layers of alternating crystal and liquid material, each layer of the order of 10-20 nm thick. Of course, on a larger scale one expects the usual stacking faults, grain boundaries, and other course defects typically found in a polycrystalline solid. Since the molecular lengths are of the order of 100 times the lamellae thickness, each molecule must pass many times through one or more of the crystal layers and is free to assume flexible and irregular configurations in the liquid layers.

PVDF is inherently polar (figure 3). The hydrogen atoms are positively charged and the fluorine atoms negatively charged with respect to the carbon atoms in the polymer. In the liquid phase, the molecules continually change shape due to rotations about carbon-carbon bonds.

The net dipole moment of a group of molecules in a liquid region will be zero in the absence of an applied electric field because of the random orientations of individual dipoles.

In the crystal phase, certain regular molecular conformations are energetically favored for crystal packing. Viewed down the molecular chain, four such conformations are shown in figure 4. All four crystal structures are long lived (whether stable or metastable) at room temperature, and three have polar unit cells. That is, a crystal of polar α, β, or γ phase has a net dipole moment. Crystal phase transformations can occur through mechanical stretching, high temperature annealing or application of large electric fields. In addition to phase changes, changes in orientation of the crystal moment can occur in large electric fields. The field induced changes in orientation and phase occur by rotations about carbon-carbon covalent bonds, or by rotation of molecular segments about their long axes, or both. The driving force is the decrease in the applied field-molecular dipole interaction energy which is extremely large. A typical molecular segment in the crystal has a dipole moment of roughly 2×10^{-28} Cm (70 Debye). The energy of interaction between it and a field of $10^8 \mathrm{Vm}^{-1}$ is several times the thermal energy at room temperature and comparable to the energies needed to rotate molecules in the crystal phase. Thus PVDF is truely ferroelectric, but with the polar alignment caused by VanderWaals forces rather than dipole-dipole forces and with a Curie temperature well above the melting range (170-200 °C) of the various crystal phases.

Model for Piezoelectricity

The preceding established the existence in PVDF of polar crystals preferentially aligned by an applied field so that a PVDF film has a net electric moment. The charge on the film due to aligned dipoles is the product of the polarization (dipole moment per unit volume) and area.

$$Q = N\mu_o (\epsilon_c + 2) <\cos \theta_o>/3l_s, \quad (1)$$
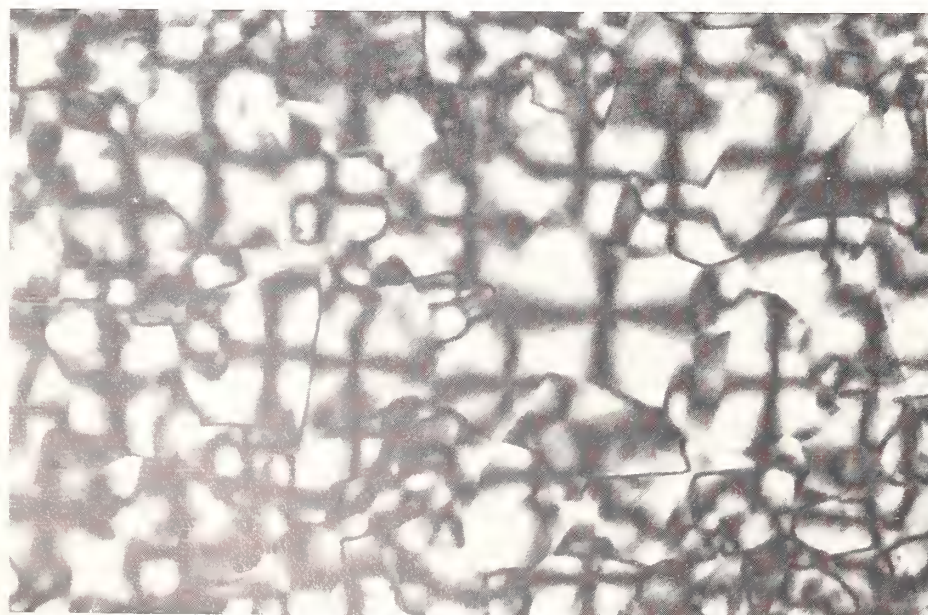

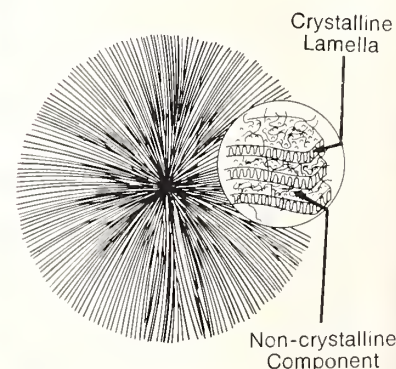FIGURE 1. Photomicrograph of a rapidly cooled melt of commercial unoriented PVDF between crossed polaroids.

FIGURE 2. A schematic diagram of a spherulite and a detail of a section emphasizing the lamellar structure of the radiating branches

where N is the number and μ_o the vacuum dipole moment of the dipoles, θ_o the angle between the dipoles and the normal to the film, l_s the film thickness and ϵ_c the permittivity of the crystal. All of these quantities are measurable.

As a beginning, we asked what the effect of temperature and pressure will be, assuming the dipoles remain orientationally frozen—the simplest possible case. This question does not preclude other possible effects, but we will at least take into account a very basic effect before looking for more subtle mechanisms. Most workers in this field have begun with special mechanisms such as special space charge distributions, changes in the molecular conformations or orientations, etc., without first eliminating thermal expansion and compressibility effects. This neglect is due in part to the relative unimportance of volume expansion in inorganic piezoelectrics.

Taking the temperature and pressure derivatives of the surface charge on the PVDF film and assuming no change in μ_o or the *mean* dipole orientation, we obtain the hydrostatic piezoelectric constant d_p and pyroelectric coefficient p_y.

$$d_p = P_o\beta_c\left[\frac{1}{3}(\epsilon_c-1) + \frac{1}{2}\phi_o^2\gamma + \frac{\partial(\ln l_s)}{\partial(\ln v_c)}\right], \quad (2)$$

$$p_y = -P_o\alpha_c\left[\frac{1}{3}(\epsilon_c-1) + \frac{1}{2}\phi_o^2[\gamma + (2T\alpha_c)^{-1}] + \frac{(\ln l_s)}{(\ln v_c)}\right] \quad (3)$$

where

$$P_o = \Phi(\epsilon_c+2)N\mu_o J_o(\phi_o) <\cos\theta_o>/3v_c, \quad (4)$$

v_c, β_c and α_c are the crystal volume and its pressure and temperature coefficients of expansion, ϕ_o and γ are the amplitude of thermally induced dipole librations and associated Gruneisen constant, Φ the crystal volume fraction and $J_o(\phi_o)$ a zeroth order Bessel function of the first kind.

Independent experimental values were used to evaluate the right hand side of eq. (2) and eq. (3) without adjustable parameters and the results are shown in figures 5 and 6 together with data obtained at NBS.

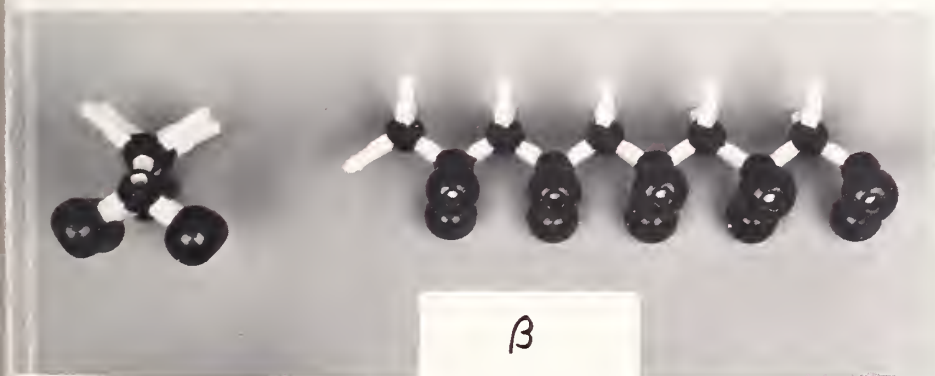FIGURE 3. Molecular model of PVDF in the all-trans conformation found in the β crystal phase. The backbone is composed of carbon atoms, the spheres represent fluorine atoms and the hydrogen atoms, if shown, would appear at the ends of the "sticks" which represent chemical bonds.
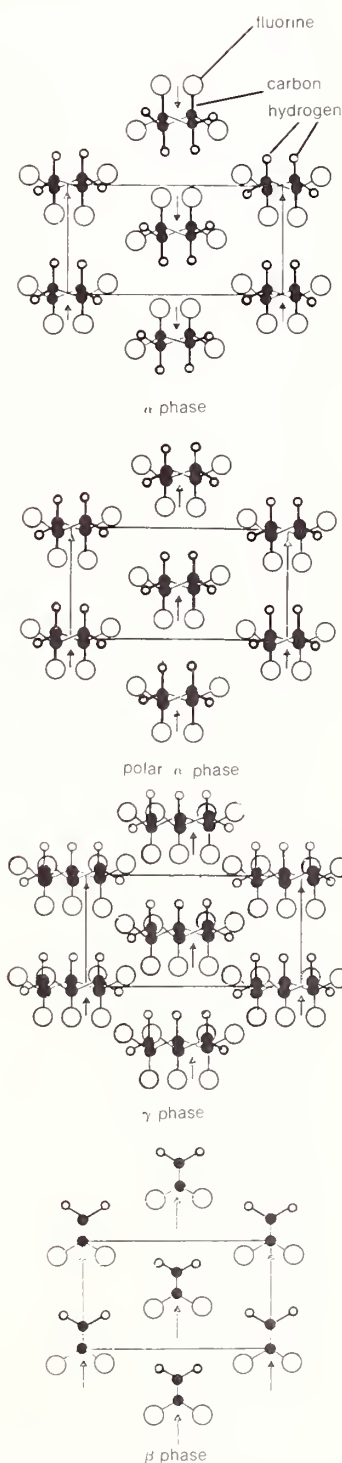

FIGURE 4. Projection of four crystal structures of PVDF viewed along the molecular axes. Dipole moments are shown by arrows.

These results show that without changing the number of dipoles, vacuum dipole moment or dipole orientation, essentially all of the observed piezoelectric and pyroelectric response of PVDF is accounted for. Additional mechanisms connected with transport of space charge, stress dependent re-versible crystallization, molecular rotations, etc., appear unjustified by the data.

Significance of this Development

Based on the above mechanism of piezoelectricity in PVDF, we can make some very strong statements about the optimization and limitations of this material.

(1) Present PVDF has about half the theoretical maximum polarization, so that improvements in performance are expected to be small.

(2) To find a "better" polymer than PVDF, one needs to have a dipole with a smaller volume and larger moment than the compact (CF_2-CH_2) group.

(3) Increasing the crystal to amorphous volume fraction can increase P_o, but will decrease sample compressibility and expansion coefficient with small net gain. Some increase in compressibility can result from incorporating small voids in the specimen.

(4) Use of the polymer is limited to temperatures below the melting point. Increased stability can be expected from increasing the crystal lamellar thickness and thus reducing the ratio of fold surface area to crystal volume.

(5) Moisture and moderate amounts of ionic impurities have negligible effect on the performance of PVDF.

(6) Piezoelectricity and pyroelectricity in PVDF are directly related to the compressibility and expansion coefficient so that both effects will exist together.

(7) The phase having the largest dipole moment will be the most active phase.

These conclusions give confidence in the dependability of PVDF transducers used within the stated limitations and provide firm guidance in the optimization of transducer processing and polymer modification efforts.

FIGURE 5. Piezoelectric coefficient of PVDF film for a change in hydrostatic pressure versus polarization. Circles represent measured data points; the solid line represents values to be expected using eq. (2) with the appropriate values of material properties.

FIGURE 6. Pyroelectric coefficient of PVDF film versus polarization. Open circles are NBS data points, solid circles are from the literature; the solid line represents values to be expected using eq. (3) with the appropriate values of material properties.

Electrochemical Noise Measurements: A New Measurement Technique for Diagnosis and Study of Localized Corrosion

Ugo Bertocci, Chemical Stability and Corrosion Division

Fluctuations in the electron potential and/or current of corroding electrodes are giving information on the breakdown and repair of protective films and are being studied as a possible means of detecting the output of localized corrosion. Iron and aluminum in solutions that can cause pitting were examined. A large increase of noise signal was detected when pitting occurred.

The detection and analysis of the fluctuations in current and potential of electrodes, which are generally called electrochemical noise, are receiving increasing attention in electrochemistry as a means for the study of some aspects of electrode kinetics [1] and are also being applied to the field of corrosion, where the method has the potential to be a useful tool, particularly for the detection of localized corrosion [2].

In the area of electrode kinetics, one of the advantages is that there is no need to apply an external signal to the system under study. The analysis of the experimental results, however, still requires further development of the mathematical models necessary for interpreting the results. As far as localized corrosion is concerned, the examination of the characteristics of the deviations from the average values of the electrode potential and current can give insight in the processes of formation of protective films and their breakdown and might be able to signal the onset of pitting when the average corrosion rate is still low.

A number of techniques can be employed to characterize the electrochemical noise. My main effort has been directed toward looking at the signals
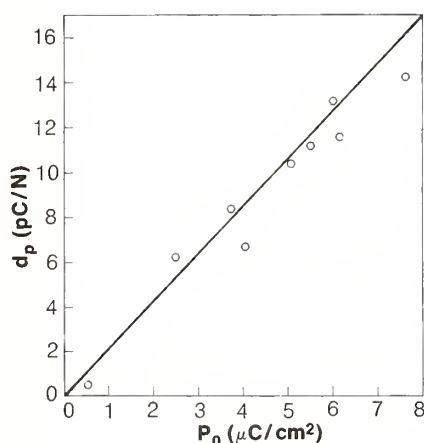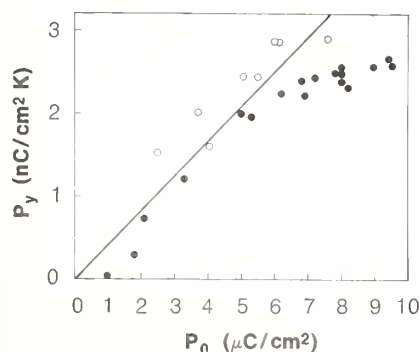
FIGURE 1. Current spectra recorded in potentiostatic conditions on different resistive loads.

In the frequency domain, through use of a spectrum analyzer. In order to minimize interference, some instruments are battery operated, and electromagnetically shielded as well as protected from mechanical vibrations. The level of instrumental noise often limits the electrochemical systems that can be examined, thus, reduction of such noise is of paramount importance in these studies.

For the purpose of studying corrosion processes, it is often convenient to control the potential of the electrode under study. This is accomplished by means of a potentiostat. Commercial instruments, however, tend to introduce noise of unacceptable levels into the circuits, preventing the study of the signals of interest. For this reason, I developed a special low-noise potentiostat with the cooperation of the Special Analytical Instrumentation Group, Center for Analytical Chemistry. The instrument is designed for the detection of fluctuations in the frequency range between 0.1 and 2000 Hz. The internal noise is of the order of $3 \cdot 10^{-8}$ V/$\sqrt{\text{Hz}}$. Figure 1 shows the noise current produced by the potentiostat on different resistive loads. With such an instrument, current fluctuations in the nA range, caused by changes in the elec-
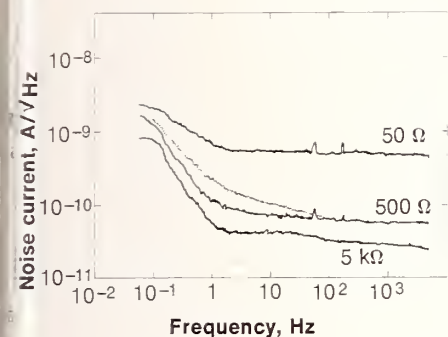
trode characteristics, can be detected above the instrumental noise.

Noise measurements are now being made on various electrodes in order to gather phenomenological information about the noise levels generated by different electrochemical processes and to test the range of usefulness of the apparatus we have developed. For instance, I studied, as examples of low-noise processes [3], the deposition of copper and nickel.

Because it is an electrode system of interest in corrosion science, I examined the Fe electrode in a neutral borate solution with a small amount of chloride added. The voltage noise under galvanostatic conditions was much larger when the electrode was polarized anodically. As shown by the spectra in figure 2, the noise levels increased by more than a factor of ten when the electrode was above the pitting potential. Correspondingly, observation of the voltage signal as a function of time revealed sudden bursts of

oscillations which were probably related to the formation of pits.

Another system I examined was Al in a boric acid: sodium metaborate mixture with and without addition of a small amount of NaCl. In the chloride-containing solution, which is known to cause pitting if the potential is raised approximately above −700 mV vs SCE (Saturated Calomel Electrode) [4], the spectra obtained below and at the pitting potential are shown in figure 3, together with the voltage spectrum.

By dividing the voltage by the current at each frequency, a plot of the absolute impedance |Z| of the electrode as a function of the frequency can be constructed. Figure 4 shows such a plot. Here again, the onset of pitting is marked by a fundamental change of the impedance at low frequency. When pitting does not occur, the random fluctuations in the current density are the system response to the voltage noise input, and the electrode behaves

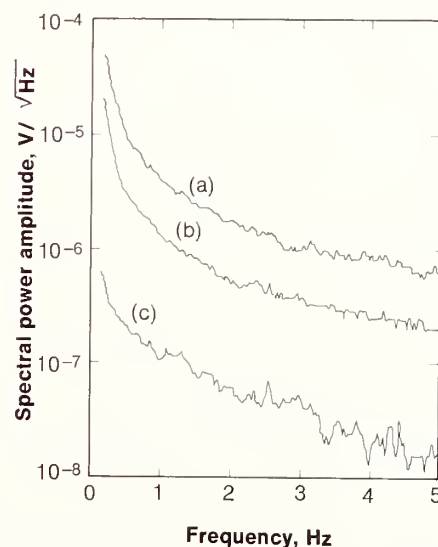FIGURE 2. Voltage spectra iron in borate solution with chloride added. (a) anodic +1050 mV versus SCE; (b) anodic +750 mV versus SCE; (c) open circuit −280 mV versus SCE. Spectra are an average of 16 spectra.
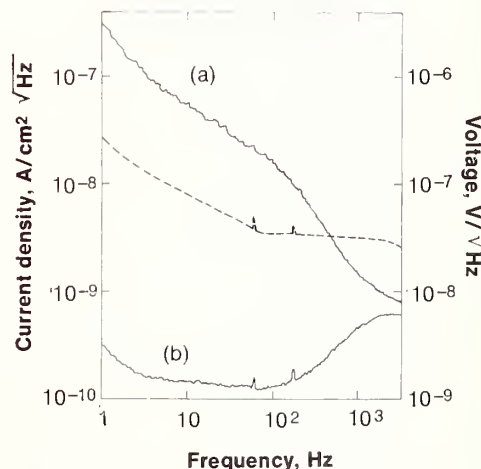

FIGURE 3. Voltage and current spectra for aluminum in borate solution with chloride added below and at the pitting potential. Current density (a) −650 mV versus SCE; (b) 800 mV versus SCE. Dashed line is voltage.
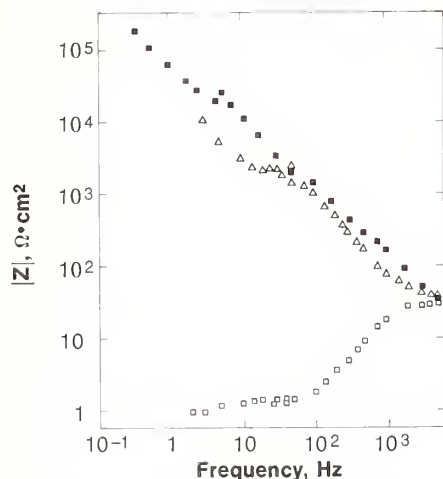
FIGURE 4. Plot of the absolute impedance $|Z|$ for aluminum in borate solution. ■ = −330 mV versus SCE (no chloride); △ = −800 mV versus SCE (0.05 M NaCl); □ = −650 mV versus SCE (0.05 m NaCl).

like a capacitor of about 0.3 $\mu F/cm^2$. Above the pitting potential, the noise current increases more than two orders of magnitude, and the impedance plot cannot be explained except as being caused by fluctuations of the electrode current, independent of the applied voltage signal.

The detection of the current noise is a good indication of the beginning of pitting, and the large fluctuations observed are probably due to hydrogen evolution from the pits [5]. I found the onset of the large current noise to be reproducible within 20 mV.

The noise current, which can be accounted for by oscillations of the order of a few percent of the average dc current, is the sum of several contributions; however, it can be shown that the two major ones are caused by fluctuations of the electrode resistance from the breaking of the protective film and the fluctuations of the double layer capacitance caused either by changes in surface area or in the thickness of the insulating film. At the moment, it is not possible to decide whether the

noise is due more to the faradaic or to the capacitative current. However, the increase in impedance at higher frequency indicates that the capacitative term is probably negligible above about 100 Hz. These results suggest that a dynamic breaking and repairing of protective films on the metal surface are responsible for the signals observed.

This work should thus provide new insights into the basic processes that control corrosion and, in so doing, also offer a new and more effective tool for detecting, characterizing, and measuring various forms of localized corrosion such as pitting.

References

[1] Tyagai V. A., *Elektrokhimiya 3*, 1331 (1967); Blanc G., Gabrielli C., Keddam M., *Electrochim. Acta 20*, 687 (1975); Blanc G., Epelboin I., Gabrielli C., and Keddam M., *J. Electroanal. Chem. 62*, 59 (1975).

[2] Iverson W. P., *J. Electrochem. Soc. 115*, 617 (1968); Okamoto G., Sugita T., Nishiyama S., and Tachibana K., *Boshoku Gijutsu 23*, 439, 445 (1974).

[3] Bertocci U., *7th International Congress on Metallic Corrosion* (Rio De Janeiro 1978). p. 2010 Abraco, Rio de Janeiro (1979). Bertocci, U., *J. Electrochem. Soc.* (submitted for publication).

[4] Pourbaix M., *Corrosion 26*, 431 (1970); Galvele J. R., and de Micheli S. M., *Corr. Sci. 10*, 795 (1970); Nisancioglu K., and Holtan H., *Corr. Sci. 18*, 835 (1978).

[5] Bergeron C. B., and Givens R. B., *J. Electrchem. Soc. 124*, 1845 (1977); Corrosion Res. Conf., NACE, Atlanta (1979).

Migration Models For Polymer Additives

Isaac C. Sanchez, Shu Sing Chang, and Leslie E. Smith, Polymer Science and Standards Division

An important problem in food packaging is the absorption into food of chemicals present in the packaging material. For the past two years, the Polymer Science and Standards Division has been studying the migration of additives from polymeric packaging materials to food simulating solvents. This study has been carried out under the aegis of an interagency agreement with the Bureau of Foods of the U.S. Food and Drug Administration. Our primary goal in this research program has been to develop a migration model which can be used as a guide for the food packaging industry and serve as a sound scientific basis for FDA regulatory decisions.

Initially our research has focused on a class of polymers called polyolefins. These polymers, of which polyethylene is the prototype, represent the majority of plastics used in food packaging applications. Most polyolefins are semi-crystalline, with the glass transition temperature of the amorphous component below room temperature. For such polymers migrations of additives at room temperature often follow simple Fickian kinetics.

We have found a "migration decision tree" (MDT), as shown below, to be a useful device in focusing attention on the specific technical questions that must be answered when evaluating migration. The basis for the MDT is that migration can be limited by any of four physical factors:
1) initial loading of additive
2) solubility of additive in food (simulating solvent)
3) equilibrium partioning of the additive between food and package
4) diffusion.

Non-Diffusion Limited Migration

The maximum permissible amount of migration of a particular additive is

Migration Decision Tree

Given: Packaging plastic (mass M_p) containing M_O gram of additive.

Compare: Migration of additive into a food simulating solvent of mass M_S to the maximum permissible dose or concentration C^*:

$$C^* = M^*/M_S$$

$M_O < M^*$

$M_O > M^*$

Acceptable Migration (load limited)

Determine: Solubility (S) of additive in simulating solvent

$S < C^*$

$S > C^*$

Acceptable Migration (solubility limited)

Determine: Is migration limited by partitioning of additive between solvent and plastic?

Residual concentration of additive in plastic must be greater than

$$C = (M_O - M^*)/M_p$$

Since the partition coefficient K is greater than S, the ratio C^*/C is compared with S:

$S < C^*/C$

$S > C^*/C$

$$\ln K = \ln S + X^\infty + 1$$

Estimate or determine: Additive polymer interaction parameter X^∞

Equilibrium extraction:

$$M_\infty = \frac{M_O}{1 + M_p/K M_S}$$

$M_\infty < M^*$

$M_\infty > M^*$

Acceptable Migration (partition limited)

Estimate or determine: Diffusuion coefficient (D) of additive in polymeric film

Estimate: Maximum migration for a package thickness, ℓ, and a shelf Jife, t:

$$M_t = 4M_O(Dt/\pi \ell^2)^{1/2}$$

$M_t < M^*$

$M_t > M^*$

Acceptable Migration (diffusion limited)

Unacceptable Migration

determined from its toxicology. This amount is presumed known and is usually expressed as a maximum allowable concentration of the additive in the food (C*).

It is obvious that any level of migration is acceptable if the initial loading of additive to the plastic package is small enough so even if all the additive migrates to the food, its concentration level will never exceed C*. This is the first branch of the MDT.

It is also obvious that if the solubility (S) of the additive in the food simulating solvent is limited and S<C*, then migration will always be within acceptable limits. This is the second branch of the MDT.

If the migration is neither load nor solubility limited, then it may be limited by partitioning. At very long times, the additive will equilibrate or partition itself between the food simulating solvent and plastic package. A residual amount of additive is always retained by the package. An example of partitioning is shown in figure 1 for the migration of radiolabeled (carbon-14) n-octadecane from low density polyethylene to a 50/50 ethanol/water mixture. Notice that more than 80 percent of the original amount of additive is retained by the polyethylene. (In this example the ratio of solvent to polymer is about 100.)
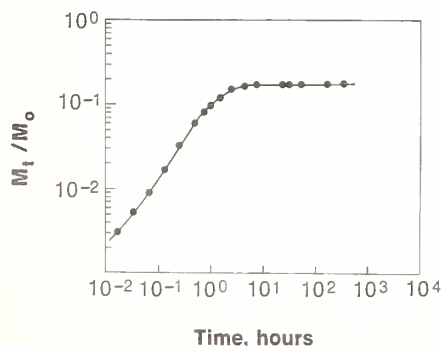
At equilibrium, the ratio of additive concentration in the solvent to its concentration in the plastic is called the *partition coefficient,* K. We have shown [1] that if the additive has only limited solubility in the food simulating solvent, then the relationship between the partition coefficient and the solubility is given by:

$$\ln K = \ln S + \chi^\infty + 1 \qquad (1)$$

where χ^∞ is a parameter (a reduced chemical potential) which characterizes the thermodynamic interaction at infinite dilution of the additive with the plastic packaging material. The parameter is also related to the volume fraction activity coefficient (γ^∞) at infinite dilution by [2]

$$\ln \gamma^\infty = \chi^\infty + 1 \qquad (2)$$

Combining eqs. (1) and (2), we obtain the simple result

$$K/S = \gamma^\infty \qquad (3)$$

Experimental values of χ^∞ are conveniently measured by inverse gas chromatography [3]. For non-polar additives and non-polar polymers, χ^∞ is invariably positive and usually falls in the range:

$$0 < \chi^\infty < 2$$

Positive χ^∞ values are indicative of an unfavorable thermodynamic interaction between additive and polymer. Values of χ^∞ larger than 2 can occur when:
1) the additive/polymer combination is polar/non-polar and/or
2) the additive is large in size.

Positive χ^∞ values imply through eq. (1) that

$$K > S.$$

In figure 2 measured values of K and S are compared for the migration of radiolabeled n-octadecane from high

density polyethylene to various ethanol/H_2O mixtures.

Direct experimental determinations of K or χ^∞ are difficult and time consuming. However, K can be easily estimated by eq. (1) from a known solubility and a theoretically estimated χ^∞. Theoretical methods of estimating χ^∞ are available [2], but even this calculation can be avoided by assuming that χ^∞ has a worst case value of 2 (or larger). Using the definition of the partition coefficient, the amount of additive that will migrate at infinite time (M_∞) can be calculated as shown in the third branch of the MDT.

Equation (1) is based on the assumption that the food simulating solvent is not absorbed by the plastic package. If the solvent is absorbed, then an appropriate correction can be made [2]. Fortunately, in most cases where partitioning is an important consideration, solvent absorption is not. For example, polyolefins do not appreciably absorb water or alcohol and it is usually aqueous and alcoholic food stuffs for which partitioning is important.

Diffusion Limited Migration

If migration is not load, solubility, or partition limited and the maximum
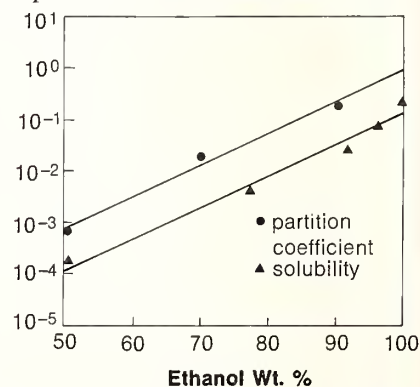
FIGURE 1. Migration of n-C₁₈H₃₈ from LDPE into 50/50 ethanol/water mixtures at 60 °C.

FIGURE 2. Partition coefficients of n-C₁₈H₃₈ between PDPE and ethanol/water mixtures and solubilities of n-C₁₈H₃₈ in ethanol/water at 60 °C.

shelf-life of the packaged food is much shorter than the time required to achieve equilibrium partitioning, migration may be diffusion limited. For simple Fickian diffusion from a plastic sheet of thickness l to an infinite reservoir of solvent, the amount of migration at time t can be estimated from the following equation [4]:

$$M_t/M_o = 4(Dt/\pi l^2)^{1/2} \qquad (4)$$

where D is the diffusion coefficient of the additive in the plastic sheet. For Fickian diffusion, M_t/M_o is linear in $t^{1/2}$ for M_o/M_t values up to about ½. For longer times eq. (4) overestimates the amount of migration. As shown in the fourth and final branch of the MDT, if the maximum shelf-life of the packaged food is known, then the maximum amount of diffusion limited migration can be calculated. (For a finite solvent reservoir, M_o is replaced by $M\infty$ in eq. (4)).

Most of our migration experiments from polyethylene (PE) have exhibited small departures from ideal Fickian behavior. The most common deviation is illustrated in figure 3 which shows the migration of the normal alkane n-$C_{32}H_{66}$ from PE to heptane and to ethanol. The migration curves tend to be slightly sigmodal in character rather than completely concave to the time axis as is characteristic of Fickian diffusion. This positive deviation, which is an unexpected acceleration of migration, is thought to be caused by the absorption and swelling action of the food simulating solvent. To test this conjecture, migration experiments were performed on high density PE containing radiolabeled n-octadecane in contact with unlabeled n-octadecane as solvent. In one experiment the PE was saturated with the labeled C_{18} (about 5 percent by weight). In this kind of experiment solvent absorption effects
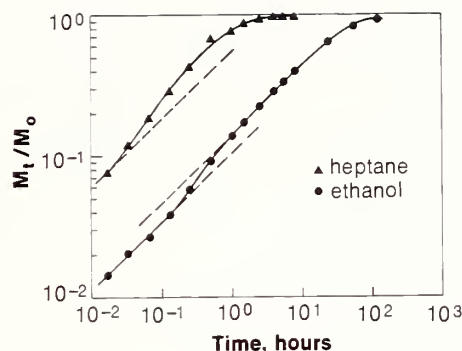

FIGURE 3. Migration of n-$C_{32}H_{66}$ from LDPE into n-heptane and ethanol at 60 °C. Dashed lines have a slope of one half.
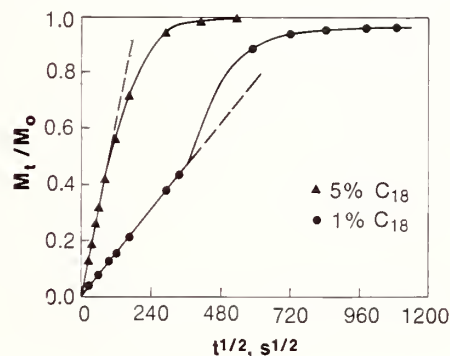

FIGURE 4. Migration of labeled n-$C_{18}H_{38}$ from HDPE into unlabeled n-$C_{18}H_{38}$ at 30 °C.

are completely absent because the PE is already fully swollen. This experiment was compared with one in which the PE was only partially swollen with labeled C_{18} (1 percent by weight). The results are shown in figure 4. As can be clearly seen, simple Fickian kinetics are observed for the fully swollen sample whereas a positive deviation is observed for the partially swollen sample.

Although solvent absorption would appear to cause migration to deviate from ideal Fickian behavior, this deviation is relatively unimportant compared to the effect that solvent absorption has on the absolute value of the diffusion coefficient. In figure 3 n-C_{32} H_{66} has an apparent diffusion coeffi-

cient in low density PE that is about 30 times larger in heptane than in ethanol.

Use of eq. (4) for migration assumes that diffusion in the plastic package is rate controlling. This is not always the case. Our experiments have shown that when the solubility of the additive is very low in the food simulating solvent (K<<1), migration often follows a t rather than a $t^{1/2}$ law. This behavior can be seen in figure 1 where the initial slope of the migration curve is approximately unity. Under conditions of low solubility and solvent stirring, diffusion of the additive through the relatively stagnant boundary layer surrounding the polymer sheet can become rate controlling. We have shown that a linear t law is consistent with boundary layer limited diffusion. We are currently working on a more general theoretical model that will bridge the gap between polymer limited and boundary layer limited migration.

References

[1] Smith, L. E., Sanchez, I. C. Chang, S. S., McCrackin, F. L., and Senich, G. A., Models for the Migration of Additives in Polyolefins, NBSIR-79-1779.

[2] Sanchez, I. C., Equilibrium Distribution of a Minor Constituent between a Polymer and Its Environment, *ACS Symposium Series* Vol. 95, R. K. Eby, ed. (American Chemical Society, Washington, DC, 1979).

[3] Senich, G. A. and Sanchez, I. C., *ACS Organic Coatings and Plastics Chemistry*, Vol. 41, 345-349. (American Chemical Society, Washington, DC, 1979).

[4] Crank, J. and Park, G. S., *Diffusion in Polymers*, Capt. 1. (Academic Press, New York, NY, 1968).

Office of the Deputy Director for Programs

 y C. Gravatt, Jr.

 ndestructive
 aluation
 rold Berger

 nes B. Beal**
 orge Birnbaum
 onard Mordfin
 rbert G. Sutter

 vironmental
 asurements
 liam H. Kirchhoff
 tie T. McClendon
 nes R. McNesby
 lter L.
 Zielinski, Jr.

 ndard Reference
 terials
 orge A. Uriano

 bert L. Alvarez
 semond K. Bell**
 Paul Cali
 Keith Kirby
 onora T. Klein
 bert E.
 Michaelis, Jr.
 nley D. Rasberry
 lliam P. Reed
 hard W. Seward
 nes I. Shultz**

 ndard Reference
 ta
 vid R. Lide, Jr.

 rman P.
 Fivozinsky
 vis H. Gevantman
 nthia A. Goldman
 rla G. Messina
 tiJoyce B. Molino
 rtrude B.
 Sherwood

Robert C. Thompson
Howard J. White, Jr.

**Measurements for
Nuclear Technology**
H. Thomas Yolken

Recycled Materials
Harvey Yakowitz

Donald A. Becker
Joseph G. Berke

**Directorate for
Measurement Services**
Arthur O. McCoubrey

**Weights and
Measures**
Albert D. Tholen

Carroll S.
 Brickenkamp
Stephen Hasko
Joe H. Kim
Henry V.
 Oppermann
Richard N. Smith
Otto K. Warnlof
Harold F. Wollin

**Measurement
Services**
Brian C. Belanger

Kenneth W. Edinger
Lee J. Kieffer
Kathryn O. Leedy
Jack L. Vogt

**Domestic and
International
Measurement
Standards**
David E. Edgerly

Helmut M.
 Altschuler
Samuel E. Chappell
**Research Associates
 and Guest Workers

*ward White is calibrating the high
olution organic mass spectrometer.
is instrument is capable of achieving
tic resolutions of better than 70,000
/ ∆M). The gas chromatographic
et feature of this instrument permits
ntifying individual organic compounds
complex mixtures such as in shale oil
ce elemental compositions of the
lecules and fragment ions are obtained.
e field desorption capability of this
ss spectrometer is used in the analysis
peptides with molecular weights of
ater than 1,000. The clinically im-
rtant peptide, angiotension I, is being
luated as a potential Standard
ference Material. This instrument has
ad applications in studying samples of
erest to several of NML's programs.*

S
even program offices have been established within
NML to focus diverse technical activities on specific
problems and goals. These offices fund, coordinate, and
direct efforts in all NML and several NEL (National
Engineering Laboratory) technical centers. Thus, they
draw on expertise in many scientific disciplines to meet
national needs for measurement services and data. The
offices can be readily separated into two distinct cate-
gories: 1) those based on traditional outputs fundamental
to the NBS mission and related to general, ongoing
national needs; and 2) those that deal with topical areas
and direct NBS expertise in measurement science toward
solving specific current problems.

Into the first category fall offices managing the tradi-
tional NBS outputs: Measurement Services, Standard
Reference Materials, and Standard Reference Data.
They provide the means for tracing measurements to the
national reference standards. Further, they provide
quality assurance for the application of NBS measure-
ment technology in the field. Dating back to the founding
of NBS, these programs have promoted the growth of
organizations which improve measurement, data, and
standardization services throughout the United States
and abroad.

The Measurement Service activities—weights and
measures, calibration coordination, and coordination of
voluntary standards—are specifically concerned with the
practical application of fundamental standards in the
real world of measurement. The weights and measures
effort, which predates NBS, provides the fundamental
standards for the exchange of goods and services in the
marketplace. Although NBS does not have statutory
authority to regulate weights and measures within a State,
it does provide State weights and measures offices with
the necessary technical support to insure fair and equita-
ble measurements throughout the Nation. It also works
to assure that State weights and measurement activities
are traceable to national standards and are capable of
dealing with the complex measurement problems of the
modern marketplace. In the area of calibration co-
ordination, Measurement Services provide leadership and
services to laboratories in industry, State and local
governments, and other Federal agencies through NBS
calibration and measurement assurance programs. A new

program has been established to improve the management and use of precision test equipment in the Federal Government. The Measurement Services staff also coordinate the NML participation in domestic voluntary standards and plays a major role in managing key international standards responsibilities. This office is specifically charged with coordinating NBS participation in the International Organization for Legal Metrology, the Treaty of the Metre organizations, the International Organization for Standardization, and the International Electrotechnical Commission and in preparing policy positions for NBS delegates to these organizations.

The Office of Standard Reference Materials produces and certifies materials standards for the quality assurance of most of the physical and chemical measurements of the United States—and the world. This program presently provides more than a thousand different Standard Reference Materials (SRM's), ranging from over 100 different steel reference materials, through such biomatrix SRM's as trace elements in spinach and bovine liver, to such physical SRM's as Mössbauer Spectroscopy standards and superconductive fixed point devices. The range of SRM's provided serves traditional measurement activity as well as measurement needs related to new technologies. Considerable effort is now going into the production of new environmental and clinical SRM's—a reflection of national concerns in these areas. Presently, the Environmental Protection Agency requires that the calibration standards used in atmospheric measurements be traceable to NBS SRM's, whenever possible.

The third traditional output program is the Office of Standard Reference Data (OSRD). The need for coordination and support at NBS of an international effort to compile and evaluate scientific and technical data has been specifically recognized by Congress in the Standard Reference Data Act of 1968. One-third of the Federal data collection effort is funded through OSRD, and another third is directly managed or coordinated through this office. In addition, OSRD and its constituent data centers in this country cooperate with other data centers throughout the world to avoid duplication of effort and to aid the promulgation of standard reference data. Data efforts in NML range from the large, ongoing data centers in chemical kinetics and thermodynamics to shorter term

data evaluation efforts in high resolution infrared spectra. A highly successful vehicle for disseminating reference data has been the *Journal of Chemical and Physical Reference Data*.

The "topical" program offices of NML presently focus the scientific and technical resources of NBS on national problems in the recycling of waste materials, nuclear technology, nondestructive testing, and the environment.

The Office of Recycled Materials is presently engaged in activities related to urban solid waste and reycled oil. Due primarily to environmental considerations, the problem of the disposal of urban waste is becoming acute for many cities across the Nation. The best solution to the disposal problem is to use waste as a resource, both for raw materials and for fuel. To be a resource standards are needed. Standards, however, are particularly difficult to set for a substance as heterogeneous as urban waste. A current major focus for this office's Resource Recovery Program is the development of standards for refuse-derived fuel.

In the Office of Measurements for Nuclear Technology current activities focuses on the need for accountability throughout the nuclear fuel cycle. This program is concerned with all aspects of the handling and measurements of nuclear fuels, from the determination of volume and flow of nuclear material through the determination of the precise isotopic composition of nuclear fuels by nondestructive evaluation, to the measurement of more accurate values of the life-times of radionuclides. Future plans include standards for nuclear waste disposal.

The Office of Nondestructive Evaluation (NDE) has as its objective the improvement of the reliability and durability of materials and structures by means, of improved NDE procedures and standards. The program's role is to help industry develop and bring to use methods for accurate and reproducible NDE measurements. This includes technical investigations of standards (both physical calibration standards and procedural documents), characterization of instruments, development of improved techniques and the assessment of the meaning of the NDE on material performance.

The Office of Environmental Measurements manages the oldest topical program in NML, the air pollution program. It has evolved since 1972 from a single effort
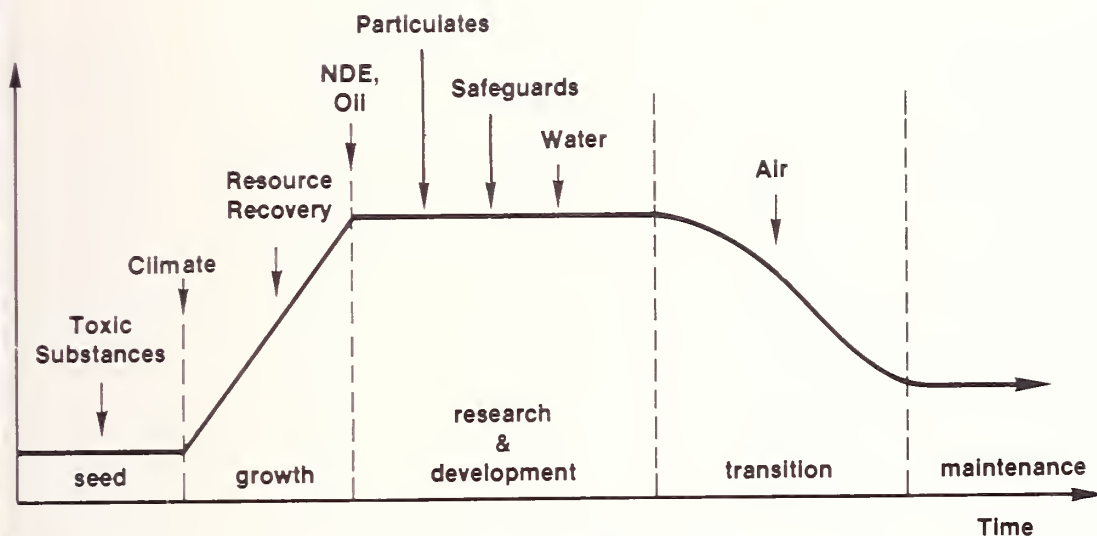
FIGURE 1. Schematic development of nationally focussed NML programs.

the problems of standardization in homogeneous air pollution, to its present major thrust in the development standards for water pollution and particulates. Areas intense effort involve the measurement and characterzation of environmental asbestos and the development of RM's for trace organic compounds in water. A recent oject resulted in a significant revision in the mechanism ozone-alkene reactions used in photochemical smog odels.

The topical programs, unlike the traditional "output" ograms, are planned for limited duration. Figure 1 ves an idealized time development chart for topical ograms and shows the approximate status of various ograms. The time axis can be quite different for the fferent programs. For example, Recycled Oil is expcted to have a lifetime of 5 to 10 years, while NDE will obably last considerably longer. Nevertheless, the chart ustrates the philosophy of the topical programs as they ply NBS expertise to national problems. When the BS contribution is complete, the program is terminated. he ongoing effort represents the transfer of the products the topical program to output programs and, possibly, me ongoing activity carried out within a technical nter. The types of products transferred to output ograms would include SRM's, data compilations, and libration services.

Load Cell Mass Comparator

Randall M. Schoonover, Length and Mass Measurements and Standards Division for Office of Weights and Measures

The calibration of mass standards upwards from 25 kg in value is presently performed on mechanical balances used as mass comparators. The slow balance response time and the handling precautions required to protect the knife-edge bearings make this a time consuming process. In addition, a large amount of laboratory space must be dedicated to a permanent installation. Economies of time and laboratory space would be effected if the mass comparisons could be accomplished using a strain gauge load cell, provided that its precision could be improved at least tenfold over its inherent repeatability. I have constructed a simple comparator based on the use of a load cell, which demonstrates that the tenfold improvement is readily attainable.

The problem in using a load cell to compare a mass standard with an unknown object of the same nominal value is that hysteresis in the cell and loading errors are too large to allow one to exchange loads in the most direct way, i.e., completely unloading the cell and reloading with a different mass. Use of a load cell in this manner is limited to a precision of 0.005 percent. However, the hysteresis and loading errors would be greatly reduced if most of the tension on the load cell could be maintained during the interchange of loads. I was able to do this in a very straightforward way, as described below.

About 90 percent of the tension on the load cell is maintained during the load interchanges by use of a coil spring. Essentially, this is accomplished by suspending the cell coaxially inside the coil spring, allowing the load to compress the spring, and then adjusting the surrounding rigid frame to pre-

vent the release of more than 10 percent of the spring tension.

Figure 1 shows the device in detail. The lifting eye carries the rigid frame and is itself suspended from a building structural member, "A" frame, etc., through a hydraulic cylinder.

A coil spring, with a predetermined spring constant and length, rests on the bed plate centered about a passageway. On the upper end of the spring rests a floating plate with its passageway similarly centered. Horizontal motion of the floating plate is restricted by vertical rods that are part of the frame. The rods, however, do not impede vertical motion of the spring and plate.

Resting on top of the floating plate are a thrust bearing and ball-and-socket assembly. The ball-and-socket permits crude vertical alignment of the cell during initial assembly. The bearing allows the spring to rotate during compression and extension and also removes torque from the cell during the loading cycle.

Adjustable shunt stops are set to interdict vertical motion of the floating plate just before full loading is reached, thus providing a rigid suspension of the cell. When the load is removed, slight vertical motion of the spring and cell is permitted before the constant load

stop runs against the bed plate. This stop is adjusted to provide about 90 percent of full load to the cell when the mass load is removed.

Universal flexure joints provide for a repeatable load axis. Without these, the minor mechanical misalignment that occurs during the load/unload cycle would degrade cell performance.

In addition to the components shown in the schematic drawing, a hydraulic lifting cylinder is required, as is a weight transport system. Dollies and tracks provide excellent weight handling (up to 1000 kg) for the existing device. Also, an electronic device is required to indicate load cell output signal. However, a single such device will suffice for loads from 25 kg to 25 000 kg.

I have constructed a realization of this device at the 225-kg (500-lb) level [1]. Using the device, calibration of 500-lb State mass standards was accomplished to a precision of 0.0002 percent. In addition, the calibration effort required only a few hours as compared to a few days for the same measurements using an equal-arm balance.

I believe that the same approach will be applicable for load cells operating in the range between 25 kg and 5 000 kg—and possibly higher. In particular, at the 25 kg level such a device operating at a precision of 0.001 percent or better would be an important contribution to industrial metrology.

Reference

[1] Schoonover, R. M., A high precision load cell mass comparator, *J. Res. NBS*, **84**, 347 (1979).
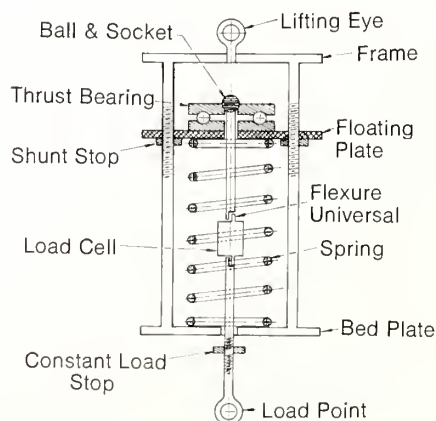

FIGURE 1. Schematic of load cell comparative.

Interagency Cooperation in Mass Spectral Data Base Dissemination

Lewis H. Gevantman, Office of Standard Reference Data

For over three years the Office of Standard Reference Data (OSRD) has been involved in a joint data dissemination project with the Environmental Protection Agency (EPA) and the National Institutes of Health (NIH). This project deals with the collection, evaluation, and dissemination of a mass spectral data file containing over 31,000 chemical compounds. The compounds profile relate largely to health and environmental concerns, but the file is sufficiently diverse to include information on chemical substances of interest to other commercial and academic areas.

Prior to OSRD involvement, the NIH/EPA Mass Spectral Data file was accessible to users via an on-line computer system as a commercially available service [1]. The entry of the OSRD into this project has broadened the methods for disseminating the data and placed a greater emphasis upon the quality of the spectra, both contained in and being added to the file. The ultimate intent is for the activity to provide a depository of the highest quality spectra and to make the high quality data available in a number of formats so as to achieve the widest dissemination tailored to user requirements. Finally, it seeks to influence the community of mass spectral data users and producers to continue to improve the quality of mass spectral data reported in the open literature.

The OSRD, in collaboration with the EPA and the NIH, has made the data base available in two forms: magnetic tape and book. The magnetic tape is available under a lease agreement [2] and is intended for use by organizations who engage in a large number of spectral analyses in the course of their normal operation. The data book [3] is intended to reach the scientific and technical audience which is involved in mass spectral measurement but does not require the degree of use implied in an automated system.

Each entry in the tape file contains a spectrum, quality index, compound name, molecular weight and formula, and the Chemical Abstracts Service (CAS) Registry Number. The entire data base is written on a single 2400-foot reel of magnetic tape in IBM unformatted Fortran(G) and is available in 9-track, 800 or 1600 bpi. Updates of data are provided on a regular (annual) basis.

The book form is published as four volumes plus an index volume. The spectra are indexed in four ways: by chemical substance name and synonyms, formula, molecular weight, and CAS Registry Number. Supplements are being produced periodically, and a complete revised set of indexes is published as each supplement appears.

Every entry is formatted as shown in figure 1. Each spectrum is accompanied by the CAS Registry Number, the molecular formula which is ordered by the Hill convention [4] and derived by computer from the CAS-supplied connection table record. The molecular weight is derived by computer from the same records using the integral atomic masses $C = 12$, $H = 1$, $O = 16$, etc. The structure diagrams, a unique feature of the book, are also computer derived from the connection table record for each substance.

The "Quality Index" (QI) employed in selecting the data is based upon a set of criteria established by F. W. McLafferty [5]. Originally the overall index was made up of seven individual factors dealing with such items as evaluation of the spectrum by an experienced mass spectroscopist, ionization conditions, impurity peaks observed, illogical neutral losses, isotopic abundance, number of peaks, and the comprehensiveness of the data. Additional factors such as compound purity and instrument calibration procedures have been added to the QI to select the spectra in the book and tape.
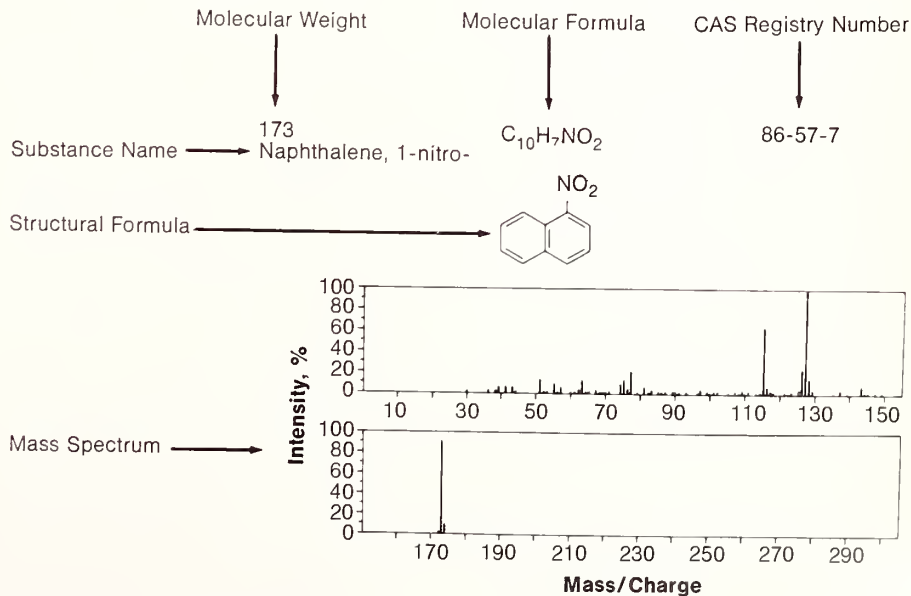

FIGURE 1. Typical mass spectrum.

Standard Reference Material For Antiepilepsy Drugs in Serum

Robert Schaffer and Dennis J. Reeder, Organic Analytical Research Division

Further efforts to refine and extend the use of quality criteria have been pursued in the OSRD. Several technical discussions have been held under the auspices of the Joint Committee for Atomic and Molecular Physical Data (JCAMP) concerning the identification and promotion of measurement specifications which would lead to the improvement of mass spectra in the open literature. A preliminary manuscript based upon the McLafferty criteria but extending and clarifying the required steps is now being prepared. Further refinement of the paper based on critiques by acknowledged experts will lead to a final document which is planned for publication in 1980. Acceptance of these criteria by the International Union for Pure and Applied Chemistry (IUPAC) is also being contemplated.

In employing the two new mechanisms for disseminating the mass spectral data the OSRD has attempted to effect the widest distribution possible. The leasing of the tapes has resulted in a number of arrangements, some related to primary (in-house) use of the tape and others to more extended use. The latter has involved lease by large corporations for distribution within their subsidiaries, lease by data services for dissemination via on-line service, lease by foreign nations for distribution of the data within the specified borders of the country, and finally lease by instrument manufacturers for incorporation of the data in an automated search file associated with experimental mass spectrometer systems. In this way, a wide and divergent group of users has been embraced.

A final step taken by the OSRD to improve the data quality and guarantee the acquisition of mass spectral data is a more recent agreement reached with the United Kingdom Mass Spec-tral Data Centre (MSDC), now based at the University of Nottingham. Originally this group, based at Aldermaston, contributed a large portion of the spectra contained in the file. After some hiatus, this group is again active and seeks to collect, evaluate, and submit for inclusion in the data file the better spectra now found in the literature. The Centre also plans to solicit spectra from industrial, academic, and miscellaneous sources for ultimate insertion into the data file, provided the data meet the quality requirements discussed above. It is believed that the renewed involvement of the MSDC should lead to the achievement of improved spectra and a system which conforms fully to the OSRD goals of improving the dissemination of scientifically reliable data.

Reference
[1] Heller, S. R., Milne, G. W. A., and Feldman, R. J., A computer-based chemical information system, Science, *195,* 253-259 (1977).
Heller, S. R., and Milne, G. W. A., *The NIH/EPA Chemical Information System*, M. M. Milne and W. J. Howe, eds., ACS Symposium No. 84, Chapt. 10, (American Chemical Society, Washington, D.C., 1978).
[2] For further information regarding the leasing of this magnetic tape, please contact: Office of Standard Reference Data, National Bureau of Standards, A323 Physics Building, Washington, D.C., 20234.
[3] Heller, S. R., and Milne G. W. A., *EPA/NIH Mass Spectral Data Base*, NSRDS-NBS 63, 5 volumes, 4685 pp. 1978. PB290661 NTIS, Springfield).
[4] Hill, E. A., *J. Amer. Chem. Soc., 22,* 478-494 (1900).
[5] Speck, D. D., Venkataraghavan, R., and McLafferty, F. W., *J. Org. Mass Spectrometry 13,* 209-213 (1978).

Physicians have depended on the laboratory testing of blood from epilepsy patients to establish that their serum levels of anticonvulsant drugs are within the medically beneficial concentration ranges. Patients might otherwise suffer seizures or toxic effects, depending on whether the drug levels are below or above the therapeutic ranges. A large-scale comparison of laboratory results from testing identical serum samples containing the commonly prescribed drugs revealed unacceptably large differences among laboratories and methods [1]. For each of the drugs tested for, the laboratories reported results ranging from not present to present in toxic amounts.

To help overcome this problem, NBS was asked to provide a Standard Reference Material (SRM) consisting of three serum samples, each to contain four antiepilepsy drugs at different concentration levels. The SRM would fill a basic role for the achievement of accurate analysis, and help ensure the reliability of analyses for these drugs. Table 1 lists the drugs and actual certified concentrations which typify medically designated levels. The SRM was to be supplied as freeze-dried material which would be reconstituted by the user by adding an exactly specified volume of water.

In order to certify an antiepilepsy drug SRM, a series of problems had to be considered: (1) analytical criteria and specifications had to be developed for selecting a special supply of each of the four drugs. These supplies would be employed in preparing the SRM and, of greater importance, they would serve as the primary standards for the certifying analyses that would be performed; (2) the serum used as the matrix for the SRM had to be compatible with the many methods in cur-

Table 1. Concentration Level, μg/mL

Drug	Toxic	Therapeutic	Subtherapeutic	Blank
Phenytoin (Diphenylhydantoin)	60.7 ± 0.9[a]	16.7 ± 0.3	4.2 ± 0.1	0
Ethosuximide	174.7 ± 0.6	75.9 ± 0.5	11.8 ± 0.4	0
Phenobarbital	103.6 ± 0.3	21.6 ± 0.2	5.3 ± 0.2	0
Primidone	18.6 ± 0.7	8.1 ± 0.2	3.6 ± 0.1	0

[a] The uncertainties represent one standard error for the above certified values. The imprecisions observed both within and between the liquid and gas chromatographic anlyses used for this certificate are included in the standard errors.

ent use and, to the degree possible, with prospective methods. This required serum that would be free from chemical and biological (e.g., immunologically active) interferences; and (3) two, independent, highly accurate analytical methods had to be developed for determining the drug levels in the SRM preparations, because NBS certification would not be based on the weighed-in concentrations. The two methods would have to yield sufficiently accurate and precise data that the assignment of values could be unambiguous. This required use of methods for achieving accuracy and precision not ordinarily utilized in clinical laboratory situations.

For selecting supplies of each of the drugs, a variety of chromatographic and spectroscopic techniques were applied to samples whose properties generally conformed with those given in the literature for the drugs. The purity of the selected supply of each drug was determined by liquid chromatography (LC), the compositions of fractions being characterized by supplemental chromatography and spectroscopy.

The specifications we set for compatibility of the serum matrix with a variety of antiepilepsy drug assay methods precluded the use of any but human serum. (Serum from a bovine source, for example, might exhibit cross-reacting antibodies to bovine components in radioimmunoassay reagents.) The large volume of serum needed required the pooling of sera. Since serum from different donors could be expected to contain different interfering substances due to individual dietary habits and drug utilization, we employed several treatments to obtain an interference-free serum. First, hepatitis-free plasma from several donors was clotted by adding calcium chloride, and the serum obtained by centrifuging. The lipoproteins were removed and the serum was heated to deactivate some of the enzymes. The serum was again centrifuged and then dialyzed to remove electrolytes. After re-equilibriation with 0.15 mol/L sodium chloride at pH 6.5 to 7.0, the serum was passed through a bed of charcoal and a 0.22-μm pore-size membrane filter into a sterile container.

We tested the processed serum by observing the clarity of the product after portions were freeze-dried and reconstituted. Unprocessed and processed serum was also tested by reversed-phase LC and gas chromatography (as described below) for evidence of interfering substances. The difference between the original and the processed serum as detected by reversed-phase LC is illustrated in figure 1. All of the serum as detected by reversed-phase LC then divided. A portion would serve as the serum blank and the remainder, in three separate portions, as the matrix for the drugs. Appropriate quantities of the four drugs were added to the three portions. The four pools were then dispensed into vials with a mechanized pipettor which was precalibrated for accurate delivery. The vials of serum were freeze-dried in a prolonged single operation to minimize any irregularity in residual moisture level, and then, when under nitrogen, they were stoppered.

A random selection of vials containing blank serum and three levels of drug-spiked serum were reconstituted with weighed quantities of water. The homogeneity of each kind was determined by differential refractometry. With the refractive index of serum about 0.01 greater than that of water, detection of variations of 0.1 percent required refractive index measurements better than 0.000 01. This was accomplished by comparing the serum samples to a reference aqueous solution containing about 100 g/L of potassium chloride, using a differential refractometer with a sensitivity about 0.000 001. The vial-to-vial variations in the reconstituted sera were less than the variance found by chemical analysis.

Quantitative analysis of drugs in serum was performed by reversed-phase LC, with a fixed-wavelength detector at 254 nm and, for primidone, a variable-wavelength detector set at 210 nm. Peak areas were determined by use of an electronic integrator. Standard samples containing each of the four drugs in 20 percent methanol-80 percent water were run alternately with serum samples. Calibration data were thus obtained concurrently with the sample analyses and were applied
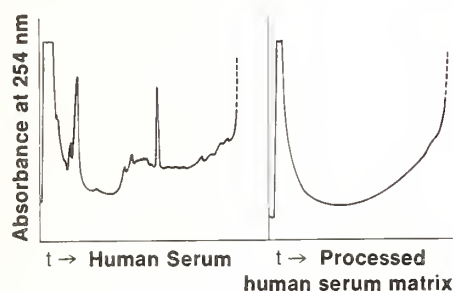
FIGURE 1. Reversed-phase liquid chromatograms of unprocessed, pooled human serum (left panel) and processed serum matrix (right panel).

to give the quantitative results. Figure 2 illustrates a typical chromatogram, recorded at 254 nm.

Our gas chromatographic results were obtained with a special column packing, GP 2 percent SP-2510 DA on 100/120 Supelcoport, to separate the anticonvulsant drugs in their underivatized forms. Flame ionization detection was used, and the output was interfaced with a computing integrator. The compounds used as internal standards in the analyses for the four drugs are listed in table 2. Uniform quantities of the internal standards were combined with 1 mL of the reconstituted SRM sample and, in separate containers, combined with the primary standard drugs taken in quantities about 2 percent lower and about 2 percent higher than the expected (from the weighed-in) quantities of the drugs in
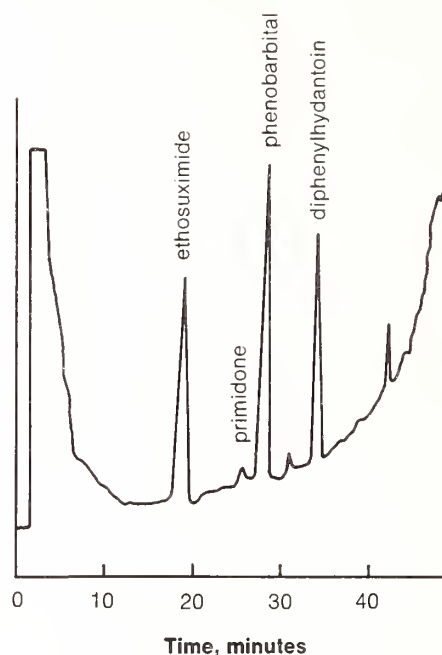

FIGURE 2. Reversed-phase liquid chromatogram of antiepilepsy drugs in processed human matrix (detection at 254 nm).

the SRM sample. Then 1.0 mL volumes of the serum blank was pipetted into the tubes containing the mixtures of primary and internal standards. Usually four SRM samples and two of the bracketing standard mixtures were analyzed as a group, as follows:

Each was acidified to pH 1 to 2 and then extracted with 10 mL of high-purity chloroform. After centrifugation, the aqueous layer was discarded and the chloroform was decanted into a
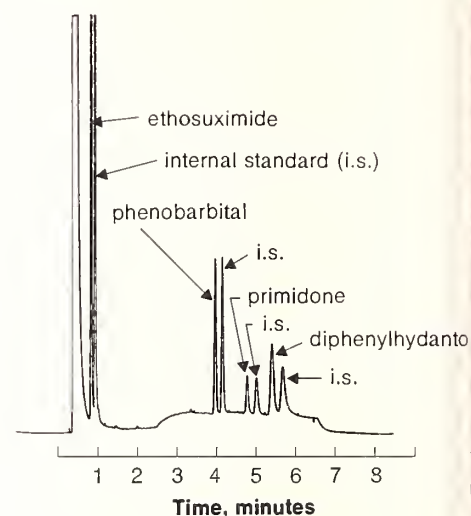

FIGURE 3. Gas chromatogram of antiepilepsy drugs.

15 mL conical centrifuge tube and evaporated at 20 °C under vacuum. The concentrate was dissolved in 50 μL of chloroform and vortex-mixed. One microliter of this solution was then injected into the gas chromatograph. Figure 3 illustrates the separations achieved by gas chromatography.

Standard reference material (SRM) 900 is now being used in clinical laboratories throughout the nation. A new comparison of laboratory results is now in progress, and preliminary findings indicate that this SRM is having a dramatic effect on the quality of the clinical tests for antiepilepsy drugs in human serum.

Reference

[1] Pippinger, K. F., Penry, J. K., White, B. G., Daly D. D., and Buddington, R., Interlaboratory Variability in Determination of Plasma Antiepileptic Drug Concentrations, *Arch. Neurol. 33,* 351-355 (1976).

Table 2. Drugs and internal standards used in GC analysis

Drug	Internal standard
Phenytoin (Diphenylhydantoin)	4-(p-Methylphenyl)-5-phenylhydantoin
Ethosuximide	α-Methyl-α-propylsuccinimide
Phenobarbital	5-Ethyl-5-(p-methylphenyl)-barbituric acid
Primidone	4-Methylprimidone

Development of Test Procedures to Determine Calorific Value of Refuse and Refuse-Derived Fuels

Eugene S. Domalski, Chemical Thermodynamics Division and Joseph G. Berke, Resource Recovery Program

Over the past two years, we have been working on a joint Department of Energy/Environmental Protection Agency project to develop information for a product specification on refuse-derived-fuels (RDF). More recently, we have been working with the Office of Recycled Materials to continue the RDF work in direct response to the mandate of the Resource Recovery and Conservation Act (RRCA) PL94-580.

The research problems stem from the fact that the calorific value of municipal solid waste (MSW) or refuse-derived-fuels (RDF) is currently determined in a bomb calorimeter by using gram-size samples which have been subjected to a high degree of processing. The processing includes grinding, shredding, milling, riffling, and pelletizing of the waste sample. Engineers who are experts in incinerator technology and solid waste processing believe that after such treatment the waste sample no longer resembles or represents the original waste. They claim that significant chemical changes take place as a result of the size reduction (from gross sizes down to below one millimeter) which is necessary in the preparation of a homogeneous waste sample for conventional calorific value determination. Similarly, such engineers have stated that the calorific value determined for the highly processed waste sample may have little or no correlation with the original heterogenerous waste. Because of the enormous heterogeneity of refuse, a suitable procedure has not emerged as yet which may be used with confidence to select and extract a truly representative sample. A suitable test procedure for the calorific value of solid waste from which a reliable thermal efficiency could be calculated would supply a mechanism by which engineers, public works administrators, and private owners could evaluate with confidence whether their large incinerators or refuse-fired boilers are in compliance with contract performance specifications. Such a test procedure can be validated from measurements carried out in a multi-kilogram capacity flow calorimeter on large samples of refuse which have undergone little or no processing. Both the business and industrial communities have expressed the need for a test procedure. In addition both American Society of Mechanical Engineers and American Society for Testing and Materials have also lent support to the NBS program.

NBS Activities

During the initial phases of the program at NBS, the tests were carried out in a 2.5 gram bomb calorimeter. However, due to the concerns of processing the material cited above, a larger sample size calorimeter was required. NBS met the challenge by building a 25-gram sample size bomb calorimeter. Processing of samples, although still required, was less severe than for the 2.5-gram unit; in addition, samples of as received-pellets of commercially produced RDF could also be combusted. The specifics of this work are available in NBS publications: NBS IR 78-1494 and NBSIR 80-1968.

Much of this work is being coordinated with the ASTM committee E-38 on Resource Recovery, which is currently working to establish standard test methods to characterize refuse-derived-fuels and enhance their potential for becoming an article of commerce. The development of markets and sales of refuse-derived-fuels will be linked strongly to appropriate characterization procedures. In particular, the calorific value, which provides a measure of the energy content of RDF, will have greater impact than any other material property on market development because burning will be an important mode of reclaiming energy from processed solid waste for at least the next decade. Thus, a test procedure for determining the calorific value will better equip commercial laboratories to certify accurately the energy content of RDF of various compositions. In addition, the determination of the calorific value of RDF at various stages of processing will identify any stages which impart a different chemical character to the solid waste.

Since many of the current incinerators for waste-to-energy systems burn unprocessed garbage as received, both ASME and ASTM expressed the need to determine the calorific value of the unprocessed garbage. To do so requires using large samples of garbage to ensure some sort of representative "grab" sample. NBS, in cooperation with DOE, is designing and plans to build and operate a multi-kilogram sample size flow calorimeter to handle unprocessed or minimally processed refuse.

To date, pilot units of the flow system using 25-gram samples have been built and tested. Currently, tests are being conducted to determine proper operating parameters of the small units that can be scaled up. Calibration work with known materials is going on to correlate between the 25-gram bomb and the 25-gram flow units. Over the next two years, NBS, with assistance from DOE will construct and operate the multi-kilogram calorimeter and conduct a variety of experiments on fuels and various fuel mixes as related to resource recovery and waste-to-energy systems. The data will include heating values, moisture, ash, and elemental analysis. Although the principal thrust of this research is on the combustion calorime-

Nuclear Fuel Assay Using Resonance Neutrons

Roald A. Schrack, James W. Behrens, and Charles D. Bowman, Nuclear Radiation Division

T**he Center for Radiation Research is developing a technique that will produce images similar to the familiar x-ray image, that will show the distribution of any isotope desired. Using neutrons generated by the NBS linear accelerator, this technique—resonance neutron radiography—provides a unique tool for determining both distribution and content of any sample. The technique is being developed as a reference standard measurement system for the NBS Nuclear Technology Program.**

try of large samples, a variety of other problem areas will be examined which have application to the conversion of waste into energy and the processing of municipal solid waste into refuse-derived-fuels. The problem areas are analysis and characterization of stack effluents, temperature measurement and materials durability in hostile environments, sample composition and characterization, combustion and pyrolysis kinetics, corrosion, and statistical studies in waste stream sampling. Various measurement techniques will be used in the research, including calorimetry, gas-liquid chromatography, spectrophotometry, infrared spectrometry, and thermometry.

This program seeks to provide accurate and timely techniques to keep track of nuclear materials. The resonance neutron radiography technique is used to measure the concentration and uniformity of distribution of fresh fuel rods and to measure nuclear material in scrap and waste from a nuclear plant.

The physical phenomenon that is utilized in the technique is the selective absorption and scattering of neutrons by the nucleus. Every isotope has a different set of energies for which it interacts with neutrons. These energies have been carefully cataloged so that the observations of a characteristic absorption pattern can be used to identify the presence of an element—and in particular the amount and isotope of the element. Previous research at NBS has determined to better than 1 percent accuracy the values of these interaction cross-sections for a wide variety of materials. The values previously determined at the Bureau were submitted to the national clearing house maintained at the Brookhaven National Laboratory on Long Island. We drew on these files in the analysis of our data.

Resonance neutron radiography thus represents a new application and use for information that has already been accumulated. The procedure used is shown in figure 1. Neutrons generated by the NBS linear accelerator are collimated down to a thin fan-shaped beam. A sample of material to be analyzed is placed in this beam. The number and location of neutrons that pass through the sample are determined with a position-sensitive neutron detector placed behind the sample. This information is accumulated in a computer as the sample is scanned. When the sample is completely scanned, the accumulated data are analyzed to produce a picture of the distribution of the desired isotope in the sample. The total amount of the isotope in the sample can then also be determined.

The ability to discern details in the distribution of the desired isotope depends on the resolution of the detector system. Commercially available detec-
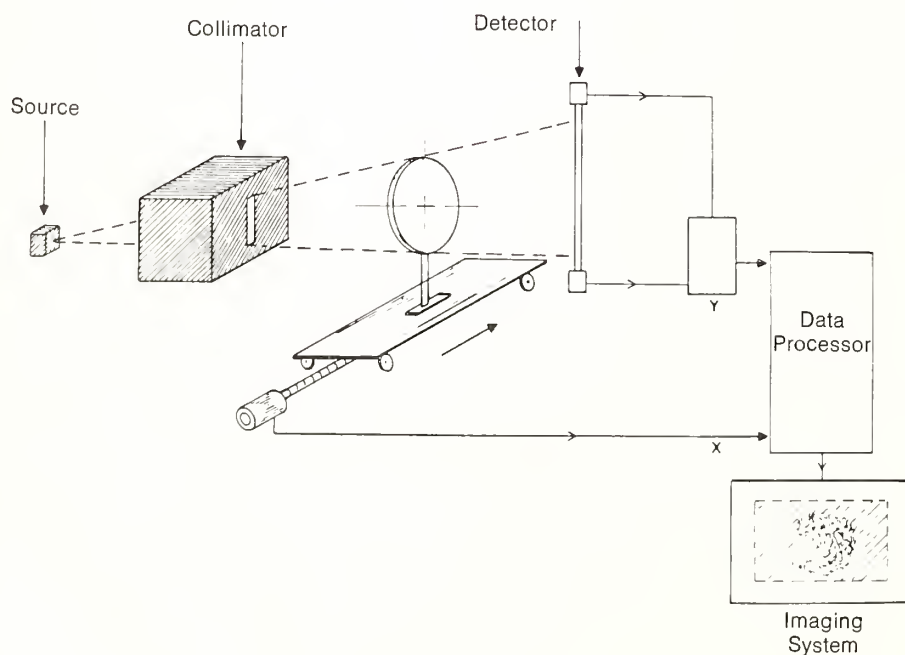

FIGURE 1. Schematic diagram of Resonance Neutron Radiography system. Neutrons are generated in a source by using the electron beam of the NBS linac. The neutrons are then collimated into a fan-shaped beam. The sample to be examined is passed through the beam to produce an image in a computer controlled system.

tors have a resolution limit of about 5 mm; details smaller than this could not be observed. Fuel pellets used in nuclear reactors are 10 mm in diameter, so the available resolution in commercial detectors does not permit a meaningful measurement of nuclear fuel. To overcome this deficiency, a high-resolution detector system was developed by NBS in collaboration with the Oak Ridge National Laboratory. This detector, shown in figure 2, has a resolution of about 1 mm and has been used in the analysis of nuclear fuel.

In addition to its value in the Nuclear Technology Program, resonance neutron radiography promises to be of value in other fields, such as nondestructive evaluation. The examination of manufactured items for hidden defects is frequently done with low-energy neutrons as well as x-rays. Hidden defects in welds can be detected before the equipment is used, preventing costly equipment failure. As an example of this type of use, a sample was made with an intentionally defective joint. Figure 3 shows the result of a resonance neutron radiography of this sample when the distribution of silver in the brazing material was made. No defect was observable with normal x-ray imaging techniques. The defect was only marginally detectable using low-energy neutron imaging techniques.

Research is continuing on the resonance neutron radiographic technique to improve accuracy and resolution and to reduce the time required to produce an image. Although the technique is now restricted to laboratories with high-energy linear accelerators, methods are being worked on to allow the technique to be used on a broader basis and thus become more available as a tool for technology.
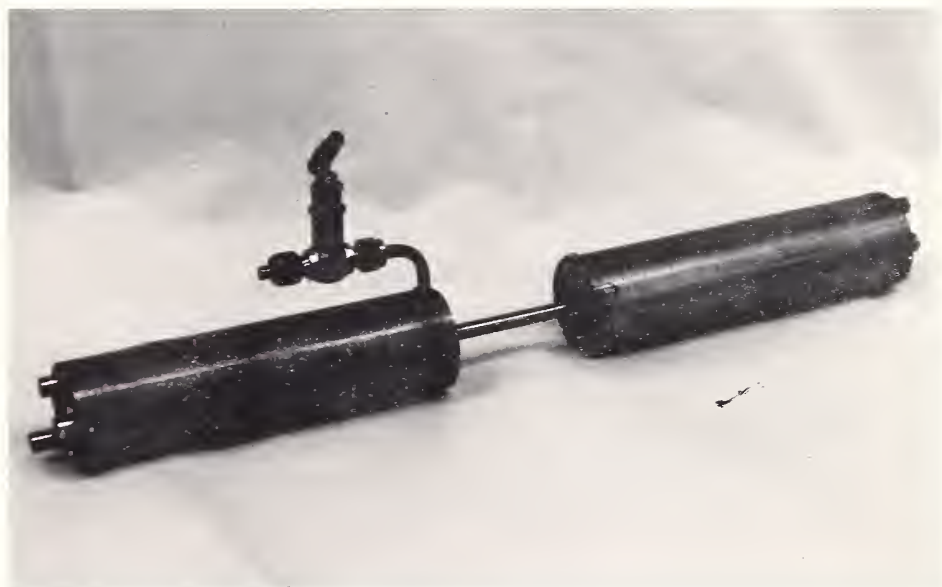

FIGURE 2. High-resolution position sensitive neutron detector. The detector region is the center small-diameter tube. Special amplifiers are enclosed in the large-diameter cylinders at each end. The valve allows the gas used in the ionization chamber to be changed to determine the effects of different mixtures and pressures. The detector is presently operating with a mixture of 3.1×10^5 pascals of ^{3}He, 7.9×10^5 pascals of xenon and 0.4 pascals of carbon dioxide. (10^5 pascal $\cong$ 1 atmosphere).
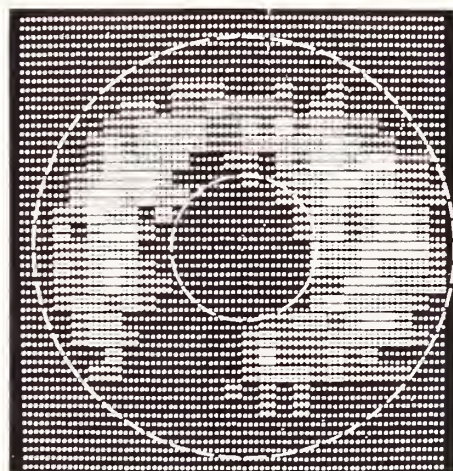

FIGURE 3. Computer-generated distribution of silver in a defective silver solder joint as determined by a resonance neutron radiographic scan.

Improved Uses of X-rays for Nondestructive Evaluation

Masao Kuriyama, William J. Boettinger and Harold E. Burdette, Metallurgy Division

The current need in industry for quality control and early detection of flaws in materials cannot easily be satisfied by simple refinements of existing NDE technology. Fundamental principles underlying the existing traditional techniques should be re-investigated from a fresh point of view. Here we will report the results of such efforts in two different aspects for NDE techniques: one is the resolution improvement of radiography and the other is the measurement of residual stresses within materials.

A. X-ray Image Magnification

Industrial applications of radiography presently demand the early real-time detection of small flaws such as tight cracks in materials. The live images of flaws or structures are recorded (or viewed) usually on a detector (an electro-optical imaging system) with similar size as the image itself. In order to detect small objects, an improvement in the resolution of real-time imaging systems is required, hopefully without loss of image brightness. However, attempts to improve the resolution usually result in a significant loss of intensity. Thus, the detectability (or intensity sensitivity) of small signal changes caused by flaws will be lost because of lack of brightness. Any approach in the improvement of resolution for real-time imaging always encounters two opposing problems: If one improves the resolution, then the brightness generally decreases, and vice versa. Present commercial image intensifiers have resolution limits determined by the multistage configuration and the fiber diameter in fiber optic plates. They may be about 50 μm, down to 10 μm at best.

We have developed [1, 2] a technique which enables us to magnify an x-ray beam containing structure information (radiography or topographic images) before it reaches a detector. This magnification capability can be used either to improve the overall resolution of existing x-ray radiographic techniques which are limited by the detector or to permit the use of less complex (and high gain) imaging systems to attain resolutions already possible. In our demonstration an x-ray magnifier displayed a detailed image of 1000 mesh gold grid (25-μm spacings) with good contrast on a real-time basis on an ordinary image intensifier of 100-μm resolution. In order to magnify an x-ray beam which contains structure information (such as one containing radiographic images), the beam is successively diffracted from two silicon crystals. The first diffraction magnifies the beam horizontally and the second in a perpendicular direction.

This magnification technique makes use of Bragg diffraction from a nearly perfect silicon crystal free from dislocations. This type of Bragg diffraction, often called *dynamical diffraction,* has unique features which are essential for making x-ray image magnification possible. When an x-ray beam diffracts from the surface of a crystal and the diffracting planes are not parallel to the crystal surface, the diffraction is termed asymmetric. There are three aspects of asymmetric dynamical diffraction which are important for the x-ray magnifier: beam magnification, reflectivity, and the acceptance angle for the diffraction. Figure 1 shows schematically the asymmetric diffraction geometry. An incident parallel monochromatic beam of x-rays is magnified in one dimension by a factor m as shown in figure 1, where θ_{in} and θ_{out} are the angles between the crystal surface and the incoming and outgoing beams, respectively. Obviously, high magnifications are obtained when θ_{in} is very small. The "quantum" efficiency of an x-ray magnifier is determined by reflectivity under Bragg conditions. The ratio of the diffracted total flux (photon/second) to the incident total flux is called the reflectivity and is a function of the deviation from the Bragg condition. For a thick perfect crystal with negligible absorption, this ratio is unity for a range of angles centered about the Bragg condition and falls to zero rapidly for larger deviation from the Bragg condition. Because the reflectivity is unity regardless of the diffracting plane, the intensity (photon/second cm^2) of a parallel beam magnified in one dimension by asymmetric diffraction from a perfect crystal is decreased by a factor (l/m) only because of the magnification of the beam area. Since refractive indices for any materials cannot be larger than one for the ordinary x-ray energy range, the unity reflectivity is the highest efficiency—that is, no loss—which one can expect in x-ray optics. As shown
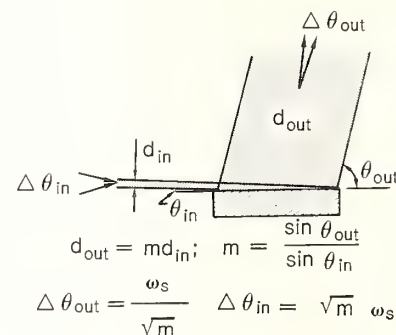

$$d_{out} = md_{in}; \quad m = \frac{\sin \theta_{out}}{\sin \theta_{in}}$$

$$\triangle \theta_{out} = \frac{\omega_s}{\sqrt{m}} \quad \triangle \theta_{in} = \sqrt{m} \; \omega_s$$

FIGURE 1. Asymmetric Bragg diffraction showing one-dimensional magnification of an x-ray beam. The cross-section of the incoming beam, d_{in}, is magnified by a factor, m, to produce the outgoing beam d_{out}. The extremely narrow divergence of the outgoing diffracted beam created by dynamical diffraction guarantees the faithful magnification of x-ray images present in the incoming beam.

in figure 1, the maximum divergence of the outgoing beam, $\Delta\theta_{out}$, is related to the quantity ω_s, which is determined by the crystal property of silicon, and is of the order of 6 arc second. This small value of θ_{out} guarantees the one-to-one correspondence of the details between the unmagnified images and the magnified images. Since the reciprocity law holds for x-ray magnifiers, demagnification needed for lithography can, in principle, be achieved by these magnifiers.

B. X-ray Residual Stress Evaluation in the Interior of Materials

One of the nondestructive methods currently used for measurements of residual stresses in industrial materials involves the application of x-ray analysis for stress measurement. X-ray diffraction phenomena are used to determine macroscopic residual stresses in engineering components. The methodology of analysis and its basic principles are well known. Briefly, when materials are under stress, x rays are diffracted with a Bragg angle which is slightly different from the Bragg angle expected in unstressed materials. The change in the Bragg angle is related to the alteration of atomic interplanar spacings when the crystal lattice of the materials is strained. As a measurement system, the essential part of this x-ray technique is the accurate measurement of lattice constants (or their changes) in materials by use of well refined Bragg diffractometry. The surface residual stress can be evaluated from the strains measured by x-ray diffractometry using a set of assumption regarding material elasticity and homogeniety. Although the accuracy obtained by this technique is, in principle, superior to any other methods, an obvious shortcoming lies in its in-

capability of detecting strains (or stresses) in the interior of bulk materials.

Currently, improved quality control of industrial components demands quantitative information concerning the stress distribution near cracks and residual stress distributions after different types of cold working and heat treating. These demands naturally lead to the necessity of measuring residual strains in the interior of materials. Ordinary Bragg diffractometry will not be sufficient to respond to these demands. There is an entirely different approach to the x-ray evaluation of residual strains although it uses the principles of x-ray diffraction. This approach involves the use of energy dispersive solid state detectors with high energy x-ray photons. The use of solid state detectors has been introduced very effectively in the fields of scanning electron microscopy (microanalysis) and x-ray fluorescence analysis of materials in the past ten years. It is called energy-dispersive spectroscopy. Unlike these successful applications, this technique has not been applied to the residual stress (strain) measurements of materials. Extremely high resolution and accuracy are required for strain measurements in comparison with the other applications. If one could improve the resolution sufficiently and overcome other important technical problems, this new system will be ideal for residual stress measurement in industry; the equipment will be compact and the results will be displayed visually and almost instantaneously, and analysis of the data will be made on site by a computer. Also this system, in general, works better for high energy photons. High energy photons also make practical the use of the transmission geometry, since the x-ray absorption coefficient of materials is ap-

proximately inversely proportional to the third power of the energy of x rays.

The use of an energy dispersive system for possible residual stress evaluation was tested in 1973 by Leonard [3], who concluded, however, that this system did not have sufficient accuracy for this purpose. We have proven that his conclusion was premature, and that it is still too soon to dismiss the possible industrial use of this technique for the evaluation of residual stresses. In so doing, we have proposed [4, 5] a method for determining a strain tensor in predetermined volumes in the interior of a material, as shown in figure 2. In energy dispersive spectroscopy, one is concerned with the energy spectral profiles and peak positions at different energy values, instead of Bragg angles which play a key role in Bragg diffractometry. Lattice constant will be measured in energy dispersive spectroscopy by the energies of diffracted photons:

$$d(A) = \left(\frac{6.199}{\sin\theta}\right) \frac{1}{E(\text{kev})} \quad . \quad (1)$$

Here, d is an atomic interplanar spacing related to lattice constants, E is the energy of diffracted photons measured from peak positions of the spectra, and the coefficient including half the scattering angle θ is constant for a given scattering geometry. For our purposes, the scattering angle should be smaller than $30°$ to ensure complete transmission geometry.

One may claim that the energy resolution of current solid state detectors is not adequate for the evaluation of residual strains. Fortunately, it has been known that each diffraction profile in the energy spectrum obtained from a solid state detector is very close to a Gaussian. If the mathematical shape is known for a spectral profile, then the claim mentioned above can be
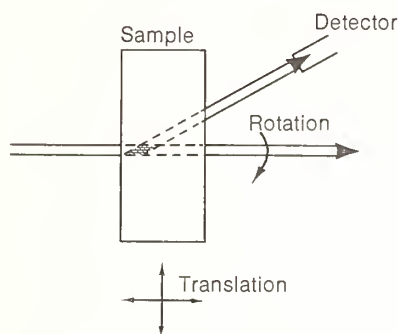
FIGURE 2. An example of the geometrical arrangements for the evaluation of residual strains in a predetermined volume inside materials. The sample is rotated three times around an x-ray beam to give six independent sets of measurements with two detectors. The mapping of strains throughout the volume of the sample is achieved by translations.

FIGURE 3. An example of the observed diffraction profile fitted with a Gaussian curve with linear background.

ideal for an industrial use on site, particularly when data are handled by a mini-computer. By no means has an energy dispersive system such as used here reached the ultimate resolution; further improvements of x-ray optics and detectors should be made, in particular, with high energy photons.

Reference

[1] Kuriyama, M., Boettinger, W. J., and Burdette, H. E., Proceedings of Symposium on Real-Time Radiologic Imaging, National Bureau of Standards, May (1978).

[2] Boettinger, W. J., Burdette, H. E., and Kuriyama, M., *Rev. Sci. Instr.,* *50* 26-30 (1979).

[3] Leonard, L., Franklin Institute Research Lab (Philadelphia) Report F-C3454 July (1973).

[4] Kuriyama, M., Boettinger, W. J., and Burdette, H. E., American Society for Nondestructive Testing, National Fall Conference, Denver, CO, 49 October (1978).

[5] Kuriyama, M., Boettinger, W. J., and Burdette, H. E., Symposium on Accuracy in Power Diffraction, National Bureau of Standards, June (1979).

circumvented: Mathematically fitting the observed peaks with Gaussian functions, one can determine the centroids (or peaks) of the profiles far more accurately than the $\Delta E/E$ value of detectors would indicate. As shown in figure 3, one can improve by a factor of 100 the accuracy of determining the centroid positions.

Figure 3 shows an example of the observed spectral profile which has been fitted by a Gaussian curve with a linear background. The accuracy of determining the centroid (or peak) position has been found to depend simply upon counting statistics. Reproducibility of those positions has also been tested; as long as the same predetermined volume is viewed, the centroid position remains identical within the statistical error. As a reference to possible instrumental instability, Ag $K\alpha$ line spectrum in each run has been fitted with a Gaussian curve. (White radiation was obtained using a Ag target tube.) The Ag $K\alpha$ line result indicates that the instability, if any, is not significant enough to jeopardize the
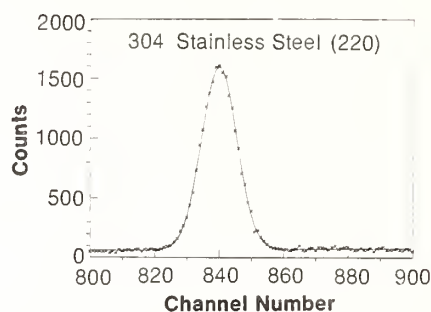
accuracy in the determination of diffraction peak positions. Our result demonstrates that the strains of 5×10^{-5} can be detected in the predetermined volume of $0.5 \times 0.5 \times 0.5$ mm^3 with reliable reproducibility, if sufficient counting statistics are established, while strains of 3×10^{-4} can easily be detected even with moderate counting statistics.

In conclusion, an energy dispersive diffraction system has demonstrated its capability as a useful tool for the determination of residual stresses inside materials, when the curve fitting technique is used simultaneously. The present demonstration has been carried out with low energy photons. The use of high energy photons certainly makes more practical the use of these energy dispersive systems for residual stress evaluation. More penetration and increased energy resolution of detectors will improve the resultant accuracy and detectability of strains. Since the energy dispersive system can be made simple and compact, without any delicate moving parts, the system is quite

High Accuracy Particle Size and Particle-Fluid Interaction Measurements Using the Particle Doppler Shift Spectrometer

David S. Bright and Robert A. Fletcher,
Gas and Particulate Science Division

W̳e have increased the accuracy and precision of the Particle Doppler Shift Spectrometer (PDSS) measurement technique through improvement of its light optics and its data reduction and analysis systems. With the PDSS, we can now determine the diameter of spherical aerosol particles in the 5- to 15-μm range with an accuracy of 0.05 μm. This high accuracy made it possible for us to study particle/fluid interactions that have been undetectable by other techniques, though such interactions have been theoretically inferred.

The basis of particle diameter measurement by the PDSS is a modification of the laser velocimetry technique. The sample cell, a vertical tube, is intersected by a horizontal laser beam. Light is scattered by both the stationary windows of the sample chamber and by any particles falling through the laser beam. Scattered light at 6° above horizontal is detected and measured with a photomultiplier having well collimated collection optics. The light scattered by the settling particles is Doppler shifted with respect to the incident light; the magnitude of the frequency shift is proportional to the settling velocity of the particle. The Doppler shifted frequency is measured by mixing the light from the particle and from the windows (unshifted light) and analyzing the resulting signals. With a Fast Fourier Transform analyzer, the amplitudes of the scattered light signals are stored according to frequency. From the frequency of the scattered light, we determine the settling velocity of the particle; from the settling velocity, we can calculate the particle's diameter by using Stokes's law.

In addition to the particle diameter information contained in the frequency of the scattered light, we are able to also obtain particle size information from the amplitude of the scattered light. The intensity of light scattered from a spherical particle is a complex function of the particle size, angle of observation relative to the incident light, the indices of refraction of the particle and the suspending media, and the wavelength of the light. The intensity of scattered light as a function of particle diameter may be calculated from Lorentz-Mie theory. The calculation for the parameters of our experiment (6° angle of observation, known wavelength, and indices of refraction) give the curve shown in figure 1, which contains many maxima and minima features. The calculated curve is experimentally equivalent to summing the scattering intensities from a uniform distribution of particles having diameters covering the range of the Mie calculations. Such a summation of intensities is also shown in figure 1 and clearly demonstrates the features of the calculated Mie curves. The duplication of the calculated Mie curve features in the experimentally obtained curve allows us to use the features in the experiment curve as accurate size calibration markers. For a given feature, the Mie calculation gives us an accurate value for the particle diameter, from which we can calculate the particle settling velocity on the basis of Stoke's law. The settling velocity can also be determined experimentally from the Doppler shift frequency for that feature of the curve. Through sophisticated data analysis, we are able to compare the settling velocities calculated from the Mie theory with the settling velocities experimentally determined from the Doppler shift such that we can detect velocity differences as
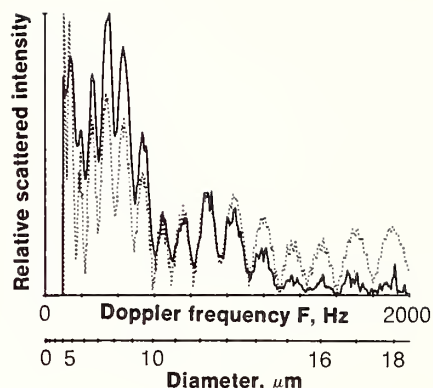

FIGURE 1. Relative scattered intensity as a function of diameter calculated from Lorentz-Mie theory (lower axis) and of Doppler frequency obtained experimentally (upper axis). . . . . is calculated data, — is experimental data.

small as a few μm/s, or equivalent to diameter differences of only 0.05 μm.

This sensitivity allowed us to verify the Stoke's equation for particles in the 5- to 15-μm diameter range. In order to accomplish this verification, it was necessary to demonstrate that we were not perturbing the settling velocities in some way. Thermal convection adds large velocity increments to the settling velocity and removes most or all size dependency, which may easily be seen in the loss of the features of the scattering curves. Though we find no evidence of thermal convection, we do find under certain sampling conditions a particle-induced fluid flow phenomena.

When a particle gravitationally settles through a fluid (air in our experiments) the drag force of the fluid results in a small momentum transfer to the fluid causing a small fluid flow in the direction of the settling particle. This flow then serves to increase the settling velocity of neighboring particles because the fluid is no longer stationary, but is moving with the settling particles.

We demonstrated this effect by comparing the following two experiments: In the first experiment, we measured the settling velocity of particles when they uniformly filled the settling chamber and compared it to the calculated velocity to verify that no velocity shift occurred. We use this sample geometry for particle size measurements. In the second experiment we measured the settling velocity of a 4-mm diameter column of settling particles in a 9-mm diameter settling chamber. The air sheath around the column of particles was void of particles. With this experimental condition we observe an increase in the settling velocity, which is particle concentration dependent, as shown in figure 2. The velocity increase represents the velocity of the induced air flow, which adds to the settling velocity.

The induced fluid flow is manifested in the second experiment because a return flow path exists—the particle-void region of the settling chamber. In the first experiment, no velocity shift is observed because the return flow is uniform over the entire volume and effectively cancels the drag effect on the particles.

The induced fluid flows we observed are on the order of 10 to 100 μm/s. An order of magnitude calculation, balancing the fluid viscous diffusion force and the Stoke's drag force, gives fluid velocities which are in good agreement with these values.

The sensitivity of the particle settling velocity to the induced flows of such low magnitude can be measured by the PDSS due to the accuracy we can obtain by using the Mie scattering curve features as size calibration markers. We know of no other technique that can determine particle diameter in the 5- to 15-μm diameter range to an uncertainty of 0.05 μm or that has the sensitivity to detect particle-fluid interactions of the low magnitudes we have described above.
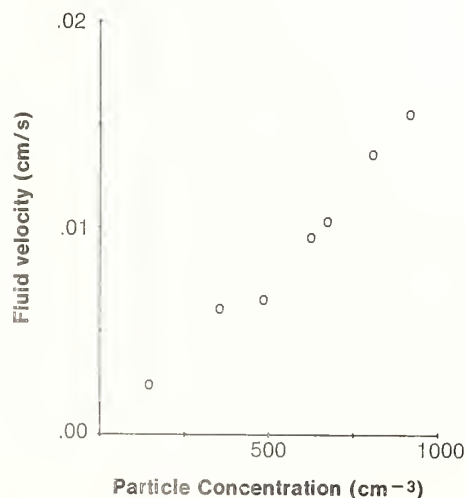

FIGURE 2. Fluid velocity as a function of particle concentration.